THE UNIVERSITY *of* EDINBURGH

Electromagnetic Characteristics of High Temperature Superconductor Coated Conductors Applied to Electric Machines

A thesis submitted by Hongye ZHANG
for the degree of Doctor of Philosophy
School of Engineering

University of Edinburgh

2021

Declaration

1) I declare that this thesis has been composed solely by myself and that it has not been submitted, in whole or in part, in any previous application for a degree. Except where states otherwise by reference or acknowledgment, the work presented is entirely my own.

2) I confirm that this thesis presented for the degree of PhD in Energy Systems, has

   i) been composed entirely by myself

   ii) been solely the result of my own work

   iii) not been submitted for any other degree or professional qualification.

3) I declare that this thesis was composed by myself, that the work contained herein is my own except where explicitly stated otherwise in the text, and that this work has not been submitted for any other degree or processional qualification except as specified. Parts of this work have been published in the work stated in the list of publications.

Signature: _____ **Date:** _____

Table of Contents

List of Figures

List of Tables

Acknowledgements

The work presented in this thesis would not have been completed without the help and support of many people. To all who have contributed, either directly or indirectly, to the completion of this thesis I am deeply grateful.

Firstly, I would like to express my most sincere gratitude to my supervisor, Dr Markus Mueller. Not accepting me as his student, I would not have pursued my PhD studies smoothly. Without his careful guidance and expert knowledge in machine designs, this project could not have been finished. The advice and professional criticism he provided throughout my PhD programme have helped me in an immeasurable way and ensured the completion of this project on time. His appreciation and selfless protection have allowed me to concentrate on my research work with full hope. I also would like to give my great thanks to Dr Zhenan Jiang from the Victoria University of Wellington, New Zealand, for sharing with me important experimental data and Dr Francesco Grilli from the Karlsruhe Institute of Technology, Germany, for his enlightening feedbacks, kind encouragement, as well as great insight for numerical modelling.

I would also like to thank my colleagues at the University of Edinburgh, without their support and friendship this journey would have been much more difficult. I want to thank my colleagues from the electrical machine group and the applied superconductivity group, in no particular order, Min Yao, Kevin Kails, Philip Machura, Hongyi Chen, Zezhao Wen, Adam Harris, Yvonne Baird, and Mbayer Abunku. Working with you all is truly an enjoyable experience. I must give my special thanks to Dr Quan Li for providing me with an opportunity of coming to Edinburgh to start my PhD studies. I also have to thank Dr Yu Cao from the Institute for Energy Systems for his knowledge and help on scientific computing.

Additionally, I must give my warmest affection and love to my parents for their wholehearted and selfless support, and my fiancée, Xi Liu, who has embellished the last year of my PhD journey, bringing me endless happiness and heartening me to pursue my research dream bravely. Finally, I would like to extend my sincere thanks to all my friends, because your emotional support has always been my source of courage to embark on new challenges.

This work was supported by the Joint Scholarship from the University of Edinburgh and China Scholarship Council (CSC) under Grant [2018] 3101.

Abstract

Superconductor technology has attracted increasing attention during the last few years because of their advancements made in the material manufacturing technology and the reduction of cost. As a result, superconducting materials have been widely applied to power industries, of which one of the most promising and popular applications is the electric machine, which is the core component of power generation and consumption on the earth. The second-generation (2G) high temperature superconducting (HTS) coated conductor (CC) has become increasingly appealing among all the superconductors on account of its commercial availability and advantageous current carrying capacity. Therefore, HTS electric machines are believed to usher in a period of development opportunities. However, there still exist many challenges related to the efficiency, cost-effectiveness, reliability, and safety of HTS machines, and the alternating current (AC) loss of HTS CCs remains one of the most significant issues. Over the years, the effort of studying the AC loss of HTS CCs has yielded many outstanding research outcomes; however, most of them have been focused on the loss estimation at power frequencies under purely sinusoidal currents and magnetic fields. In fact, the electromagnetic environment in electric machines is abundant in high-frequency ripple fields and harmonics, especially for high-speed rotating machines. Therefore, the AC loss characteristics of HTS CCs at high frequencies remain unclear, to some extent. Aiming to analyse systematically the AC loss properties of HTS CCs applied to electrical machines within a wide frequency band, from the power frequency to kHz level, this thesis adopts analytical equations, numerical modelling methods, as well as experimental measurements. In doing so, this project hopes to contribute to the loss quantification and controlling of HTS CCs in electrical machines, providing a useful reference for the design of large-scale superconducting devices.

This thesis starts by providing a comprehensive literature review of the state of the art of AC loss related studies. The analytical formulae, modelling methods, measurement approaches, as well as reduction techniques for the AC loss of HTS materials in both low- and high-frequency fields are systematically summed up. The review work clarifies the research status of the AC loss of superconducting materials applied to electric machines, elucidating that the electromagnetic loss characteristics of HTS CCs deserve further investigation, especially at high frequencies in high-speed rotating machines.

Numerical models are an indispensable tool for studying the anisotropic electromagnetic properties of high temperature superconductors (HTSCs), thus numerical modelling is chosen as a primary method in this thesis to study the AC loss of HTS CCs employed in electric machines. The methodologies adopted to build the simulation models are introduced, which are based on Maxwell's equations and the finite element method (FEM). The numerical models here are developed mainly through two formulations, namely ***T***-formulation (***T*** represents current vector potential) and ***H***-formulation (***H*** denotes magnetic field), which can be achieved by FORTRAN 90 or incorporated into COMSOL Multiphysics.

Dynamic loss is a crucial component of the AC loss of HTS field windings in superconducting machines, which occurs when the HTS CC carrying a direct current (DC) is exposed to an AC magnetic field. Therefore, the dynamic loss of HTS CCs is explored in detail. The dependence of dynamic loss on the material properties (critical current density and *n*-value) is investigated. Then, a novel formulation is derived to describe the full-range variation of dynamic loss. At last, three new parameters are defined to characterise the non-linearity of dynamic resistance. The proposed analytical formulae and parameters are validated by the ***T***-formulation based numerical model and experimental measurements.

In superconducting machines, the HTS CCs are usually utilized in the form of stacks and coils. Therefore, besides a single HTS CC, the transport current loss, magnetization loss, dynamic loss, and the total AC loss of HTS stacks, coils (circular and racetrack coils), and trapped field stacks (TFSs) over a wide frequency band, from the power frequency to kHz level, are studied respectively. The ***H***-formulation based 2D and 3D numerical models are mainly adopted here, which are validated by published experimental data. It is found that the widely used thin film approximation in modelling which only considers the superconducting layer of HTS CCs is inapplicable at high frequencies (higher than 100 Hz for magnetization loss) due to the skin effect, and the non-superconducting parts (the copper stabilizer, silver overlayer, and substrate) have to be taken into account. AC loss varies non-linearly with the frequency of the AC transport current or magnetic field because of the electromagnetic interactions between different layers. The shielding effect between different turns of an HTS coil is also explored, which can enhance the dynamic loss in the middle turns of the coil while the magnetization loss occupies the majority in the outer turns at high frequencies. The electromagnetic properties of a curved HTS TFS under high-frequency cross fields are investigated, too, which possesses geometrical applicability for cylindrical rotating shafts. It is demonstrated that the widely adopted 2D-axisymmetric models are inapplicable to study the anisotropic electromagnetic distributions of TFSs because of the emergence of the

electromagnetic criss-cross. High-frequency ripple fields can drive induced current towards the periphery of the HTS TFS due to the skin effect, leading to a fast rise of AC loss and even an irreversible demagnetization of the TFS.

In order to combine AC loss analysis and machine applications, a special magnet made of HTS coils in the form of a Halbach array is exploited in the designs of an air-cored wind turbine generator and an electrodynamic wheel (EDW) used for maglev, through numerical modelling in COMSOL Multiphysics. The HTS Halbach Array magnet (HAM) can focus the magnetic flux inside the coil loop, greatly increasing the magnetic flux density in the airgap and the power density of the machine. The HTS HAM represents a generic topology/approach for the design of fully air-cored superconducting machines. The proposed HTS HAM EDW can generate higher thrust and lift forces, and greatly reduce the weight of the magnets compared with the conventional design with permanent magnets (PMs), opening the way to future on-road maglev vehicles. It is also illustrated that, for modelling the electro-mechanical performance of large-scale HTS devices, e.g., synchronous electric machines, the HTS field coils can be reasonably equivalized as conventional ones carrying the same DC so that the computation complexity can be largely decreased.

This thesis starts with the application of superconductors to electric machines, analyses thoroughly the loss characteristics of HTS CCs, stacks, coils, and TFSs over a wide frequency band from the power frequency to kHz level. It is believed that this research work can help researchers in the communities of applied superconductivity and electrical machines better understand the electromagnetic properties of different HTS topologies, provide a useful reference for the quantification and controlling of AC loss, and thus give a significant guideline for the design of high power density superconducting machines.

Acronyms and Abbreviations

HTS	high temperature superconducting
HTSC	high temperature superconductor
CC	coated conductor
2G	second-generation
BSCCO	bismuth strontium calcium copper oxide
REBCO	rare-earth barium copper oxide
YBCO	yttrium barium copper oxide
MgB_2	magnesium diboride
NbTi	niobium titanium
LTSC	low temperature superconductor
LN2	liquid nitrogen
LHe	liquid helium
LH_2	liquid hydrogen
AC	alternating current
DC	direct current
PM	permanent magnet
Maglev	magnetic levitation
BCS	Bardeen-Cooper-Schrieffer
1D, 2D, 3D	one-dimensional, two-dimensional, three-dimensional
TFM	trapped field magnet
TFS	trapped field stack
HAM	Halbach array magnet
EDW	electrodynamic wheel
rpm	revolutions per minute
FEM	finite element method

List of Publications

- **H. Zhang**, M. Yao, Z. Jiang, Y. Xin, and Q. Li, "Dependence of Dynamic Loss on Critical Current and *n*-Value of HTS Coated Conductors," *IEEE Trans. Appl. Supercond.*, vol. 29, no. 8, pp. 1-7, 2019. (Recommended by the Associate Editor)

- **H. Zhang**, M. Yao, K. Kails, P. Machura, M. Mueller, Z. Jiang, Y. Xin, and Q. Li, "Modelling of electromagnetic loss in HTS coated conductors over a wide frequency band", *Supercond. Sci. Technol*., vol. 33, no. 2, 205004, 2020.

- **H. Zhang**, H. Chen, Z. Jiang, T. Yang, Y. Xin, M. Mueller, and Q. Li, "A full-range formulation for dynamic loss of HTS coated conductors," *Supercond. Sci. Technol*., vol. 33, no. 5, 05LT01, 2020.

- **H. Zhang**, Q. Li, O. Ubani, and M. Mueller, "High Temperature Superconducting Halbach Array Topology for Air-cored Electrical Machines," *J. Phys.: Conf. Ser*, vol. 1559, 012140, 2020.

- **H. Zhang**, C. Hao, Y. Xin, and M. Mueller, "Demarcation Currents and Corner Field for Dynamic Resistance of HTS Coated Conductors," *IEEE Trans. Appl. Supercond.*, vol. 30, no. 8, pp. 1-5, 2020. (Recommended by the Associate Editor)

- **H. Zhang**, P. Machura, K. Kails, H. Chen, and M. Mueller, "Dynamic loss and magnetization loss of HTS coated conductors, stacks, and coils for high-speed synchronous machines," vol. 33, no. 8, 084008, *Supercond. Sci. Technol*., 2020.

- **H. Zhang** and M. Mueller, "Electromagnetic properties of curved HTS trapped field stacks under high-frequency cross fields for high-speed rotating machines," *Supercond. Sci. Technol.*, vol. 34, no. 4, 045018, 2021.

- **H. Zhang**, K. Kails, P. Machura, and M. Mueller, "Conceptual Design of Electrodynamic Wheels Based on HTS Halbach Array Magnets," *IEEE Trans. Appl. Supercond.*, vol. 31, no. 5, pp. 1-6, 2021.

- **H. Zhang**, Z. Wen, F. Grilli, K. Gyftakis, and M. Mueller, "Alternating current loss of superconductors applied to superconducting electrical machines," *Energies*, vol. 14, no. 8, pp. 2234, 2021.

- K. Kails, **H. Zhang**, P. Machura, M. Mueller, and Q. Li, "Dynamic loss of HTS field windings in rotating electric machines," *Supercond. Sci. Technol*., vol. 33, no. 4, 045014, 2020.

- K. Kails, **H. Zhang**, M. Mueller, and Q. Li, "Loss characteristics of HTS coated conductors in field windings of electric aircraft propulsion motors," *Supercond. Sci. Technol.*, vol. 33, no. 6, 064006, 2020.

- P. Machura, **H. Zhang**, K. Kails, and Q. Li, "Loss characteristics of superconducting pancake, solenoid and spiral coils for wireless power transfer," *Supercond. Sci. Technol*., vol. 33, no. 7, 074008, 2020.

- Z. Wen, **H. Zhang**, and M. Mueller, "Machine Learning Combined Sensitivity Analysis for the output characteristics of HTS dynamo flux pumps," *Supercond. Sci. Technol*., 2021. (Under review)

- K. Kails, M. Yao, **H. Zhang**, P. Machura, M. Mueller and Q. Li, "T-formulation based numerical modelling of dynamic loss with a DC background field," *J. Phys.: Conf. Ser*, vol. 1559, 012145, 2020.

Chapter 1. Introduction

1.1 Research Background

Electrical machines are the key component of the power industry and have been extensively employed in power generation, transportation, defence, industrial electrical automation, as well as household appliances, etc. [1-2]. Electrical generators produce virtually all artificial electrical energy on Earth, and electric motors are responsible for approximately 40% of overall power consumption all over the world [3]. With the progress of worldwide industrialization and urbanization, the electricity demand is increasing rapidly, which has brought a negative impact on the global environment, due to the consumption of natural resources like fossil fuels [4]. Therefore, the electromechanical energy conversion efficiency and energy utilization efficiency of electrical machines are crucial to green energy and sustainable energy strategies. However, despite many attempts to improve the efficiency and power density of conventional machines [5-8], their incremental advances have not brought about a fundamental qualitative change. For instance, although the existing electrical machine technologies have satisfied the development of electric vehicles [9-10], they cannot achieve the step change in power density required for electric aircraft and marine transport [11]. In wind turbines, the use of direct drive eliminates the need for a mechanical gearbox, but the low speed high torques encountered in renewable energy converters results in a very large-diameter machine with high mass [12-13]. Both transport and energy sectors are experiencing an electrical revolution in the transition to net zero emissions, but the limited power density of traditional electrical machines requires radical progress. Superconducting machines, characterized by high efficiency and power density, open the way to zero-emission transport and power systems [14-15].

With respect to superconducting wind power industry, a Japanese feasibility study project to realize a 10 MW-class HTS wind turbine, commissioned by New Energy and Industrial Technology Development organization (NEDO), was carried out from 2013 to 2015 [16]. The designed HTS turbine generator is partially superconducting with copper stator windings. The NEDO generator was estimated to achieve an efficiency of 97.6%, with an outer diameter 26.6% less than that of the conventional PM machine. The Advanced Technology Group at Converteam developed an HTS hydroelectric turbine generator rated at 1.79 MW, 5.25 kV, 28 poles and 214 rpm [17]. It is a partially superconducting machine with HTS field windings

composed of Bi-2223 tapes cooled to 30 K and conventional stators. Converteam also initiated a 5-10 year project to produce an HTS synchronous offshore turbine rated at 8 MW and 12 rpm. The conceptual design was finished in 2006, showing that the generator was of 5 m diameter with a mass of just over 100 tons [18]. American Superconductor (AMSC) designed a 10 MW HTS offshore wind turbine generator, SeaTitan, from 2010 to 2012 [19]. It is an air-cored synchronous machine, and the adopted Amperium HTS wire can carry over 100 times more power than copper wires of the dimensions. As a result, this HTS engine has a diameter of 5 m with the weight of 160 tons, which is half in size and 80% in weight of the similarly rated permanent magnet turbine generator. In general, the generator can provide efficiencies of up to 96%. Suprapower, ended in 2017, was a 5-year project intended to design a 10 MW direct-drive offshore superconducting turbine generator and superconducting electromagnet coils making up a full rotor [20-21]. The coils were manufactured from magnesium diboride (MgB_2) wires in the shape of racetrack. Copper was used to reinforce the MgB_2 wires and help with the conduction of heat. Although the power level of Suprapower was already over 10 MW, people still seek to build bigger wind turbines with higher power density, such as the project InnWind [22-23]. This $23.2 million project begun in 2012, aiming to build 10 and 20 MW turbines with MgB_2 at the lowest cost possible. As for the 20 MW design, it needs large amount of steel to compensate for the reduction of applied superconducting materials. Therefore, it remains tricky for superconducting turbine generators to achieve both light weight, small size, and beneficial cost. France also came up with a 20 MW turbine project called EolSupra20 [22]. MgB_2 was used in both the rotor and the stator. The EolSupra20 turbine decreased largely the total mass as well as the size, e.g., at 178 metric tons, it accounted for barely one-third of the conventional generator's size. To verify the competence of superconducting wind turbines, a $16.3 million EU project called EcoSwing was launched and a 3.6 MW onshore turbine was installed in March 2019 [24]. The EcoSwing turbine generator doubled the power density and achieved a 40% smaller bulk as well as a 15% cost decrease over those of market leaders. Different from the above-mentioned projects, EcoSwing chose the HTS material, YBCO, despite its higher cost than MgB_2. Compared to MgB_2, YBCO has better current-carrying capacity and the cooling method for YBCO is more straightforward. In May 2019, the testing of the turbine generator was completed at the Fraunhofer Institute for Wind Energy Systems' DynaLab, which was the first superconducting machine ever to have such tests. Then, it was embedded in an 88-meter-tall 3.6 MW turbine in Denmark to do the field testing. The HTS wind turbine realized its target power range, including more than 650 hours of grid operation. This shows the successful technology transfer from superconductor science to turbine industries. In 2019, the U.S. Department of Energy (DOE) decided to fund

projects totaling up to $8 million to develop more efficient, smaller, and lighter-weight wind turbines with lower costs for both onshore and offshore applications [25]. Among them, two projects are about superconducting wind turbines, undertaken by AMSC and GE. The aim of AMSC is to develop a high-efficiency turbine generator that incorporates HTS materials to replace conventional PMs in the rotor part, potentially reducing size and weight by half. As for GE, it plans to manufacture a high-efficiency ultra-light LTS offshore generator rated at beyond 12 MW. For AMSC, the advantage of its proposal lies in relatively higher operating temperature and easier implementation of cryogenics. However, the main challenge is the high cost of commercial HTS CCs. As a comparison, the advantage of GE's design is the low-cost LTS wires in lengths, but it has to use costly liquid helium to cool the superconducting windings to 4 K.

According to the Flightpath 2050 published by the European commission, Europe is seeking reductions in emissions of aircraft, namely a reduction in CO2 by 75% and NOx and particulates by 90% compared to the 2000 baseline. Superconducting electric machines provide a possibility to achieve this target, which can generate the required power-to-weight ratio greater than 10 kW/kg for medium to long distance aircraft. 'Advanced Air Transport Technology' (AATT) project was proposed by NASA aiming at achieving the reduction goal of fuel burn, noise, NOx emissions, as well as field length [26-27]. N3-X, a 300-passenger hybrid wing body superconducting aircraft with turboelectric distributed propulsion (TeDP) has been designed. As for the propulsion system of this aircraft, two wing-tip mounted superconducting turbo-generators in freestream conditions are used and an array of 15 superconducting-motor-driven propulsors are embedded on the upper surface of the aircraft near the trailing edge. Fully superconducting synchronous machines have been chosen for the propulsion system. MgB_2 wires are best candidate material for the stator winding to minimize AC losses. Compared with the reference airplane, the Boeing B777-200LR flying 13890 km with a cruise speed of 0.84 Mach, the proposed N3-X superconducting aircraft is assumed to realize a 70% reduction of fuel burn. The advanced superconducting motor experimental demonstrator (ASuMED) project, launched in May 2017 and funded by the European Union, is developing a 1 MW fully HTS synchronous motor for future electric aircrafts. The final aim of this project is to realize its Flightpath 2050 objectives [28]. The target of this 1 MW motor is to achieve a power-to-weight ratio of 20kW/kg and an efficiency of no less than 99% at 6000 rpm. HTS field trapped stacks are applied to the rotor [29], which are cooled by gaseous helium within the operating temperature window between 27 and 35 K. HTS coils are used as the stator winding, cooled by liquid hydrogen (LH_2). The project received an overall funding of over 4 million euros from the EU and is now in its final stage. Rolls Royce has been working

on an exemplary superconducting hybrid-electric aircraft with the support from the German nationally funded project TELOS [30]. Taking a hypothetically hybrid electric 220-passenger aircraft with a mission range of 2500 nm as an example, it has an overall length of 44.5 m and a maximum take-off mass of 101 tons. Radial-flux-type fully superconducting electric motors and generators are adopted. The rotor winding is consisted of DC racetrack HTS coils, and the stator winding is composed of MgB_2 wires, both of which are cooled by LH_2 to around 20-25 K. Modelling results showed that the designed fully superconducting machines could achieve a maximum power to weight ratio of about 38.1 kW/kg whereas 40.4 kW/kg. In addition, Rolls Royce and Siemens have put forward together a comprehensive concept design of a high-power superconducting generator for future hybrid-electric aircraft [31]. A short-range aircraft, A320, has been taken as the studied object. 10 MW and 7 000 rpm are set as the baseline for the power rating and rotational speed of the superconducting generator, respectively. [31] shows that a power density beyond 20 kW/kg is achievable with HTS coils as the rotor winding and a two-layer distributed armature winding made of Litz-wires. The rotor is cooled by LH_2 to around 20 K.

It can be seen that, from the above-mentioned superconducting machine projects, the majority of machine designs are based on conventional topologies, in which the field or armature windings (or both) are built with superconducting coils or replaced by trapped field magnets (TFMs). AC loss is caused by the movement of magnetic vortices within the superconductor when experiencing time-varying currents or magnetic fields [32]. Inside electric machines, the electromagnetic environment is complicated, composed of abundant AC electromagnetic signals and high-frequency harmonics, especially for high-speed rotating machines. As a result, AC loss of superconductors becomes a key challenge for machine designs, in that not only does it affect the construction of cryocoolers and impair the efficiency of the system, but it also causes security hazards in case of quench (for superconducting coils) or demagnetization (for TFMs). The main concern regarding AC loss comes from armature windings [33]. To avoid high AC loss, a number of researchers have adopted partially superconducting machines, i.e., superconductors are only used as field sources by means of direct current (DC) carrying coils or TFMs, and armature windings are made of conventional conductors [34-35]. However, it appears difficult for partially superconducting machines to achieve a power density higher than 20 kW/kg required for future aviation [11]. Nowadays, targeted at high power superconducting machines for aircraft and aerospace applications, more and more researchers begin to focus on fully superconducting machines. As a result, AC loss of superconductors becomes inevitably one of the most challenging issues to be solved.

Figure 1.1.1 shows the AC loss per unit length of an example 12-mm-wide HTS CC and its filamentized tapes exposed to an externally applied AC magnetic field with an amplitude varying from 1 to 100 mT, at 40 Hz [36]. It can be seen that the AC loss of the HTS CC increases positively with the applied magnetic field, and for a CC without filaments, the power dissipation per unit length can attain 1 W/m even under a field as low as 20 mT at a low frequency of 40 Hz. The power is dissipated at cryogenic temperature, e.g., at the liquid nitrogen temperature 77 K, which can constitute a big cryogenic burden.

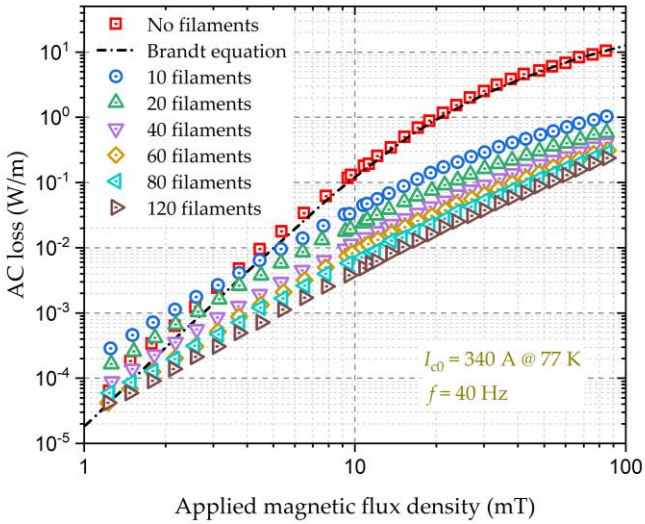

Figure 1.1.1 Variation of the AC loss of a 12 mm wide YBCO CC and its filamentized tapes with externally applied AC magnetic fields. The self-field critical current, *I*c0, of the YBCO CC is 340 A at 77 K, and the frequency, *f*, of the AC magnetic field is 40 Hz. Experimental data are from [36].

Table 1 presents the estimated heat load of HTS motors and generators employing different HTS materials at the operating temperature. To remove the heat load contributed by the AC loss, high cooling power is expected. Table 2 shows the ideal and practical Carnot specific power at a working temperature varying from 4.2 to 273 K. Carnot specific power is the quantity of watts needed at ambient temperature to offer 1 W of refrigeration at the lower working temperature [37].

Table 1. Estimated heat load of HTS machines at the operating temperature [37].

HTS machines	Power level	BSCCO heat load	YBCO heat load
Generators	10-500 MW	100-500 W at 25-40 K	100-500 W at 50-65 K
Motors	1-10 MW	50-200 W at 25-40 K	50-200 W at 50-65 K

Table 2. Ideal and practical Carnot specific power at distinct working temperatures [37].

Working temperature (K)	Ideal Carnot specific power (W)	Practical Carnot specific power (W) (when heat load > 100 W)
273	0.11	0.4
77	2.94	12-20
50	5.06	25-35
20	14.15	100-200
4.2	71.14	11000

At present, commercially available refrigerators function far below the Carnot efficiency, i.e., their practical Carnot specific power is much higher than the ideal one, as shown in Table 2. According to Figure 1.1.1, and Tables 1 and 2, it is not difficult to conclude that the heat load due to the AC loss of HTS materials applied to electrical machines proposes a big challenge for the design of cryogenic systems.

In summary, to promote the development and commercialization of superconducting machines, the unavoidable AC loss has to be studied. The first and most important step is to investigate the loss characteristics of superconducting materials applied to electrical machines. Commercially available HTS CCs have been chosen as the study object throughout the thesis because not only do they have higher critical temperature, critical current, and critical magnetic field, but they are also expected to have an acceptable cost in the near future with the advancement of processing techniques and material science.

1.2 Thesis Statement

Although the AC loss of HTS CCs has been widely studied, the vast majority of the relevant research has been conducted at AC power frequencies (50 Hz or 60 Hz) and the high-frequency behaviours of HTS CCs remain unclear. The AC transport current loss and magnetization loss have been extensively studied, however the dynamic loss of HTS CCs carrying a DC exposed to an AC magnetic field has not been systematically explored (dynamic loss can dominate the total loss in field windings of superconducting machines), especially at high frequencies. In response to the above-mentioned issues, through investigating the properties of different types of AC losses (dynamic loss, transport current loss, and magnetization loss) of distinct HTS

topologies (single CC, stacks, circular coils, racetrack coils, and trapped field stacks) over a wide frequency band, the aim of this thesis is to help researchers better comprehend the electromagnetic behaviours and loss properties of HTS CCs applied to electric machines, deepen people's understanding of the AC loss mechanism, and provide a useful reference for the design of high power density superconducting machines.

1.3 Contributions of the Thesis

This thesis aims to figure out the electromagnetic performance and AC loss characteristics of HTS CCs applied to electric machines over a wide frequency range, from power frequencies to kHz level. Different types of AC losses, including dynamic loss, transport current loss, and magnetization loss, of distinct HTS topologies, including a single CC, a stack, a circular coil, a racetrack coil, and a curved TFS, have been studied in detail. The innovative points and contributions of the thesis can be summarized as follows:

(1) A comprehensive review of the state of the art of AC loss related topics has been presented, including the adopted superconducting materials in electric machines, loss calculation formulae, modelling methods, measurement approaches, as well as loss reduction techniques. This review work is believed to help researchers better understand the research status of AC loss in superconductors and to provide a useful reference for superconducting machine designs, especially for those functioning at high speeds for future aviation.

(2) The dependence of dynamic loss and dynamic resistance on the critical current and *n*-value of HTS CCs has been clarified, and the non-linear variation of dynamic loss with the external magnetic field at a high load ratio has been revealed, which further add upon the existing knowledge regarding the interaction of dynamic loss with the HTS properties and external electromagnetic environments.

(3) The previously existing analytical equations cannot be used to explain or predict the non-linear variation of dynamic loss and dynamic resistance of HTS CCs. A completely novel formulation has been derived in this thesis to characterize the non-linearity of dynamic loss and dynamic resistance taking into account the $J_c(\boldsymbol{B})$ dependence of CCs, which can be used for full ranges of both magnetic fields and current load ratios.

(4) Three new parameters, including the lower demarcation current, the upper demarcation current and the corner field, have been defined with explicit formulae to quantify the linear and non-linear regions of dynamic resistance. The proposed novel full-range formulation for dynamic loss and dynamic resistance as well as the newly defined parameters can be used for accurate loss calculation and controlling in HTS magnets, rotating machines, and flux pumps.

(5) The widely adopted thin film approximation has proven to be inapplicable for modelling HTS CCs at high frequencies due to the electromagnetic interactions between different layers (e.g., it is inapplicable at frequencies higher than 100 Hz for modelling magnetization loss). A ***T***-formulation based multilayer numerical model for HTS CCs, considering the HTS layer, substrate, silver overlayer, and copper stabilizers, has been developed and then validated by experimental measurements. The proposed multilayer numerical model has provided an effective modelling tool to study HTS CCs.

(6) The frequency dependence of dynamic loss and magnetization loss of HTS CCs, stacks and coils over a wide range up to 20 kHz has been clarified. The previously existing definition of the dynamic region has proven to be invalid at kHz level, which shrinks rapidly with increasing frequency and magnetization loss plays a progressively important role due to the skin effect. The shielding effect in HTS stacks and coils has been found to be able to enhance the significance of dynamic loss.

(7) Despite several numerical models established for flat HTS TFSs, a comprehensive analysis of curved ones was lacking, which possess geometrical applicability for cylindrical rotating shafts. The widely adopted 2D-axisymmetric models are demonstrated to be inapplicable to study the electromagnetic distributions of TFSs because of the emergence of the electromagnetic criss-cross defined in this thesis. Current and magnetic flux density distributions, as well as loss properties of a curved HTS TFS have been studied in detail, through 3D numerical modelling, under perpendicular and cross fields with varying frequencies ranging from 50 Hz to 20 kHz.

(8) A novel HTS Halbach Array topology for air-cored electric machines has been put forward. The proposed HTS Halbach array magnets (HAMs) can not only generate a higher power density and decrease the magnet weight for the example C-GEN machine, but also represents a generic topology/approach for the design of fully air-cored superconducting machines, eliminating heavy iron cores.

(9) Conventional electrodynamic wheels (EDWs) are designed based on PMs, which generate limited thrust and lift forces while having a low power density. In order to enhance the feasibility of EDWs in maglev vehicles, a novel design of EDWs based on high-HTS HAMs has been proposed. Simulation results show that the proposed HTS HAM EDW can generate higher thrust and lift forces, improve the magnetic flux density distribution in the airgap, and greatly reduce the weight of the magnets compared with the conventional design. Additionally, it has been illustrated that, for studying the electro-mechanical performance of large-scale HTS devices, e.g., synchronous electric machines, the HTS field coils can be reasonably equivalized

as conventional ones carrying the same DC so that the computation complexity can be largely decreased. The proposed HTS HAM EDW is believed to open the way to future maglev on-road vehicles.

The contributions of this thesis are summarised in the following impact statement, given by my supervisor Prof Markus Mueller.

Impact Statement:

"Since September 2018, Hongye has been working on the investigation of electromagnetic characteristics of high temperature superconductors applied to electric machines. His research work has led to the publication of 9 journal articles with one more under review. During his studies, he has spotted the non-linearity of dynamic loss of HTS tapes and derived a creative full-range formulation to describe this non-linearity. Based on this novel equation, he has defined three new parameters to quantify the non-linear region of dynamic loss. Given that the high-frequency harmonics are inevitable in superconducting machines, Hongye has studied the electromagnetic behaviour and loss properties of HTS tapes, stacks, coils, and trapped field stacks in high-frequency environments systematically. He has demonstrated that the widely adopted thin film approximation is inapplicable for the modelling of HTS tapes at high frequencies and put forward a new multilayer numerical model considering both the superconducting and non-superconducting components of HTS tapes. His research work not only involves theoretical derivation and exploration of material properties but also includes the design of superconducting machines. Taking a 1MW C-GEN wind turbine generator that was designed and built by my spin off company, we have proposed an HTS Halbach array topology for air-cored superconducting machines which is capable of producing more than 4 times the power as the PM machine within the same volume. In addition, he has proposed a conceptual design of electrodynamic wheels equipped with HTS Halbach arrays used for maglev. In summary his research work is innovative and valuable in both theory and application, which will help other researchers in the field to better comprehend the electromagnetic behaviour and loss properties of HTS tapes, deepen people's understanding of the AC loss mechanism, and provide a useful reference for the design of air-cored superconducting machines."

An outline of the thesis structure is provided in the following section to summarise the content of each chapter.

1.4 Outline of the Thesis

In chapter 2, a comprehensive literature review of the AC loss related topics is presented. At first, a brief introduction to the discovery history of superconductivity and the superconducting materials that can be applied to electric machines is given with a particular attention to the REBCO CCs. The fundamental theoretical models for HTSCs are presented. Then, the existing analytical formulae, numerical modelling methods, and measurement approaches to quantify the AC loss of HTSCs are systematically summarized, as well as their constraints and disadvantages. At last, a brief review of the widely adopted AC loss reduction techniques is performed. This chapter helps clarify the state of the art of the AC loss related research work, especially in the domain of electrical machines.

The numerical modelling methods adopted in this thesis are introduced in Chapter 3. The finite element method (FEM) is utilized to model HTS CCs based on Maxwell's equations, which is achieved by two formulations, namely the ***T***-formulation (***T*** represents current vector potential) and the ***H***-formulation (***H*** refers to magnetic field). The ***T***-formulation based numerical model is firstly obtained in FORTRAN 90 with open source code to allow greater flexibility on customizing the functions. The ***H***-formulation is also chosen here because it is the mostly used formulation to model HTS topologies, which can be easily implemented into COMSOL Multiphysics. Therefore, both the ***T***-formulation and ***H***-formulation have been exploited to model distinct HTS topologies, from 1-dimensional (1D) tapes, 2-dimensional (2D) circular coils, to 3-dimensional (3D) racetrack coils and trapped field stacks.

Chapter 4 mainly discusses the dynamic resistance and dynamic loss of HTS CCs, because dynamic loss is an important component of the total AC loss of HTS field windings inside superconducting machines. At first, the dependence of dynamic loss on the material properties, e.g., the critical current and *n*-value of HTS CCs, is investigated through the ***T***-formulation based 1D numerical modelling and experimental measurements. In this work, it is found that the non-linearity of the dynamic loss at high external fields and high load ratios cannot be explained by the existing analytical equations. Therefore, a completely novel formulation to characterize the non-linearity of dynamic loss is then derived, which can be used for full ranges of both magnetic fields and current load ratios. Afterwards, to quantify the turning points charactering the transition between linear and non-linear regions of dynamic resistance and dynamic loss, three new parameters are defined with explicit formulae, including lower and higher demarcation currents, as well as corner field. This chapter serves to adds upon the knowledge regarding dynamic resistance and dynamic loss, which is particularly significant

for accurate loss estimation and controlling in HTS magnets, rotating machines, and flux pumps.

In chapter 5, the electromagnetic performance of HTS CCs over a wide frequency band, reaching MHz level, is explored numerically, given the fact that the fundamental frequency component and harmonics in very high-speed (7-50 krpm) electric machines can attain kHz level. First of all, the transport current loss and magnetization loss characteristics of a single HTS CC within the frequency range of 50 Hz-1 MHz are studied with the ***T***-formulation and ***H***-formulation based 2D numerical modelling methods. Results show that the widely adopted thin film approximation is inapplicable at high frequencies due to the skin effect, and in this case the multilayer structure of HTS CCs has to be taken into account, including the cooper stabilizers, silver overlayer, and substrate besides the HTS layer. On this basis, the dynamic loss and magnetization loss of a single HTS CC, HTS stacks, as well as circular and racetrack coils over the frequency band from 50 Hz to 20 kHz are studied with the ***H***-formulation based 2D and 3D numerical models. Results show that the existing definition of the dynamic region is no longer valid at kHz level, which shrinks rapidly with increasing frequency and magnetization loss plays a progressively important role due to the skin effect. Meanwhile, the shielding effect in HTS stacks and coils can enhance the significance of dynamic loss. At last, a 3D modelling of TFSs under the influence of high-frequency cross fields is conducted based on the ***H***-formulation, because TFSs are an alternative for high field magnets applied to superconducting machines, given their excellent field trapping ability and thermal stability. Current and magnetic flux density distributions, as well as loss properties of a curved HTS TFS are studied in detail, under perpendicular and cross fields with varying frequencies ranging from 50 Hz to 20 kHz. Results show that, the widely adopted 2D-axisymmetric models are inapplicable to study the electromagnetic distributions of TFSs because of the emergence of the newly defined electromagnetic criss-cross. High-frequency ripple fields can drive induced current towards the periphery of the HTS TFS due to the skin effect, leading to a fast rise of AC loss and even an irreversible demagnetization of the stack. This chapter points out the necessity of considering the multilayer structure of HTS CCs when modelling them in high-frequency environment, and investigated the high-frequency behaviours of HTS CCs, stacks, coils and TFSs systematically.

Chapter 6 is focused on the application of HTS coils in large scale superconducting devices. In this section, a special arrangement of HTS coils is introduced to form Halbach array magnets and utilized in two applications, namely air-cored electrical machines and electrodynamic suspension, a type of maglev. At first, taking a 1 MW C-GEN wind turbine

generator as an example, an ***H***-formulation founded HTS HAM model is built in COMSOL Multiphysics with the homogenization method. Simulation results show that the proposed HTS HAM C-GEN generator can achieve a power density more than 4 times higher than the conventional design with PMs, with a reduced magnet weight of around half of the previous prototype. Then, a conceptual design of EDWs based on HTS HAMs is presented, in which the HTS HAMs are used to replace the PMs. The proposed electrodynamic wheel is modelled with the ***A***-formulation and ***T***-formulation based finite element methods in COMSOL Multiphysics. Simulation results show that the proposed HTS HAM EDW can generate higher thrust and lift forces, improve the magnetic flux density distribution in the airgap, and greatly reduce the weight of the magnets compared with the conventional design. In addition, it is demonstrated that for studying the electro-mechanical performance of large-scale HTS devices, e.g., synchronous electric machines, the HTS field coils can be reasonably equivalized as conventional ones carrying the same DC so that the computation complexity can be largely decreased. This chapter exploits HTS coil-based magnets in two distinct cases and analyses the AC loss in practical applications through combined modelling methods.

In Chapter 7, a summary of the research tasks completed thus far is presented. The contributions of this PhD project are also illuminated. The discussion of possible improvements and the potential direction of research is also made at the end of this chapter.

Chapter 2. AC Loss of Superconductors Applied to Electric Machines – an Overview

2.1 Introduction

Starting from a summary of the milestones in the discovery of superconductivity and different types of superconductors, this chapter aims to illuminate the state of the art of AC loss related research work and figure out its future research trends in superconducting machine domains. Since REBCO (e.g., YBCO) coated conductors are chosen as the study object in this thesis, their basic material characteristics and theoretical models used for numerical analysis will be specially discussed. A comprehensive overview of AC loss related topics will be presented, including superconducting materials adopted in electrical machines, loss mechanism, analytical formulae for loss calculation, numerical modelling methods, loss measurement approaches, as well as loss reduction techniques. This review work is believed to help researchers better understand the research status of AC loss in superconductors and to provide a useful reference for superconducting machine designs, especially for those functioning at high speeds for future aviation.

2.2 Superconductivity and Superconductors

2.2.1 Milestones in the discovery of superconductivity

Superconductivity was first discovered by H. Kamerlingh Onnes at Leiden University in 1911. When he cooled mercury to the temperature of liquid helium (LHe), 4 K, its resistance decreased abruptly so that it could not be detected (the transition temperature was later called the critical temperature, T_c) [38]. Shortly, in 1913, the Nobel Prize was awarded to Kamerlingh Onnes "for his investigations on the properties of matter at low temperatures which led, inter alia, to the production of liquid helium." The nowadays famous ‘Meissner effect’ is used to describe the strong diamagnetism in superconductors, i.e., the induced current in a superconductor can repel the externally applied magnetic field, which was first observed in 1933 by W. Meissner and R. Ochsenfeld [39]. The development of quantum mechanics in the 1920s and 1930s opened up ways to understand superconductivity. In 1935, brothers F. and H. London developed the London equations, which was the first successful attempt to characterize the electrodynamic performance of superconductors theoretically [40]. The

London equations can not only explain the Meissner effect, but also predict the field penetration depth in a superconductor. The field penetration depth was then validated experimentally by E. T. S. Appleyardand, J. R. Bristow, and H. London in 1939 [41]. In subsequent decades the superconductivity of a series of metals, alloys, and compounds were discovered one after another. The superconductivity of niobium nitride (NbN) was first measured at T_c = 16 K by G. Aschermann et al in 1941 [42]. In 1950, Ginzburg-Landau theory was put forward by V. Ginzburg and L. Landau [43], according to which the free energy of a superconductor near the superconducting transition can be expressed in terms of a complex order parameter field. Based on the Ginzburg-Landau theory, in 1957, A. Abrikosov found that the field penetrates in a triangular lattice of quantized tubes of flux vortices in a type-II superconductor in a high magnetic field [44]. As shown in Figure 2.2.1 (a), a Type-I superconductor possesses only one transition field, i.e., when the applied field exceeds the critical field B_c, the superconducting state will be destroyed and it will behave like a normal conductor. As a comparison, a Type-II superconductor exhibits a mixed state defined by two critical fields, B_{c1} and B_{c2}, as shown in Figure 2.2.1 (b). In the mixed state, the Type-II superconductor is partially penetrated by the applied magnetic field in the form of vortices (or flux tubes) [44], which arrange themselves into a regular array known as the Abrikosov vortex lattice. Compare with Type-I superconductors, Type-II superconductors usually have higher current carrying capacity at higher external magnetic fields because B_{c2} of Type-II superconductors can be hundreds of times greater than B_c of Type-I superconductors.

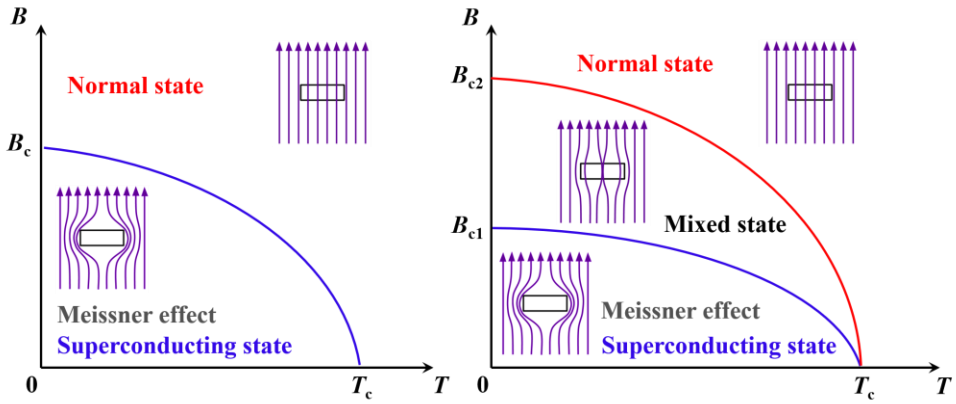

(a) (b)

Figure 2.2.1 State transition of Type-I and Type-II superconductors with varying temperature and magnetic field.

In 1953, G. F. Hardy and J. D. Hulm uncovered the superconducting properties of vanadium-silicon (V_3Si) at T_c = 17.1 K [45]. The superconductivity of niobium tin (Nb_3Sn) was first discovered in 1954 by B. T. Matthias et al [46]. Bardeen-Cooper-Schrieffer (BCS) theory, the

first extensively accepted quantum theory describing superconductivity as a macroscopic effect resulting from the condensation of Cooper pairs, was proposed by J. Bardeen, L. Cooper, and J. R. Schrieffer in 1957 [47-48]. BCS theory can successfully explain the superconductivity of some elements and simple alloys at sufficiently low temperatures, which led to the Nobel Prize in 1972. However, BCS is not adequate to explain the superconductivity in HTSCs. In 1962, B. D. Josephson theoretically predicted the Cooper pair tunnelling (known as the "Josephson effect" today) between two superconductors separated by a thin insulating barrier [49], and then won the Nobel Prize in 1973 for this significant work. In also 1962, T. G. Berlincourt and R. R. Hake reported the high critical current density and high critical magnetic field of niobium titanium (NbTi) [50], and shortly Westinghouse developed the first commercial NbTi wire [51].

The above-mentioned superconductors are all classified into low temperature superconductors (LTSCs) because their critical temperatures do not exceed 30 K. The 1980s started the journey of extraordinary discovery of HTSCs. In 1980, K. Bechgaard et al reported the first organic superconductor $(TMTSF)_2PF_6$ with T_c = 0.9 K, at an external pressure of 11 kbar [52]. In 1986, K. A. Müller and J. G. Bednorz made a breakthrough discovery that the lanthanum barium copper oxide (LBCO) exhibited superconductivity at 30 K [53]. Then, just one year later, Müller and Bednorz were awarded the Nobel Prize in 1987 "for their important break-through in the discovery of superconductivity in ceramic materials". LBCO is the first HTSC discovered in history, however it still needs to be cooled by LHe to achieve the transition temperature. The first HTSC that can function above the boiling point of LN_2 (77 K), yttrium barium copper oxide (YBCO), was discovered in 1987 by M. K. Wu et al at the University of Alabama-Huntsville with T_c = 93 K [54]. Later on, in 1988, Z. Z. Sheng and A. M. Hermann announced the discovery of the HTS bulk, thallium barium calcium copper oxide (TBCCO) with T_c = 127 K (for $Tl_2Ba_2Ca_2Cu_3O_{10}$) [55]. In 1993, A. Schilling et al reported a critical temperature record of 135 K in $HgBa_2Ca_2Cu_3O_{8+\delta}$ [56]. In 2001, J. Nagamatsu et al found the superconductivity of MgB_2 with T_c = 39 K [57], which can be primarily described by BCS theory in that it behaves more like a metallic than a cuprate superconductor. In 2003, Ginzburg and Abrikosov won partially the Nobel prize for their contributions to the Ginzburg-Landau-Abrikosov-Gor'kov (GLAG) theory. The iron-based superconductors are considered as the second family of HTSCs to distinguish from the cuprates, e.g., $SmO_{0.85}FeAs$ can achieve a critical temperature of 55 K. The superconductivity of the iron-based superconductors was first discovered in $La(O_{1-x}F_x)FeAs$ by Y. Kamihara et al in 2008 [58]. Very interestingly, in 2011, K. Deguchi et al found that hot alcoholic beverages, e.g., red wine, are effective in

inducing superconductivity in $FeTe_{1-x}S_x$, and it was assumed that the alcoholic beverages would play an important role in supplying oxygen into the sample as a catalyst [59].

A brief discovery history of superconductivity before 2015 can be summarized in Figure 2.2.2. Since 2015, multiple significant achievements have been made in looking for superconductors with higher critical temperatures, which can operate at the temperature of liquid carbon dioxide (sublimation point at atmospheric pressure 194.6 K). In 2015, A. P. Drozdov et al found the superconductivity in a H_2S sample with T_c higher than 200 K at a pressure above 150 GPa [61]. In 2019, Drozdov et al also reported the superconductivity in lanthanum hydride at 250 K at a pressure of about 170 GPa [62]. The first room-temperature superconductivity was discovered in a carbonaceous sulfur hydride by E. Snider et al in 2020, with a maximum superconducting transition temperature of 287.7±1.2 K at 267±10 Gpa [63].

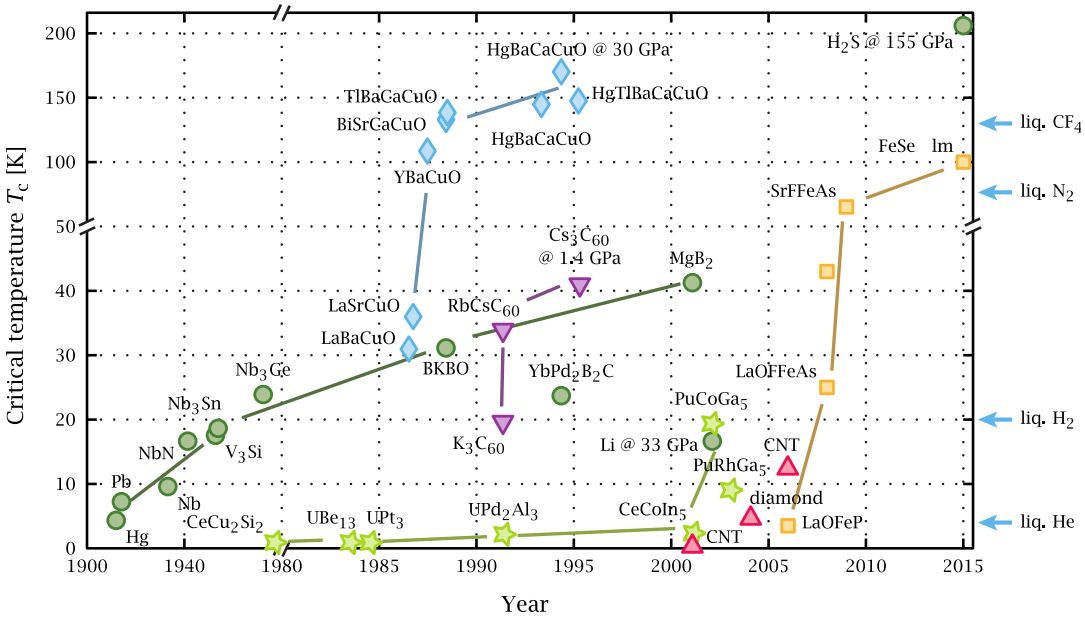

Figure 2.2.2 Discovery history of superconductors before 2015, CC BY-SA 4.0, adapted from [60].

Nevertheless, we need to note that the origin of high temperature superconductivity remains unclear. Two main theories are endorsed by most physicists, namely the resonating valence bond (RVB) theory and the spin fluctuation theory. The RVB theory was put forward by P. W. Anderson in 1987 [64], which states that in copper oxide lattices, electrons from neighbouring copper atoms interacting to form a valence bond can act as mobile Cooper pairs with doping. In 2014, B. Dalla Piazza et al found that fractional particles can happen in quasi 2D magnetic materials and thus supported the RVB theory [65]. The spin fluctuation theory was proposed by P. Monthoux, A. V. Balatsky, and D. Pines in 1991 [66], with which the high critical temperatures and energy-gap behaviours of cuprate superconductors, e.g., YBCO, can be well

explained. In 2018, Y. Cao et al spotted the unconventional superconductivity in twisted bilayer graphene with a twist angle of about 1.1° at T_c = 1.7 K [67-68]. The unusual superconductivity in the purely carbon-based, two-dimensional twisted bilayer graphene provides insights into the physics of HTSCs.

2.2.2 Superconducting materials

Superconducting materials can be categorized into LTSCs, e.g., NbTi, and HTSCs, e.g., REBCO (rare-earth barium copper oxide), BSCCO (bismuth strontium calcium copper oxide), and MgB_2, according to their critical temperatures. For LTSCs, their critical temperatures are normally below 30 K. As for superconducting coils, nowadays most researchers in the applied superconductivity community concentrate on HTS CC based coils because they can operate in LN_2 with higher critical temperature in addition to higher critical current and critical magnetic field. Certainly, HTSCs have better current carrying capacity if they operate at lower temperatures. The cost of commercial HTS materials, e.g., ~69 $/m for a 12-mm-wide YBCO tape [69], is a primary factor limiting the development of HTS machines. With the advancement of processing techniques and material science, HTS materials are expected to have a lower cost in the near future. LTSCs, in spite of worse current carrying capacity compared to HTSCs, have still been used in several designs because of their relatively lower material cost. However, they have to operate at LHe or LH_2 temperature, thus the cryogenic systems of LTS machines are generally more complicated and costly [70-71]. Concerning AC loss, MgB_2 possesses the advantage of a round wire compared with a flat tape, thus it has the potential to become a low AC loss superconductor operating below 30 K [72]. Given this fact, many fully superconducting machine designs have adopted MgB_2 coils as armature windings to avoid unbearable AC loss [73-75]. To maintain high electrical and magnetic loadings, while decreasing AC loss, multifilamentary HTS CCs have been implemented into electrical machines as an alternative [76]. The typical structure and composites of different superconductors can be found in Figure 2.2.3. The unit cost, critical temperature, and current carrying capacity of different materials are presented in Table 3.

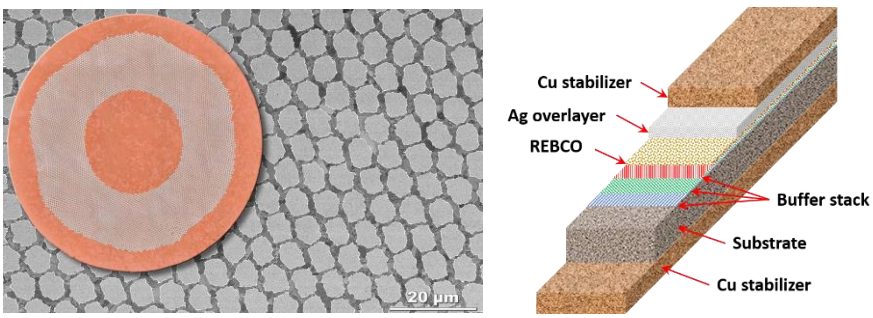

(a) (b)

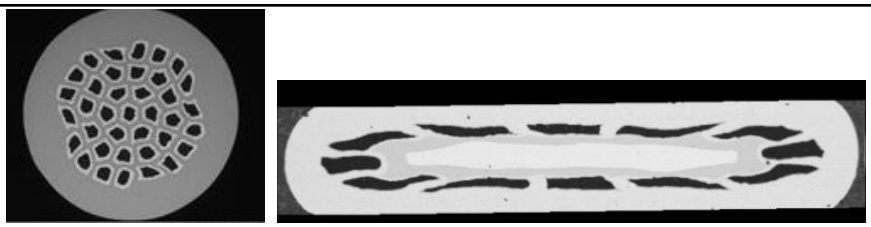

(c)

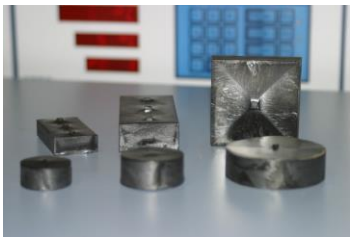

(d)

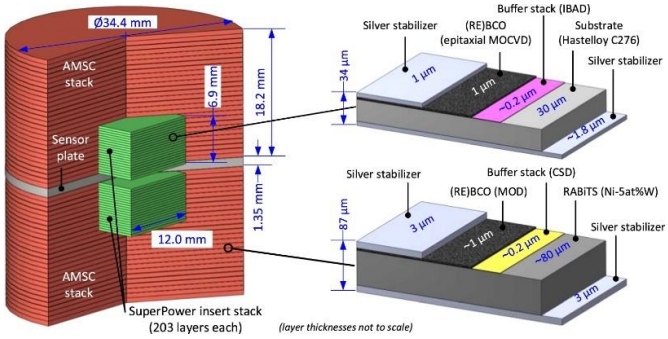

(e)

Figure 2.2.3 Diagrams of the superconductors applied to electrical machines: (a) Cross section of a NbTi wire (LTSC). Illustration courtesy of Peter J. Lee, NHMFL; (b) Multilayer structure of an REBCO coated conductor (HTSC); (c) Cross sections of round and flat MgB_2 superconductors. Image courtesy of G. Grasso (© ASG Superconductors); (d) Photo of REBCO bulk superconductors, © evico GmbH; (e) Diagram of a trapped field HTS stack. Adapted from [77].

Table 3. Reported commercial superconductor specifications. Data are from [78-89].

Material	Unit cost	T_c	I_{c0}
REBCO (12 mm-width)	~227 $/(kA·m)	up to 119 K	400 - 600 A (SuperPower, 77 K)
REBCO (4 mm-width)	~230 $/(kA·m)	up to 119 K	>100 A (SuperOX, 77 K) min. 88 - min. 152 A (SuperPower, 77 K) min. 130 A (AMSC, enhanced pinning, 77 K) >165 A (Fujikura, 77 K) >150 A (SuNAM, 77K) ~150 A (Shanghai SC, 77K) >100 A (SWCC, 77 K)
Bi-2223	17.4 $/(kA·m)	110 K	~170 - ~200 A (SEI, 77 K)

NbTi (LTSC)	0.8 $/(kA·m)	9.5 K	Up to 3 kA (SuperCon, 4.2 K)
MgB_2	20 $/(kA·m)	39 K	~157 A (MgB_2/Ga(30), 4.2 K)
NdFeB (PM)	28.9 $/kg	/	/
Copper	11.6 $/kg	/	/
Iron (Silicon steel)	1.6 $/kg	/	/

T_c - critical temperature; I_{c0} – critical current in the self-field; PM – permanent magnet.

TFMs consist of bulk superconductors and TFSs, most of which are manufactured by REBCO, despite the existence of MgB_2 bulks. TFMs can give a magnetic field up to a significant degree higher contrasted with conventional PMs. Besides, different from electromagnets like coils, no connection to a power supply is needed for TFMs. In 2014, Durrell et al reported a trapped field of 17.6 T at 29 K in a stack of two silver doped GdBCO superconducting bulk samples [90]. A record-high trapped field of 16.1 T in MgB_2 bulk has been recently achieved at 20 K by Hirano et al using pulsed-field magnetization (PFM) [91]. The possibility of the application of bulk superconductors to electrical machines has been discussed by many researchers. Kurbatova et al have presented an electromagnetic analysis of an electrical generator equipped with HTS bulks on the rotor and revealed that the generator performance depends on the HTS properties and the parameters of the magnetization [92]. Izumi et al have developed an axial-gap-type synchronous machine utilizing GdBCO bulks as field poles, which is meant for low-speed ship propulsion [93]. Bulk superconductors can also serve as lightweight and compact magnetic shields in electrical machines, as reported by Leveque et al [94]. However, a pivotal disadvantage of bulk superconductors lies in their thermal instability at low temperatures, making it hard to exploit the high critical current under 30 K [95]. In addition, external mechanical support is required in the utilization of bulk superconductors on account of their restricted mechanical strength. Compared with bulk superconductors, TFSs have better thermal stability and mechanical strength on the grounds that the copper stabilizers and silver overlayer of REBCO CCs have a thermal conductivity over a significant degree higher than REBCO, and the Hastelloy substrate has a more grounded tensile strength contrasted with REBCO. A trapped field of 17.7 T at 8 K in a stack of HTS tapes was reported by Patel et al in 2018 [77]. The application of TFSs as field poles to a 1MW superconducting demonstrator motor is being explored in the EU project ASuMED [28]. As mentioned in [96], in terms of the energization method, TFMs can avoid the application of

current leads during operation compared to DC superconducting coils. However, the maximum size of TFMs can be limited by the existing production technology, especially for TFSs, and they can experience a possible demagnetization under cross fields [97], bringing a threat to the safe operations of superconducting electrical machines.

2.2.3 REBCO coated conductor

The discovery history of HTSCs has been presented in Section 2.2.1. As mentioned in Section 2.2.2, the commercially available HTSCs are mainly composed of REBCO, BSCCO, and MgB_2. BSCCO and MgB_2 wires are commonly recognized as the first generation (1G) HTS wires. Compared to MgB_2, REBCO and BSCCO can operate in LN_2 (77 K) which is much cheaper than LH_2 (20 K) and LHe (4.2 K) with easier production process and more convenient storage. Therefore, the cost of the cryogenic systems used for REBCO and BSCCO can be much lower employing LN_2 as the cryogenic coolant. Compare with BSCCO wires, REBCO CCs are considered as the 2G HTS wires because they can offer better performance in magnetic fields and mechanical strength in addition to less preparation time [98]. Besides, with the advancement of processing techniques and material science, REBSO CCs are expected to have a lower cost in the near future. Therefore, this thesis considers REBCO CCs as the most promising commercially available HTS wires and has chosen REBCO CCs as the study object. The typical physical structure of a REBCO CC is shown in Figure 2.2.3 (b), composed of the copper stabilizer, silver overlayer, HTS layer, as well as magnetic/non-magnetic substrate.

YBCO is the most commonly used REBCO material in commercial CCs. The Crystalline structure of YBCO is shown as Figure 2.2.4. The yttrium atoms are located between the CuO_4 planes, and the barium atoms are situated between the CuO_2 ribbons (chains) and the CuO_4 planes. The electrical resistivity within the CuO_4 planes is much lower than that of the CuO_2 ribbons thus electrical currents mainly flow within the CuO_4 sheets (*a*-*b* planes), leading to a large anisotropy in superconducting and non-superconducting properties [100]. Compared to other adopted rare earth elements in HTSCs, e.g., gadolinium (Gd) or europium (Eu), yttrium has smaller ionic radius thus higher charge carrier density can be found in the superconducting CuO_4 planes. Additionally, YBCO has a lower electronic anisotropy and higher irreversibility field compared to GdBCO and EuBCO [101]. Therefore, YBCO becomes the ideal raw material for the production of commercial HTS CCs. With the improvement of the commercial availability of YBCO CCs, they have been applied to more and more large scale power applications, of which one of the most promising industries is superconducting machines.

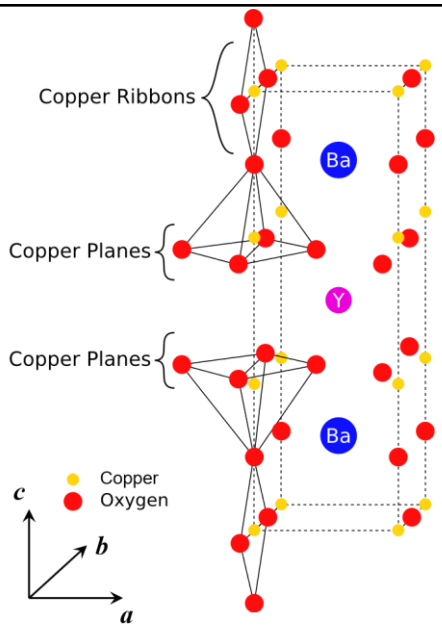

Figure 2.2.4 Part of the lattice structure of YBCO. CC BY-SA 3.0 adapted from [99].

2.2.4 Fundamental models for HTSC

To study the performance of superconducting power applications, it is of great interest to know the electromagnetic characteristics of the adopted superconductors. For example, for designing an HTS machine, we need to estimate its efficiency through analytical or numerical modelling methods. In this case, we need to quantify the loss generated in the HTS CCs, and thus the current and magnetic field distributions inside the HTS CCs have to be clarified. Three fundamental models are usually used to describe the characteristics of current density and magnetic flux density in HTSCs, including the Bean model [102], the Kim-Anderson model [103-104], and the ***E-J*** power law [105].

2.2.4.1 Bean model

In the Bean model [102], under external magnetic fields, the magnetized HTSC can be simply divided into two regions: the current carrying part and the current free part. The current carrying region is assumed to be at the critical state, i.e., this region has been penetrated by the external magnetic field and has been completely filled with the current featured by the critical current density of $\pm J_c$ (J_c represents the upper limit of current density in the HTSC). On the contrary, the external field has not penetrated into the current free region, consequently no electric field is generated in this region where the current density is thus taken as zero. When the magnetic field penetrates the entire HTSC, it will enter the critical state as a whole and the current density in any part of the HTSC will attain the critical current density $\pm J_c$.

To better describe the Bean model, let us consider a classic example in terms of the magnetization process of an infinite HTS slab [106], as shown in Figure 2.2.5. The slab has a width of 2*w* and a thickness of *h*, which is exposed to a magnetic field along with the *z*-axis. According to Faraday's law, a current along with the *y*-axis will be induced in the *x*-*y* plane. Taking a cross section of the slab in the *y*-*z* plane for further analysis, the magnetic flux density and current density distributions along with the width are also demonstrated in Figure 2.2.5 (a)-(c). It can be seen that the external magnetic field starts to penetrate the material from the edge of the material (which is actually also true in the case of self-field). The penetration depth is dependent on the magnitude of the magnetic field and the critical current density of the HTSC. In Figure 2.2.5, B^* refers to the full penetration magnetic field or characteristic field, which is determined by $B^* = \mu_0 J_c d/2$ for a round wire with a diameter of *d* [106]. From Figure 2.2.5 (a), (b) to (c), it can be concluded that with the augmentation of the amplitude of the external field, the area of the effective penetrated regions increase accordingly until the field amplitude attains B^* at which the entire HTS slab is fully penetrated. The current density in the penetrated regions is always characterized by $\pm J_c$. However, when the external field exceeds *B**, the slab remains fully penetrated, and the current density reaches the upper limit and keeps the value of $\pm J_c$.

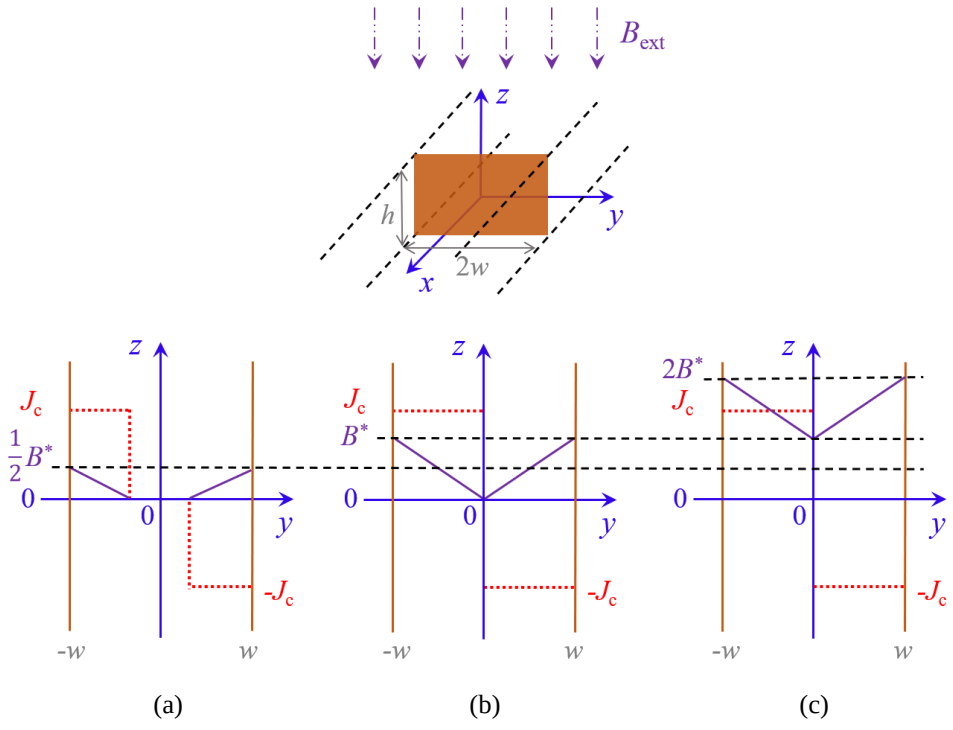

Figure 2.2.5 The magnetic flux density and current density distributions of an infinite HTS slab exposed to an external magnetic field B_{ext} described by the Bean Model. *B** refers to the full penetration magnetic field (a) $B_{ext} = B^*/2$. (b) $B_{ext} = B^*$. (c) $B_{ext} = 2B^*$.

The Bean model has been successfully exploited to qualitatively analyze the electromagnetic properties of HTSCs. However, the upper limit of the current density, namely the critical current density, has been assumed to be constant in any part of the superconductor, which has proven to be over-simplified in the quantification of loss properties in HTSCs. Therefore, a more accurate model, the Kim-Anderson model [103-104] has been proposed to reflect the electromagnetic distributions in type-II superconductors.

2.2.4.2 Kim-Anderson model

The critical current density represents the maximum current carrying capacity of a superconductor, which is dependent on the inherent properties of the superconducting material, i.e., the microstructure properties, e.g., the lesser of the intragrain current density (controlled by flux pinning) or the intergrain current density (depending on the strength of the superconducting link across the boundary, and on the relative orientation between the two grains in the case of anisotropic superconductors) [107]. In practical superconducting applications, we need to accurately predict the critical currents of the adopted superconductors at the macro level. Unlike the Bean model, Kim [103] and Anderson [104] pointed out that, the critical currents of type-II superconductors can vary with the local magnetic field (including the self-field generated by the transport current and the external field), and the ambient temperature. Therefore, an empirical equation was proposed by Kim and Anderson (later called the Kim-Anderson model) to characterize the field and temperature dependency of the critical current density, as

$$J_c(\boldsymbol{B},T)=\frac{J_{c0}(T)}{1+\frac{\|\boldsymbol{B}\|}{B_0}} \tag{2.1}$$

where $J_{c0}(T)$ represents the critical current density in self-field (with zero external field) at the temperature T, $\boldsymbol{B}$ refers to the local magnetic field, and B_0 denotes the characteristic field (a constant determined by the material property). The $J_{c0}(T)$ dependence for superconductors was first discovered by Onnes in 1913 [108], with an expression to describe the temperature dependence of the critical current density of mercury, as

$$J_{c0}(T)=J_{c0}(0)\left(1-\frac{T}{T_c}\right) \tag{2.2}$$

Throughout the thesis, the cooling power of the cryocooler has been assumed to be sufficient to remove the heat dissipation in the studied HTS CCs opportunely. In this case, the $J_{c0}(T)$ dependence has not been considered, i.e., the temperature of the studied CCs has been

considered as constant. Therefore, I have focused on the field dependence of the critical current. As the magnetic field perpendicular to the *a-b* plane of type-II superconductors dominate the $J_c(\boldsymbol{B})$ dependence, a simplified expression of (2.1) was proposed by N. Nibbio et al [109], as

$$J_c(\boldsymbol{B}) = \frac{J_{c0}}{1 + \frac{\|\boldsymbol{B}_\perp\|}{B_0}} \tag{2.3}$$

where $\boldsymbol{B}_\perp$ refers to the local magnetic field perpendicular to the *a-b* plane of type-II superconductors ($\boldsymbol{B}_\perp$ is perpendicular to the wide surface in the case of an HTS CC).

In order to consider the dependence of critical current on the field orientation, Gömöry put forward a semi-empirical Kim model with an orthonormal field dependence [110]

$$J_c(\boldsymbol{B}) = \frac{J_{c0}}{\left(1 + \sqrt{\frac{k^2\|\boldsymbol{B}_\parallel\|^2 + \|\boldsymbol{B}_\perp\|^2}{B_0}}\right)^\alpha} \tag{2.4}$$

where $\boldsymbol{B}_\parallel$ represents the local magnetic field parallel to the surface of the HTS CC, and $\boldsymbol{B}_\perp$ denotes the corresponding perpendicular component. k means the anisotropy factor, with $k < 1$. α refers to the exponent of the $J_c(\boldsymbol{B})$ dependence.

T. A. Coombs and H. S. Ruiz et al have recently studied the magneto-angular dependence of J_c, and put forward a more general $J_c(\boldsymbol{B}, \theta)$ dependence as [111-112]

$$J_c(\boldsymbol{B},\theta) = \frac{J_{c0}}{\left[1 + \varepsilon_\theta\left(\frac{\|\boldsymbol{B}\|}{B_0}\right)^\beta\right]^\alpha} \tag{2.5}$$

with

$$\varepsilon_\theta = \sqrt{\gamma^{-1}\sin^2(\theta) + \cos^2(\theta)} \tag{2.6}$$

where θ represents the angle between the field vector and the crystallographic *a-b* plane of the HTSC (i.e., when $\boldsymbol{B}$ is perpendicular to the wide surface of the CC, $\theta = \pi/2$), γ refers to the electron mass anisotropy ratio, α and β are both constants.

2.2.4.3 E-J power law

The ***E-J*** power law, proposed by Rhyner [105], is one of the most important models that can reflect the basic electromagnetic characteristics of HTSCs, which is written as

$$E = E_0 \cdot \left(\frac{J}{J_c} \right)^n \tag{2.7}$$

where E_0 represents the characteristic electric field at which the critical current is defined, and usually $E_0 = 10^{-4}$ V/m. n is the power exponent, depending on the intrinsic properties of the HTS material. The ***E*-*J*** power law reflects the non-linear correlation between the electric field and the current density inside the HTSCs, which can fit well to the non-linear experimental *I*-*V* curves for many HTSCs. From (2.7), we can derive a non-linear resistivity for HTSs, as

$$\rho = \frac{E}{J} = \frac{E_0}{J_c} \cdot \left(\frac{J}{J_c} \right)^{n-1} \tag{2.8}$$

(2.8) demonstrates a continuously varying resistivity in HTSCs, which is distinguished from the Beam model in which the resistivity is assumed to be zero. When $n = 1$, the conductor has a constant resistivity (at a fixed temperature and under a fixed magnetic field) and thus it shows a linear Ohm's law as in normal conductors, e.g., copper. For $n > 1$, the higher the n-value the closer (2.8) is to the Bean model, i.e., the Bean model corresponds to the case of $n = \infty$. According to the therory of flux creep proposed by Anderson [104], when a transport current flows in superconductor, flux creep occurs due to the thermal fluctuation. Then, an electric field is generated, as well as the loss. The theory of flux creep can be well described by the ***E*- *J*** power law.

2.3 Analytical Formulae for AC Loss Calculation

It is a common practice (related to experiments) to categorize AC loss based on the AC source (transport current or external field). Therefore, AC loss can be classified into two kinds of power dissipation, namely, transport current loss and magnetization loss. Transport current loss is caused by the carried current inside the superconductor in the absence of external magnetic fields, and magnetization loss describes the dissipation due to purely external magnetic fields without transport current. Magnetization loss consists of hysteresis loss, coupling loss, and eddy current loss. Hysteresis loss is generated by flux pinning and the loss per cycle is proportional to the area of the hysteresis loop. Coupling loss occurs due to the flowing of eddy current induced by external magnetic fields between filaments in multifilamentary conductors. Therefore, coupling loss can also be a problem for striated HTS CCs. Eddy current loss is the ohmic energy dissipation generated by the eddy current in the metal matrix. Transport current loss includes hysteresis loss and flux flow loss. Hysteresis loss occurs because the carried time-varying current provides the self-field. Flux flow loss happens

due to more and more flux lines moving in the superconductor with the increase of transport current (or load ratio between the transport current and critical current in self-field) [113].

Let us consider a thin HTS film with the width of 2*w* and the thickness of *h*, as shown in Figure 2.3.1 (a), having I_{c0} as the self-field critical current. When the HTS film is exposed to an AC magnetic field perpendicular to its wide surface, with the amplitude of B_{ext}, the Brandt equation can be utilized to quantify the average magnetization power loss per unit length (W/m), P_{mag}, as [114-116]

$$P_{mag} = 4\pi\mu_0 w^2 f H_0 H_c \left\{ \frac{2H_c}{H_0} \ln\left[\cosh\left(\frac{H_0}{H_c} \right) \right] - \tanh\left(\frac{H_0}{H_c} \right) \right\} \tag{2.9}$$

where $H_0 = B_{ext} / \mu_0$, H_c denotes the characteristic field given by $I_{c0}/(2w\pi)$, μ_0 is the free space permeability, and *f* refers to the frequency of the AC field. As demonstrated in Figure 1.1.1, the Brandt equation agrees well with the experimental data for the 12-mm-wide HTS CC.

In the absence of external magnetic fields, when the HTS thin film carries an AC current with the amplitude of I_t, according to the Norris equation, the average transport power loss per unit length (W/m), P_{trans}, can be written as [117]

$$P_{trans} = \frac{\mu_0 f I_{c0}^{\ 2}}{\pi} \left[(1-i)\ln(1-i) + (1+i)\ln(1+i) - i^2 \right] \tag{2.10}$$

where *i* represents the load ratio, determined by $i = I_t / I_{c0}$, and *f* is the frequency of the AC current.

When the HTS film carries an AC transport current and simultaneously experiences an AC magnetic field, both of which share the same frequency *f* and the same phase, the total average power dissipation per unit length can be calculated by [118][1]

$$P_{AC} = \frac{\mu_0 f I_{c0}^{\ 2}}{4\pi} \left(\frac{b}{w} \right) \left(P_1 - p P_2 \right) \tag{2.11}$$

with

$$P_1 = \alpha A \cdot \operatorname{arcosh}\alpha - \alpha^2 + \beta B \cdot \operatorname{arcosh}\beta - \beta^2 + 2 \tag{2.12}$$

$$P_2 = -A(\alpha + 2\beta) \cdot \operatorname{arcosh}\beta - B(2\alpha + \beta) \cdot \operatorname{arcosh}\alpha + 2(\alpha + \beta)^2 \cdot \operatorname{arctanh}\frac{AB}{\alpha\beta + 1} + 2AB \tag{2.13}$$

[1] Formula (11) in [118] contains a typo: in the expression for P_2, the last term, 2AB, should be a plus sign, not a minus.

where $b = w\sqrt{1-i^2}\sqrt{1-c^2}$, $c = \tanh\left[\pi B_{ext}/(\mu_0 J_{c0} h)\right]$, $p = \text{sign}(i-c)$, $\alpha = w(1+ic)/b$, $\beta = w(1-ic)/b$, $A = \sqrt{\alpha^2 - 1}$, $B = \sqrt{\beta^2 - 1}$.

Additionally, the analytical techniques and formulae used to describe the transport current and magnetization losses of infinite stacks and arrays of thin tapes have been reviewed by Mikitik et al in [119]. For an infinite stack of superconducting tapes with stack periodicity L_y, as shown in Figure 2.3.1 (b), P_{trans} is given by [120]

$$P_{trans} = \frac{\mu_0 f I_t^2}{\pi} \int_0^1 (1-2s) \ln\left[\frac{\cosh^2(\pi w / L_y)}{\cosh^2(\pi i s w / L_y)} - 1\right] ds \tag{2.14}$$

where I_t is the carried transport current in each tape. P_{mag} is written as [121]

$$P_{mag} = \frac{\mu_0 f I_{c0}^2}{\pi} \left(\frac{L_y}{\pi w}\right)^2 h_0^2 \int_0^1 (1-2s) \ln\left[\frac{\sinh^2(\pi w / L_y)}{\cosh^2(h_0 s)} + 1\right] ds \tag{2.15}$$

where $h_0 = \pi H_0 / (J_{c0} h)$.

With respect to an infinite array of coplanar superconducting tapes with array periodicity L_x, as shown in Figure 2.3.1 (c), P_{trans} and P_{mag} can be calculated by [120-121]

$$P_{trans} = \frac{\mu_0 f I_t^2}{\pi} \int_0^1 (1-2s) \ln\left[1 - \frac{\tan^2(\pi i s w / L_x)}{\tan^2(\pi w / L_x)}\right] ds \tag{2.16}$$

$$P_{mag} = \frac{\mu_0 f I_{c0}^2}{\pi} \left(\frac{L_x}{\pi w}\right)^2 h_0^2 \int_0^1 (1-2s) \ln\left[1 - \frac{\sin^2(\pi w / L_x)}{\cosh^2(h_0 s)}\right] ds \tag{2.17}$$

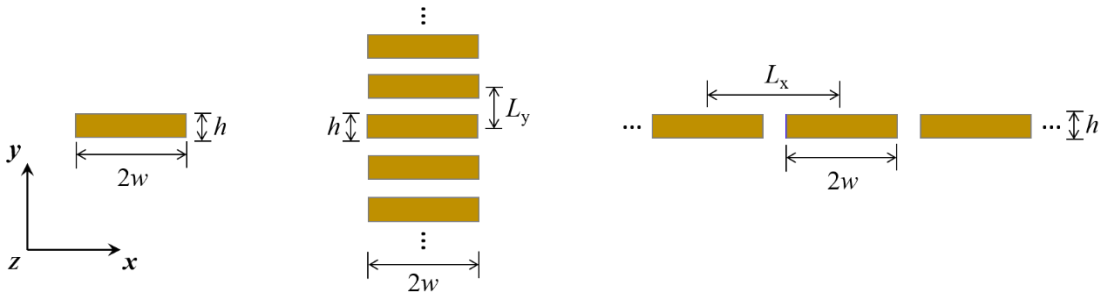

Figure 2.3.1 Cross sections of the infinitely long thin HTS tape, stack, and array, each HTS layer having the width of width 2*w* and thickness of *h*: (a) Single HTS layer; (b) Stack of HTS tapes with stack periodicity L_y; (c) Array of coplanar superconducting tapes with array periodicity L_x.

For field coils embedded on the rotor in a superconducting machine, each HTS CC carries DC and is exposed to time-varying magnetic fields. In this case, dynamic loss (W/m) occurs in the HTS layer and can be calculated by [122]

$$P_{\mathrm{dyn,l}} = 4wfI_{\mathrm{t}}i\left(B_{\mathrm{ext}} - B_{\mathrm{th}}\right) \tag{2.18}$$

where B_{th} is the threshold field defined by

$$B_{\mathrm{th}} = \frac{\mu_0 h J_{\mathrm{c0}}}{2\pi}\left[\frac{1}{i}\ln\left(\frac{1+i}{1-i}\right)+\ln\left(\frac{1-i^2}{4i^2}\right)\right] \tag{2.19}$$

However, (2.18) can only be utilized to depict the linearity of dynamic loss at low load ratio and simultaneous low external fields. In fact, when an HTS CC with a high load ratio experiences a high external magnetic field, its dynamic loss will vary in a non-linear way with the external field, putting the CC in the danger of a quench. Therefore, I have proposed a novel full-range formulation for dynamic loss (W/m) of HTS CCs in [123], expressed as

$$P_{\mathrm{dyn}} = 4wfI_{\mathrm{t}}i\left(B_{\mathrm{ext}} - B_{\mathrm{th}}\right) + E_0 I_{\mathrm{t}} i^{n+1}\cdot\left\{\begin{array}{l} 1+\displaystyle\sum_{p=0}^{n/2-1}\frac{n!}{(2p+1)!\left[n-(2p+1)\right]!}\left(\frac{B_{\mathrm{ext}}}{B_0}\right)^{2p+1}\left(\frac{1}{2}\right)^{2p+1}\cdot\frac{2^{3p+2}\cdot p!}{\pi\displaystyle\prod_{q=0}^{2p+1}(2q+1)} \\ +\displaystyle\sum_{p=0}^{n/2-1}\frac{n!}{(2p+2)!\left[n-(2p+2)\right]!}\left(\frac{B_{\mathrm{ext}}}{B_0}\right)^{2p+2}\left(\frac{1}{2}\right)^{2p+2}\cdot\frac{(2p+2)!}{\left[(p+1)!\right]^2} \end{array}\right\} \tag{2.20}$$

where n is the power exponent in the E-J power law. In (2.20), n is even. When n is odd, the upper bound of summation needs to be changed accordingly, as

$$P_{\mathrm{dyn}} = 4wfI_{\mathrm{t}}i\left(B_{\mathrm{ext}} - B_{\mathrm{th}}\right) + E_0 I_{\mathrm{t}} i^{n+1}\cdot\left\{\begin{array}{l} 1+\displaystyle\sum_{p=0}^{(n-1)/2}\frac{n!}{(2p+1)!\left[n-(2p+1)\right]!}\left(\frac{B_{\mathrm{ext}}}{B_0}\right)^{2p+1}\left(\frac{1}{2}\right)^{2p+1}\cdot\frac{2^{3p+2}\cdot p!}{\pi\displaystyle\prod_{q=0}^{2p+1}(2q+1)} \\ +\displaystyle\sum_{p=0}^{(n-1)/2-1}\frac{n!}{(2p+2)!\left[n-(2p+2)\right]!}\left(\frac{B_{\mathrm{ext}}}{B_0}\right)^{2p+2}\left(\frac{1}{2}\right)^{2p+2}\cdot\frac{(2p+2)!}{\left[(p+1)!\right]^2} \end{array}\right\} \tag{2.21}$$

With respect to BSCCO tapes, an engineering formula has been proposed to describe their AC power dissipation per unit length at 77 K by Rabbers et al [124], written as

$$P_{\mathrm{tot}}(B_{\mathrm{ext}}, I_{\mathrm{t}}, \alpha) = f\cdot\left[\frac{C_1(\alpha){B_{\mathrm{ext}}}^{P}\cdot C_2(\alpha)B_{\mathrm{ext}}}{C_1(\alpha){B_{\mathrm{ext}}}^{P}+C_2(\alpha)B_{\mathrm{ext}}} + C_3 {I_{\mathrm{t}}}^{q} + C_4(\alpha)B_{\mathrm{ext}}{I_{\mathrm{t}}}^{2}\right] \tag{2.22}$$

where α represents the orientation of the externally applied magnetic field (the angle between the field vector and the normal vector of the tape wide surface); the AC transport current and external AC magnetic field share the same frequency f; the parameters C_1, C_2, C_3, C_4, p, and q have to be derived from measured data, in which C_1, C_2, and C_4 depend on α. (2.22) shows an average deviation of 10% compared to the measured results. It has to be noted that (2.22) can only be obtained through curve fitting, thus an experimental measurement of AC loss is necessary. Therefore, the significance of (2.22) lies in decreasing the number of tests while predicting the loss under different B_{ext} and I_t.

For MgB_2 wires, the superconducting filaments are inserted in the resistive matrix. Under the influence of external magnetic fields, hysteresis loss P_{hys} (W/m) and a collective coupling loss P_{cp} (W/m) are generated, which can be obtained by [33]

$$P_{hys} = \frac{2fB_{ext}^{\ 2}}{\mu_0}\frac{\lambda}{1+4\pi^2 f^2 \tau_\alpha^{\ 2}}\Gamma\left(\frac{\beta}{\sqrt{1+4\pi^2 f^2 \tau_\alpha^{\ 2}}}\right) \tag{2.23}$$

$$P_{cp} = \frac{4fB_{ext}^{\ 2}}{\mu_0}\frac{\pi^2 f \alpha \tau_\alpha}{1+4\pi^2 f^2 \tau_\alpha^{\ 2}} \tag{2.24}$$

where λ is the fraction of the wire that is superconducting, $\tau\alpha$ represents the LR constant of the wire cross-section, α is the internal eddy current shielding factor, β denotes the ratio between B_{ext} to the penetration field of the filaments, and Γ refers to a normalized function based on β.

2.4 Numerical Modelling Methods

Analytical equations can help understand the AC loss mechanism and figure out the loss influential factors, from the theoretical perspective. However, analytical loss calculations are imperfect in that the formulae have been derived based on some fundamental assumptions, e.g., constant critical current, homogenous external field, thin film approximation for HTS CCs, etc. [114-123]. Besides, the analytical equations are normally limited to simple structures, e.g., single tapes or wires, thus in superconducting machines, the analytical equations are not enough to accurately quantify the practical AC loss. Therefore, numerical models appear to be an indispensable tool for the design of superconducting machines. Simulation of HTS devices is challenging in view of the nonlinear ***E-J*** power law and the high aspect ratio of the HTS layer, which results in hard convergence and a huge amount of degrees of freedom (DOF). Grilli et al have made a comprehensive review of the methods for calculating AC loss before 2014 in [37]. As pointed out in [37], the main step to calculate the AC loss in superconductors is to solve the electromagnetic state variables, e.g., current density ***J***, magnetic field ***H***, electric

field $\boldsymbol{E}$, current vector potential $\boldsymbol{T}$, magnetic vector potential $\boldsymbol{A}$, and magnetic scalar potential $\boldsymbol{\phi}$(or $\boldsymbol{\Omega}$), etc**.** Once these variables are obtained, the AC loss can be calculated according to the methods presented in Section II-C in [37]. The primary modelling of HTS CCs is based on Maxwell's equations and the FEM, which is typically achieved by four kinds of formulations, including the $\boldsymbol{T}$-$\boldsymbol{\phi}$ formulation [125-127], the $\boldsymbol{A}$-$\boldsymbol{V}$ formulation [128-135], the $\boldsymbol{E}$-formulation [136], and the $\boldsymbol{H}$-formulation [137-141]. The four formulations have been summarized in Table 4.

Table 4. Typical formulations used to solve Maxwell's equations with numerical models [137]

Formulation	Equations	Definitions
$\boldsymbol{T}$-$\boldsymbol{\phi}$	$\nabla\times\rho\nabla\times\boldsymbol{T}=-\mu\frac{\partial(\boldsymbol{T}-\nabla\phi)}{\partial t}$ $\nabla^2\phi=0$	$\boldsymbol{J}=\nabla\times\boldsymbol{T}$ $\boldsymbol{H}=\boldsymbol{T}-\nabla\phi$ $\rho=\rho(J)$
$\boldsymbol{A}$-$\boldsymbol{V}$	$\nabla^2\boldsymbol{A}=\mu\sigma\left(\frac{\partial\boldsymbol{A}}{\partial t}+\nabla V\right)$ $\nabla\cdot\left(\sigma\frac{\partial\boldsymbol{A}}{\partial t}+\sigma\nabla V\right)=0$	$\boldsymbol{B}=\nabla\times\boldsymbol{A}$ $\boldsymbol{E}=-\frac{\partial A}{\partial t}-\nabla V$ $\sigma=\sigma(\boldsymbol{E})$
$\boldsymbol{E}$	$\nabla\times\nabla\times\boldsymbol{E}=-\mu\frac{\partial(\sigma\boldsymbol{E})}{\partial t}$	$\nabla\times\boldsymbol{E}=-\frac{\partial\boldsymbol{B}}{\partial t}$ $\sigma=\sigma(\boldsymbol{E})$
$\boldsymbol{H}$	$\nabla\times\rho\nabla\times\boldsymbol{H}=-\mu\frac{\partial\boldsymbol{H}}{\partial t}$	$\boldsymbol{J}=\nabla\times\boldsymbol{H}$ $\rho=\rho(J)$

The option of a formulation is in principle arbitrary, however, in certain cases a specific formulation is advantageous. The $\boldsymbol{T}$-$\boldsymbol{\phi}$ formulation was first proposed by Amemiya in 1998 to simulate 2D superconducting wires [125], in which the current vector potential $\boldsymbol{T}$ on each node was defined to describe the current density $\boldsymbol{J}$, with $\boldsymbol{J}=\nabla\times\boldsymbol{T}$. Later on, Sugita et al have applied the thin film approximation to the HTS CC, and the current component perpendicular to the wide surface of the CC is neglected [126]. In this way, the modelling of HTS films turns into a 1D problem. The $\boldsymbol{T}$-$\boldsymbol{\phi}$ formulation based 1D numerical model has been demonstrated to possess the highest calculation efficiency for simulating the HTS layer among the four formulations because $\nabla\times\boldsymbol{T}$ is simply calculated by the two vector potentials on both sides of each element [127]. However, the magnetic field components parallel to the wide surface of the HTS CCs cannot be considered with the thin film approximation, thus some errors can be introduced to the simulation of HTS coils. Brandt has proposed an integral equation for the time derivative of the current density in simple geometries, starting from calculating the magnetic vector potential $\boldsymbol{A}$ [128]. Then, Otten and Grilli have presented a step-by-step deduction of Brandt's strategy for a thin film, a rectangular bar, as well as a cylindrical bulk

[129], and the corresponding MATLAB codes have been published online for easier access to the model [130]. An ***A*-*V*** formulation-based simulation module was first developed in the commercial finite element program Flux2D by Nibbio et al in 2001, which is appropriate for the numerical method naturally written in terms of the magnetic vector potential ***A*** [131]. Afterwards, Cedrat's Flux3D has been put forward as an industrial-strength FEM package to solve 3D problems [132]. Stenvall and Tarhasaari have presented the mathematical background of a co-tree gauged ***T*-ϕ** FEM solver [133] and ***A*-*V*-*J*** formulation [134] for computing the hysteresis losses of superconductors, and the two formulations have been compared with the ***H***-formulation in terms of DOF, computation time, and accuracy [135]. In [135], the authors show that the ***A*-*V*-*J*** formulation needs denser meshes to get solid outcomes compared to the ***H***- and ***T*-ϕ** formulations, but the ***A*-*V*-*J*** formulation based solver can be less time-consuming versus the other solvers in computation speed with the same mesh. The ***E***-formulation has been put forward to avoid the derivative calculation. However, according to [136], it may lead to convergence problems in finite geometries with a strongly nonlinear ***E*-*J*** power law, especially for an *n*-value greater than 20. Nowadays, the most extensively adopted formulation is the ***H***-formulation [137-139]. The quick evolution of the ***H***-formulation is contributed by its intuitiveness, fast convergence, and ease of implementation within COMSOL Multiphysics [140]. Nevertheless, the ***H***-formulation still has its drawbacks. For instance, the solution of a vector field is needed in non-conducting regions, which expands the size of the linear matrix to be computed and thus increases the complexity of solving [141]. Moreover, a dummy resistivity needs to be applied to the air region, which degrades the matrix conditioning [141].

Figure 2.4.1 shows the variation of the AC loss of a 10-mm wide HTS CC with a 75-μm thick Ni-W layer (magnetic substrate) carrying sinusoidal transport currents. The non-linearities of the HTS layer and the substrate have been well considered in the numerical model. It can be seen that the modelled total AC loss of the whole CC based on the ***H***-formulation is in good agreement with the measured data. Through numerical modelling, we can access quantities not available from measurements, e.g., the loss distribution in different layers of the CC, and the saturation of magnetic loss, etc. It should be noted that the AC loss in the HTS layer of a CC with a magnetic substrate is different from that of a CC with a non-magnetic substrate. In this case, the analytical formulae, e.g., the Norris equation, are not accurate to calculate the AC loss and thus numerical modelling is the best and only way to quantify the loss in the HTS layer.

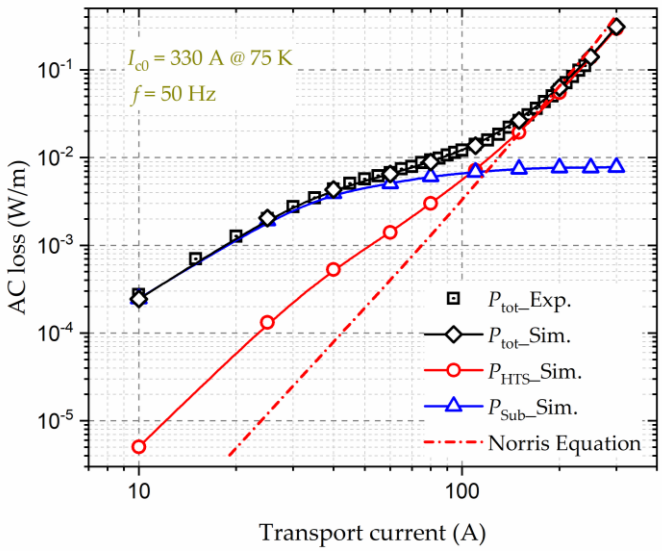

Figure 2.4.1 Variation of the AC loss of a 10 mm wide HTS CC with a magnetic substrate with sinusoidal transport currents. The self-field critical current, I_{c0}, of the HTS CC is 330 A at 75 K, and the frequency, f, of the AC magnetic field is 50 Hz. Experimental data are taken from [142]. Exp.-Experiment, Sim.-Simulation.

In HTS machines with coil-shaped magnets, a large number of HTS CCs are needed. Naturally, the modelling of HTS machines becomes very complicated and time-consuming, no matter which type of formulation is chosen. In order to mitigate the simulation complexity, most of the researchers have only focused on the superconducting parts in electric machines and choose 2D models to study the cross section of HTS coils, stacks of tapes, and bulks [143-154]. However, the electromagnetic environment inside electric machines is quite complex, and is also decided by non-superconducting parts, like iron cores and iron slotted structures. In addition, conventional conductors can become a severe heat load, which affects the design of cryogenic systems. Therefore, it is more reasonable to model both superconducting and non-superconducting sections simultaneously to accurately predict the loss distribution inside electrical machines. In order to achieve this requirement, different combinations of formulations have been developed. As presented in [155], an ***H*-*A*** formulation-based FEM framework has been applied to the modelling of rotating machines with HTS windings. It has been pointed out that the ***H***-formulation is more reliable than the ***A***-formulation as far as the simulation of flux dynamics in superconductors by means of the ***E*-*J*** power law is concerned. Therefore, the ***H***-formulation has been employed in the superconducting parts, and the ***A***-formulation has been used in the outer iron stator poles. A ***T*-*A*** formulation based 2D numerical model for simulating large-scale superconducting stack/coil has been exploited in [145, 149, 156-159]. The ***T***-formulation has been used to calculate the current density in

superconductors, and the ***A***-formulation has been employed to obtain the magnetic flux density in the whole space. The proposed ***T-A*** formulation based numerical model has proven to be much more efficient than the ***H***-formulation based reference model [145]. Both [155] and [156] demonstrate that the numerical modelling of moving superconductors does not present additional difficulties compared with static cases. In [156-157], the electromagnetic results calculated based on the ***T-A*** formulation have been compared with those from the ***H-A*** formulation. Due to the thin-film approximation adopted in the ***T-A*** formulation, the ***T-A*** formulation has proven to be more efficient and time-saving than the ***H-A*** formulation. The ***T-A*** formulation has recently been applied to the design of a 10-MW HTS wind turbine generator in [159], and the model building methodology combining the resistive model and the superconducting model has been introduced. The modelling results of an example machine regarding the magnetic field and current density distributions are shown in Figure 2.4.2 [160]. The ***H-ϕ*** formulation has been used by a few researchers to simulate superconductors in GetDP [161-162]. However, the implementation of the ***H-ϕ*** formulation into COMSOL Multiphysics has just been reported recently in detail for the first time in [141]. The ***H***-formulation has been applied to superconductors, and the ϕ physics has been introduced to current-free domains. Compared to the ***H***-formulation, the application of the ***H-ϕ*** formulation can largely decrease the size of the linear matrix to be solved and the number of DOF, thus the computational time can be reduced by nearly a factor of two for a given relative error [141]. The ***H-ϕ*** formulation is believed to be an advantageous alternative for modelling superconducting machines considering both the superconducting and non-superconducting components.

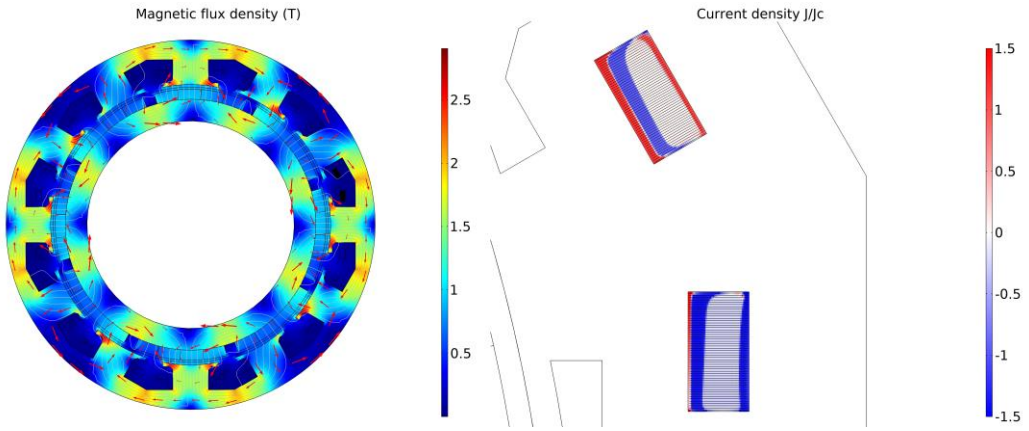

(a) (b)

Figure 2.4.2 2D modelling results of a superconducting wind turbine generator equipped with HTS coils, based on the *T-A* formulation [160]: (a) Magnetic flux density distributions; (b) Current density distribution in the HTS coils, J/J_c.

To overcome the limitations of the full models, some simplification approaches have been put forward, e.g., the homogenization and multi-scaling methods. The homogenization model for HTS CCs was developed by Zermeno et al [163-164], which represents significant progress of large-scale superconductor modelling regarding computational speed. Given that the resistivity values of air and normal conductors are several orders of magnitude higher than that of superconductors, only the superconducting layer's volume fraction is considered in the homogenization model. In this way, the stack of HTS tapes can be considered as a homogeneous bulk, with an equivalent field dependence of the critical current as [165]

$$J_{\mathrm{c,eq}} = J_{\mathrm{c}} \cdot f_{\mathrm{HTS}} = \frac{J_{\mathrm{c0}}}{\left(1+\sqrt{\frac{k^2\left\|\boldsymbol{B}_{\parallel}\right\|^2+\left\|\boldsymbol{B}_{\perp}\right\|^2}{B_0}}\right)^{\alpha}} \cdot \frac{h_{\mathrm{HTS}}}{t} \tag{2.25}$$

where h_{HTS} and t are the thickness of the HTS layer and that of the CC, respectively. In [163], the homogenization model is 113.5 times faster than the reference $\boldsymbol{H}$-formulation based reference model for simulating a stack composed of 64 tapes, with an accepted error of less than 2%. However, it needs to be pointed out that the homogenization model only works for CCs with non-magnetic substrates.

The large aspect ratio of HTS CCs, in the order of 10^3~10^4, causes a big constraint in the number of DOF to be solved so that conventional meshing using elements with an aspect ratio close to unity cannot meet the demand of fast computation for a large number of turns. In light of this, a multi-scaling approach has been developed by Zermeno et al for the superconductor modelling [150, 166-167]. The basic idea is to estimate the magnetic field of coils with a fast coil model first, and then parallelize the calculation with the obtained field by dividing the computation domain into multiple smaller domains [150]. Of course, the multiscale meshing techniques also need to be considered, as illustrated in [166]. The application of the multiscale modelling method largely reduces the number of DOF, requires less calculation memory, and allows parallel computation, thus it is considered as the fastest model in [167] compared with the $\boldsymbol{H}$-formulation based reference model and the homogenization method. However, it should be pointed out that the use of a coil sub-model with uniform current density can introduce a large error, especially for low current amplitude. Therefore, we need to find a good trade-off between computational time and accuracy.

A novel simplification method, named densification, has recently been proposed by Berrospe-Juarez et al in [168]. The HTS tapes forming part of a stack and their neighboring tapes can be merged by the densification method, resulting in fewer tapes to be modelled. All

the possible combinations of the homogenization, multi-scaling, and densification methods applied to the ***H***- and ***T-A*** formulations have been analyzed in [168], including in total 14 modelling strategies. It is concluded that the ***T-A*** homogenous model has the highest computational efficiency, but it is limited to cases where the thin film approximation of HTS CCs is applicable. In contrast, the ***H***-formulation has a wider scope of application as it can be used to study systems made of wires with various geometries, e.g., MgB_2 wires. It should be underlined that the ***H*** iterative multi-scale strategy can be exploited to model large-scale applications nearly with no size limitation.

Although 2D numerical models can reflect the electromagnetic properties of superconducting devices in many cases, e.g., infinitely long conductors, it is not considered trustworthy enough to predict the behavior of a 3D superconducting device in a specific shape [169]. For example, when the ratio between the thickness of a racetrack coil and its diameter cannot be neglected, a 3D numerical model is necessary to accurately quantify the AC loss. In [169], an ***A-V*** formulation based numerical model has been extended from 2D to 3D for simulating the magnetization of superconductors. The electromagnetic properties of curved HTS TFSs under high-frequency cross fields have been explored in [170] through the ***H***-formulation based numerical modelling. It is concluded that the 2D axisymmetric model to approximate a square TFS as a round bulk is inapplicable for studying the electromagnetic distributions of TFSs, thus a 3D model has to be employed [170]. An ***H***-formulation based full 3D time-dependent electromagnetic model for Roebel cables have been proposed in [171]. An efficient 3D FEM model based on the ***T-A*** formulation has been developed in [172], which is 10 times faster than ***H***-formulation based 3D modelling method. In [141], the ***H-ϕ*** formulation based 3D modelling of the magnetization of HTS bulks has been investigated systematically. As concluded, cubic is the ideal element order for 3D modelling for both ***H***-formulation and ***H-ϕ*** formulation in terms of the computational time as well as accuracy. More 3D modelling work of superconductors can be found in [37, 137, 173-177].

There exist other modelling methods for the calculation of AC loss, such as the integral equation method for thin tapes solved with finite elements by Brambilla et al [178], and the Minimum Magnetic Energy Variation (MMEV) method [179] as well as Minimum Electro-Magnetic Entropy Production (MEMEP) method developed by Pardo et al [180-181]. Although the integral equation method is much faster and computationally less demanding than FEM models, it is difficult to be applied to complex 3D superconducting structures. As for the MMEV and MEMEP methods, they are computationally time-efficient and potentially promising for demanding 3D problems. However, these methods are less commercially

available compared to FEM based numerical models that can be incorporated into commercial software, e.g., COMSOL Multiphysics, as described before. In addition to COMSOL Multiphysics, ANSYS is also widely utilized to build numerical models for superconductors [182-184].

Despite the above-mentioned state of the art of the existing modelling methods for superconducting machines, a few issues remain to be solved or deserve further investigation:

(1) Aerospace electrical machines operate at very high speeds (7-50 krpm), and thus the superconductors in HTS machines ought to be capable of functioning in high-frequency magnetic fields (~0.2-2 kHz) [15]. Until now, the vast majority of numerical models are based on the thin film approximation and only the HTS layer is considered, which has proven inapplicable for high frequencies beyond 100 Hz (in the case of the quantification of magnetization loss) for the first time by my research work [185-187] (which will be presented in detail in Chapter 5). Therefore, the multilayer physical structure of the commercial HTS CC has to be taken into account, composed of e.g., the HTS layer, copper stabilizers, silver overlayer, and substrate, as shown in Figure 2.2.3 (b). Musso et al have also studied the AC loss distributions in various layers of HTS CCs by use of the $\boldsymbol{A}-\boldsymbol{V}$ formulation and concluded that the contribution to the total losses of the non-superconducting layers parts is strengthened when the field frequency surpasses 1 kHz [188]. However, the electromagnetic interaction among different layers can largely increase the number of DOF and computational complexity, especially for 3D modelling of racetrack coils.

(2) The electromagnetic environment in electrical machines is quite complex, composed of high-frequency harmonics. Therefore, the electromagnetic signals are not purely sinusoidal. The vast majority of numerical models concentrate on the AC loss with standard sinusoidal AC transport current or magnetic fields. Although some simulation work of AC loss has considered both the DC background field, AC ripple field, and non-sinusoidal currents [189-192], the input signals for simulation are not real synthetic signals generated inside practical electrical machines. Consequently, the performance of HTS CCs under a complex synthetic electromagnetic environment deserves further exploration.

(3) The magnetic field distribution inside HTS machines is determined by both the superconducting and non-superconducting parts, thus just modelling the superconductors is not sufficient to reflect the overall power dissipation of the machine that decides the design of cryogenic systems. The non-superconducting parts can contain conventional conductors, iron cores, and permanent magnets, thus their electromagnetic interaction with the superconductors

has to be considered. However, the existing numerical models have rarely considered the influence of non-superconducting parts.

(4) 3D numerical models of superconducting machines are still lacking due to a large number of DOF and high computation complexity. Studies on convergence and computational speed in 3D models have to be thoroughly conducted to improve simulation efficiency.

(5) Besides the electromagnetic properties, the thermal characteristics of superconductors should also be investigated because they directly affect the design of cryocoolers and quench protection. An electro-thermal numerical model for high-speed superconducting machines needs to be developed.

(6) The stability of superconducting materials is extremely important to the normal functioning of the machine. The high centrifugal force in high-speed electrical machines brings a big challenge to the design of rotating field coils. Apart from the necessary mechanical simulation, online monitoring and fault detection methods of HTS machines have not been studied due to the lack of superconducting machine demonstrators.

2.5 AC Loss Measurement Approaches

There exist three main approaches for measuring AC loss of superconductors, namely electric, magnetic and calorimetric methods [193].

2.5.1 Electric method

The electric method is extensively used because of its fast measurement speed and high sensitivity. The electric method is usually exploited to measure AC transport current loss and magnetization loss, which consists of three types of techniques: the pick-up coil method, lock-in amplifier method, and the combination of the two techniques. Two typical electrical circuits of the pick-up coil method [194] and the lock-in amplifier technique [113] are presented in Figure 2.5.1.

The pick-up coil method is often applied to measure the magnetization loss of superconducting samples [195-198]. The measurement system is usually composed of the AC power supply, cryostat, AC electromagnet, pick-up coil, compensation coil, compensation circuit, isolation amplifier, as well as data acquisition and processing parts, as shown in Figure 2.5.1 (a). The AC power dissipation per unit length (W/m) can be obtained by [199]

$$P_{\mathrm{mag}} = -\frac{AGf}{VN\mu_0}\int_0^{1/f}\left(V_{\mathrm{p}} - kV_{\mathrm{c}}\right)B_{\mathrm{ext}}\,dt \tag{2.26}$$

where A and V are the sample volume and cross-sectional area surrounded by the main coil, respectively; N denotes the turn number per unit length of the main pick-up coil; V_p and V_c represent separately the induced voltage in the pick-up coil and the compensation coil; k refers to an adjustable coefficient. G is the geometrical correction factor, which has to be calculated for different arrangements of pick-up coils and tested samples.

Yang et al have derived a general formulation used for the calibration of the pick-up coils with distinct geometries and concluded that the AC loss of round/square wires can always be measured with errors less than 10% using coils of any turn and dimensions [195]. Souc et al have measured the AC loss and the voltage signals of single pancake coils using different pick-up coils with the help of a transformer and found that the AC loss can be measured through voltage taps on a turn close to the coil average to avoid the difficulties in correcting the huge inductive signal of the whole coil when the number of turns is greater than 10 [196]. Different from the conventional pick-up coil method, a calibration-free method has been proposed by Souc et al to measure magnetization loss [200]. A coil wound in parallel to the AC field magnet is employed as the measurement coil, and a compensation system is utilized to eliminate the eddy current loss in the coil winding. Consequently, the magnetization loss of the sample of any geometry can be determined by measuring the power supplied by the AC source to the AC magnet without calibration.

The lock-in amplifier technique is usually applied to the measurement of transport current loss of HTS CCs and non-inductive coils [201-207]. The measurement system is usually composed of the AC power supply, cryostat, non-inductive voltage divider, compensation coil, and acquisition system, as shown in Figure 2.5.1 (b).

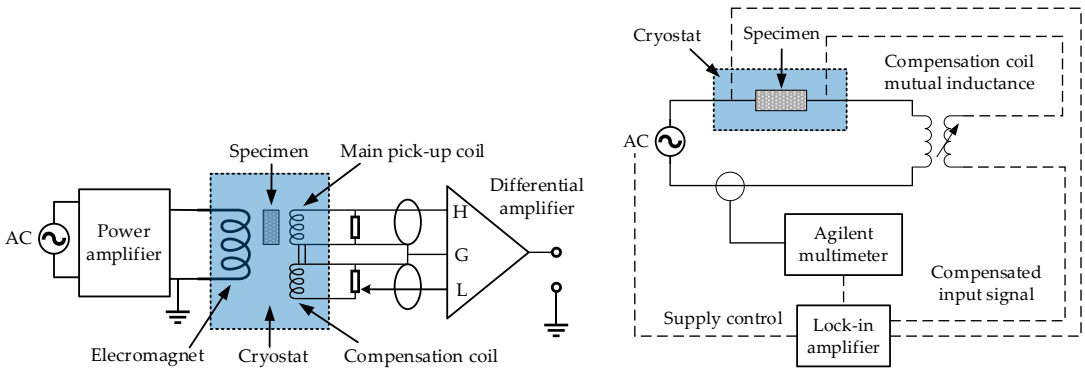

Figure 2.5.1 Typical electric circuits for the AC loss measurement. (a) Pick-up coil method [194]. (b) Lock-in amplifier technique [113].

Time-domain periodical current, i(t), and voltage, u(t), can be expressed in the form of Fourier expansion, as [192]

$$i(t) = i_0 + \sum_{n=1}^{\infty} a_n \sin(n\omega t + \varphi_n) \tag{2.27}$$

$$u(t) = u_0 + \sum_{n=1}^{\infty} b_n \sin(n\omega t + \phi_n) \tag{2.28}$$

where i_0 and u_0 are separately the DC components of the current and voltage; a_n and b_n represent the Fourier coefficients; φ_n and ϕ_n are phase-related constants. When the transport current is purely sinusoidal, the average power dissipation can be written as

$$P_{\text{trans}} = i_0 u_0 + \frac{1}{2} a_1 b_1 \sin(\varphi_1 - \phi_1) \tag{2.29}$$

It can be seen that, from (2.29), P_{trans} depends on the first harmonics. With the lock-in amplifier technique, the transport power loss per unit length (W/m) of an HTS CC can be written as

$$P_{\text{trans}} = \frac{I_{\text{rms}} U_{\text{rms}}}{L} \tag{2.30}$$

where I_{rms} means the root of mean square (RMS) value of the AC transport current carried by the sample CC; U_{rms} is the RMS value of the loss voltage component; L denotes the studied length of the sample.

In [207], Pei et al have developed a high-precision digital lock-in measurement technique using a lock-in amplifier and nano-voltage meter, and it can resolve signals at the nano-volt level. Different from conventional electric methods, Souc and Gömöry have developed a compact cold-core toroidal transformer system and proposed an auxiliary contactless loop based electric method to measure the transport current loss of long superconducting samples [208]. This measurement method could be applied to complex structures, e.g., superconducting cables, and help monitor the quality of long pieces of superconducting tapes. To deal with the disadvantages of conventional compensation coils, e.g., low mechanical control precision, narrow compensation range, and voltage with harmonic components, Liao et al have proposed an automatic compensation method with phase detection and feedback control algorithm for measuring the AC loss of HTS coils [209]. This method possesses a higher degree of automation and can be potentially applied to different objects in complex environments. In practice, the superconducting elements are normally put inside a metallic containment vessel, in which additional AC loss can be generated due to the induced eddy current. Therefore, Pei et al have measured the total AC loss of a YBCO coil in different containment vessels using a

compensation coil and recommended the vessel with a non-metallic material to minimize the eddy current loss [210]. Shen et al have recently developed a distinct lock-in amplifier method to measure the transport current loss, with which the unknown inductive part of the obtained voltage can be eliminated by alternating the inductance of the compensating coil, and thus the loss can be calculated without phase control [211]. An electric measurement method without the application of a lock-in amplifier has been recently put forward by Breschi et al [212]. This approach includes a Hilbert transform based treatment procedure in terms of the voltage and current signals of the HTS sample, allowing one to analyze the harmonic components of the signals with a remarkable noise reduction. Sytnikov et al have proposed a digital phase shift method for the AC loss measurement of HTS power cables, which has provided a fast and simple way to estimate the AC loss with an error ±25%, without the application of expensive lock-in amplifiers [213]. This electric method has recently been adopted in [214] to analyze the performance of a 23 kV/60 MVA class tri-axial HTS power cable for real-grid applications in Korea.

When the superconductor carries an AC transport current and is simultaneously exposed to an AC magnetic field of the same phase, the combination of pick-up and lock-in amplifier techniques should be adopted to measure the total loss. Rabbers et al have proposed an “8” shaped pick-up loop and voltage tap combined measurement method, which can be used to measure separately the transport current loss and magnetization loss of an HTS tape, and the total AC loss has been obtained by summing the two type of losses [215]. In order to measure the total AC loss in HTS CCs carrying AC transport current in an AC transverse magnetic field, Jiang and Amemiya have developed a linked pick-up coil (LPC) to reduce the error in the measured magnetization loss due to the variation of field orientation and used the combination of an internal compensation coil and a non-inductive shunt resistor to reduce the LPC output voltage and phase error [216]. Schwartz et al have designed a versatile AC loss and stability characterization facility suitable for various temperatures between 35 to 100 K [217]. This facility allows for total AC loss measurements under simultaneous AC transport currents and background fields, and the sample can rotate to vary its orientation with respect to the field. Vojenciak et al have studied the influence of the voltage taps position on the AC loss of the HTS tapes and pointed out that the placement of voltage contacts outside the current leads is beneficial for the protection of the sample against thermal runaway, but the eddy current loss in normal metal is unavoidable during the loss measurement [218].

The above-mentioned AC loss measurement methods perform well when the carried current is purely sinusoidal. However, as pointed out in Section 3, the superconductors applied to

electrical machines have to work with non-sinusoidal signals, namely harmonics. De Bruyn et al have specified in [192] that the total AC loss is not always the result of a linear contribution of different harmonics when the transport current is not purely sinusoidal. Therefore, to measure the AC loss in superconducting machines, the conventional electric methods need to be improved. A direct electric method has been proposed in [192], which is achieved by directly measuring the current and voltage over the specimen. Therefore, the average P_{trans} can be calculated by

$$P_{\text{trans}} = \frac{1}{NT}\int_{t=t_0}^{t=t_0+NT} u(t)i(t)dt \tag{2.31}$$

where T is the current cycle, N is an integer. The diagram for the measurement system is shown in Figure 2.5.2. Zhu et al have recently proposed an integral method for measuring the AC loss of HTS coils carrying non-sinusoidal current [219]. The current flowing through the HTS coil is obtained by measuring the voltage of the inductance-free resistor (divider). The proposed integral method has provided a useful tool for measuring the AC loss of superconductors carrying non-sinusoidal currents, which is of great significance for the loss quantification in superconducting machines.

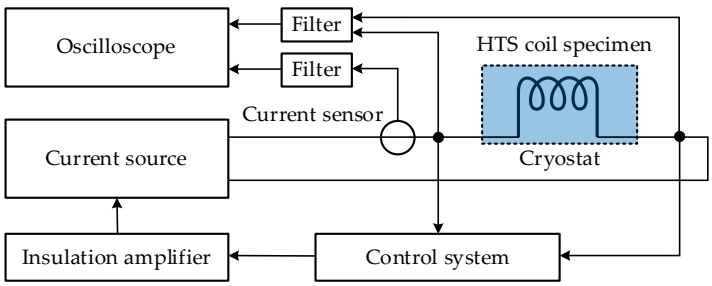

Figure 2.5.2 Schematic diagram of the experimental setup for measuring transport AC loss in superconducting specimen [192].

As mentioned above, dynamic loss happens when the HTS CC carrying DC is exposed to time-varying magnetic fields, which can dominate the total loss of field coils in superconducting machines. The experimental setup for the measurement of the dynamic loss of HTS CCs is shown in Figure 2.5.3, designed by Jiang et al [220]. This system is mainly composed of a custom-built AC magnet, a DC power supply that provides transport current, and a cryogenic container to maintain the operating temperature. The dynamic loss is calculated by measuring the voltage along with the transport current of the coated conductor sample. The measurement method has been extensively applied to much experimental exploration of dynamic resistance and dynamic loss of HTS CCs [32, 122-123, 220-223]. Ogawa has studied the dynamic loss and magnetization loss of an HTS pancake coil with a

double pick-up coil method and found that the dynamic resistance can mitigate the DC of the coil when it is operated in the permanent current mode [197].

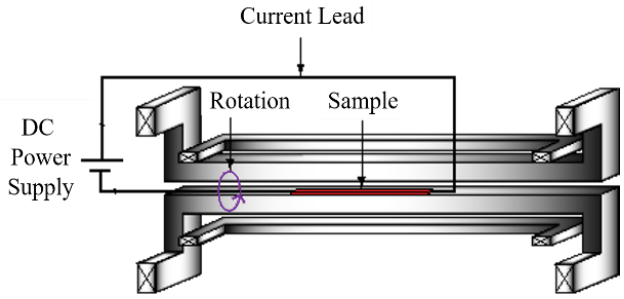

Figure 2.5.3 Experimental setup for measuring the dynamic loss of HTS CCs [220].

2.5.2 Magnetic method

The magnetic method is regularly used to measure the hysteresis loss of superconductors. By measuring the voltages over pick-up coils around the superconducting specimen, which are then multiplied by the field strength and integrated over one cycle, the variation in the magnetic moment of the specimen can be identified [224]. The magnetic moment of the superconductor can be measured with several methods, such as pick-up coils, Hall probes, superconducting quantum interference devices (SQUID), and vibrating-sample magnetometers (VSM). The measurement system is usually composed of the AC magnet, cryostat, pick-up coil, compensation coil, high-current amplifier, as well as the data acquisition system.

According to [193], for small superconducting samples, the hysteresis loop can be measured by SQUID and VSM methods to obtain the hysteresis power loss per unit length (W/m), as

$$P_{\text{hys}} = CAf\,\mu_0 \oint H_{\text{ext}}\,dM = -CAf\,\mu_0 \oint M\,dH_{\text{ext}} \tag{2.32}$$

where A is the geometrical cross-sectional area of the sample, C represents the effective area coefficient (C = 1 at low frequencies), H_{ext} denotes the AC external magnetic field strength, and M stands for the measured magnetization. Hysteresis loss can also be acquired by measuring the imaginary part of complex AC susceptibility. In a superconducting machine, the HTS field windings are always exposed to a large DC background field with a relatively small AC ripple field. In this case, P_{hys} can be calculated by

$$P_{\text{hys}} = CAf\,\frac{\pi B_{\text{m}}{}^2}{\mu_0}\,\chi'' \tag{2.33}$$

where χ'' is the measured imaginary part of the AC susceptibility, and B_{m} is the amplitude of the AC magnetic field. The minimum measurable loss value can attain 10^{-6}~10^{-5} W/m with the

magnetic method. The equivalent circuit for a typical AC susceptibility measurement system is shown in Figure 2.5.4.

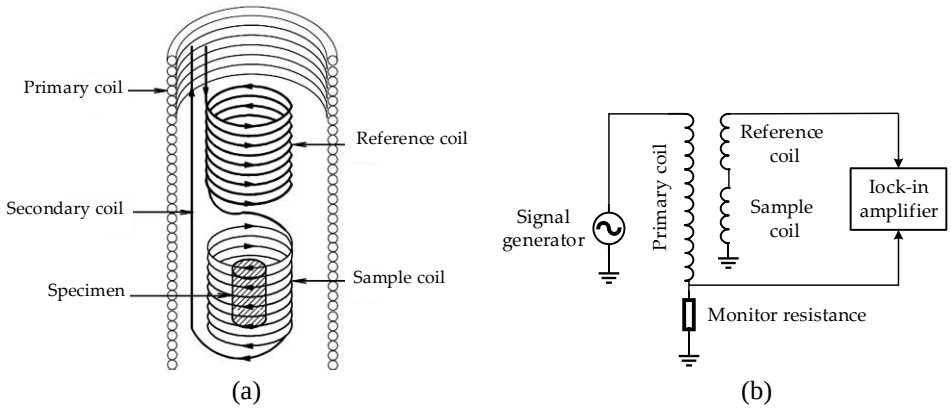

Figure 2.5.4 Diagrams of the measurement systems for AC susceptibility of superconductors [225]: (a) Geometrical arrangement of different coils; (b) Equivalent circuit for the measurement system using the magnetic method.

Pardo et al have measured the AC loss and voltage signal in a pancake coil made of CCs with the ferromagnetic substrate utilizing a SQUID magnetometer at 100 K [226]. However, it appears that the SQUID and VSM techniques are too slow for measurement at power frequencies. For varying magnetic fields with different orientations, the pick-up magnetic methods seem to be the best choice. Gomory has measured the AC susceptibility with a pick-up coil and lock-in amplifier combined method [227]. Kajikawa et al have proposed a perpendicular-field loss measurement method for superconducting coils using a pair of pick-up coils, which enables the measurement of long-length samples in a compact apparatus [228]. Iwakuma et al have applied a saddle-shaped pick-up coil to measure the magnetization loss of superconducting tapes and windings because it can avoid the end effect by using longer sample wires [229-231]. The saddle-shaped pick-up coil based magnetic method has recently been used in [232] to quantify the AC loss of perpendicularly stacked REBCO CCs. To characterize the AC loss of a coil wound cable-in-conduit conductor (CICC) in pulsed regimes, Muzzi et al have modified the pick-up coils with an extra-compensation procedure [233]. Fisher et al have developed a simple calibration-free method based on the dipole approximation, which allows obtaining both the AC loss and orientation of the sample magnetic moment [234]. More recent experimental measurement work based on the magnetic method can be found in [235-236].

2.5.3 Calorimetric method

If the superconducting sample carrying an AC current is exposed to an AC magnetic field, the conventional electric method will be applicable for the AC loss measurement only when

the current and field are varying at the same frequency and in phase. It is practical to have the transport current and magnetic field out of phase in superconducting machines. In this case, the calorimetric method becomes a superior alternative. In [237-238], the influence of the phase shift between the transport current and the external magnetic field on the AC loss of the HTS tape has been investigated using both the electric method and calorimetric method. As a comparison, though the electric method has higher sensitivity, the calorimetric method can provide higher reliability. Besides, the disturbance of alternating currents or magnetic fields is intrinsic in the electric and magnetic measurement approaches, which is not a concern for the calorimetric method. Therefore, the calorimetric method can be applied to a complicated electromagnetic environment. With the calorimetric method, the total AC loss can be obtained by the measurement of either the temperature rise of the superconductors or the evaporated cryogen.

2.5.3.1 Measurement of the temperature rise

The thermal conductivity measurement technique was first put forward by McConnell and Critchlow for the determination of superconducting AC power loss [239]. To measure the temperature variation, cryogenic thermometers, cryostat, thermal isolation material, and voltage taps are usually needed. The calibration of the thermometers is the first step. Then, the variation of the thermal conductivity of the superconducting sample with temperature needs to be measured. Once the temperature distribution along the sample is known, the total AC power dissipation can be obtained by [239]

$$P_{\mathrm{AC}} = \frac{8KA \cdot \Delta T}{L^2} \tag{2.34}$$

where K, A, and L represent the thermal conductivity, cross-sectional area and length of the superconducting sample, respectively. ΔT denotes the temperature difference between the sample center and its ends. It is claimed that the thermal conductivity measurement technique is possibly able to measure a loss of 2×10^{-10} W/cm with an uncertainty of about 30% [239].

In order to measure the low losses of superconductors operated at liquid-helium temperature calorimetrically, Schmidt and Specht have developed a temperature-rise-measurement based method with a resolution of 10^{-8} W [240]. The superconducting sample is placed into a vacuum vessel and connected via a thermal resistance to the liquid-helium bath. However, to measure low loss of less than 1 μW, three conditions must be fulfilled: no additional eddy current losses generated in the structure, limited self-heating power in the thermometer attached to the sample, and stable temperature of the heat sink. Dolez et al have proposed a null calorimetric method for measuring the AC loss of superconducting tapes without any compensation and

any size and shape restriction [241], and then this method has been ameliorated in [242] to overcome the insufficient thermalization of the tape extremities and thermocouple reference junctions. Although it was demonstrated in [241-242] that the proposed null calorimetric method was able to measure losses of 10^{-8} W/cm, its accuracy and uncertainty were not discussed in detail. To simplify the experimental setup and save measurement time, Ashworth and Suenaga have reported a simple technique to measure the AC losses using a differential thermocouple [243]. However, this technique has a low resolution limit of approximately 0.01 W/m. See et al have reported a calorimetric method to determine the AC losses of superconducting samples in superimposed DC and AC fields/currents by measuring the change in resistance due to temperature variation [244-245]. The measurement system can achieve operating temperature from 2 to 300 K [245].

For the superconductors located in electrical machines, they can experience rotating magnetic fields. In view of this situation, Ghoshal et al have adopted the calorimetric method based on the temperature variation of the superconductor thermally insulated from the cooling bath [246]. The principle of this calorimetric method is shown in Figure 2.5.5, in which the tested specimen is placed in a vacuum vessel and connected to the coolant by thermal resistance. The NASA Glenn Research Center has recently developed a LH_2-based test rig, which can be used to measure the AC loss of HTS stator coils in rotating magnetic fields with the thermocouples between the range of 18 to 28 K (extensible to 95 K using GHe or LN2 as a working coolant) [247]. The system can be applied with the following test parameters: injected current (0 to 400 A), magnetic field (0 to 0.6 T), phase angle between induced voltage and injected current (–180° to 180°), and frequency (0 to 400 Hz).

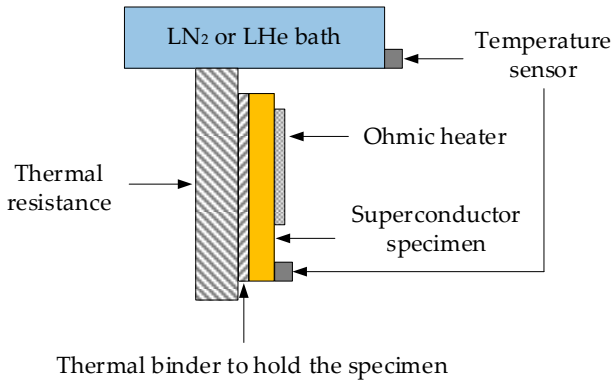

Figure 2.5.5 Diagram of the calorimetric measurement system for AC loss of superconductors, adapted from [246].

Another temperature variation detection method is by optical fiber Bragg grating (FBG) [248], which makes use of the wavelength variance dependence of temperature described by

$$\Delta\lambda_B = \alpha_T \Delta T = \lambda_B (\xi + \alpha)\Delta T \quad (2.35)$$

where λ_B stands for the wavelength of the optical FBG; α constants. The minimum measurable loss by the temperature rise measurement method is approximately 10^{-4} W/m. The measurement system using FBG is presented in Figure 2.5.6. Compared to the conventional calorimetric methods, the FBG sensor possesses the advantages of rapid response and anti-electromagnetic interference, it is thus capable of measuring the AC loss of HTS applications in a complicated electromagnetic environment at a faster speed.

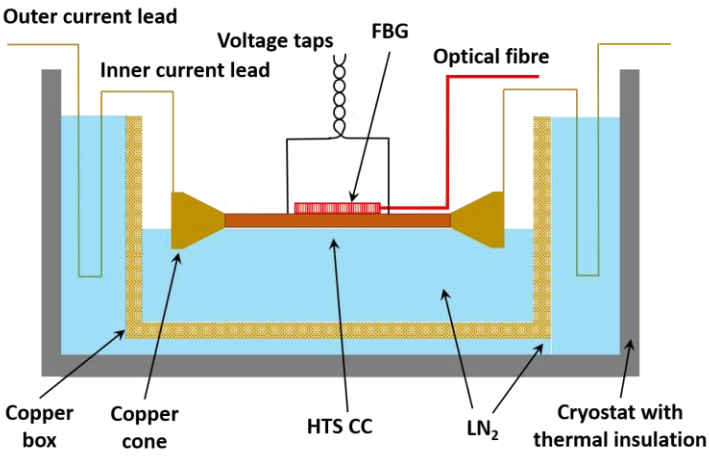

Figure 2.5.6 Diagram of the calorimetric measurement system based on the optical fiber Bragg grating for AC loss of HTS tapes, adapted form [248].

2.5.3.2 Measurement of the cryogen evaporation

The temperature rise due to dissipated energy will lead to the evaporation of the cryogen; thus, the measurement of AC loss can be achieved by measuring the gas flow volume of the evaporating cryogen, namely the boil-off method [249]. The corresponding measurement system mainly consists of the AC power supply, non-metal cryostat, cryogen, heat exchanger, thermostat, and gas flow meter. The AC power dissipation (W/m) can be obtained by [193]

$$P_{AC} = CAf \int_{T_b}^{T_m} \gamma C(T) dT = CAf \left[H(T_m) - H(T_b) \right] \quad (2.36)$$

where A is the geometrical cross-sectional area of the sample; C represents the effective area coefficient; T_b is the environment temperature; T_m stands for the average temperature rise; $\gamma C(T)$ is the volumetric heat capacity of the superconductor; $H(T)$ refers to the enthalpy of the cryogen at temperature T.

It should be noted that the measurement of cryogen evaporation is time-consuming and does not possess a high accuracy, with the minimum measurable loss of 10^{-4}~10^{-2} W/m. With this

method, Kuroda has measured the AC losses of superconducting solenoidal coils with a resolution of 10^{-3} W [250]. However, it is difficult to maintain the thermal equilibrium of the liquid-cryogen-filled cryostat, which affects the measurement accuracy. To overcome this disadvantage, Kuroda has then proposed a modified boil-off method without a pre-calibration, and the AC loss is obtained by multiplying the generating rate of the helium gas by a constant [251]. After improvement, the accuracy and measurement range could attain ±3% and 3-170 mW, respectively. Okamoto et al have developed an apparatus for applying the nitrogen boil-off method to measure the AC losses in HTS coils at liquid nitrogen temperature, and a sensitivity of about 0.1 W was achieved [252]. Yuan et al have measured the transport current loss of a pancake coil with the LN_2 boil-off measurement technique and the electric method, respectively. The experimental results are consistent with the model calculations, though there exists a discrepancy between the modelling results and the electric method based experimental data at large currents [253]. Figure 2.5.7 (a) shows a calorimetric system to measure the total AC loss of superconducting tapes or coils based on the boil-off of liquid nitrogen, proposed by Murphy et al [254]. With the help of the proposed calorimeter system, a permanent magnet rotor has been designed to simulate the electromagnetic environment of an electrical machine, and the AC loss of one armature coil carrying AC current exposed to rotating fields has been measured, as shown in Figure 2.5.7 (b). The calorimetric system can measure low losses from a few milliwatts to several hundred milliwatts [254].

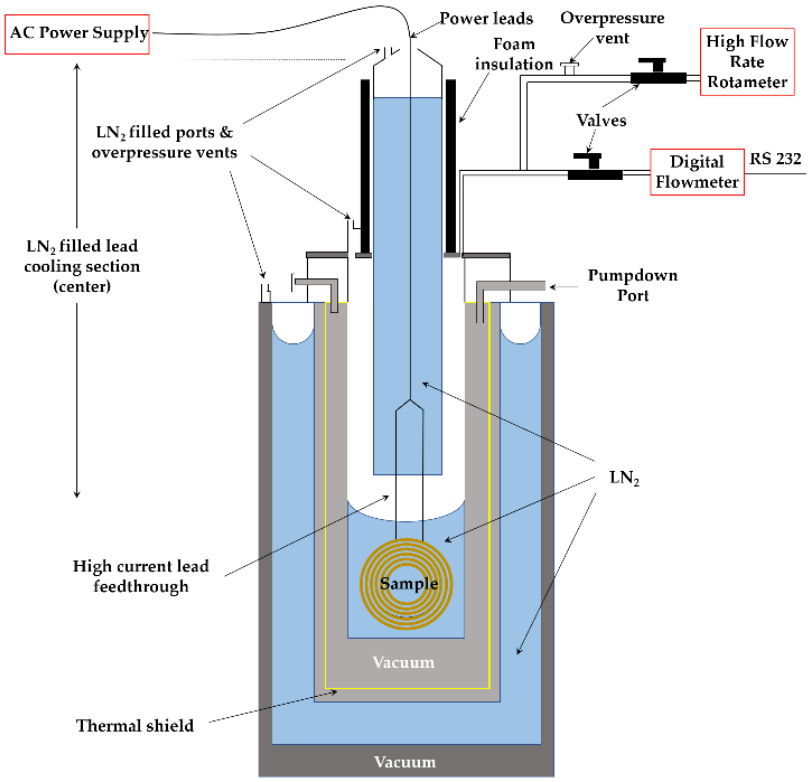

(a)

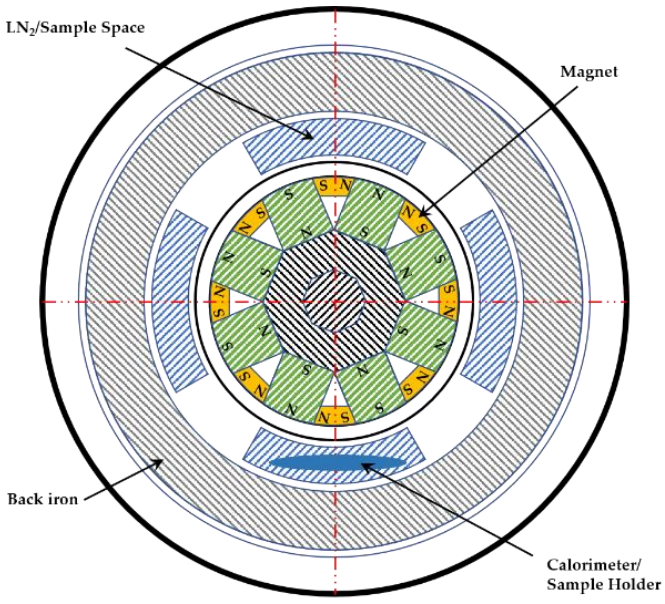

(b)

Figure 2.5.7 Diagram of LN_2 boil-off calorimeter system for measuring AC losses of HTS tapes and coils, adapted form [254]: (a) AC transport current loss measurement of an HTS coil; (b) AC loss measurement of an armature coil in the environment of an electrical machine.

2.5.4 Comparison of AC loss measurement methods

The comparison among three different measurement methods has been summarized in Table 5. Nowadays, the measurement of AC loss has been concentrated on simple single HTS tape or stacks of tapes [215-216, 255-257], and stationary coils [258-263]. It can be seen that the most widely adopted method is the electric method. Nevertheless, it should be noted that most of the experimental measurements are conducted with pure sinusoidal currents or fields (or both in phase at the same frequency). As far as the AC loss measurement in high-speed electric machines is concerned, the extensively used traditional electric method is inapplicable for measurement in a high-frequency electromagnetic environment containing harmonics. Significant progress has been made in [264] in which Zhang et al have measured the AC loss of HTS stator coils under rotational magnetic fields inside an axial flux type machine demonstrator. However, for simplification, the tested unit is one circular coil rather than widely used racetrack coils, and the measurement has been conducted under low frequencies of less than 150 Hz. Therefore, for the measurement of AC loss in a high-speed superconducting machine, an efficient and highly accurate method remains to be developed.

Table 5. Comparison among different AC loss measurement methods

Measurement Methods	Main purpose	Advantages	Disadvantages
Electric method	Transport current loss; total AC loss	Fast; high sensitivity; high accuracy; able to measure low AC loss	Compensation coil needed; lock-in amplifier can only work with pure sinusoidal signals; easy introduction of harmonics.
Magnetic method	Magnetization loss	Fast; high sensitivity; high accuracy; able to measure low AC loss	Limited to static measurement; pick-up coils easily interfered by external magnetic fields;
Calorimetric method	Total loss	Disregarding object shape; disregarding working conditions; able to measure large scale specimen	Poor sensitivity; weak accuracy; long time consumption; possible disturbance from thermal effects of non-superconductors.

2.6 AC loss Reduction Techniques

2.6.1 Filamentation of HTS CCs

The large cross-sectional aspect ratio of HTS CCs leads to a high magnetization loss. Therefore, to reduce AC loss, the striation of the HTS layer to a filamentary structure has been proposed [265-269]. Two types of techniques can be used to divide the HTS layer: striation before or after REBCO synthesis [268-269]. The former is the processing of the substrate by etching, lift-off, mechanical scribing, and ink-jet printing for the synthesis of the striated HTS layer or the barrier between filaments. The latter includes laser ablation, mechanical cutting, and chemical etching, etc. Godfrin et al have made a comparison of the two striation techniques in [269]. The diagram of the filamentation of a typical HTS CC is presented in Figure 2.6.1.

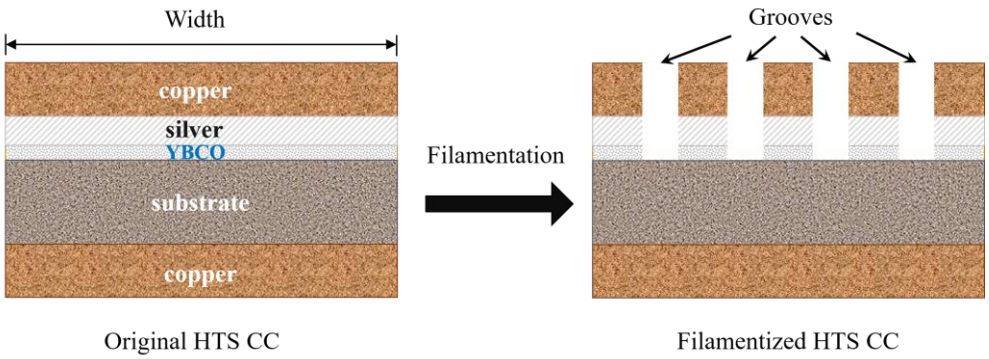

Figure 2.6.1 Diagram of the filamentation of a typical HTS coated conductor (cross section).

As illustrated in Figure 1.1.1, the filamentation of HTS CCs can effectively decrease the AC loss, and the loss reduction effect gets enhanced with the increasing number of filaments. According to Equation (2.9), the magnetization loss is proportional to the square of the width of the HTS CC, thus a reduction by a factor N is expected if the HTS layer is striated to N filaments. However, this is true only at sufficiently high fields because at lower fields the superconductor volume penetrated by the field is larger in uncoupled filaments than in a nonstriated CC [36] and hence the loss of a filamentized CC can be greater than that of the original one, as shown in Figure 1.1.1. The influence of subdividing YBCO films into arrays of parallel strips on AC loss was revealed experimentally for the first time in [270]. Then, in [271], it has been demonstrated that the laser striation process has little influence on the critical current of the tape with a small number of filaments. However, when increasing the number of filaments, as illustrated in [269], the critical current of each CC will experience a degradation. In [272], the authors point out that an AC loss decrease proportional to the number of filaments only happens when the filaments in perpendicular magnetic fields are decoupled. However, this is not the case in practical machine applications because the filaments are

coupled by current leads. The coupling loss between filaments can largely increase the total AC loss, which is proportional to the frequency and the square of the external magnetic field [265]. As illustrated in [265], a decrease of coupling loss at high frequencies can be achieved by increasing the transverse resistivity and by reducing the twist pitch. It should be noted that though the filamentation of the CC can help decrease the overall AC loss, the mechanical strength of each filament degrades. Therefore, once one filament breaks down due to a localized defect, hotspot, or a mechanical shock, the superconducting state of the CC can be destroyed. To solve this problem, bridges can be exploited to enhance the connectivity between filaments. In [273], AC losses of striated and nonstriated RABiTS CCs were measured and compared. The results showed that the application of bridges can increase the total AC loss due to significant filament coupling; however, the total AC loss was still much lower than that of CCs without filamentation. Therefore, the number and arrangement of filaments can bring about a trade-off between the current sharing capacity and total AC loss of HTS CCs. It is not sufficiently effective to decrease AC loss simply by cutting the CC into filaments because of the incomplete flux penetration in between the filaments [274]. Therefore, virtual transverse crosscuts have been proposed in [275] to introduce flux penetration in between the filaments more uniformly, which can help magnetically decouple the filaments and further reduce AC loss. Indium bridges across crosscuts can be used to guarantee the continuity of the current flow. The improvement of striation methods can also help with the reduction of AC loss. A significant loss reduction method in HTS CCs with transposed filaments has been reported in [276]. The proposed CC is made of two diffusively bonded silver-clad commercial CCs with zigzag patterned filaments partially separated by a dielectric layer. In [276], the authors demonstrate that the optimization of the bonding process and the decrease of the filament size contribute positively to the AC loss reduction. In [277], a scalable laser lithographic process has been applied, including laser patterning a resist coating, and etching. Results have demonstrated that the critical current is not degraded for striation width over 150 μm, and the AC loss can be decreased effectively. Different from conventional filamentary HTS CCs, a soldered-stacked-square (3S) wire has been proposed in [278]. The manufacturing principle is to mechanically cut HTS CCs into 1-mm-wide ones, solder through a soldering furnace, and stack them into a wire, as shown in Figure 2.6.2. [278] reported that the 3S wire can help to reduce AC loss by 80% compared with originally uncut tapes.

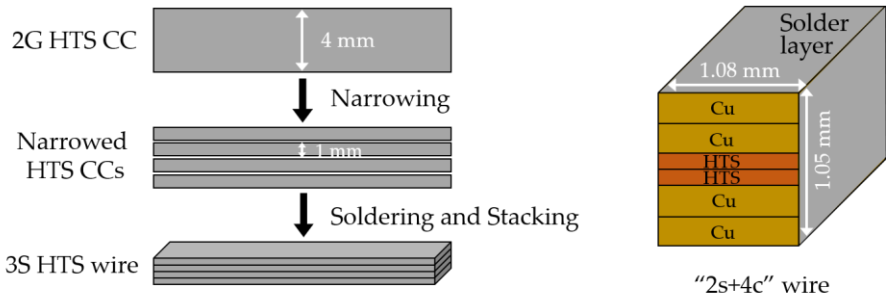

Figure 2.6.2 Diagram of the 3S wire, adapted from [278]: (a) Fabrication process of the 3S wire; (b) Cross-sectional view of the 3S wire with 2s+4c (2 superconducting layers + 4 copper stabilizers).

2.6.2 Roebel, Rutherford-type, and CORC® cables

Another method to reduce the AC loss of HTS CCs is to change their physical arrangements, e.g., the Roebel concept [279-281], Rutherford cable [282-283], and Conductor on Round Core (CORC®) wire [284-286]. The Roebel cable concept was proposed by Ludwig Roebel in 1914 to produce a low-loss copper cable [286]. The first HTS Roebel cable was developed by the Siemens Corporate Technology group using BSCCO-2223 tapes in 2004 [279], and later the Karlsruhe Institute of Technology applied the Roebel structure to REBCO CCs in 2006 [280]. The diagram of a typical Roebel cable [287] is shown in Figure 2.6.3 (a), in which the HTS CCs are cut in a specially designed zigzag pattern. Because of their periodically repeating and transposed physical properties, Roebel cables can effectively reduce the transport current loss and magnetization loss compared with conventional HTS stacks, especially at medium-high currents and low magnetic fields [280]. [281] has shown that the decrease of strand width can further help lower AC loss. As mentioned before, the filamentation of HTS CCs can help with the reduction of AC loss. However, at high frequencies, the coupling loss between filaments will increase rapidly and begin to dominate. To minimize the high-frequency coupling loss, the Rutherford cable structure has been proposed by Wilson, which does not require complex twist geometries [282]. It has been demonstrated that the Rutherford configuration is a promising candidate to realize the ultimate low AC loss [283]. The conventional Rutherford-type cabling technique is suitable for round strands of superconductors [288], e.g., BSCCO-2212 and NbTi wires, as shown in Figure 2.6.3 (b). To extend the Rutherford-type design towards 2G flat HTS CCs, the concept of twisting stacked tapes has been firstly introduced by Takayasu et al [289], based on which Uglietti et al have developed a novel flat HTS cable by winding the HTS strands around a central copper former [290, 291], as shown in Figure 2.6.3 (c). Although the design of the twisted flat HTS cables was proposed for fusion magnets with high current carrying capacity, they are believed

to possess the potential to be applied as superconducting machine windings to achieve low AC loss. The CORC® cabling approach was initiated by Van der Laan et al [284], which is achieved by the helical winding of REBCO CCs on a round former, as shown in Figure 2.6.3 (d). The decrease of the width and thickness of commercial REBCO CCs has enabled the production of flexible, round, and multifilamentary HTS wires [285]. Vojenčiak et al have demonstrated that the magnetization loss in CORC® cables wound from striated CCs containing 5 filaments can be reduced by a factor of almost 5 at fields higher than the penetration field [292]. Terzioglu et al have concluded that the copper tube former can contribute to the transport current loss and magnetization loss of CORC® cables, thus an optimized former material with low electrical conductivity and high thermal conductivity should be employed to reduce the AC loss [293]. Yagotintsev et al have compared the AC loss and inter-tape contact resistance of multiple cabling methods, including REBCO CORC®, Roebel, and stacked tape cables [294]. It is found that the CORC® cable has lower hysteresis loss in an alternating magnetic field perpendicular to the wide side of the REBCO layer, compared with Roebel cables and non-twisted conductors. Nevertheless, it should be noted that twisting of filaments has the possibility of damaging the microstructure and grain orientations, thus the critical current of the CC can be severely affected.

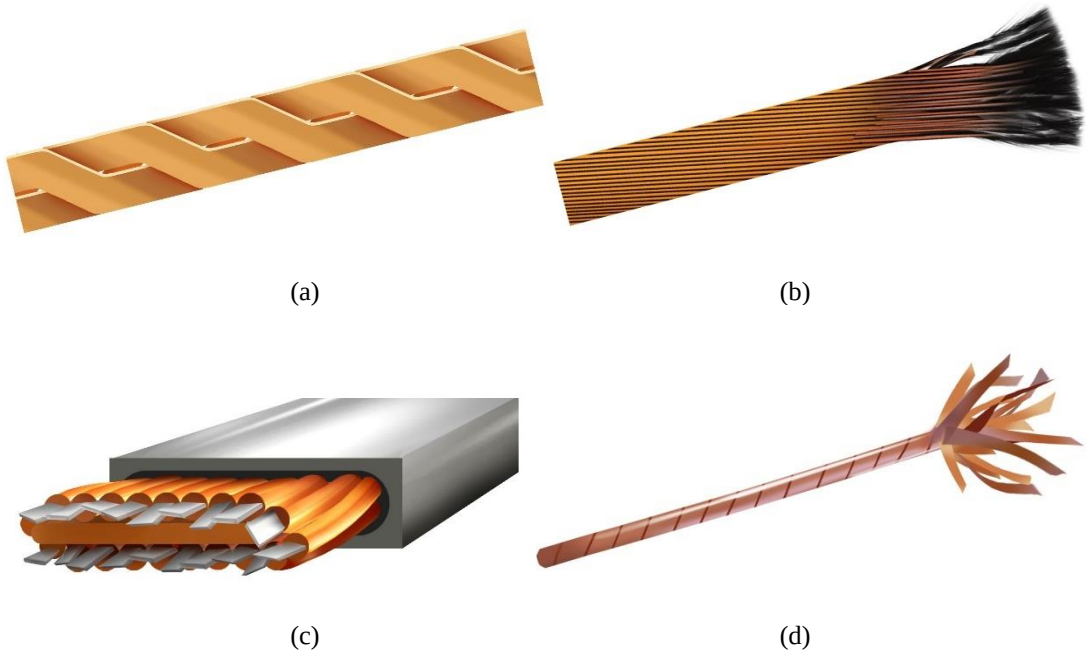

Figure 2.6.3 Pictures of Roebel and Rutherford-type cables: (a) Roebel cables fabricated from HTS CCs, adapted from [287]; (b) Rutherford cable made from round superconducting wires, adapted from [288]; (c) Twisted flat HTS cable made from HTS CCs, adapted from [291]; (d) CORC® wire, adapted from [286].

2.6.3 Flux diverters

In addition to the modifications to the physical structure of HTS CCs, the application of magnetic materials as flux diverters in electrical machines can also serve to decrease the AC loss of superconductors. In [295-296], Gömöry has demonstrated that adding ferromagnetic covers on the edges of a single HTS CC or a stack of tapes can effectively reduce the magnetization loss. However, the reduction effect becomes weaker with the increase of CC numbers. The ferromagnetic shielding effect in HTS CCs was first experimentally observed in [297] and the ferromagnetic materials' potential of loss reduction has been evaluated. As pointed out in [297], an ideal flux diverter material should exhibit low saturation field densities, low hysteresis loss, and high permeability. A YBCO pancake coil with two ring-shaped magnetic diverters made of an iron-based amorphous alloy has been tested in [298], and the results have shown that the reduction of AC loss is due to the magnetic mirror effect rather than change of the coil critical current. However, Pardo has pointed out that the hysteresis loss in the magnetic materials can degrade the reduction effect of flux diverters. The effect of flux diverters on the reduction of transport current loss has been verified in [299], and it is shown that the ideal diverter material should have a high saturation field and a low remnant field. Liu has studied the geometric dimension and location optimization of the magnetic flux diverter for a better loss reduction effect [300-302]. Results in [300] have shown that the flux diverter exhibits a negative effect on the CC critical current, depending on the width, height of the diverter, and the gap between the diverter and the HTS coils. [301] shows that, besides the positions of flux diverters, their loss reduction effect is also related to the load ratio between the transport current and critical current, e.g., the use of flux diverters in the middle and end positions of the double pancake coil can reduce the AC loss by 70%. The frequency-dependence of the diverter effect for the transport current loss of a YBCO coil has been investigated within the range of 10 Hz~5 kHz in [302], and the arrangement of the HTS coil and flux diverters are presented in Figure 2.6.4. Interestingly, the effect of flux diverters for HTS coils with magnetic substrate depends on both the load ratio and frequency: at low load ratios and high frequencies, the flux diverter will increase the total loss, because under such conditions the eddy current loss and ferromagnetic loss (in both diverter and the magnetic substrate) will be enhanced. However, the effectiveness of flux diverters for non-magnetic-substrate-based HTS coils at high frequencies still deserves further investigation in the future.

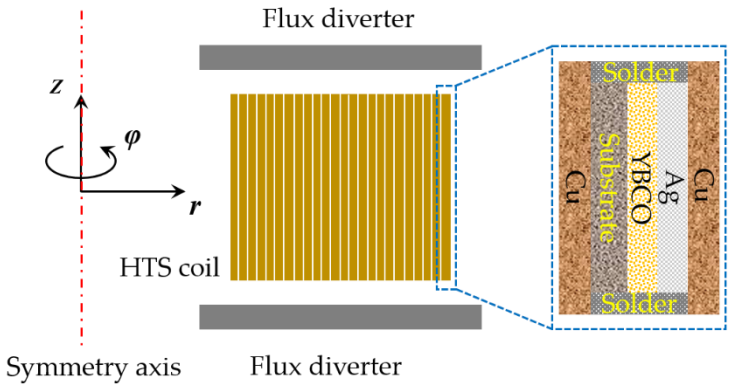

Figure 2.6.4 Arrangement of the HTS coils and ferromagnetic flux diverters [302].

2.6.4 Winding techniques

Apart from the structure modification of superconductors and the application of ferromagnetic flux diverters, winding techniques are another effective way to decrease the AC losses of coils. Kawagoe et al have proposed a winding method for multilayer-type conductors composed of stacked Rutherford-type cables by controlling the twist angle around the conductor axis, which can help decrease the total AC loss by 74% compared to the conventional winding method [303]. Heydari et al have applied two auxiliary windings to reduce the leakage flux in HTS transformers so that the AC loss of HTS coils can be decreased by about 13.6% [304]. Kim et al have employed a metal-clad (MC) winding technique for non-insulated (NI) HTS coils to enhance the turn-to-turn resistance by adding a 5-μm-thick coating of stainless steel to a copper-stabilized HTS CC [305]. It has been demonstrated that the NI coil has the least AC loss, followed by the NI coil with the MC winding technique, and the insulated coil has the highest AC loss. However, it should be noted that the AC transport current loss tests in [305] were performed at 20 Hz, i.e., at low frequencies. Therefore, the effectiveness of the added metal clad in high-frequency electromagnetic environment (e.g., in high-speed rotating machines) remains unclear. In addition, the application of such metal clad can definitely increase the total mass of the machine windings. The influence of turn-to-turn resistivity on the AC loss of HTS coils has been recently discussed by Wang et al in [306], in which a grading turn-to-turn resistivity technique has been put forward to reduce the total AC loss on the outer turns while keeping good thermal stability on the middle turns of the NI HTS coils used for electrical aircraft propulsion. Simpson et al have invented a shaped profile winding for minimal AC loss in conventional electrical machines [307], as shown in Figure 2.6.5, which maximizes slot area utilization to realize an improved low-speed and DC performance while achieving low AC loss. As pointed out by Simpson and Kails from the University of Bristol, the proposed shaped profile winding technique can have the potential to

be adapted to superconducting windings in the future. Recently, Jiang et al have reported a 15% loss reduction in a 3-phase 1 MVA HTS transformer by exploiting the anisotropic field dependence of the critical current of HTS CCs [308]. By orienting the CC or coil appropriately with respect to the external field, a substantial AC loss reduction can be achieved.

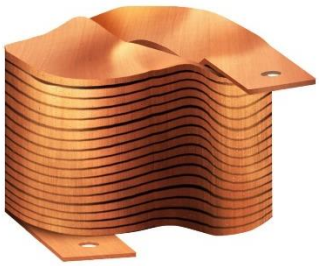

Figure 2.6.5 Diagram of the shaped profile winding [307].

To sum up, the existing AC loss reduction methods have provided some significant design guidelines for us, but a few challenges remain:

(1) The filamentation of HTS CCs, the Roebel, the Rutherford as well as the CORC cables can help with the reduction of AC loss. However, their electro-thermal performances under the skin effect and coupling effect between filaments in the practical machine environment (especially at high frequencies for high-speed rotating machines) is still unclear, therefore their loss reduction effectiveness needs to be further explored.

(2) Flux diverters have proven to be useful to decrease the AC loss of superconductors, but this effectiveness gets weaker with the increase of the number of turns in a coil. Besides, the hysteresis loss in ferromagnetic flux diverters increases rapidly with increasing frequency. In this way, the flux diverter at high frequencies can become a severe heat load itself. Therefore, the contribution of flux diverters to the total loss distribution at high frequencies inside superconducting machines needs more investigation.

(3) Winding techniques appear to be a useful alternative for the AC loss reduction of HTS coils. When the coils are implemented into rotating machines, besides the electromagnetic performance, their mechanical strength, thermal characteristics, as well as processing difficulty also need to be considered. A balance needs to be reached between the AC loss reduction and total mass augmentation for the design of superconducting machines.

2.7 Conclusion

This chapter has reviewed multiple AC loss related topics with respect to superconducting machines: adopted superconducting materials, AC loss mechanism and analytical formulae,

modelling methods, measurement approaches, as well as loss reduction techniques. The main conclusions are presented as follows.

The main advantage of LTSCs lies in their relatively lower cost. MgB_2 has been employed in many armature coils because of its filamentary structure which can achieve a relatively lower AC loss. HTS CCs, fabricated from REBCO or BSCCO, possess larger current carrying capacity and higher critical field, thus they can bring a higher electric and magnetic load to superconducting machines. Although the cryogenic system for superconductors has not been discussed in this chapter, we have to note that its cost plays an important role in the design of superconducting machines. Compared to LTSCs and MgB_2, both of which usually function in LHe at 4 K, HTS tapes have higher critical temperature thus they can be cooled by LN_2 operating at 77 K. Therefore, the cost of the cryogenic system used for HTS CCs can be relatively lower. In addition, the material cost of HTS CCs is expected to decrease soon with the advancement of processing techniques and material science. Hence, HTS CCs are believed to have a good application prospect in superconducting machines. HTS bulks and trapped field magnets are also competent candidates as field sources in superconducting machines, which can avoid the application of current leads during operation.

The existing analytical equations to calculate AC loss are mainly focused on HTS thin films. The analytical formulae can help easily understand the loss mechanism and its influential factors, which are conveniently used to predict the AC loss of HTS CCs in simple structures. However, when the HTS CCs are wound into complex structures, e.g., racetrack coils widely used in electrical machines, we need to utilize numerical modelling or measurement methods to quantify the total loss. The two principle reasons are: 1) The analytical formulae have been derived based on some necessary approximations and assumptions, which become inapplicable in complex machine environment; 2) There always exist harmonics in electrical machines composed of high-frequency components, and the interactions between the superconducting and non-superconducting layers of HTS CCs at high frequencies cannot be correctly reflected by the existing equations. Therefore, it remains an open subject for researchers to develop analytical models to predict the AC loss of complex geometries employed in a complicated electromagnetic environment.

The widely adopted numerical modelling methods for the AC loss quantification of superconductors are mainly consisted of: 1) Maxwell's equations-based FEM achieved by four types of basic formulations, including the $\boldsymbol{T}$-$\boldsymbol{\phi}$ formulation, the $\boldsymbol{A}$-$\boldsymbol{V}$ formulation, the $\boldsymbol{E}$-formulation, and the $\boldsymbol{H}$-formulation and their several combinations, e.g., the $\boldsymbol{H}$-$\boldsymbol{A}$ formulation, $\boldsymbol{T}$-$\boldsymbol{A}$ formulation, and $\boldsymbol{H}$-$\boldsymbol{\phi}$ formulation; 2) Integral equation method for thin tapes solved with

FEM; 3) Minimum Magnetic Energy Variation method; 4) Minimum Electro-Magnetic Entropy Production method. Maxwell's equations-based FEM can be easily incorporated into commercially available software, e.g., COMSOL Multiphysics and Ansys, and the interactions between superconducting and non-superconducting parts inside machines can be considered, thus this approach is recommended for the AC loss estimation in HTS machines. Given that a great number of HTS CCs are needed in electrical machines, the modelling of superconducting windings can be computationally complicated and time-consuming. To improve the computational efficiency, three simplification techniques can be exploited, including the homogenization, multi-scaling, and densification methods. For modelling a large number of HTS turns at low frequencies, both the ***H***-formulation and ***T-A*** formulation-based homogenization methods have a high computational speed with acceptable accuracy. The application of the multiscale modelling method can largely reduce the number of DOF, requiring less calculation memory, and thus it can further save computation time. The densification method leads to fewer tapes to be modelled. However, the 3D modelling of HTS racetrack coils considering the multilayer structure of each HTS CC in rotating electrical machines remains a big challenge to overcome.

Besides numerical modelling, significant contributions have been realized in the instrumentation and measurement of AC loss in superconductors. More specifically, AC loss measurement techniques can be categorized into the electric method, the magnetic method, and the calorimetric method. The electric method has been most widely used because of its relatively higher sensitivity and shorter measurement duration. For measuring the total AC loss composed of transport current loss and magnetization loss, the electric method and calorimetric method are suggested. Considering the complex electromagnetic environment composed of high-frequency harmonics inside electrical machines, the calorimetric method seems to be the best choice because it disregards the object shape and working conditions, being also able to measure large scale specimen. However, the sensitivity of the calorimetric method is relatively poorer, and it takes longer duration for measuring compared to the electric and magnetic methods. The conventional electric method has been improved to measure the AC loss of superconducting coils carrying non-sinusoidal currents or in the case of phase shift between the measurement voltage and transport current, which is of great significance for the loss quantification in electrical machines. Nevertheless, an efficient and accurate experimental method remains to be developed to measure the total AC loss of superconductors applied in a complicated electromagnetic environment with harmonics inside practical electrical machines.

Concerning the AC loss reduction techniques, the modification of superconductor structures has been widely investigated, e.g., the filamentation of HTS CCs, the 3S wire, the Roebel structure, the Rutherford concept, as well as the CORC® wire. However, it should be pointed out that the filamentation process can potentially weaken the mechanical strength and critical current of the HTS CC. Although the filamentary structure can help with the reduction of AC loss at low frequencies, e.g., Roebel cables, it can bring about a high coupling loss between different filaments at high frequencies. The Rutherford design can mitigate the coupling loss, however, twisting of filaments has the possibility of damaging the microstructure and grain orientations, thus the critical current of the CC can be severely affected. The tube former can contribute to the AC loss of CORC® cables, thus an optimized former material with low electrical conductivity and high thermal conductivity needs to be investigated. Ferromagnetic flux diverters have been demonstrated to be useful for decreasing the AC loss of superconductors, despite that the effectiveness drops with the increase of turn numbers. We need to realize that the ferromagnetic materials can favor the total power dissipation of electrical machines, thus the effect of flux diverters applied to high-speed rotating machines deserves further exploration. Winding techniques can also be exploited to achieve the AC loss reduction of superconducting coils, e.g., the NI HTS coils and shaped profile windings. However, the mechanical and thermal characteristics of superconducting coils should also be taken into account when they are applied to practical electrical machines.

Evidently, remarkable original contributions have pushed forward the area of AC loss analysis, modelling, measurement, and controlling in superconductors. This chapter has clarified the state of the art of AC loss related research work with regards to superconductors, providing a useful reference for loss quantification and loss reduction techniques in superconducting machines. Additionally, this chapter exposes gaps in our understanding and knowledge and opens up the challenges that need to be addressed for the design of high-speed superconducting machines, delivering a helpful guideline for future research efforts.

Chapter 3. Numerical modelling methods for various HTS topologies

3.1 Introduction

In this chapter, the numerical modelling methods adopted in the thesis are presented. Based on Maxwell's equations, the numerical models for HTS CCs are built with the finite element method (FEM), which is achieved by two different formulations, namely the ***T***-formulation and the ***H***-formulation. At first, the governing equation based on the ***T***-formulation is derived for a 1D thin film, which only considers the HTS layer of the CC. However, given that at high frequencies the non-superconducting layers cannot be neglected, the conventional ***T***-formulation is then extended to the copper stabilizers, silver overlayer and substrate. Consequently, a 2D multilayer model is established for HTS CCs with open source code in FORTRAN 90, which is then validated by experimental data. Given that the ***H***-formulation can be easily implemented into FEM software, e.g., COMSOL Multiphysics, it has become the most widely exploited modelling method for HTSCs. Therefore, the ***H***-formulation based numerical models for HTS CCs are also presented, including the homogenization model and the multilayer model, from 2D to 3D implementation within COMSOL Multiphysics.

3.2 T-formulation Based Numerical Model

3.2.1 Governing Equation

As analyzed in Chapter 2, the ***T***-formulation is selected here because of some distinctive advantages, including high calculation speed and memory efficiency. The conventional ***T***-formulation based numerical model for HTS CCs only considers the HTS thin film, as it has a far greater current carrying capacity compared with non-superconducting layers. The thin film approximation for HTS CCs have been extensively adopted to simplify the modelling process, neglecting the influence of the thickness on the modelling. Considering the case of infinitely long straight CC, we only need to study the cross section of the CC. The 1D cross sectional diagram of the HTS thin film is shown in Figure 3.2.1, with the thickness h, and the width $2w$.

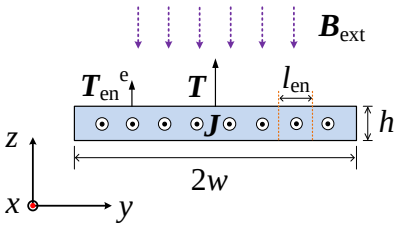

Figure 3.2.1 Cross-sectional diagram of the HTS film modelled with the *T*-formulation. *J* represents the current density, B_{ext} denotes the perpendicular external magnetic flux density.

$\boldsymbol{T}$, the current vector potential , is defined as

$$\boldsymbol{J} = \nabla \times \boldsymbol{T} \tag{3.1}$$

where $\boldsymbol{J}$ represents the current density along the CC width.

According to Faraday's law, we have

$$\nabla \times \boldsymbol{E} = -\frac{\partial \boldsymbol{B}}{\partial t} \tag{3.2}$$

with

$$\boldsymbol{B} = \boldsymbol{B}_s + \boldsymbol{B}_{ext} \tag{3.3}$$

where $\boldsymbol{E}$ denotes the electric field, $\boldsymbol{B}$ represents the magnetic flux density, $\boldsymbol{B}_s$ is the self-magnetic flux density produced by the transport current, and $\boldsymbol{B}_{ext}$ refers to the externally applied flux density perpendicular to the wide surface of the HTS CC.

As claimed by Ohm's law, it is obtained that

$$\boldsymbol{E} = \frac{1}{\sigma}\boldsymbol{J} \tag{3.4}$$

where σ is the conductivity of the studied material.

According to (3.1)-(3.4), we have

$$\frac{1}{\sigma}\nabla \times (\nabla \times \boldsymbol{T}) = -\frac{\partial (\boldsymbol{B}_s + \boldsymbol{B}_{ext})}{\partial t} \tag{3.5}$$

The self-magnetic flux density is determined by the transport current, which can be calculated by Biot-savart law, as

$$\boldsymbol{B}_s = \frac{\mu_0}{4\pi}\iiint_V \frac{(\boldsymbol{J}dV) \times \boldsymbol{r}}{r^3} \tag{3.6}$$

where μ_0 is the permeability of the free space, dV is the volume element, and $\boldsymbol{r}$ is the full displacement vector from dV to the observation point.

On the basis of (3.5) and (3.6), we obtain

$$\frac{1}{\sigma}\nabla^2 T - \frac{\partial}{\partial t}\left(\frac{\mu_0}{4\pi}\iiint_V \frac{\nabla\times\boldsymbol{T}\times\boldsymbol{r}}{r^3}dV + \boldsymbol{B}_{\text{ext}}\right) = 0 \tag{3.7}$$

In our case, for the cross section of the single HTS thin film, it is equivalized as a 1D line segment with a width of 2w, as shown in Figure 3.2.1. The line segment is discretized into a number of finite elements, and each element has a width of l_{en}. As a result, every element can be considered as an infinitely long straight wire carrying the current $\boldsymbol{J}\cdot h\cdot l_{\text{en}}$. Given that the transport current in the HTS film flows along the x-axis, $\boldsymbol{T}$ is thus perpendicular to the current flowing surface, i.e., parallel to the y-axis. In the second part of (3.7), the current vector potential belongs to each element, different from the $\boldsymbol{T}$ in the first item. Therefore, we use $T_{\text{en}}^{\text{e}}\boldsymbol{n}'$ to mark the element current vector potential (which is made of two components belonging to two nodes, respectively), in which $\boldsymbol{n}'$ is the normal vector at the current source element. Consequently, the dimensionality of (3.7) can be reduced to 1 and the governing equation can be written as

$$\frac{1}{\sigma}\nabla^2 T - \frac{\mu_0 h l_{\text{en}}}{2\pi}\cdot\frac{\partial}{\partial t}\sum_{\text{en}=1}^{\text{emax}}\frac{\nabla\times(T_{\text{en}}^{\text{e}}\boldsymbol{n}')\cdot\hat{\boldsymbol{x}}}{r_{\text{en}}} - \frac{\partial \boldsymbol{B}_{\text{ext}}}{\partial t}\cdot\boldsymbol{n} = 0 \tag{3.8}$$

where r_{en} represents the distance between the current source element and the calculation point, $\boldsymbol{n}$ is the normal vector at the calculation point, and emax refers to the total number of elements, with emax = 2w / l_{en}.

3.2.2 Discretization of the Governing Equation

To pursue the numerical analysis, the differential equation (3.8) has to be converted to a discrete form. It has been demonstrated in [309] that the Galerkin method is advantageous in terms of convergence when solving the Poisson equation. (3.8) is in essence a Poisson equation, thus the Galerkin method is adopted to discretize (3.8). The interpolation function for every element is noted as N, then we can get

$$\iiint_V N_k\left[\frac{1}{\sigma}\nabla^2 T - \frac{\mu_0 h l_{\text{en}}}{2\pi}\cdot\frac{\partial}{\partial t}\sum_{\text{en}=1}^{\text{emax}}\frac{\nabla\times(T_{\text{en}}^{\text{e}}\boldsymbol{n}')\cdot\hat{\boldsymbol{x}}}{r_{\text{en}}} - \frac{\partial \boldsymbol{B}_{\text{ext}}}{\partial t}\cdot\boldsymbol{n}\right]dV = 0 \tag{3.9}$$

where k is the node number of each element. Considering that each line segment element is composed of two nodes, k = 1, 2.

(3.9) can be further written as

$$\iiint_V N_k \cdot \frac{1}{\sigma}\nabla^2 T dV = \iiint_V N_k \cdot \frac{\mu_0 h}{2\pi}\cdot\frac{\partial}{\partial t}\sum_{en=1}^{emax}\frac{l_{en}\nabla\times(T_{en}^e \boldsymbol{n}')\cdot\hat{\boldsymbol{x}}}{r_{en}}dV + \iiint_V N_k \cdot \frac{\partial \boldsymbol{B}_{ext}}{\partial t}\cdot\boldsymbol{n}dV \quad (3.10)$$

For the left side in (3.10), we have

$$\begin{aligned}\iiint_V N_k \cdot \frac{1}{\sigma}\nabla^2 T dV &= \iiint_V N_k \cdot \frac{1}{\sigma}\cdot\left(\frac{\partial^2 T}{\partial x^2}+\frac{\partial^2 T}{\partial y^2}+\frac{\partial^2 T}{\partial z^2}\right)dV \\ &= \iiint_V \frac{1}{\sigma}\cdot\left\{\frac{\partial}{\partial x}\left(N_k\cdot\frac{\partial T}{\partial x}\right)+\frac{\partial}{\partial y}\left(N_k\cdot\frac{\partial T}{\partial y}\right)+\frac{\partial}{\partial z}\left(N_k\cdot\frac{\partial T}{\partial z}\right)\right\}dV \\ &\quad -\iiint_V \frac{1}{\sigma}\cdot\left(\frac{\partial N_k}{\partial x}\cdot\frac{\partial T}{\partial x}+\frac{\partial N_k}{\partial y}\cdot\frac{\partial T}{\partial y}+\frac{\partial N_k}{\partial z}\cdot\frac{\partial T}{\partial z}\right)dV\end{aligned} \quad (3.11)$$

With Green's function, (3.11) can be transformed into

$$\begin{aligned}\iiint_V N_k \cdot \frac{1}{\sigma}\nabla^2 T dV &= \oiint_S \frac{1}{\sigma}\cdot N_k \cdot \frac{\partial T}{\partial n}dS - \int_{width}\frac{1}{\sigma}\cdot\frac{\partial N_k}{\partial y}\cdot\frac{\partial T}{\partial y}dy \\ &= \sum_{boundary}\frac{1}{\sigma}\cdot N_k\cdot\frac{\partial T^{bnd}}{\partial n} - \int_{width}\frac{1}{\sigma}\cdot\frac{\partial N_k}{\partial y}\cdot\frac{\partial T}{\partial y}dy\end{aligned} \quad (3.12)$$

where T^{bnd} is the current vector potential on the boundary of the studied region.

In the same way, for the two terms on the right side, we have

$$\iiint_V N_k \cdot \frac{\mu_0 h}{2\pi}\cdot\frac{\partial}{\partial t}\sum_{en=1}^{emax}\frac{l_{en}\nabla\times(T_{en}^e \boldsymbol{n}')\cdot\hat{\boldsymbol{x}}}{r_{en}}dV = \int_{width} N_k \cdot \frac{\mu_0 h}{2\pi}\cdot\frac{\partial}{\partial t}\sum_{en=1}^{emax}\left(\frac{l_{en}}{r_{en}}\cdot\frac{\partial T_{en}^e}{\partial y}\right)dy \quad (3.13)$$

$$\iiint_V N_k \cdot \frac{\partial \boldsymbol{B}_{ext}}{\partial t}\cdot\boldsymbol{n}dV = \int_{width} N_k \cdot \frac{\partial B_{ext,z}}{\partial t}dy \quad (3.14)$$

According to (3.12)-(3.14), (3.10) can be transformed into

$$\begin{aligned}&\sum_{boundary}\frac{1}{\sigma}\cdot N_k\cdot\frac{\partial T^{bnd}}{\partial n} \\ &= \int_{width}\left[\frac{1}{\sigma}\cdot\frac{\partial N_k}{\partial y}\cdot\frac{\partial T}{\partial y}+N_k\cdot\frac{\mu_0 h}{2\pi}\cdot\frac{\partial}{\partial t}\sum_{en=1}^{emax}\left(\frac{l_{en}}{r_{en}}\cdot\frac{\partial T_{en}^e}{\partial y}\right)+N_k\cdot\frac{\partial B_{ext,z}}{\partial t}\right]dy\end{aligned} \quad (3.15)$$

The right term in (3.15) is the integral of three items over the width of the HTS film, which can be written as the sum of the segment integrals within each element, as

$$\sum_{\text{boundary}} \frac{1}{\sigma} \cdot N_{\text{ke}} \cdot \frac{\partial T^{\text{bnd}}}{\partial n} = \sum_{\text{emax}} \left\{ \int_{l_{\text{en}}} \left[\frac{1}{\sigma} \cdot \frac{\partial N_{\text{ke}}}{\partial y} \cdot \frac{\partial T^{\text{e}}}{\partial y} + N_{\text{ke}} \cdot \frac{\mu_0 h}{2\pi} \cdot \frac{\partial}{\partial t} \sum_{\text{en}=1}^{\text{emax}} \left(\frac{l_{\text{en}}}{r_{\text{en}}} \cdot \frac{\partial T_{\text{en}}^{\text{e}}}{\partial y} \right) + N_{\text{ke}} \cdot \frac{\partial B_{\text{ext,z}}}{\partial t} \right] dy \right\} \tag{3.16}$$

where N_{ke} is the interpolation function in each element, and T^{e} is the current vector potential for each element. Every element consists of two nodes, thus T^{e} can be expressed as

$$T^{\text{e}} = \sum_{\text{k}=1}^{2} N_{\text{ke}} \cdot T_{\text{ke}} \tag{3.17}$$

with

$$\begin{cases} N_{1\text{e}}(y) = \dfrac{y_{2\text{e}} - y}{y_{2\text{e}} - y_{1\text{e}}} \\ N_{2\text{e}}(y) = \dfrac{y - y_{1\text{e}}}{y_{2\text{e}} - y_{1\text{e}}} \end{cases} \tag{3.18}$$

where $y_{1\text{e}}$ and $y_{2\text{e}}$ represent separately the coordinates for the left and right nodes of each studied element, as shown in Figure 3.2.2.

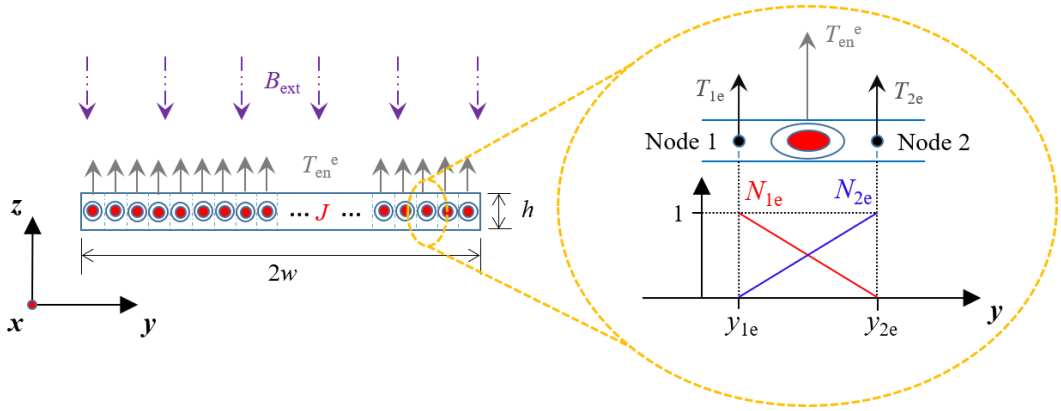

Figure 3.2.2 Discretization of the 1D HTS film. $N_{1\text{e}}$ and $N_{2\text{e}}$ represent the interpolation functions applied to both nodes of each element.

By applying the standardized local coordinate system, we obtain

$$\begin{cases} N_{1\text{e}}(\varphi) = \dfrac{1}{2}(1 - \varphi) \\ N_{2\text{e}}(\varphi) = \dfrac{1}{2}(1 + \varphi) \end{cases} \tag{3.19}$$

with

$$\varphi = \frac{2y - \left(y_{1e} + y_{2e}\right)}{y_{2e} - y_{1e}} \tag{3.20}$$

Therefore, we can get

$$\int_{l_{en}} N_{ke}(y)dy = \int_{-1}^{1} N_{ke}(\varphi) \cdot \left(\frac{dy}{d\varphi}\right) d\varphi \tag{3.21}$$

The summation of the boundary current vector potential term on the left side of (3.16) equals to zero, since the Dirichlet boundary condition is chosen here, and $\boldsymbol{T}$ does not vary along the z-axis. On the basis of (3.17)-(3.21), (3.16) can be written as

$$\sum_{emax} \left\{ \int_{-1}^{1} \left[\frac{1}{\sigma} \frac{\partial N_{ke}}{\partial y} \cdot \left(\frac{\partial}{\partial y} \sum_{k=1}^{2} N_{ke} \cdot T_{ke} \right) + N_{ke} \frac{\mu_0 h}{2\pi} \cdot \frac{\partial}{\partial t} \left(\sum_{en=1}^{emax} \frac{l_{en}}{r_{en}} \cdot \frac{\partial T_{en}^{e}}{\partial y} \right) + N_{ke} \frac{\partial B_{ext,z}}{\partial t} \right] \left(\frac{dy}{d\varphi} \right) d\varphi \right\} = 0 \tag{3.22}$$

According to (3.18), we have

$$\frac{\partial N_{ke}}{\partial y} = \mp \frac{1}{y_{2e} - y_{1e}} \tag{3.23}$$

Hence, on the basis of (3.17), we can obtain

$$\begin{aligned} \frac{\partial}{\partial y} \cdot \sum_{k=1}^{2} N_{ke} \cdot T_{ke} &= \sum_{k=1}^{2} \left(\frac{\partial N_{ke}}{\partial y} \cdot T_{ke} + \frac{\partial T_{ke}}{\partial y} \cdot N_{ke} \right) \\ &= \frac{1}{y_{2e} - y_{1e}} \left(T_{2e} - T_{1e}\right) + N_{1e} \cdot \frac{\partial T_{1e}}{\partial y} + N_{2e} \cdot \frac{\partial T_{2e}}{\partial y} \end{aligned} \tag{3.24}$$

Further, the first term in (3.22) can be transformed into

$$\begin{aligned} &\sum_{emax} \left\{ \int_{-1}^{1} \left[\frac{1}{\sigma} \frac{\partial N_{ke}}{\partial y} \cdot \left(\frac{\partial}{\partial y} \sum_{k=1}^{2} N_{ke} \cdot T_{ke} \right) \right] \left(\frac{dy}{d\varphi} \right) d\varphi \right\} \\ &= \sum_{emax} \left\{ \frac{1}{\sigma} \int_{-1}^{1} \left[\left(\mp \frac{1}{y_{2e} - y_{1e}} \right) \cdot \left(\frac{T_{2e} - T_{1e}}{y_{2e} - y_{1e}} + N_{1e} \cdot \frac{\partial T_{1e}}{\partial y} + N_{2e} \cdot \frac{\partial T_{2e}}{\partial y} \right) \right] \left(\frac{y_{2e} - y_{1e}}{2} \right) d\varphi \right\} \\ &= \sum_{emax} \left\{ \frac{1}{\sigma} \left(\mp \frac{1}{y_{2e} - y_{1e}} \right) \cdot \left(\frac{y_{2e} - y_{1e}}{2} \right) \cdot \left[\frac{2(T_{2e} - T_{1e})}{y_{2e} - y_{1e}} + \int_{-1}^{1} \left(N_{1e} \cdot \frac{\partial T_{1e}}{\partial y} + N_{2e} \cdot \frac{\partial T_{2e}}{\partial y} \right) d\varphi \right] \right\} \end{aligned} \tag{3.25}$$

From (3.19), we know that

$$\int_{-1}^{1} N_{ke}(\varphi) d\varphi = 1 \tag{3.26}$$

Then, (3.25) can be rewritten in the form of a matrix, as

$$\begin{aligned}
&\sum_{\text{emax}}\left\{\int_{-1}^{1}\left[\frac{1}{\sigma}\frac{\partial N_{\text{ke}}}{\partial y}\cdot\left(\frac{\partial}{\partial y}\sum_{\text{k=1}}^{2}N_{\text{ke}}\cdot T_{\text{ke}}\right)\right]\left(\frac{dy}{d\varphi}\right)d\varphi\right\}\\
&=\sum_{\text{emax}}\left\{\frac{2}{\sigma}\cdot\left(\frac{y_{2\text{e}}-y_{1\text{e}}}{2}\right)\cdot\left(\mp\frac{1}{y_{2\text{e}}-y_{1\text{e}}}\right)\cdot\left(\frac{1}{y_{2\text{e}}-y_{1\text{e}}}\right)\left[T_{2\text{e}}-T_{1\text{e}}\right]\right\}\\
&=\sum_{\text{emax}}\frac{2}{\sigma}\cdot\left(\frac{y_{2\text{e}}-y_{1\text{e}}}{2}\right)\cdot\begin{bmatrix}\left(-\frac{1}{y_{2\text{e}}-y_{1\text{e}}}\right)^{2} & -\left(\frac{1}{y_{2\text{e}}-y_{1\text{e}}}\right)^{2}\\ -\left(\frac{1}{y_{2\text{e}}-y_{1\text{e}}}\right)^{2} & \left(\frac{1}{y_{2\text{e}}-y_{1\text{e}}}\right)^{2}\end{bmatrix}\cdot\begin{bmatrix}T_{1\text{e}}\\ T_{2\text{e}}\end{bmatrix}
\end{aligned}\tag{3.27}$$

In the same way, for the second term in (3.22), we have

$$\begin{aligned}
&\sum_{\text{emax}}\left\{\int_{-1}^{1}N_{\text{ke}}\frac{\mu_0 h}{2\pi}\cdot\frac{\partial}{\partial t}\left(\sum_{\text{en=1}}^{\text{emax}}\frac{l_{\text{en}}}{r_{\text{en}}}\cdot\frac{\partial T_{\text{en}}^{\text{e}}}{\partial y}\right)\left(\frac{dy}{d\varphi}\right)d\varphi\right\}\\
&=\sum_{\text{emax}}\frac{\mu_0 h}{2\pi}\cdot\frac{l_{\text{en}}}{r_{\text{en}}}\cdot\left(\frac{y_{2\text{e}}-y_{1\text{e}}}{2}\right)\cdot\frac{\partial}{\partial t}\cdot\sum_{\text{en=1}}^{\text{emax}}\left\{\int_{-1}^{1}\left[N_{\text{ke}}\cdot\left(\sum_{\text{k=1}}^{2}N_{\text{ke}}\right)\cdot\left(\frac{1}{\partial y}\sum_{\text{k=1}}^{2}N_{\text{ke}}\cdot T_{\text{ke}}\right)\right]d\varphi\right\}
\end{aligned}\tag{3.28}$$

Given that

$$\begin{cases}\int_{-1}^{1}N_{1\text{e}}(\varphi)\cdot N_{1\text{e}}(\varphi)d\varphi=\int_{-1}^{1}N_{2\text{e}}(\varphi)\cdot N_{2\text{e}}(\varphi)d\varphi=\frac{2}{3}\\ \int_{-1}^{1}N_{1\text{e}}(\varphi)\cdot N_{2\text{e}}(\varphi)d\varphi=\frac{1}{3}\end{cases}\tag{3.29}$$

(3.28) can be rewritten as

$$\begin{aligned}
&\sum_{\text{emax}}\left\{\int_{-1}^{1}N_{\text{ke}}\frac{\mu_0 h}{2\pi}\cdot\frac{\partial}{\partial t}\left(\sum_{\text{en=1}}^{\text{emax}}\frac{l_{\text{en}}}{r_{\text{en}}}\cdot\frac{\partial T_{\text{en}}^{\text{e}}}{\partial y}\right)\left(\frac{dy}{d\varphi}\right)d\varphi\right\}\\
&=\sum_{\text{emax}}\frac{\mu_0 h}{2\pi}\cdot\frac{l_{\text{en}}}{r_{\text{en}}}\cdot\left(\frac{y_{2\text{e}}-y_{1\text{e}}}{2}\right)\cdot\begin{bmatrix}\frac{2}{3} & \frac{1}{3}\\ \frac{1}{3} & \frac{2}{3}\end{bmatrix}\cdot\begin{bmatrix}-\frac{1}{y_{2\text{e}}-y_{1\text{e}}} & \frac{1}{y_{2\text{e}}-y_{1\text{e}}}\\ -\frac{1}{y_{2\text{e}}-y_{1\text{e}}} & \frac{1}{y_{2\text{e}}-y_{1\text{e}}}\end{bmatrix}\cdot\begin{bmatrix}\frac{\partial T_{1\text{e}}}{\partial t}\\ \frac{\partial T_{2\text{e}}}{\partial t}\end{bmatrix}
\end{aligned}\tag{3.30}$$

Then, for the third term in (3.22), we have

$$\begin{aligned}
&\sum_{\text{emax}}\left\{\int_{-1}^{1}\left(N_{\text{ke}}\frac{\partial B_{\text{ext,z}}}{\partial t}\right)\left(\frac{dy}{d\varphi}\right)d\varphi\right\}\\
&=\sum_{\text{emax}}\int_{-1}^{1}\begin{bmatrix}N_{1\text{e}}\\ N_{2\text{e}}\end{bmatrix}\cdot\frac{\partial B_{\text{ext,z}}}{\partial t}\cdot\left(\frac{dy}{d\varphi}\right)d\varphi=\sum_{\text{emax}}\frac{y_{2\text{e}}-y_{1\text{e}}}{2}\cdot\begin{bmatrix}\frac{\partial B_{\text{ext,z}}}{\partial t}\\ \frac{\partial B_{\text{ext,z}}}{\partial t}\end{bmatrix}
\end{aligned}\tag{3.31}$$

To sum, based on (3.27), (3.30) and (3.31), the discretized governing equation for the 1D HTS thin film with the Galerkin method can be written as

$$\sum_{\text{emax}}\left\{\begin{array}{l}[\boldsymbol{A}]\\ \dfrac{2}{\sigma}\cdot\left(\dfrac{y_{2e}-y_{1e}}{2}\right)\cdot\begin{bmatrix}\left(-\dfrac{1}{y_{2e}-y_{1e}}\right)^2 & -\left(\dfrac{1}{y_{2e}-y_{1e}}\right)^2\\ -\left(\dfrac{1}{y_{2e}-y_{1e}}\right)^2 & \left(\dfrac{1}{y_{2e}-y_{1e}}\right)^2\end{bmatrix}\cdot\begin{bmatrix}T_{1e}\\ T_{2e}\end{bmatrix}\\ +\dfrac{\mu_0 h}{2\pi}\cdot\dfrac{l_{en}}{r_{en}}\cdot\left(\dfrac{y_{2e}-y_{1e}}{2}\right)\cdot\begin{bmatrix}\frac{2}{3} & \frac{1}{3}\\ \frac{1}{3} & \frac{2}{3}\end{bmatrix}\cdot\begin{bmatrix}-\dfrac{1}{y_{2e}-y_{1e}} & \dfrac{1}{y_{2e}-y_{1e}}\\ -\dfrac{1}{y_{2e}-y_{1e}} & \dfrac{1}{y_{2e}-y_{1e}}\end{bmatrix}\cdot\begin{bmatrix}\dfrac{\partial T_{1e}}{\partial t}\\ \dfrac{\partial T_{2e}}{\partial t}\end{bmatrix}\\ [\boldsymbol{B}]\\ +\dfrac{y_{2e}-y_{1e}}{2}\cdot\begin{bmatrix}\dfrac{\partial B_{\text{ext,z}}}{\partial t}\\ \dfrac{\partial B_{\text{ext,z}}}{\partial t}\end{bmatrix}\\ [\boldsymbol{C}]\end{array}\right\}=0 \tag{3.32}$$

In fact, (3.32) can be further expressed as

$$[\boldsymbol{A}]\{\boldsymbol{T}\}+[\boldsymbol{B}]\left\{\frac{\partial \boldsymbol{T}}{\partial t}\right\}+[\boldsymbol{C}]=\boldsymbol{0} \tag{3.33}$$

where [***A***], [***B***] and [***C***] are separately the calculation results of the first, second and third terms of the discretized governing equation, and {***T***} is the column vector consisting of the scalar variable at all nodes of the elements.

The backward difference method is used for solving (3.33), then we get

$$[\boldsymbol{A}]\{\boldsymbol{T}_{[n]}\}+[\boldsymbol{B}]\left\{\frac{\boldsymbol{T}_{[n]}-\boldsymbol{T}_{[n-1]}}{\Delta t}\right\}+[\boldsymbol{C}]=\boldsymbol{0} \tag{3.34}$$

where $\boldsymbol{T}_{[n]}$ and $\boldsymbol{T}_{[n-1]}$ are separately the column vector of the current vector potential for the time step n and n-1, and Δt is the time interval between two time steps.

On the basis of (3.34), we get

$$\{\boldsymbol{T}_{[n]}\}=\left([\boldsymbol{A}]+\frac{[\boldsymbol{B}]}{\Delta t}\right)^{-1}\left([\boldsymbol{B}]\frac{\{\boldsymbol{T}_{[n-1]}\}}{\Delta t}-[\boldsymbol{C}]\right) \tag{3.35}$$

It needs to be pointed out that, the ***E-J*** power law of the HTS film is reflected by σ in [***A***], with

$$\sigma_{\mathrm{HTS}} = \frac{J_{\mathrm{c}}}{E_0}\left(\frac{J_{\mathrm{c}}}{\|\nabla \times \boldsymbol{T}\|}\right)^{n-1} \tag{3.36}$$

In the 1D ***T***-formulation based numerical model, since the HTS CC has been approximated as an infinitely thin film, we adopt here the $J_{\mathrm{c}}(\boldsymbol{B})$ dependence as shown in (2.3). Then, (3.36) can be transofrmed into

$$\sigma_{\mathrm{HTS}} = \frac{J_{\mathrm{c0}}}{E_0}\left(\frac{J_{\mathrm{c0}}}{\|\nabla \times \boldsymbol{T}\|}\right)^{n-1} \frac{1}{\left(1+\|\boldsymbol{B}_{\perp}\|/B_0\right)^{n}} \tag{3.37}$$

3.2.3 Solving the Interpolated Governing Equation

According to Figure 3.2.2, we know that the boundaries of the HTS thin film can be directly described by the ***T*** values on both ends, thus the Dirichlet boundary condition is chosen here. In order to impose the transport current and magnetic field into the HTS film at the beginning, we assume that: 1) the transport current (per unit thickness) is concentrated on the two ends of the thin film; 2) the external magnetic field can fully penetrate the HTS thin film, thus the externally applied flux density can be implemented to each element. Then, the general current density and magnetic flux density distributions along the width of the HTS film are calculated from the boundaries to the central regions.

The imposed approximations can lead to errors thus we need to take the iterative method to get steady and reproducible simulation results with acceptable deviation. Two different iterative approaches, namely the Gauss-Seidel method and the Newton Raphson method, have been discussed and compared in [310]. The Gauss-Seidel method is relatively easier to be complied with the open source code and costs relatively less computation time during per iteration on account of its relatively simpler iteration structure. As a comparison, though the Newton Raphson method possesses faster convergence speed, it costs more time in calculating the derivative of the equation and Jacobian matrix. As demonstrated, in the ***T***-formulation based numerical model, most of the computational time is spent on solving the interpolated governing equations. Therefore, it is of great importance to save the computational time in each iteration, thus the Gauss-Seidel method is adopted. To further improve the computational efficiency, the Successive Under Relaxation (SUR) method is exploited so that the iteration numbers become adjustable, and a minimum iteration number needed for convergence can be decided. More introduction on the SUR method can be found in [310].

Based on the above-mentioned analysis, the flow chart for modelling the electromagnetic characteristics of HTS CCs is presented in Figure 3.2.3. The whole computation procedure is

achieved with open source code in FORTRAN 90. The ***T***-formulation based numerical model can also be built in COMSOL Multiphysics, with which a case study for modelling the circular coils used in the HTS Halbach array magnets of electromagnetic wheels will be presented in Chapter 6. Given that the realization of the ***T***-formulation in COMSOL Multiphysics is similar to that of the ***H***-formulation, the ***H***-formulation based numerical model is mainly presented hereinafter.

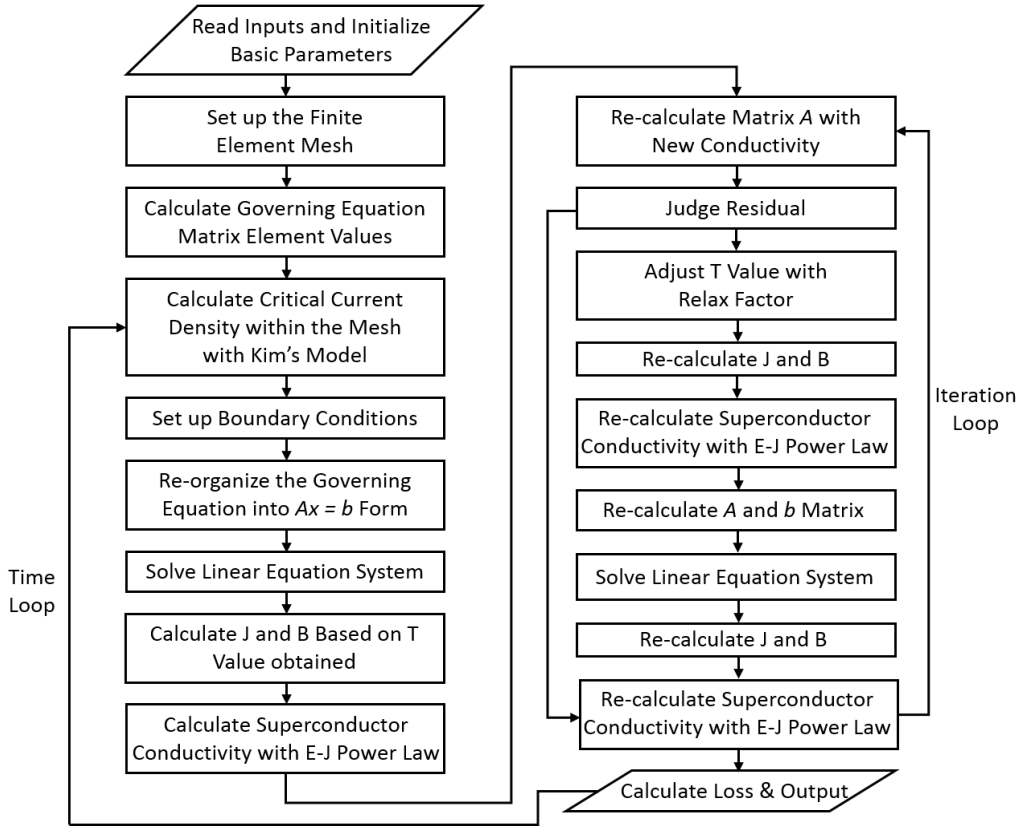

Figure 3.2.3 Flow chart for modelling the electromagnetic characteristics of HTS CCs [310].

3.2.4 Multilayer Numerical Model for HTS CCs

It is reasonable to only consider the HTS layer for modelling the current and magnetic field distributions of HTS CCs at low frequencies because the conductivity of the HTS layer is much greater than that of the non-superconducting parts and almost all the current just flows in the HTS layer. However, when HTS CCs are employer in electrical machines, they will have to experience high-frequency magnetic fields, e.g., harmonics. Under such circumstances, the electromagnetic interactions between the HTS and non-superconducting parts have to be considered, in that the current can flow into non-superconducting layers due to the skin effect. Therefore, we need to build the multilayer numerical model for HTS CCs, takin into account the copper stabilizers, silver overlayer, and substrate.

The typical commercial HTS CC is composed of two copper stabilizers, one silver overlayer and one substrate besides the thin HTS layer, as shown in Figure 3.2.4. We apply the same modelling technique to the non-superconducting layers thus the original 1D thin film model is expanded into a 2D multilayer model. In this way, the governing equation for each layer can be written as

$$\frac{1}{\sigma_{\mathrm{i}}}\nabla^2 T_{\mathrm{i}} - \frac{\mu_0 h_{\mathrm{i}}}{2\pi}\cdot\frac{\partial}{\partial t}\sum_{\mathrm{j}=1}^{5}\sum_{\mathrm{en}=1}^{\mathrm{emax}}\frac{l_{\mathrm{en}}\nabla\times(T_{\mathrm{en,j}}^{\mathrm{e}}\boldsymbol{n}')\cdot\hat{\boldsymbol{x}}}{r_{\mathrm{en,j}}} - \frac{\partial \boldsymbol{B}_{\mathrm{ext}}}{\partial t}\cdot\boldsymbol{n} = 0 \tag{3.38}$$

where σ_{i} and h_{i} are separately the conductivity and thickness of the i-th layer (i = 1, 2, 3, 4, 5), and T_{i} signifies the current vertor potential for the i-th layer. $r_{\mathrm{en,j}}$ represents the distance between the current source element and the calculation point; however, $r_{\mathrm{en,j}}$ is decided by not only the the distance between different elements along the y-axis in the same layer, but also the distance between various layers along the z-axis. Therefore, the real thicknesses of distinct layers have to be considered. In (3.38) we use i to mark the calculated layer, and j to label the currenr source layer.

Similarly, the Galerkin method is adopted to discretize each layer into emax elements, each of which is composed of two nodes. Then, we obtain the interpolated governing equation, as

$$\iiint_V N_{\mathrm{i,k}}\cdot\frac{1}{\sigma_{\mathrm{i}}}\nabla^2 T_{\mathrm{i}}dV - \iiint_V N_{\mathrm{i,k}}\cdot\frac{\mu_0 h_{\mathrm{i}}}{2\pi}\cdot\frac{\partial}{\partial t}\sum_{j=1}^{5}\sum_{\mathrm{en}=1}^{\mathrm{emax}}\frac{l_{\mathrm{en}}\nabla\times(T_{\mathrm{en,j}}^{\mathrm{e}}\boldsymbol{n}')\cdot\hat{\boldsymbol{x}}}{r_{\mathrm{en,j}}}dV - \iiint_V N_{\mathrm{i,k}}\cdot\frac{\partial \boldsymbol{B}_{\mathrm{ext}}}{\partial t}\cdot\boldsymbol{n}dV = 0 \tag{3.39}$$

where $N_{\mathrm{i,k}}$ (k = 1, 2) is the interpolation function for the i-th layer, and k denotes the node number of each element. With Green's function, (3.39) can be transformed into

$$\begin{aligned}&\sum_{\mathrm{boundary}}\left(\frac{1}{\sigma_{\mathrm{i}}}\cdot N_{\mathrm{i,k}}\cdot\frac{\partial T_{\mathrm{i}}^{\mathrm{bnd}}}{\partial n}\right)\\ &=\int_{\mathrm{width}}\left[\frac{1}{\sigma_{\mathrm{i}}}\cdot\frac{\partial N_{\mathrm{i,k}}}{\partial y}\cdot\frac{\partial T_{\mathrm{i}}}{\partial y} + N_{\mathrm{i,k}}\cdot\frac{\mu_0 h_{\mathrm{i}}}{2\pi}\cdot\frac{\partial}{\partial t}\sum_{\mathrm{j}=1}^{5}\sum_{\mathrm{en}=1}^{\mathrm{emax}}\left(\frac{l_{\mathrm{en}}}{r_{\mathrm{en,j}}}\cdot\frac{\partial T_{\mathrm{en,j}}^{\mathrm{e}}}{\partial y}\right) + N_{\mathrm{i,k}}\cdot\frac{\partial B_{\mathrm{ext}}}{\partial t}\right]dy\end{aligned} \tag{3.40}$$

where $T_{\mathrm{i}}^{\mathrm{bnd}}$ is the current vector potential on the boundary of the claculated layer. (3.40) is then solved following the same procedure elaborated in Section 3.2.2 and 3.2.3. However, one more loop needs to be added to the FORTRAN program, because for calculating the current density or magnetic flux density of one fixed element in a specific layer, all the other elements of the 5 layers have to be considered as the current sources.

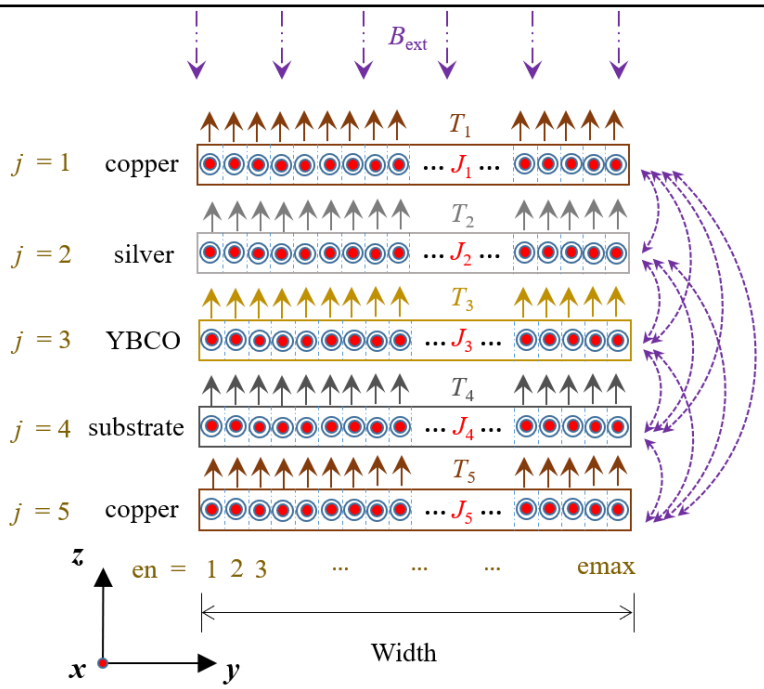

Figure 3.2.4 2D modelling diagram of 5-layer HTS CC based on the *T*-formulation. B_{ext} signifies the external magnetic field perpendicular to the CC surface.

At high frequencies, the transport current or induced current tends to redistribute among different layers due to the skin effect. On this occasion, we need to consider the conductivity of various layers, considering that the five layers in Figure 3.2.4 are in parallel and the equivalent circuit is shown in Figure 3.2.5.

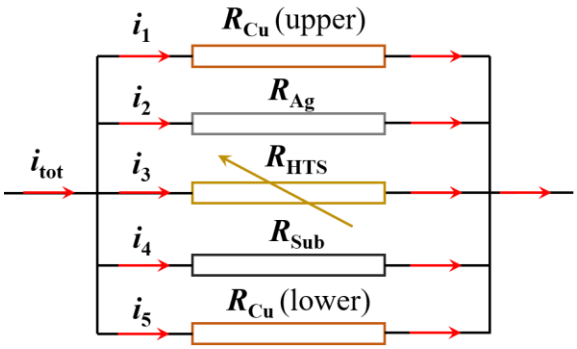

Figure 3.2.5 Equivalent circuit model of the 5-layer HTS CC. *R* denotes the equivalent resistance for each layer.

The total current is the sum of branch currents which flow through all the 5 layers, which is written as

$$i_{tot} = \sum_{j=1}^{5} i_j = \sum_{j=1}^{5} \iint_{S_j} J dS_j \tag{3.41}$$

where i_j and S_j represent the transport current and cross-sectional area of the j-th layer.

According to the ***E*-*J*** pow law, as shown in Equation (2.8), the resistivity of the HTS layer has a non-linear correlation with the current density thus in Figure 3.2.5 the equivalent resistance of the HTS layer is variable. The redistribution of current in the 5 layers is determined by their equivalent resistance per unit length (R_j, Ω/m). Based on Ohm's law, we can obtain

$$R_j = \frac{E}{i_j} = \frac{E_0 \left(J/J_c \right)^n \big|_{(y_0, z_0)}}{\iint_{S_j} J dS_j} \tag{3.42}$$

where E is the electric field (electric potential per unit length) of the HTS CC, which is identical for all the parallel layers and can be calculated based on the ***E*-*J*** power law at any point (y_0, z_0) on the cross section of the HTS layer. By use of the ***T***-formulation based multilayer numerical modelling method, a case study to analyse the loss redistribution in different layers of an HTS CC will be presented in detail in Chapter 5.

3.3 H-formulation Based Numerical Models

3.3.1 2D multilayer model

According to Faraday's law and Constitutive law, we have

$$\nabla \times \boldsymbol{E} = -\mu_0 \mu_r \frac{\partial \boldsymbol{H}}{\partial t} \tag{3.43}$$

where μ_0 and μ_r represent the free space permeability and the relative permeability of the studied material, respectively.

According to Ampere's law

$$\boldsymbol{J} = \nabla \times \boldsymbol{H} \tag{3.44}$$

and Ohm's law, (3.43) can be written as

$$\nabla \times \left(\frac{1}{\sigma} \nabla \times \boldsymbol{H} \right) = -\mu_0 \mu_r \frac{\partial \boldsymbol{H}}{\partial t} \tag{3.45}$$

In the ***H***-formulation based numerical model, both the magnetic fields perpendicular and parallel to the wide surface of the CC can be considered, thus we adopt here the the semi-empirical $J_c(\boldsymbol{B})$ dependence as shown in Equation (2.4). Therefore, on the basis of Equation (3.45), (2.4) and and the ***E*-*J*** power law, we can obtain the ***H***-formulation based governing equation for the HTS layer of the CC, as

$$\frac{E_0}{{J_{c0}}^n}\left(1+\mu_0\mu_r\sqrt{\frac{k^2\left\|\boldsymbol{H}_{\parallel}\right\|^2+\left\|\boldsymbol{H}_{\perp}\right\|^2}{B_0}}\right)^{\alpha n}\cdot\left\|\nabla\times\boldsymbol{H}\right\|^{n-1}\cdot\nabla\times\left(\nabla\times\boldsymbol{H}\right)+\mu_0\mu_r\frac{\partial\boldsymbol{H}}{\partial t}=0 \quad (3.46)$$

where $\boldsymbol{H}_{\parallel}$ and $\boldsymbol{H}_{\perp}$ are the parallel and perpendicular components of the local magnetic field with respect to the wide surface of the CC, respectively.

In order to implement the ***H***-formulation in COMSOL Multiphysics, in a 2D geometry, we assume that the transport current (or induced current) is perpendicular to the cross section of the CC, i.e., the current is along the *z*-axis. According to (3.43)-(3.44), thus we have

$$\begin{bmatrix}\frac{\partial E_z}{\partial y}\\ -\frac{\partial E_z}{\partial x}\end{bmatrix}=-\mu_0\mu_r\begin{bmatrix}\frac{\partial H_x}{\partial t}\\ \frac{\partial H_y}{\partial t}\end{bmatrix} \quad (3.47)$$

$$J_z=\frac{\partial H_y}{\partial x}-\frac{\partial H_x}{\partial y} \quad (3.48)$$

Then, based on the ***E***-***J*** power law, we obtain

$$E_z=E_0\left(\frac{J_z}{J_c(\boldsymbol{B})}\right)^n=E_0\left[\frac{1}{J_c(\boldsymbol{B})}\left(\frac{\partial H_y}{\partial x}-\frac{\partial H_x}{\partial y}\right)\right]^n \quad (3.49)$$

Substituting (3.49) into (3.47), we can obtain the 2D partial differential equations to be solved in COMSOL Multiphysics.

The HTS CC sample is composed of 5 parallel layers, each of which carries a prescribed current $i_n(t)$, with n = 1, 2, 3, 4, 5. For the transport current $i_n(t)$, we have

$$i_n(t)=\iint_{S_n}J dA \quad (3.50)$$

where S_n is the cross-sectional area of the nth layer.

To calculate the instantaneous loss for each layer, we have

$$P_n(t)=\iint_{S_n}\boldsymbol{E}\cdot\boldsymbol{J}\mathrm{d}S_n \quad (3.51)$$

For periodic input signals, e.g., AC transport current or AC magnetic field, the average power dissipation can be expressed as

$$P_n=\frac{2}{T}\int_{T/2}^{T}\int_{S_n}\boldsymbol{E}\cdot\boldsymbol{J}dS_n dt \quad (3.52)$$

Therefore, the total loss of the CC can be written as

$$P_{\text{tot}} = \sum_{n=1}^{5} P_n \tag{3.53}$$

The ***H***-formulation based multilayer models are built and solved in the time domain of COMSOL Multiphysics, as shown in Figure 3.3.1. The HTS CC is surrounded by air and a Dirichlet boundary condition is used. For the air region, free triangular mesh with normal size has been chosen. For the HTS CC, both the width and the thickness of each layer have been discretized into a fixed number of segments and thus each element in the CC region is in a rectangular shape. In order to well reflect the skin effect at high frequencies, we need to ensure that the meshing of the CC is sufficiently fine, especially in the two outer copper layers. Therefore, the number of segments along the thickness of layer has been decided proportionally, e.g., in Figure 3.3.1, one segment has been chosen for the HTS layer (typically with a thickness of 1 μm) and 20 segments have been set for both the upper and lower copper stabilizers, respectively (the thickness of each copper stabilizer is typically 20 μm).

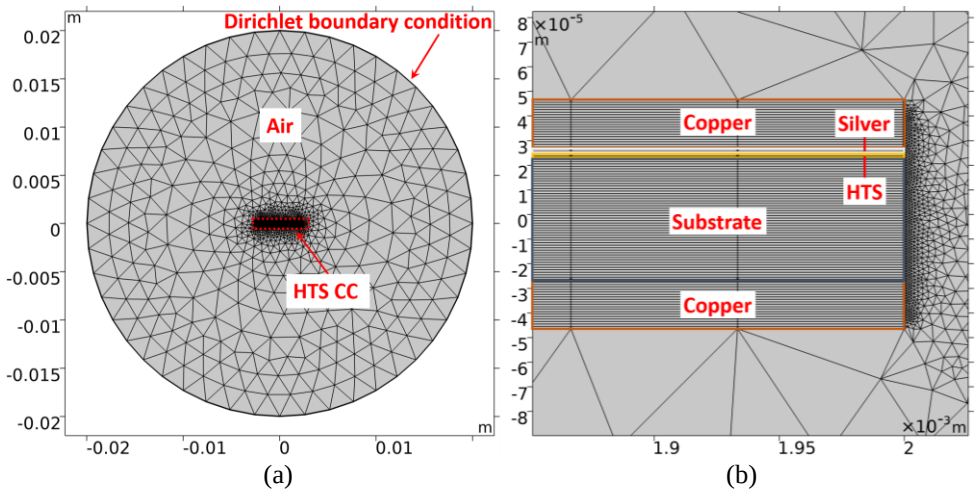

Figure 3.3.1 2D modelling diagram of the 5-layer HTS CC based on the *H*-formulation in COMSOL Multiphysics. (a) Mesh of the whole calculation domain, including the HTS CC and the air region. (b) Mesh details of the rightmost part of the HTS CC.

3.3.2 Homogenization method

As mentioned in Section 2.4, to simplify the multilayer model and save computational time, a homogenization model has been proposed in [163-164]. In this model, a single HTS CC has been presented as a unit cell composed of all 5 layers, and only the superconducting material's volume fraction has been considered, as shown in Figure 3.3.2. Thus, for the homogeneous CC, the equivalent critical current density $J_{c,eq}$ can be expressed as Equation (2.25). In this way, the total power loss per unit length of the HTS CC will be written as

$$P_{\text{tot}} = \frac{2}{T}\int_{T/2}^{T}\int_{\sum_{n=1}^{5} S_n} \boldsymbol{E}_{\text{homo}} \cdot \boldsymbol{J}_{\text{homo}} dSdt \tag{3.54}$$

The ***H***-formulation based homogenization model has been established in COMSOL Multiphysics in the same way as the multilayer model. The difference is that the HTS CC part has been characterized by a homogeneous electrical conductivity determined by (2.25).

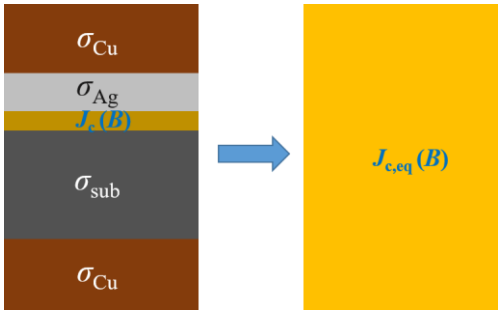

Figure 3.3.2 Diagram of the homogenization process.

3.2.3 3D FEM modelling

The basic governing equation for 3D models is the same as Equation (3.45). Here we will focus on the implementation of the ***H***-formulation into COMSOL Multiphysics. In a 3D orthogonal coordinate system, Faraday's law gives

$$\begin{bmatrix} \frac{\partial E_z}{\partial y} - \frac{\partial E_y}{\partial z} \\ \frac{\partial E_x}{\partial z} - \frac{\partial E_z}{\partial x} \\ \frac{\partial E_y}{\partial x} - \frac{\partial E_x}{\partial y} \end{bmatrix} = -\mu_0\mu_r \begin{bmatrix} \frac{\partial H_x}{\partial t} \\ \frac{\partial H_y}{\partial t} \\ \frac{\partial H_z}{\partial t} \end{bmatrix} \tag{3.55}$$

According to Ampere's law, we have

$$\begin{bmatrix} J_x \\ J_y \\ J_z \end{bmatrix} = \begin{bmatrix} \frac{\partial H_z}{\partial y} - \frac{\partial H_y}{\partial z} \\ \frac{\partial H_x}{\partial z} - \frac{\partial H_z}{\partial x} \\ \frac{\partial H_y}{\partial x} - \frac{\partial H_x}{\partial y} \end{bmatrix} \tag{3.56}$$

Based on the ***E-J*** power law of HTSCs, we obtain

$$\begin{bmatrix} E_x \\ E_y \\ E_z \end{bmatrix} = E_0 \begin{bmatrix} \dfrac{J_x}{J_c(\boldsymbol{B})} \left(\dfrac{\|\boldsymbol{J}\|}{J_c(\boldsymbol{B})} \right)^{n-1} \\ \dfrac{J_y}{J_c(\boldsymbol{B})} \left(\dfrac{\|\boldsymbol{J}\|}{J_c(\boldsymbol{B})} \right)^{n-1} \\ \dfrac{J_z}{J_c(\boldsymbol{B})} \left(\dfrac{\|\boldsymbol{J}\|}{J_c(\boldsymbol{B})} \right)^{n-1} \end{bmatrix} \tag{3.57}$$

where $\|\boldsymbol{J}\| = \sqrt{J_x^2 + J_y^2 + J_z^2}$. Substituting (3.56) and (3.57) into (3.55), we can obtain the 3D partial differential equations to be solved in COMSOL Multiphysics. Here, it needs to be noted that, in a 3D space, the $J_c(\boldsymbol{B})$ dependence is related to the relative vector relationship between the studied HTS geometry and the local magnetic field. For example, for the modelling of an HTS racetrack coil, the $J_c(\boldsymbol{B})$ dependence is position dependent because the field components perpendicular and parallel to the wide surface of the CCs are not simply along the coordinate axes at the circular parts. The 3D modelling of HTS racetrack coils and TFSs will be presented in detail in Chapter 5.

3.4 Validation of the T-formulation Based Modelling Method

In this thesis, the ***H***-formulation based modelling method will be mainly utilized in Chapter 5, where the experimental validation of the ***H***-formulation based numerical models for different HTS topologies will be presented. In this section, we will focus on the validation of the proposed ***T***-formulation based multilayer numerical model built with the open source code under FORTRAN environment.

Two case studies for different types of HTS CCs have been presented in this section. The AC transport current losses of a 12-mm-wide SCS 12050 CC with a non-magnetic substrate and a 4-mm-wide RABiTS CC with a magnetic substrate were measured in [311] and [202], respectively. The corresponding experimental data have been referenced here. The specifications of the two CCs for simulation are shown in Table 6.

Based on the proposed ***T***-formulation based multilayer numerical method, the transport current power losses per unit length (W/m) for the two CC samples have been simulated and compared with the experimental data. The simulated transport current loss for each layer of the CC, the simulated total loss, the analytical results and the measured data are depicted together in Figure 3.4.1. The amplitude of the applied current varies from 20 A to 150 A, and its AC frequency is chosen as 1 kHz. It can be seen that the simulated, experimental and

analytical results agree well with each other. The total loss increases rapidly with transport current, which confirms the effectiveness of the Norris equation described by (2.10). In this case, the frequency of the applied current is only 1 kHz, thus the vast majority of losses have been concentrated in the HTS layer. It should be noted that the least loss is generated in the substrate layer because it is non-magnetic with a high resistivity.

Table 6. Specifications for the simulation of the referenced two HTS CCs

Symbol	Parameter	Value	
		SCS 12050 [311]	RABiTS [202]
w	half width of the CC	12 mm	4 mm
h_{HTS}	YBCO film thickness	1 μm	1 μm
h_{Cu}	Copper stabilizer thickness	20 μm (upper and lower)	50 μm (upper and lower)
h_{Ag}	Silver overlayer thickness	2 μm (upper) 1.8 μm(lower)	3 μm
h_{Sub}	Substrate thickness	50 μm	75 μm
ρ_{Cu}	Copper resistivity	3.0×10^{-9} Ω·m	3.0×10^{-9} Ω·m
ρ_{Ag}	Silver resistivity	2.7×10^{-9} Ω·m	2.7×10^{-9} Ω·m
ρ_{Sub}	Substrate resistivity	1.25×10^{-6} Ω·m	6.3×10^{-8} Ω·m
I_{c0}	critical current in self-field	300 A	108 A
n	n-value	30	30
T_o	operating temperature	77 K	
E_0	characteristic E-field	10^{-4} V/m	
μ_0	free space permeability	$4\pi \times 10^{-7}$ H/m	

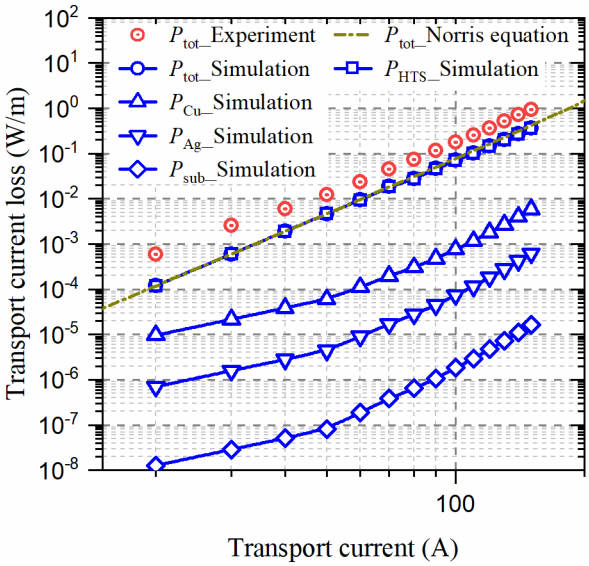

Figure 3.4.1 The variation of transport current loss with transport current for the HTS CC SCS 12050 sample. The frequency of the applied current f = 1 kHz.

The simulated, experimental and analytical results for the RABiTS HTS CC with a magnetic substrate are presented in Figure 3.4.2. The amplitude of the applied current has been chosen as 45 A, and its AC frequency varies from 210 Hz to 15 kHz. With regard to total loss, it can

be found that the simulation results are in good accordance with the experimental data, which verifies the effectiveness of the proposed multilayer modelling method. However, the calculated AC loss by the Norris equation shows an evident bias. In fact, according to the loss distribution in different layers, we can find that most losses are generated in the copper stabilizers rather than the HTS layer especially for f > 300 Hz, thus (2.10) cannot predict the loss variation correctly.

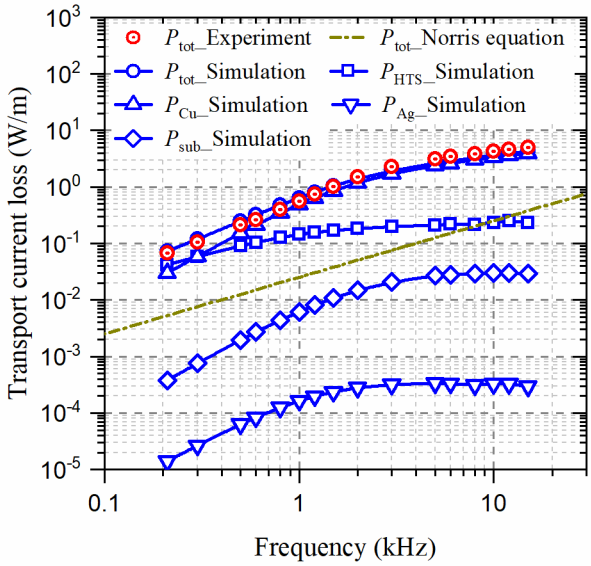

Figure 3.4.2 The variation of transport current loss with frequency for the RABiTS HTS CC sample. The amplitude of the applied current is 45 A.

It should be pointed out that the loss in the copper layers of the tested tape becomes dominant at a much lower frequency compared with the CC analysed before with a non-substrate layer. In addition, distinguished from CCs with a non-magnetic substrate, for this tested tape the loss in the substrate layer is much higher than that in the silver layer. In fact, as mentioned in [202], the presence of a magnetic substrate strongly increases the hysteresis loss of the CC, and the critical current of the HTS layer increases with frequency, thus the loss in the HTS layer exhibits a marginally declining trend. With the increase of frequency, due to the skin effect and the superimposed effect of all the layers, the majority of losses are generated in the copper stabilizers (especially the lower one) [202].

In addition, it can be concluded that the HTS CCs with magnetic substrates are more vulnerable to frequency, and their transport current loss in the copper stabilizers can turn dominant at a rather lower frequency of several hundred Hz. The results show that the CCs with copper stabilizers and magnetic substrates cannot work efficiently at high-frequency bands over 1 kHz, thus the no-insulation technique using CCs without copper stabilizers could

be more appropriate for high-frequency applications.

3.5 Conclusion

In this chapter, the numerical modelling methods utilized in this thesis for HTS CCs have been introduced, which are achieved based on the ***T***-formulation and ***H***-formulation, respectively. As a result, four different models have been presented, namely the ***T***-formulation based thin film model, the ***T***-formulation based multilayer model, the ***H***-formulation based multilayer model, as well as the ***H***-formulation based homogenization model. Different from the widely adopted numerical models which approximate the CC as an infinitely thin HTS film, the proposed multilayer models take into account both the superconducting and non-superconducting layers, including the copper stabilizers, silver overlayer, and substrate in addition to the HTS layer. The ***T***-formulation based numerical models have been built with the open source code under FORTRAN environment. The governing equation has been derived in detail from Maxwell's equations, then the Galerkin method has been adopted to discretize this equation with FEM. The Gauss-Seidel method has been used as the iterative approach to obtain the stable results. To further improve the computational efficiency, the Successive Under Relaxation method has been exploited to achieve a minimum iteration number needed for convergence. The proposed ***T***-formulation based multilayer numerical model has been validated through experimental measurements at frequencies up to kHz level. The ***H***-formulation based numerical modelling methods are nowadays the most widely used simulation approaches for HTS CCs, thus the implementation of the ***H***-formulation into COMSOL Multiphysics (from 2D to 3D) has also been introduced. In the following chapters, the presented modelling methods will be employed to analyze the AC loss characteristics of HTS CCs.

Chapter 4. Dynamic loss and dynamic resistance of HTS CCs

4.1 Introduction

Dynamic resistance and dynamic loss are generated when the HTS CC carrying a DC is exposed to an AC magnetic field. Dynamic loss can dominate the total loss in the field coils of synchronous superconducting machines, and a non-linearly fast rise of the dynamic loss can lead to the quench of HTS CCs. Therefore, it is of significant importance to figure out the characteristics of dynamic loss and dynamic resistance as well as their influencing factors. Although the changing pattern of the dynamic loss/resistance in respect of some external electromagnetic excitation factors has been studied a lot, their variation properties for different types of HTS CCs with distinct critical current and *n*-value are still not clear. In addition, the non-linear variation of dynamic loss and dynamic resistance at both high external fields and high load ratios cannot be explained or predicted by the previously existing analytical equations. In this chapter, the dependence of dynamic loss on the critical current and *n*-value of HTSCs will be explored. Then, a novel formulation will be proposed to describe the non-linearity of dynamic loss. At last, three new parameters will be defined to quantify the linear and non-linear regions of dynamic loss and dynamic resistance.

4.2 Origin of Dynamic Loss and Dynamic Resistance

Dynamic resistance and dynamic loss are important parameters to evaluate the performance of HTS CCs in power equipment, which can bring about a quench. They are generated when the HTS CC carrying a DC is exposed to an AC magnetic field. Let us consider an HTS layer with the width of 2w, the thickness of h, and the self-field critical current of I_{c0}, as shown in Figure 4.2.1. The critical current density of the HTS layer is thus $J_{c0} = I_{c0} / (2wh)$. The HTS layer experiences simultaneously a DC, I_t, and an applied AC field $\boldsymbol{B}_{app}$ perpendicular to the wide surface of the HTS layer with the amplitude of B_{ext}. According to Faraday's law, the voltage along the HTS layer can be calculated by

$$\oint_{abcd} \boldsymbol{E}d\boldsymbol{l} = -\iint_S \frac{d\boldsymbol{B}_{app}}{dt} d\boldsymbol{A} \tag{4.1}$$

where S is the rectangular surface enclosed by the four studied lines, a, b, c, and d.

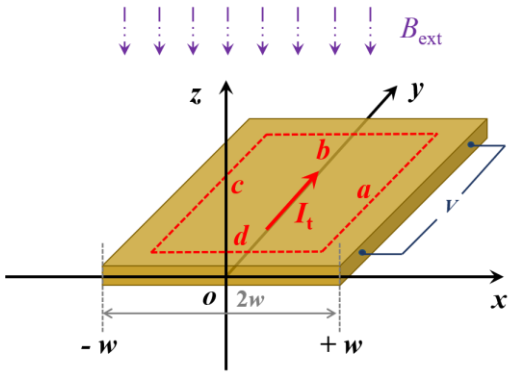

Figure 4.2.1 Schematic of the studied HTS layer experiencing both a DC and an AC external field.

In practical applications, the typical width of an HTS CC is of several mm, which is far less than its length. Therefore, b and d are much shorter than a and c, i.e., the contribution of b and d can be neglected in (4.1). The voltage along the line a can thus be written as

$$V = \int_a Edl = -\iint_S \frac{d\boldsymbol{B}_{app}}{dt} d\boldsymbol{A} - \int_c Edl \tag{4.2}$$

To simplify the calculation, the line c is chosen to be located in the region across which no flux moves [312], thus the second term on the right of (4.2) is zero and we can obatin

$$V = -\int_S \frac{d\boldsymbol{B}_{app}}{dt} d\boldsymbol{A} \tag{4.3}$$

It can be seen from (4.3) that the voltage along the length of the HTS layer is dependent on the time variation of the external field in the area determined by a and c. It is known that the external magnetic field penetrates the HTS layer from its edges with a certain penetration depth p. If a and c are situated in the central region of the HTS layer defined by $-w+p < x < w-p$, as shown in Figure 4.2.2 (a), the central region cannot be penetrated at low magnetic fields. In this case, dB_{ext}/dt is equal to zero in the central region, i.e., $V = 0$ according to (4.3). As a result, the transport DC can flow through the central region without resistivity, i.e., the dynamic resistance $R_{dyn} = 0$. From this case we can find that there exists a threshold field, B_{th}, below which the dynamic resistance of the HTS layer remains zero. When B_{ext} is greater than B_{th}, the central region will be penetrated, and the transport DC will occupy a section defined by $-iw < x < iw$ (i is the load ratio between I_t and I_{c0}), named as the dynamic region, as presented in Figure 4.2.2 (b). Therefore, in this case, a voltage is generated in the dynamic region based on (4.3) in which the transport DC experiences the dynamic resistance as well as dynamic loss.

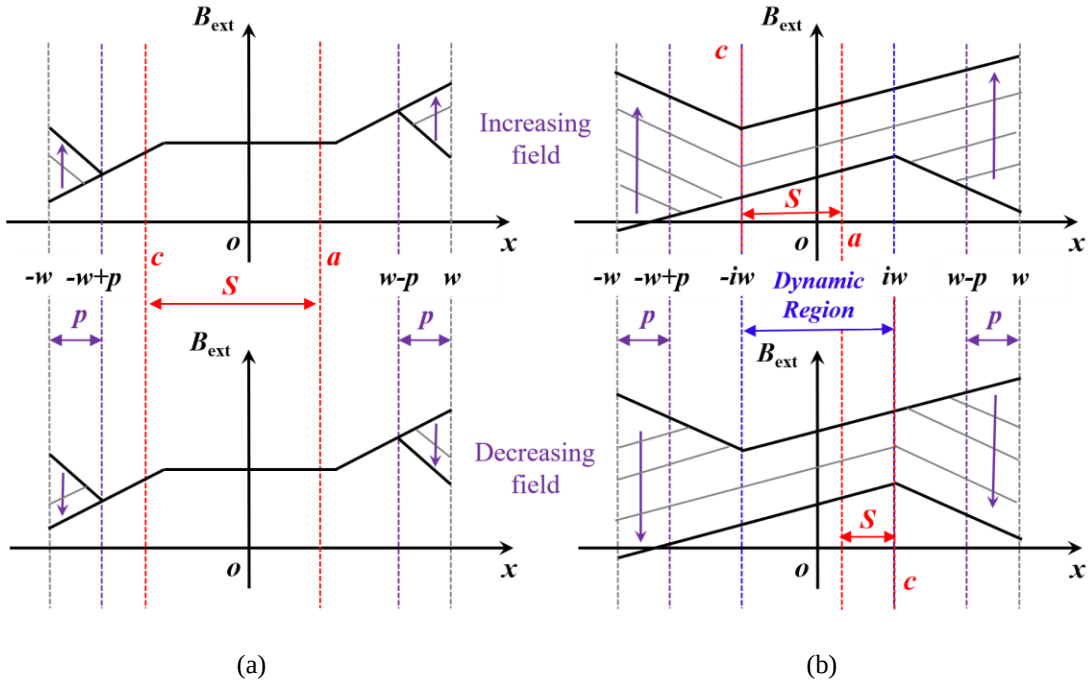

(a) (b)

Figure 4.2.2 Magnetic field profiles inside the studied HTS layer experiencing both a DC and an AC external field. (a) Case of $B_{ext} < B_{th}$ in which the field cannot penetrate the central region defined by $-w+p < x < w-p$. (b) Case of $B_{ext} > B_{th}$ where dynamic resistance/loss occurs in the dynamic region defined by $-iw < x < iw$. The line a is located at any position inside the dynamic region. The line c is situated at the boundaries of the dynamic region (electric centre-line) and thus no flux moves across it.

According to the above analyses, it can be concluded that B_{th} is not only the lower limit of the field that can penetrate the central region characterized by $-w+p < x < w-p$, but also the lower limit of the field that can give rise to a resistance in the dynamic region featured by $-iw < x < iw$. Therefore, B_{th} can be determined by $iw = w-p$. It should be pointed out that in [312], the penetration depth has been determined in the case of an external field parallel to the wide surface of the slab. However, the penetration depth/field is geometry-dependent and in our case the applied field is perpendicular to the wide surface of the HTS layer. Therefore, in order to calculate B_{th}, we need to find an appropriate penetration field, B_p, for a thin HTS strip exposed to a perpendicular magnetic field. According to [220], B_p can be determined by the B value at the maxima of the Γ curve, with

$$\Gamma = P_{BI} / B_{ext}{}^2 \tag{4.4}$$

where P_{BI} is the Brandt expression for magnetisation loss, and

$$P_{BI} = 4 f w^2 J_{c0} B_{ext} \left[\frac{2B_c}{B_{ext}} \ln\left(\cosh \frac{B_{ext}}{B_c} \right) - \tanh\left(\frac{B_{ext}}{B_c} \right) \right] \tag{4.5}$$

$$B_c = \frac{\mu_0 J_{c0}}{\pi} \tag{4.6}$$

In essence, P_{BI} in (4.5) is identical to P_{mag} in (2.9). (4.5) is used here to simplify the determination of B_p.

Based on (4.4), (4.5) and (4.6), the penetration field can be obtained as

$$B_p = 4.9284 \frac{\mu_0 J_{c0} h}{\pi} \tag{4.7}$$

B_{th} is determined by $iw = w\text{-}p$, yielding

$$B_{th} = (1-i) B_p = 4.9284 \frac{\mu_0 J_{c0} h}{\pi} (1-i) \tag{4.8}$$

According to Figure 4.2.2 (b), dynamic loss is determined by the magnetic flux traversing the dynamic region of the HTS layer during an AC cycle. On the basis of (4.3) and (4.8), through a series of derivation and calculation (the details can be found in [220, 312]), dynamic power loss, P_{dyn}, and dynamic resistance, R_{dyn}, are obtained as

$$P_{dyn} = I_t \cdot \Delta\Phi \cdot f = I_t^2 \cdot R_{dyn} = I_t^2 \cdot \frac{4wLf}{I_{c0}} (B_{ext} - B_{th}) \tag{4.9}$$

where $\Delta\Phi$ is the perpendicular flux crossing the HTS layer during one AC cycle. More details concerning the characteristics of the traversing magnetic flux will be presented in the following sections.

4.3 Dependence of Dynamic Loss on Critical Current and n-value

Dynamic resistance and dynamic loss are determined by not only the outer electromagnetic environment, e.g., the applied transport current (I_t) and the external magnetic field (B_{ext}), but also the intrinsic characteristics of the HTS CC, e.g., the critical current in self-field critical current (I_{c0}) and the *n*-value. In addition, the functioning mechanism of I_{c0} and *n*-value on the dynamic loss/resistance have not been systematically studied. Therefore, it is necessary to clarify the dependence of dynamic loss and resistance on I_{c0} and *n*-value of HTS CCs.

Based on the ***T***-formulation based numerical model in Chapter 3, this section will calculate the dynamic loss and the dynamic resistance with different I_{c0} and *n*-value. The simulated results will be validated in comparison with the corresponding experimental measurement data and analytical expressions. Through this work, the variation characteristics of the dynamic loss and resistance relating to $I_{c0,}$ and *n*-value will be systematically figured out. The results can be used to accurately predicate the dynamic loss and resistance for different types of HTS CCs, and further be a useful reference for loss control.

4.3.1 Analysis method

The numerical model of the 1D thin strip was developed by use of the finite element method based on the ***T***-formulation. The $J_c(\boldsymbol{B})$ dependence, as shown in Equation (2.3) has been taken into account here, with $B_0 = 0.135$ T. When an HTS CC carries a DC transport current under an AC magnetic field, the DC I_t occupies the dynamic region of the superconducting layer with the width of $2iw$, leaving the rest with width $2(1-i)w$ free on both sides [312]. Therefore, on the basis of the $J_c(\boldsymbol{B})$ dependence, the dynamic loss during one cycle, Q_{dyn} (J), can be formulated by

$$Q_{dyn} = \frac{hL}{f} \cdot \int_{(1-i)w}^{(1+i)w} E \cdot J dy = \frac{E_0 hL}{{J_{c0}}^n f} \int_{(1-i)w}^{(1+i)w} J^{n+1} \cdot \left(1 + \frac{B_\perp}{B_0}\right)^n dy \tag{4.10}$$

where i is the ratio between the transport current I_t and I_{c0}, w is the half width of the HTS CC, and L is its length. f is the frequency of the AC field. $E_0 = 10^{-4}$ V/m.

As presented in Section 4.2, dynamic power loss can also be calculated by (4.6). On the basis of (4.9), the dynamic loss during one cycle can be rewritten as

$$Q_{dyn} = \frac{P_{dyn}}{f} = {I_t}^2 \cdot \frac{4wL}{I_{c0}} (B_{ext} - B_{th}) \tag{4.11}$$

For the convenience of description, here I define the normalized dynamic loss in unit length (J/m), $Q_{dyn,n}$, and dynamic resistance in unit length (Ω/m/Hz), $R_{dyn,n}$, during one cycle as

$$\begin{cases} Q_{dyn,n} = \dfrac{Q_{dyn}}{L} = {I_t}^2 \cdot \dfrac{4w}{I_{c0}} (B_{ext} - B_{th}) \\ R_{dyn,n} = \dfrac{R_{dyn}}{Lf} = \dfrac{4w}{I_{c0}} (B_{ext} - B_{th}) \end{cases} \tag{4.12}$$

Then, their differentiation with respect to I_{c0} can be obtained as

$$\begin{cases} \dfrac{\partial Q_{dyn,n}}{\partial I_{c0}} = -4w \cdot \dfrac{{I_t}^2}{{I_{c0}}^2} (B_{ext} + \dfrac{2.4642\mu_0}{\pi w} I_t) \\ \dfrac{\partial R_{dyn,n}}{\partial I_{c0}} = -4w \cdot \dfrac{1}{{I_{c0}}^2} (B_{ext} + \dfrac{2.4642\mu_0}{\pi w} I_t) \end{cases} \tag{4.13}$$

4.3.2 Results and analyses

The numerical model has been established based on the size of an HTS CC manufactured by SuperPower, Inc., which is 4 mm wide comprising a 1-μm-thin film of YBCO. A wide range of I_{c0} from 80 A to 160 A has been simulated and an external magnetic field was applied perpendicular to the surface of the HTS CC with varying magnitudes.

The experimental setup for measuring P_{dyn} is shown in Figure 4.3.1. It is mainly composed of an AC electromagnet built with copper racetrack coils which can produce a flux density up to 100 mT, a Hewlett Packard 6682A DC power supply which provides I_t varying between 0-240 A, a Keithley 2182 nano-voltage meter for averaged voltage measuremnt across the voltage taps attached on the middle of the sample conductor, and a cryostat containing liquid nitrogen. An adjustable capacitor bank is connected in series with the AC magnet to enable different resonance frequencies [220]. The voltage measurement leads are wound on a cylindrical surface enclosing the tape to achieve inductively cancelling voltage taps attached to the sample [216]. P_{dyn} is obtained by multiplying the measured time-averaged voltage across the sample with the DC transport current. For the tested 15-cm-long HTS CC in the experiment, with n = 22.5 and I_{c0} = 105.3 at 77 K, it was placed in the uniform field region between the poles of the electromagnet which produced an external AC magnetic field of 26.62 Hz with a magnitude varying between 0 and 100 mT.

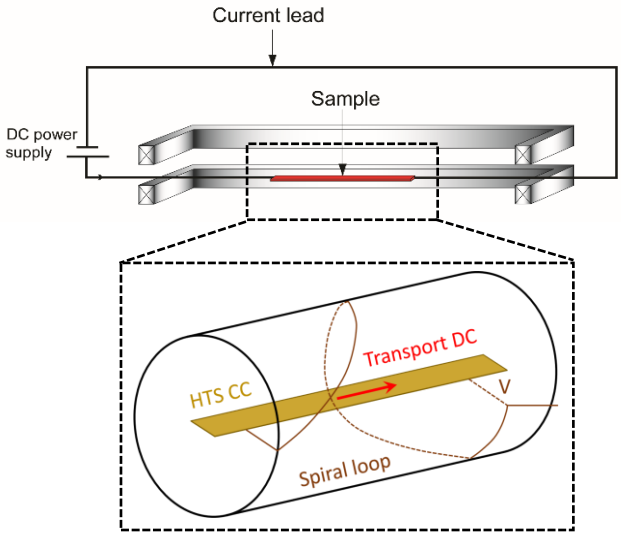

Figure 4.3.1 Schematic of the experimental setup to measure the dynamic loss of an HTS CC.

4.3.2.1 Influence of I_{c0} on $Q_{dyn,n}(I_t)$

When the amplitude of the externally applied magnetic field B_{ext} is chosen as 40 mT, for different I_{c0}, the dynamic loss curves with respect to I_t are presented in Figure 4.3.2. In Figure 4.3.2, the solid lines with symbols represent the simulated results, the dash-dot lines signify the analytical results by Equation (4.12), and the symbols without lines are the experimentally measured results. All these results show good agreement with each other, though the simulated dynamic loss is slightly higher than that of the analytical expression, which is in accordance with [313]. It can be found that for the same transport current I_t under the same AC magnetic field, less dynamic loss is generated in the CC with a higher I_{c0}. Taking I_t = 60 A as an example

for illustration, when changing I_{c0} from 80 to 120 A (40 A of augmentation), the normalized dynamic loss varies from 15 to 8 mJ/m (reduction of 7 mJ/m). Meanwhile, when I_{c0} is increased from 120 to 160 A (40 A of augmentation), the dynamic loss drops to 5.8 mJ/m (reduction of 2.2 mJ/m). On this basis, it is not hard to conclude that the changing rate of dynamic loss with respect to I_{c0} decreases with the increase of I_{c0}, which can be quantitatively described by (4.13). Therefore, it is not always cost-efficient to decrease the dynamic loss simply by increasing I_{c0}.

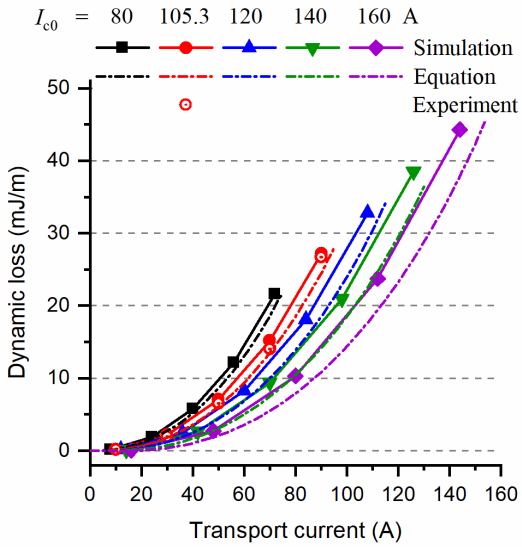

Figure 4.3.2 Normalized dynamic loss for different HTS CCs with different I_{c0} when changing transport current, under an AC magnetic field of 40 mT. (I_{c0} = 80 A, 105.3 A, 120 A, 140 A, 160 A. I_t / I_{c0} is set at 10%, 30%, 50%, 70%, and 90%).

In fact, the effect of I_{c0} on the dynamic loss is tightly linked to the current load rate I_t / I_{c0}, which can be explained by Figure 4.3.3. Figure 4.3.3 shows the J and B profiles of different HTS CCs with distinct I_{c0} while carrying the same transport current, I_t = 40 A, exposed to an AC magnetic field of which the amplitude B_{ext} = 40 mT. It can be seen that, with the increase of I_{c0}, the J profiles move towards each other and lead to a smaller effective region to carry the transport current. The B profiles have the same trend as the J profiles when I_{c0} gets larger. Here the shaded area signifies the amount of traversing magnetic flux during one AC period, which determines how much dynamic loss is generated. Therefore, with the augment of I_{c0}, the effective region to carry transport current shrinks and then less magnetic flux traverses this region, resulting in less dynamic loss.

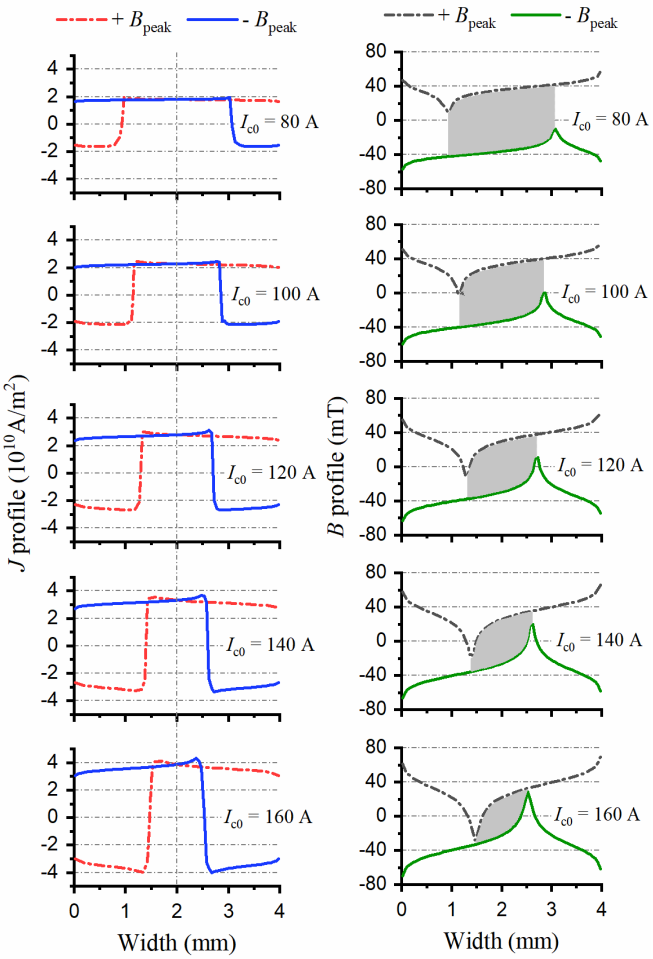

Figure 4.3.3 *J* and *B* profiles for different HTS CCs with different I_{c0} when carrying the same transport current, I_t = 40 A, under an AC magnetic field of 40 mT. (I_{c0} = 80 A, 105.3 A, 120 A, 140 A, 160 A, respectively.)

4.3.2.2 Influence of I_{c0} on $R_{dyn,n}(I_t)$

Exposed to the same externally applied magnetic field with B_{ext} = 40 mT, for different I_{c0}, the variation characteristics of the dynamic resistance in respect of I_t are presented in Figure 4.3.4. The solid lines with symbols signify the simulation results. In general, the changing trend of the dynamic resistance with respect to I_{c0} follows the same property as the dynamic loss. In other words, for the same transport current I_t, the CC with a higher I_{c0} has a lower dynamic resistance, which complies with (4.12) and Figure 4.3.3. Taking also I_t = 60 A as an example, when changing I_{c0} from 80 to 120 A, the normalized dynamic resistance varies from 4 to 2.3 μΩ/m/Hz (with a difference of 1.7 μΩ/m/Hz). However, when I_{c0} is increased from 120 to 160 A, the dynamic resistance decreases to 1.3 μΩ/m/Hz (with a difference of 1 μΩ/m/Hz).

Therefore, we can conclude that the changing rate of dynamic resistance with respect to I_{c0} also decreases with the increase of I_{c0}, which complies well with (4.13).

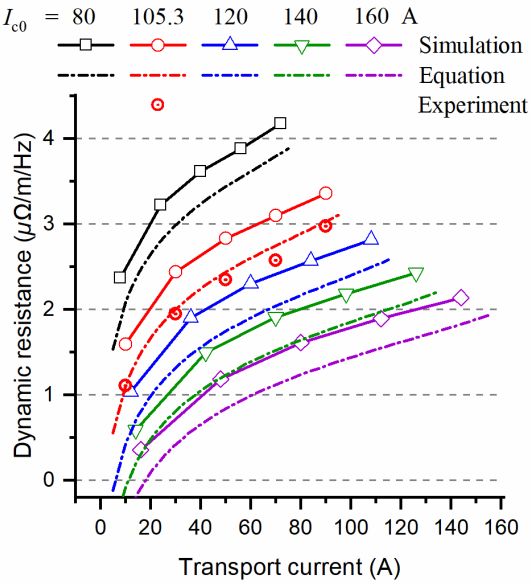

Figure 4.3.4 Normalized dynamic resistance for different HTS CCs with different I_{c0} when changing transport current, under an AC magnetic field of 40 mT. (I_{c0} = 80 A, 105.3 A, 120 A, 140 A, 160 A, the load rate is set at 10%, 30%, 50%, 70%, and 90%).

It is also of interest to notify that, $R_{dyn,n}$ increases in a non-linear way with I_t, according to the simulated results. This nonlinearity can not be explained by (4.12). Actually, Liu et al [317] mentioned that (4.8) provided good agreement with all previously-published experimental data only for a high load rate (especially for i > 10%). Mikitik and Brandt [316] have proposed another expression for the threshold field as follows:

$$B_{th} = \frac{\mu_0 J_{c0} h}{2\pi}\left[\frac{1}{i}\cdot\ln\left(\frac{1+i}{1-i}\right)+\ln\left(\frac{1-i^2}{4i^2}\right)\right] \tag{4.14}$$

The nonlinearity of (4.14) has been verified experimentally in [220]. According to (4.12) and (4.14), we have

$$R_{dyn,n} = \frac{4w}{I_{c0}}\cdot B_{ext} - \frac{\mu_0}{\pi}\left[\frac{1}{i}\cdot\ln\left(\frac{1+i}{1-i}\right)+\ln\left(\frac{1-i^2}{4i^2}\right)\right] \tag{4.15}$$

The calculated dynamic resistance by (4.15) is depicted in Figure 4.3.4 with dash-dot lines, and the experimental data are plotted with only symbols, both of which agree well with the variation trend of the simulated results. Therefore, it is verified that the dynamic resistance is actually in a non-linear correlation with the transport current.

4.3.2.3 Influence of I_{c0} on $Q_{dyn,n}(B_{ext})$ and $R_{dyn,n}(B_{ext})$

When I_{c0} changes from 80 A to 160 A, the variation properties of the normalized dynamic loss $Q_{dyn,n}$ and dynamic resistance $R_{dyn,n}$ relating to the externally applied magnetic field are simulated and compared in Figure 4.3.5. The transport current is chosen as I_t = 40 A, and the amplitude of the applied magnetic field ranges from 0 to 100 mT. In Figure 4.3.5, among all the $Q_{dyn,n}(B_{ext})$ and $R_{dyn,n}(B_{ext})$ curves, the solid lines with symbols represent the simulated results, the dash-dot lines signify the calculated results by (4.12), and the symbols without lines are obtained by experiment. It can be found that the simulated results show a good agreement with the analytical expression, while they are in better accordance with the experimental data.

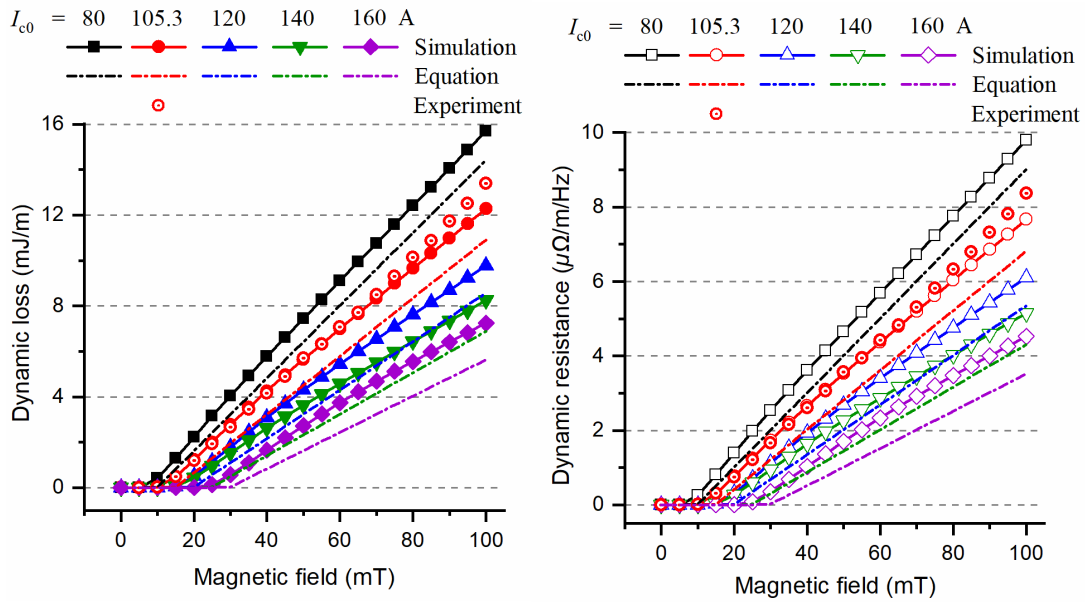

Figure 4.3.5 Normalized dynamic loss and dynamic resistance for different HTS CCs with different I_{c0} when changing externally applied magnetic field from 0 - 100 mT. (I_{c0} = 80 A, 105.3 A, 120 A, 140 A, 160 A, I_t is set as 40 A). (a) Dynamic loss. (b) Dynamic resistance.

Overall, the dynamic loss and the dynamic resistance show the same trend with the increase of B_{ext}, in that a higher magnetic field can bring more flux that traverses the HTS layer. Under the same B_{ext}, it can be seen that more dynamic loss and resistance are generated in the HTS CC with a lower I_{c0}. In fact, when carrying the same I_t, a smaller I_{c0} means a higher current load rate. Therefore, in this case, the effective region to carry transport current is larger and more flux will traverse this conductor, then leading to a higher dynamic loss and resistance.

Furthermore, the changing rates of dynamic loss and dynamic resistance decrease in a non-linear way with the increase of I_{c0}. Taking B_{ext} = 60 mT as an example for illustration, when I_{c0} changes from 80 to 120 A by 40 A, the normalized dynamic loss varies from 9 to 5 mJ/m with a difference of 4 mJ/m. However, when I_{c0} increases from 120 to 160 A, the reduction of dynamic loss is just 1.4 mJ/m. As far as dynamic resistance is concerned, it can be analysed in the same way. The above conclusions can be confirmed by (4.13).

It is worth mentioning that only beyond the threshold field can the dynamic loss and dynamic resistance be generated. With the augment of I_{c0}, the critical current density will increase accordingly, which results in a higher B_{th}. In fact, the magnetic flux firstly penetrates into the HTS CC from its boundaries to form walls, and then the walls break up into vortices with the increase of B_{ext} [318]. Prior to that B_{ext} goes beyond B_{th}, the vortices will not diffuse towards the center of the CC; thus, no dynamic loss is produced. For the HTS CC with a higher I_{c0}, a greater amount of magnetic flux will be needed to penetrate into its interior to form irregular penetrating flux regions, which are the sources of vortex creations.

4.3.2.4 Influence of I_{c0} on B_{cor}

On the basis of Figure 4.3.5 (a), when continuing to increase B_{ext}, the $Q_{dyn,n}(B_{ext})$ curves are shown in Figure 4.3.6. The solid lines with symbols represent the simulated results, and the dash-dot lines are obtained by (4.12). It is of interest to note that, under a high enough B_{ext}, the $Q_{dyn,n}(B_{ext})$ curves show a fast-rising nonlinearity, which is distinguished from (4.12). Here the external magnetic field bringing a sudden change of the dynamic loss is defined as the "corner field", B_{cor}. Actually, this sudden change appears because of the field dependence of the critical current density $J_c(\boldsymbol{B})$. With the increase of B_{ext}, the critical current density of the HTS CC will turn lower and its real critical current will be reduced, as a consequence, the load rate will easily go beyond 100% and rapid growth of dissipated power will be generated [312].

At B_{cor}, the real critical current I_{cor} can be approximated as

$$I_{cor} = \frac{I_{c0}}{1 + B_{cor}/B_0} \tag{4.16}$$

Taking I_{c0} = 80 A in Figure 4.3.6 as an example for illustration, the corner field of its $Q_{dyn,n}(B_{ext})$ curve is around 200 mT, then in this case I_t / $I_{cor\,(200\,mT)}$ = 1.24 > 100%. Therefore, at B_{cor} the real load rate is already greater than 1. From Figure 4.3.6, it can be found that when increasing I_{c0} from 80 to 160 A, B_{cor} changes from 80 mT to approximately 300 mT. Actually, when carrying the same transport current, the HTS CC with a higher I_{c0} has a stronger capacity to withstand the current induced by the external magnetic field and it will be harder for the

transport current to go beyond the critical current. Therefore, in this case, B_{cor} increases with I_{c0}. In other words, for a high load rate I_t / I_{c0}, the HTS CC is more susceptible to the external magnetic field and its dynamic loss is more likely to have a sudden change under relatively lower B_{ext}.

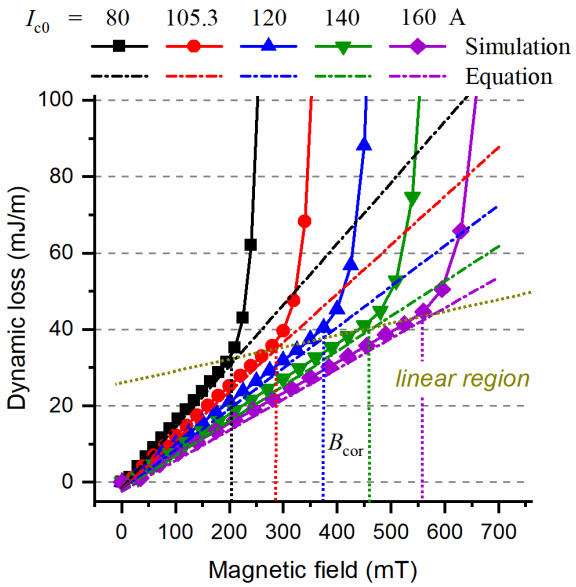

Figure 4.3.6 Dynamic loss for different HTS CCs with different I_{c0} when changing externally applied magnetic field from 0 - 500 mT. (I_{c0} = 80 A, 100 A, 120 A, 140 A, 160 A. I_t is set as 40 A). n = 25.

4.3.3 Dependence of dynamic loss on n-value

Considering that the $Q_{dyn,n}(B_{ext})$ and $R_{dyn,n}(B_{ext})$ curves have the same variation pattern, thus for this section, only the dynamic loss will be discussed.

Taking the tested HTS CC with I_{c0} = 105.3 A as a prototype for numerical modelling, with the variation of the n-value the simulated dynamic losses are presented in Figure 4.3.7, as well as the measured results. Figure 4.3.7 (a) shows that for low load rate (e.g., I_t / I_{c0} = 30%), the n-value does not have a significant influence on the dynamic loss. However, when the load rate turns high enough (e.g., I_t / I_{c0} = 90%), as shown in Figure 4.3.7 (b), the dynamic loss increases rapidly after reaching B_{cor}. Besides, the larger the n-value, the higher the increasing rate, and the lower B_{cor}. In detail, when the n-value changes from 20 to 60, B_{cor} decreases from 50 to 25 mT. From n = 20 to 40, B_{cor} drops with a difference of 20 mT; however, from n = 40 to 60, B_{cor} drops with a difference of only 5 mT. Therefore, the declining rate of B_{cor} gets smaller with the increase of the n-value.

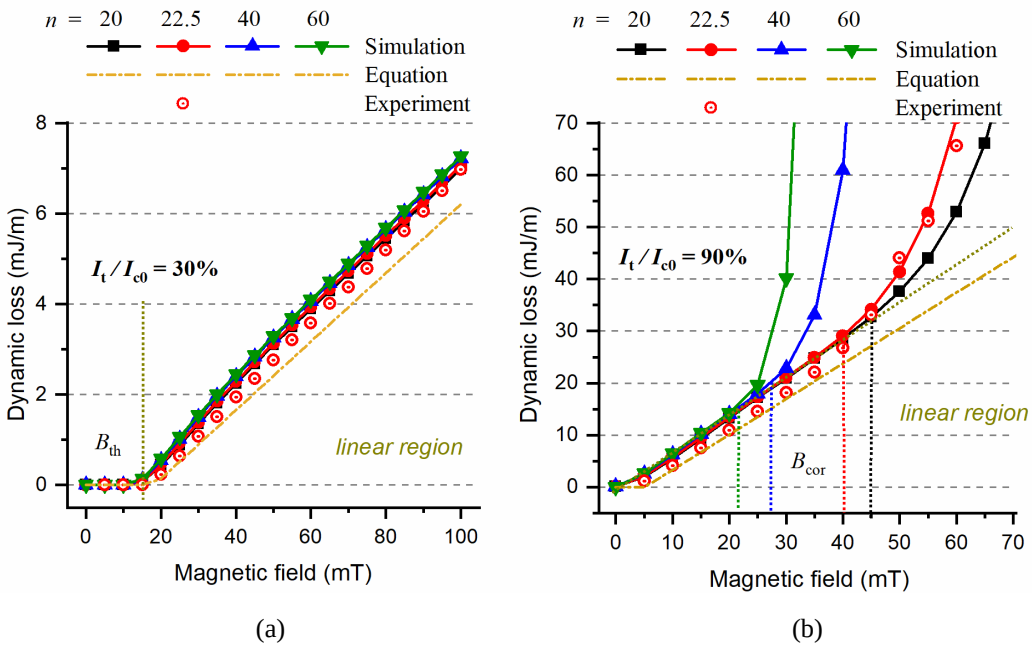

Figure 4.3.7 Dynamic loss for different HTS CCs with different *n*-value when changing externally applied magnetic field from 0 - 100 mT (I_{c0} = 105.3 A). (a) I_t / I_{c0} = 30%. (b) I_t / I_{c0} = 90%.

In fact, according to (4.10), we know that the dynamic loss is tightly linked to the power function $f(B) = (1+ B_\perp /B_0)^n$, caused by the $J_c(\boldsymbol{B})$ dependence. At low I_t/I_{c0}, and under small B_{ext}, $B_\perp$ is far inferior to B_0. In this way, $f(B)$ approaches to 1, thus the *n*-value does not have a significant impact on the dynamic loss and the $Q_{dyn,n}(B_{ext})$ curve shows linearity. In contrast, at high I_t/I_{c0}, under the influence of B_{ext}, $B_\perp$ will become comparable to B_0. In this case, $f(B)$ will be greatly affected by the *n*-value and after B_{cor} the dynamic loss will increase in the form of the power function. With the augment of the *n*-value, this power function has a higher power index and the dynamic loss will have a higher rate of change. Therefore, the higher the *n*-value, the smaller B_{cor}.

4.3.4 Summary

The influences of I_{c0} on the $Q_{dyn,n}(I_t)$ curve, the $R_{dyn,n}(I_t)$ curve, the $Q_{dyn,n}(B_{ext})$ curve and the $R_{dyn,n}(B_{ext})$ curve have been studied, respectively. Furthermore, the "corner field" B_{cor} has been defined for describing the dynamic loss/resistance in the case where I_t gets superior to $I_c(B_{ext})$. At last, the effect of the *n*-value on the nonlinearity of the dynamic loss/resistance has been specially analyzed. Section 4.3 has clarified the dependence of the dynamic loss and dynamic resistance on the critical current and the *n*-value of HTS CCs. Based on simulation and experimental results, we found that under the same external electromagnetic environment, dynamic loss and resistance reduces along with increasing I_{c0}. At higher transport current I_t (above 50% I_{c0}), the influence of I_{c0} on dynamic loss and resistance is more obvious, since in

principle the load rate I_t/I_{c0} directly determines the magnetic flux traversing the HTS CC.

(1) In general, both the dynamic loss and the dynamic resistance increase linearly with the external magnetic field, until it reaches the corner field B_{cor}. When B_{ext} goes beyond B_{cor}, dynamic loss increases in the form of the power function due to the $J_c(\boldsymbol{B})$ dependence. For a lower I_{c0} (e.g., load rate above 50%), HTS CCs are more sensible to external magnetic field, and their B_{cor} is lower.

(2) *n*-value is another key property to affect the correlation between dynamic loss/resistance and external magnetic fields. The higher the *n*-value is, the faster the dynamic loss and resistance increases along with B_{ext}, and the smaller B_{cor} becomes.

(3) The changing rates of dynamic loss and dynamic resistance decrease in a non-linear way with the increase of I_{c0}; thus, it is not always cost-effective to reduce dynamic loss/resistance by simply increasing I_{c0} during the manufacture of HTS CCs.

It should be emphasized that the nonlinearity of the dynamic loss and the dynamic resistance at high load rate while under high external magnetic field (e.g., I_t/I_{c0} above 90%, B_{ext} above 45 mT, with n = 22.5) cannot be explained and predicted by the existing analytical equations. Therefore, the numerical modeling method proposed in this paper can more accurately describe the variation properties of the dynamic loss and resistance. Last but not the least, the nonlinearity of the $R_{dyn,n}(I_t)$ curve has been validated experimentally, which further confirms the correctness of (4.14).

4.4 A Full-range Formulation for Dynamic Loss of HTS CCs

Based on (4.9), the widely adopted analytical expression for dynamic power loss, $P_{dyn,l}$ (W), can be written as

$$P_{dyn,l} = 4wfLI_t i\left(B_{ext} - B_{th}\right) \tag{4.17}$$

where B_{th} is the threshold field, defined by (4.14).

The linearity of dynamic loss with respect to B_{ext}, as shown in (4.18), has been well verified by many studies [220, 312, 314-315]. However, according to Section 4.3, when the HTS CC with a high *i* is exposed to a high external magnetic field, the dynamic loss exhibits a non-linearity with the augmentation of field intensity and the CC is under the risk of quench [222, 313, 319]. A critical-state model for dynamic resistance has been proposed to describe this non-linearity in [312]. When B_{ext} is far greater than B_{th}, the dynamic power dissipation in a slab-like superconductor can be written as [312]

$$P_{\mathrm{dyn,nl}} = I_{\mathrm{t}}^{\,2} \cdot \frac{4wfL}{I_{\mathrm{c0}}} \cdot \left(B_{\mathrm{ext}} + \frac{B_{\mathrm{ext}}^{\,2}}{B_0} \right) \tag{4.18}$$

where B_0 is the characteristic field constant in the $J_c(\boldsymbol{B})$ dependence.

However, it appears that the measured dynamic resistance rises much faster than the analytical results obtained by (4.18) [312]. Therefore, the existing analytical expressions, (4.17) and (4.18), have proven to be inapplicable to characterize the non-linearity of dynamic loss, and the magnetic field and current load ratio causing the sudden rise in loss are still unclear. In [220], a time-averaged DC flux flow resistance has been introduced to explain the non-linear fast rise of dynamic resistance, which provides a good description of the deviation from linearity at high currents. On the basis of this work, I have studied the current density and magnetic flux density distributions inside the HTS CC in detail, and proposed a new formulation for dynamic loss, which considers a full-range of magnetic fields and load ratios.

4.4.1 Formulation Derivation

When an HTS CC carries a DC transport current under an AC magnetic field, the transport current occupies the dynamic region of the superconducting layer with width $2iw$ in the center of the CC. Therefore, based on (4.10), the dynamic power loss (W) can be formulated by

$$P_{\mathrm{dyn}} = \frac{hL}{T} \int_0^T \int_{(1-i)w}^{(1+i)w} E \cdot J dy dt \tag{4.19}$$

Considering the $J_c(B)$ dependence defined by (2.3) and the $\boldsymbol{E}$-$\boldsymbol{J}$ power law determined by (2.7), (4.19) can be transformed to

$$P_{\mathrm{dyn}} = \frac{hL}{T} \int_0^T \int_{(1-i)w}^{(1+i)w} E_0 \left[\frac{J \cdot \left(1 + |B_\perp| / B_0\right)}{J_{\mathrm{c0}}} \right]^n J dy dt = \frac{E_0 hLf}{J_{\mathrm{c0}}^{\,n}} \int_0^T \int_{(1-i)w}^{(1+i)w} J^{n+1} \cdot f\left(B\right) dy dt \tag{4.20}$$

with

$$f\left(B\right) = \left[1 + \frac{\left| B_{\mathrm{ext}} \sin\left(2\pi ft\right) - B_{\mathrm{s}} \right|}{B_0} \right]^n \tag{4.21}$$

where $B_\perp$ is the local magnetic field perpendicular to the wide surface of the CC. $B_\perp$ is decided by both B_{ext} and the self-field B_{s}. The negative sign indicates the direction of the field vector.

Although the current density and magnetic distribution along the width of the CC has been studied by Brandt, it is not feasible to calculate the integration in (4.20) directly by analytical methods [114]. However, the non-linear fast rise of dynamic loss occurs when the real load ratio $I_t / I_c(B)$ is approaching 1, i.e., when the CC is in a critical state. In this case, we can

simplify (4.20) by investigating the current density and magnetic flux density characteristics in the dynamic region.

Firstly, the J properties needs to be studied. According to the Bean Model, when the superconductor is in a critical state, the current density distribution along the width of the HTS CC should be characterized by the critical current $\pm J_c$. Here, concerning dynamic loss, we assume that the dynamic region is fully occupied by I_t. To verify this assumption, the ***T***-formulation based numerical modeling method has been adopted here. We define the average current density during one cycle T in the dynamic region, J_{avg}, as

$$J_{avg} = \frac{1}{T} \cdot \frac{1}{2iw} \cdot \int_0^T \int_{(1-i)w}^{(1+i)w} J dy dt \tag{4.22}$$

During the simulation, the transport current I_t has been fixed as 60 A. When I_{c0} decreases from 160 to 80 A (i.e., whne i increases from 0.375 to 0.75), the relationship between i and J_{avg}/J_t under different B_{ext} has been presented in Figure 4.4.1. Here, J_t is the average current density determined by the transport current, with $J_t = I_t/(2wh)$. It can be seen that with the increase of i, J_{avg} will get close to J_t. In other words, the dynamic region with the width of $2iw$ is the effective region to carry transport current and in the critical state, the dynamic region has been filled with I_t. Therefore, the current density distribution in the dynamic region should be decided by J_t.

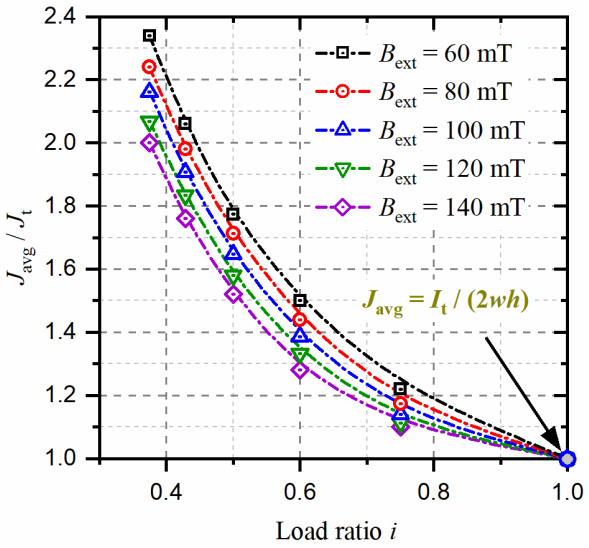

Figure 4.4.1 The relationship between J_{avg}/J_t and i under different B_{ext} varying from 60 to 140 mT. Transport current I_t = 60 A.

Next, the magnetic flux density properties in the dynamic region needs to be explored. In (4.21), B_s at any position inside the dynamic region, y_0, is decided by

$$B_s(y_0)=\frac{\mu_0 h}{2\pi}\left[\int_0^{(1-i)w}\frac{J(y)}{(y_0-y)}dy-\int_{(1-i)w}^{y_0}\frac{J(y)}{(y_0-y)}dy+\int_{y_0}^{2w}\frac{J(y)}{(y-y_0)}dy\right] \tag{4.23}$$

with $(1\text{-}i)w \le y_0 \le (1+i)w$.

Based on the above analysis, $J(y)$ is determined by J_t, so (4.23) can be simplified as

$$B_s(y_0)=\frac{\mu_0 h J_t}{2\pi}\cdot\ln\left(\frac{(2w-y_0)\cdot y_0}{[y_0-(1-i)w]^2}\right) \tag{4.24}$$

Then the average self-field flux density in the dynamic region can be calculated by

$$\overline{B_s}=\frac{1}{2iw}\int_{(1-i)w}^{(1+i)w}B_s(y_0)\,dy_0=\frac{\mu_0 h J_t}{2\pi}\left[\frac{1}{i}\ln\left(\frac{1+i}{1-i}\right)+\ln\left(\frac{1-i^2}{4i^2}\right)\right]=i\cdot B_{th} \tag{4.25}$$

According to (4.14), it is evident that B_{th} decreases with i. Therefore, at a high load rate, B_s becomes much smaller compared to B_{ext}, i.e., $B_\perp$ will be dominated by the external field. In this case, we have

$$f(B)\approx\left[1+\frac{\left|B_{ext}\sin(2\pi ft)\right|}{B_0}\right]^n \tag{4.26}$$

Based on the above formulae, (4.20) can be transformed to

$$\begin{aligned}P_{dyn,nl}&=\frac{E_0 hLf}{{J_{c0}}^n}\int_0^T\int_{(1-i)w}^{(1+i)w}\left(\frac{I_t}{2wh}\right)^{n+1}\cdot f(B)\,dydt\\&=\frac{E_0 LfI_t}{2w}i^n\int_0^T\int_{(1-i)w}^{(1+i)w}f(B)\,dydt\\&=E_0 LI_t i^{n+1}\cdot f_{avg}(B)\end{aligned} \tag{4.27}$$

with the average of $f(B)$ defined as

$$f_{avg}(B)=\frac{1}{T}\cdot\frac{1}{2iw}\cdot\int_0^T\int_{(1-i)w}^{(1+i)w}f(B)\,dydt \tag{4.28}$$

According to Binomial Theorem

$$(a+b)^n=\sum_{k=0}^{n}\frac{n!}{k!(n-k)!}\cdot a^{n-k}\cdot b^k \tag{4.29}$$

(4.26) can be expanded into

$$\begin{aligned} f(B) &= \left[1+\frac{\left|B_{\text{ext}}\sin(2\pi ft)\right|}{B_0}\right]^n \\ &= 1+n\frac{\left|B_{\text{ext}}\sin(2\pi ft)\right|}{B_0}+\frac{n(n-1)}{2!}\left(\frac{\left|B_{\text{ext}}\sin(2\pi ft)\right|}{B_0}\right)^2+\frac{n(n-1)(n-2)}{3!}\left(\frac{\left|B_{\text{ext}}\sin(2\pi ft)\right|}{B_0}\right)^3+\cdots \end{aligned} \tag{4.30}$$

According to Euler's formula

$$e^{ix}=\cos x+i\sin x \tag{4.31}$$

we have

$$\begin{aligned} \sin^N x &= \left[\frac{1}{2i}\left(e^{ix}-e^{-ix}\right)\right]^N \\ &= \left(\frac{1}{2i}\right)^N\cdot\sum_{k=0}^{N}\frac{N!}{k!(N-k)!}\left(e^{ix}\right)^{N-k}\left(-e^{-ix}\right)^k \\ &= \left(\frac{1}{2i}\right)^N\cdot\sum_{k=0}^{N}\frac{N!}{k!(N-k)!}(-1)^k\begin{Bmatrix}\cos\left[(N-2k)x\right]\\ +i\sin\left[(N-2k)x\right]\end{Bmatrix} \end{aligned} \tag{4.32}$$

When N is odd, we have

$$\left|\sin^N x\right| = \left(\frac{1}{2}\right)^N\left|\sum_{k=0}^{N}\frac{N!}{k!(N-k)!}(-1)^k\sin\left[(N-2k)x\right]\right| \tag{4.33}$$

On the contrary when N is even we get

$$\left|\sin^N x\right| = \left(\frac{1}{2}\right)^N\left|\sum_{k=0}^{N}\frac{N!}{k!(N-k)!}(-1)^k\cos\left[(N-2k)x\right]\right| \tag{4.34}$$

Based on (4.29)-(4.34), (4.28) can be expanded to

$$\begin{aligned} f_{\text{avg}}(B) &= \frac{1}{T}\cdot\frac{1}{2iw}\cdot\int_0^T\int_{(1-i)w}^{(1+i)w}f(B)\,dydt \\ &= \frac{1}{T}\cdot\frac{1}{2iw}\cdot\int_0^T\int_{(1-i)w}^{(1+i)w}\left[1+\frac{\left|B_{\text{ext}}\sin(2\pi ft)\right|}{B_0}\right]^n dydt \\ &= \sum_{k=0}^{n}\frac{n!}{k!(n-k)!}\left(\frac{B_{\text{ext}}}{B_0}\right)^k\cdot\frac{1}{T}\int_0^T\left|\sin^k(2\pi ft)\right|dt \\ &= \sum_{k=0}^{n}\frac{n!}{k!(n-k)!}\left(\frac{B_{\text{ext}}}{B_0}\right)^k\cdot\frac{1}{T}\int_0^T\left|\left(\frac{1}{2i}\right)^k\cdot\sum_{m=0}^{k}\frac{k!}{m!(k-m)!}(-1)^m\begin{Bmatrix}\cos\left[2\pi(k-2m)\,ft\right]\\ +i\sin\left[2\pi(k-2m)\,ft\right]\end{Bmatrix}\right|dt \end{aligned} \tag{4.35}$$

When *n* is even, (4.35) can be written as

$$
\begin{aligned}
& f_{\text{avg}}(B) \\
&= \sum_{p=0}^{n/2-1} \left\{ \begin{array}{l} \dfrac{n!}{(2p+1)!\left[n-(2p+1)\right]!}\left(\dfrac{B_{\text{ext}}}{B_0}\right)^{2p+1}\left(\dfrac{1}{2}\right)^{2p+1} \\ \cdot\dfrac{1}{T}\displaystyle\int_0^T \left| \sum_{m=0}^{2p+1} \frac{(2p+1)!}{m!(2p+1-m)!}(-1)^m \left\{\sin\left[2\pi(2p+1-2m)\,ft\right]\right\} \right| dt \end{array} \right\} \\
&+ \\
& \sum_{p=0}^{n/2-1} \left\{ \begin{array}{l} \dfrac{n!}{(2p+2)!\left[n-(2p+2)\right]!}\left(\dfrac{B_{\text{ext}}}{B_0}\right)^{2p+2}\left(\dfrac{1}{2}\right)^{2p+2} \\ \cdot\dfrac{1}{T}\displaystyle\int_0^T \left| \sum_{m=0}^{2p+2} \frac{(2p+2)!}{m!(2p+2-m)!}(-1)^m \left\{\cos\left[2\pi(2p+2-2m)\,ft\right]\right\} \right| dt \end{array} \right\} \\
&= 1 \\
&+ n\left(\frac{1}{2}\right)^1\left(\frac{B_{\text{ext}}}{B_0}\right)^1 \cdot \frac{4}{\pi} \\
&+ \frac{n(n-1)}{2!}\left(\frac{1}{2}\right)^2\left(\frac{B_{\text{ext}}}{B_0}\right)^2 \cdot \frac{2!}{(1!)^2} \\
&+ \frac{n(n-1)(n-2)}{3!}\left(\frac{1}{2}\right)^3\left(\frac{B_{\text{ext}}}{B_0}\right)^3 \cdot \frac{32}{3\pi} \\
&+ \frac{n(n-1)(n-2)(n-3)}{4!}\left(\frac{1}{2}\right)^4\left(\frac{B_{\text{ext}}}{B_0}\right)^4 \cdot \frac{4!}{(2!)^2} \\
&+ \frac{n(n-1)(n-2)(n-3)(n-4)}{5!}\left(\frac{1}{2}\right)^5\left(\frac{B_{\text{ext}}}{B_0}\right)^5 \cdot \frac{512}{15\pi} \\
&+ \frac{n(n-1)(n-2)(n-3)(n-4)(n-5)}{6!}\left(\frac{1}{2}\right)^6\left(\frac{B_{\text{ext}}}{B_0}\right)^6 \cdot \frac{6!}{(3!)^2} \\
&+ \cdots + \left(\frac{1}{2}\right)^n\left(\frac{B_{\text{ext}}}{B_0}\right)^n \cdot \frac{n!}{\left[(n/2)!\right]^2} \\
&= 1 + \sum_{p=0}^{n/2-1} \frac{n!}{(2p+1)!\left[n-(2p+1)\right]!}\left(\frac{B_{\text{ext}}}{B_0}\right)^{2p+1} \cdot \frac{2^{p+1}\cdot p!}{\pi\displaystyle\prod_{q=0}^{2p+1}(2q+1)} \\
&\quad + \sum_{p=0}^{n/2-1} \frac{n!}{(2p+2)!\left[n-(2p+2)\right]!}\left(\frac{B_{\text{ext}}}{B_0}\right)^{2p+2}\left(\frac{1}{2}\right)^{2p+2} \cdot \frac{(2p+2)!}{\left[(p+1)!\right]^2}
\end{aligned}
\tag{4.36}
$$

Therefore, based on (4.36), (4.27) can be written as

$$P_{\mathrm{dyn,nl}} = E_0 L I_{\mathrm{t}} i^{n+1} \cdot f_{\mathrm{avg}}(B)$$

$$= E_0 L I_{\mathrm{t}} i^{n+1} \cdot \left\{ \begin{array}{l} 1 + \sum_{p=0}^{n/2-1} \frac{n!}{(2p+1)!\left[n-(2p+1)\right]!} \left(\frac{B_{\mathrm{ext}}}{B_0}\right)^{2p+1} \cdot \frac{2^{p+1} \cdot p!}{\pi \prod_{q=0}^{2p+1} (2q+1)} \\ + \sum_{p=0}^{n/2-1} \frac{n!}{(2p+2)!\left[n-(2p+2)\right]!} \left(\frac{B_{\mathrm{ext}}}{B_0}\right)^{2p+2} \left(\frac{1}{2}\right)^{2p+2} \cdot \frac{(2p+2)!}{\left[(p+1)!\right]^2} \end{array} \right\} \tag{4.37}$$

It should be emphasized that $P_{\mathrm{dyn,nl}}$ in (4.37) is derived on the basis that the HTS CC is at relatively high i and simultaneous high B_{ext}, which can only be used to characterize the non-linearly fast-rising part of the $P_{\mathrm{dyn}}(B_{\mathrm{ext}})$ curve. In (4.17), $P_{\mathrm{dyn,l}}$ is used to describe the linear correlation between dynamic loss and B_{ext}. There will be a cross point between the $P_{\mathrm{dyn,l}}(B_{\mathrm{ext}})$ and $P_{\mathrm{dyn,nl}}(B_{\mathrm{ext}})$ curves as at low external magnetic field, B_{ext} is much smaller than B_0, thus the n-value does not play an important role and $P_{\mathrm{dyn,nl}}$ will approach 0. However, at high external fields, B_{ext} becomes comparable to B_0, then under the influence of the n-value, P_{dyn} will increase rapidly in the form of a power function. In short, before the cross point, $P_{\mathrm{dyn,l}}$ is far greater than $P_{\mathrm{dyn,nl}}$, and vice versa. On the basis of the above analysis, we have proposed a full-range analytical equation for calculating dynamic loss, as

$$P_{\mathrm{dyn}} = P_{\mathrm{dyn,l}} + P_{\mathrm{dyn,nl}}$$

$$= 4wfLI_{\mathrm{t}} i \left(B_{\mathrm{ext}} - B_{\mathrm{th}}\right) + E_0 L I_{\mathrm{t}} i^{n+1} \cdot \left\{ \begin{array}{l} 1 + \sum_{p=0}^{n/2-1} \frac{n!}{(2p+1)!\left[n-(2p+1)\right]!} \left(\frac{B_{\mathrm{ext}}}{B_0}\right)^{2p+1} \cdot \frac{2^{p+1} \cdot p!}{\pi \prod_{q=0}^{2p+1} (2q+1)} \\ + \sum_{p=0}^{n/2-1} \frac{n!}{(2p+2)!\left[n-(2p+2)\right]!} \left(\frac{B_{\mathrm{ext}}}{B_0}\right)^{2p+2} \left(\frac{1}{2}\right)^{2p+2} \cdot \frac{(2p+2)!}{\left[(p+1)!\right]^2} \end{array} \right\} \tag{4.38}$$

In (4.37) and (4.38), n is even. When n is odd, the upper bound of summation needs to be changed accordingly, as

$$P_{\mathrm{dyn,nl}}$$

$$= 4wfLI_{\mathrm{t}} i \left(B_{\mathrm{ext}} - B_{\mathrm{th}}\right) + E_0 L I_{\mathrm{t}} i^{n+1} \cdot \left\{ \begin{array}{l} 1 + \sum_{p=0}^{(n-1)/2} \frac{n!}{(2p+1)!\left[n-(2p+1)\right]!} \left(\frac{B_{\mathrm{ext}}}{B_0}\right)^{2p+1} \cdot \frac{2^{p+1} \cdot p!}{\pi \prod_{q=0}^{2p+1} (2q+1)} \\ + \sum_{p=0}^{(n-1)/2-1} \frac{n!}{(2p+2)!\left[n-(2p+2)\right]!} \left(\frac{B_{\mathrm{ext}}}{B_0}\right)^{2p+2} \left(\frac{1}{2}\right)^{2p+2} \cdot \frac{(2p+2)!}{\left[(p+1)!\right]^2} \end{array} \right\} \tag{4.39}$$

$$P_{\mathrm{dyn}} = 4wfLI_{\mathrm{t}}i\left(B_{\mathrm{ext}}-B_{\mathrm{th}}\right)+E_0LI_{\mathrm{t}}i^{n+1}\cdot\left\{\begin{array}{l}1+\displaystyle\sum_{p=0}^{(n-1)/2}\frac{n!}{(2p+1)!\left[n-(2p+1)\right]!}\left(\frac{B_{\mathrm{ext}}}{B_0}\right)^{2p+1}\cdot\frac{2^{p+1}\cdot p!}{\pi\displaystyle\prod_{q=0}^{2p+1}(2q+1)}\\ +\displaystyle\sum_{p=0}^{(n-1)/2-1}\frac{n!}{(2p+2)!\left[n-(2p+2)\right]!}\left(\frac{B_{\mathrm{ext}}}{B_0}\right)^{2p+2}\left(\frac{1}{2}\right)^{2p+2}\cdot\frac{(2p+2)!}{\left[(p+1)!\right]^2}\end{array}\right\} \tag{4.40}$$

To verify the correctness of the proposed full-range formulation, both numerical modelling and experimental methods have been adopted. In addition, based on the time-averaged DC flux-flow resistance term mentioned in [220], P_{dyn} can also be fitted by

$$P_{\mathrm{dyn}} = 4wfLI_{\mathrm{t}}i\left(B_{\mathrm{ext}}-B_{\mathrm{th}}\right)+LfI_{\mathrm{t}}^{\,n+1}\int_0^{1/f}\frac{E_0}{I_{\mathrm{c}}\left(\left|B_{\perp}\right|\right)^n}dt \tag{4.41}$$

(4.41) will be compared with (4.38) or (4.40) in the next section.

4.4.2 Formulation Validation

The numerical model of the HTS CC was developed by use of finite element method based on the ***T***-formulation. The experimental setup for measuring P_{dyn} has been introduced in Section 4.3.2. For the HTS CCs with different I_{c0} varying from 80 to 160 A while carrying I_{t} = 60 A, they are exposed to external AC magnetic fields with increasing amplitude between 10-500 mT. The simulated P_{dyn} (solid symbols) and the analytical results calculated by (4.13) (short dash lines), (4.33) (dash-dot lines), (4.34) (solid lines) as well as (4.37) (dash lines) are depicted together in Figure 4.4.2.

Figure 4.4.2 shows that there exists a cross-field between the $P_{\mathrm{dyn,l}}(B_{\mathrm{ext}})$ and $P_{\mathrm{dyn,nl}}(B_{\mathrm{ext}})$ curves, as mentioned above. Before the cross-field, $P_{\mathrm{dyn}}(B_{\mathrm{ext}})$ agrees well with (4.17), which shows a linear correlation. After the cross-field, $P_{\mathrm{dyn}}(B_{\mathrm{ext}})$ is in good accordance with (4.37), which is in the form of a summation of power functions. In general, the simulated $P_{\mathrm{dyn}}(B_{\mathrm{ext}})$ agrees well with (4.38) in the full magnetic field range. Although (4.41) also describes the non-linearity of P_{dyn}, it appears to be much larger in terms of value. (4.38) has been derived through a rigorous process, providing a more accurate result. Furthermore, (4.41) is given based on the estimation of the time-average DC flux flow resistance, which cannot intuitively account for the non-linearity of P_{dyn} in the form of a summation of power functions. With regards to the cross-field, it increases inversely with i. In fact, for a lower i the CC has a larger capacity to withstand the induced current by the external magnetic field, thus it will be harder for I_{t} to go beyond the real critical current $I_{\mathrm{c}}(\boldsymbol{B})$. Therefore, the cross-field increases with I_{c0}

for a fixed I_t, which complies with the $J_c(\boldsymbol{B})$ dependence and the conclusions drawn in Section 4.2.

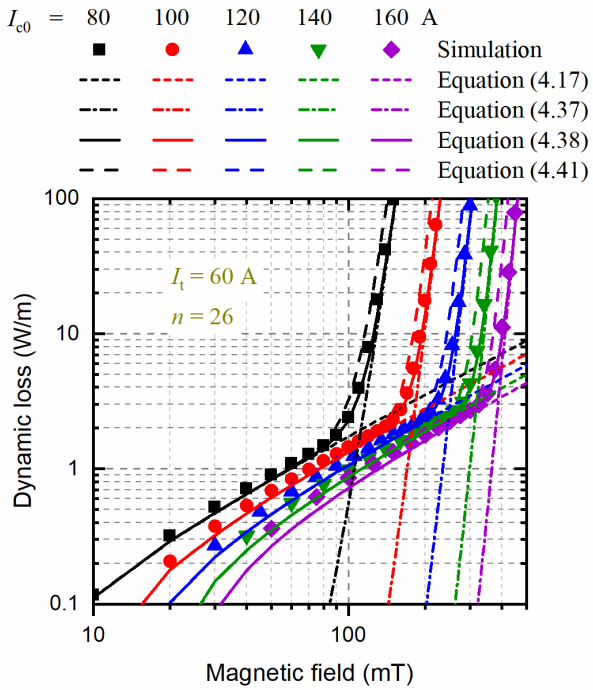

Figure 4.4.2 Dynamic loss of HTS CCs with different I_{c0} when changing B_{ext} from 0-500 mT, at 50 Hz.

Two different YBCO CCs have been tested, of which the specifications are shown in Table 7. The simulated P_{dyn} based on the ***T***-formulation, the measured experimental data, and the analytical results obtained by (4.17), (4.18), (4.37) [(4.39)], and (4.38) [(4.40)] for the two tested CC samples are presented together in Figure 4.4.3. It can be found that the experimental data is in good agreement with the simulation results and the proposed equations (4.38) and (4.40). The $P_{dyn}(B_{ext})$ curve exhibits an evident non-linearity with the increase of the external magnetic field, which is significantly different from the previously widely-adopted analytical equations (4.17) and (4.18). It should be pointed out that the relatively poor agreement between the simulation and experiment at low magnetic fields for the CC sample with I_{c0} = 87.67 A is due to its effective width, which is different from its physical width. As mentioned in [320], the effective width of the CC sample under study is ~12% less than the physical wire width due to the edge damage of the conductor during or after manufacture, normally in the slitting processes. However, it does not affect the validity of (4.38), in that it describes well the non-linearity of P_{dyn} under high magnetic fields.

Table 7. Specifications for tested HTS CCS

Symbols	Parameters	Value	
		Sample 1	Sample 2
w	half width of the CC	2 mm	2 mm
h_{HTS}	YBCO film thickness	1 μm	1 μm
I_{c0}	critical current in self-field	105.3 A	87.67 A
I_t	transport current	95 A	79 A
n	n-value	23	22
f	frequency of the AC field	26.62 Hz	67.89 Hz
B_0	magnetic field constant	0.135 T	0.17 T
T_o	operating temperature	77 K	
E_0	characteristic E-field	10^{-4} V/m	
μ_0	free space permeability	$4\pi \times 10^{-7}$ H/m	

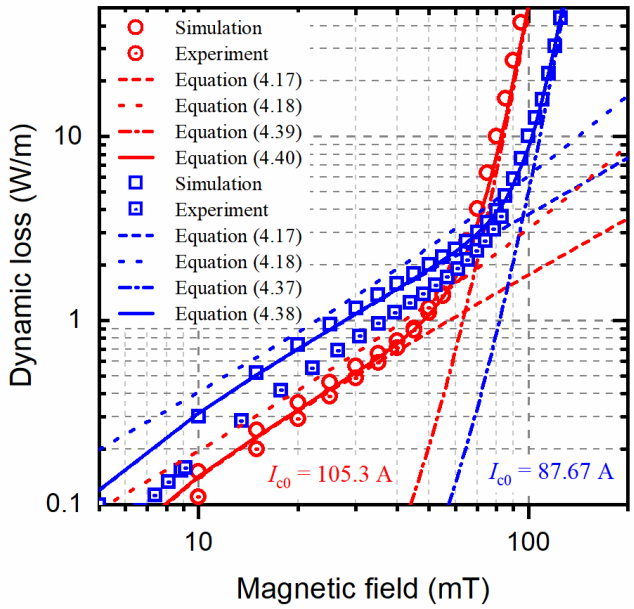

Figure 4.4.3 Simulated, measured and analytical dynamic loss of two different HTS CCs. The results in red are for the CC with I_{c0} = 105.3 A, and those in blue are for the CC with I_{c0} = 87.67 A. According to [320], the effective width of the CC with I_{c0} = 87.67 A has been chosen as $2w$ = 3.51 mm.

With respect to computational complexity, analytical methods generally require far less computing time and resources than the FEM based numerical modelling. In our case, (4.38) and (4.40) can be simply calculated in a few seconds using MATLAB. However, it requires more time and effort to build and run a FEM model. For example, the computational time to obtain P_{dyn} of a single HTS layer with the ***T***-formulation based numerical model is tens of seconds or longer, depending on the solving accuracy and number of mesh elements. Therefore, the proposed formulations (4.38) and (4.40) represent a more efficient and convenient way to calculate dynamic loss compared with numerical models.

4.4.3 Summary

Based on the $J_c(\boldsymbol{B})$ dependence and $\boldsymbol{E}$-$\boldsymbol{J}$ power law, through investigation of the characteristics of current density and magnetic flux density distributions in the dynamic region of HTS CCs, a new analytical expression for dynamic loss has been proposed. This expression considers a full-range of magnetic fields and load ratios. At low external fields and simultaneous low load ratios, dynamic loss is in a linear correlation with the external magnetic field. At both high magnetic fields and high load ratios, it is in the form of a summation of power functions. This new formulation can be used to characterize the non-linear variation of dynamic loss, which cannot be accurately predicted and explained by the existing analytical methods. The proposed formulae have been well verified by the $\boldsymbol{T}$-formulation based numerical modeling method and experiments, which can be achieved in MATLAB and dramatically save computational effort compared with numerical modelling methods. The cross-field has also been studied, of which the variation complies well with the $J_c(\boldsymbol{B})$ dependence. This work comprehensively demonstrates the variation of dynamic loss at different load ratios and magnetic fields. It can serve as a guide for loss controlling and avoiding quench in the application of HTS CCs, especially with regards to machine windings.

4.5 Demarcation Currents and Corner Field

The dependence of the nonlinearity between dynamic loss and the external magnetic field on n-value and critical current has been preliminarily analyzed in Section 4.3. A full-range formulation for dynamic loss has been derived based on Binomial Theorem and Euler's formula in Section 4.4. On the basis of Section 4.3 and 4.4, this section is to further investigate the influencing factors of the non-linearity of dynamic resistance and quantify its linear region. At first, an analytical formula for dynamic resistance based on the $J_c(\boldsymbol{B})$ dependence has been presented, which considers a wide range of transport current and external magnetic field. Then, combined with the definition of the threshold field and the existing linear equation of dynamic resistance, the lower demarcation current, I_{dl}, the upper demarcation current, I_{du}, and the corner field, B_{cor}, have been defined with explicit formulae. Next, with the aid of the $\boldsymbol{T}$-formulation based numerical modeling method, the dynamic resistances under different load rates and external magnetic fields have been simulated. Experimental measurements have been conducted accordingly at 77 K.

4.5.1 Analytical expressions of I_{du}, I_{dl}, and B_{cor}

Based on Equation (4.9), the linear equation for calculating the dynamic resistance of an HTS thin film can be formulated by

$$R_{\mathrm{dyn,l}} = \frac{4wfL}{I_{\mathrm{c0}}} \cdot \left(B_{\mathrm{ext}} - B_{\mathrm{th}} \right) \tag{4.42}$$

where B_{th} is the threshold field determined by (4.8).

As mentioned in Section 4.2, when dynamic resistance occurs, the dynamic region is occupied by the transport current with a width of $2iw$. Therefore, based on the $J_{\mathrm{c}}(\boldsymbol{B})$ dependence and $\boldsymbol{E}$-$\boldsymbol{J}$ power law, dynamic resistance can also be written as

$$R_{\mathrm{dyn}} = \frac{hLf}{I_{\mathrm{t}}^{\,2}} \int_0^{1/f} \int_{(1-i)w}^{(1+i)w} EJ dy dt = \frac{E_0 hLf}{I_{\mathrm{t}}^{\,2} J_{\mathrm{c0}}^{\,n}} \int_0^{1/f} \int_{(1-i)w}^{(1+i)w} J^{n+1} \left(1 + \frac{|B_{\perp}|}{B_0} \right)^n dy dt \tag{4.43}$$

where $B_{\perp}$ is the field component perpendicular to the wide surface of the CC, which is determined by both the external field $B_{\mathrm{ext}} \cdot \sin(2\pi ft)$ and the self field B_{s}.

Based on (4.43) and the derivation of dynamic loss in Section 4.4, the flux flow resistance proposed in [220] can be formulated by

$$R_{\mathrm{FF}} = \frac{E_0 L}{I_{\mathrm{t}}} i^{n+1} \cdot f_{\mathrm{avg}}\left(B \right) \tag{4.44}$$

In (4.44), $f_{\mathrm{avg}}(B)$ is the average magnetic field in the dynamic region, defined as (4.36). It should be noted that in (4.36) n is even. When n is odd, the upper bound of summation needs to be changed accordingly, as

$$\begin{aligned} f_{\mathrm{avg}}(B) = 1 + & \sum_{p=0}^{(n-1)/2} \frac{n!}{(2p+1)!\left[n-(2p+1) \right]!} \left(\frac{B_{\mathrm{ext}}}{B_0} \right)^{2p+1} \cdot \frac{2^{p+1} \cdot p!}{\pi \prod_{q=0}^{2p+1} (2q+1)} \\ & + \sum_{p=0}^{(n-1)/2-1} \frac{n!}{(2p+2)!\left[n-(2p+2) \right]!} \left(\frac{B_{\mathrm{ext}}}{B_0} \right)^{2p+2} \left(\frac{1}{2} \right)^{2p+2} \cdot \frac{(2p+2)!}{\left[(p+1)! \right]^2} \end{aligned} \tag{4.45}$$

It has been mentioned in [220] that, the dynamic resistance of HTS CCs should be contributed by both the linear hysteretic resistance and non-linear flux flow resistance. Therefore, the full-range formulation for dynamic resistance can be written as

$$R_{\mathrm{dyn}} = R_{\mathrm{dyn,l}} + R_{\mathrm{FF}} = \frac{4wfL}{I_{\mathrm{c0}}} \cdot \left(B_{\mathrm{ext}} - B_{\mathrm{th}} \right) + \frac{E_0 L}{I_{\mathrm{t}}} i^{n+1} \cdot f_{\mathrm{avg}}\left(B \right) \tag{4.46}$$

4.5.1.1 Demarcation currents

The $R_{\mathrm{dyn}}(I_{\mathrm{t}})$ curve is composed of two non-linear regions and one linear region, thus two turning points should be defined to characterize the transition between linear and non-linear

regions. I_{du} is named as the upper demarcation current, which denotes the transition from the linear region to the non-linear region at high currents. I_{du} is defined as the point where $R_{dyn,l}$ and R_{FF} share the same rate of change, i.e.,

$$\frac{\partial R_{dyn,l}}{\partial I_t}\Big|_{I_t=I_{du}} = \frac{\partial R_{FF}}{\partial I_t}\Big|_{I_t=I_{du}} \tag{4.47}$$

Therefore, we have

$$\frac{4.9284\mu_0 fL}{\pi I_{c0}} = \frac{nE_0 L}{{I_{c0}}^{n+1}} {I_{du}}^{n-1} \cdot f_{avg}(B) \tag{4.48}$$

I_{du} is thus derived as

$$I_{du} = \left[\frac{4.9284\mu_0 f \cdot {I_{c0}}^n}{n\pi E_0 \cdot f_{avg}(B)} \right]^{\frac{1}{n-1}} \tag{4.49}$$

I_{dl} is named as the lower demarcation current, which denotes the transition from the non-linear region to the linear region at low currents. To decide I_{dl}, another expression for B_{th} has been used here, as shown in (4.14). Given that (4.14) agrees well with (4.8) in the linear part, we define I_{dl} as the point where the changing rate of R_{dyn} decided by (4.42) and (4.8) is equal to that decided by (4.42) and (4.14), thus

$$\frac{\mu_0 fL}{\pi} \cdot \frac{I_{c0}}{{I_{dl}}^2} \cdot \ln\left(\frac{I_{c0}+I_{dl}}{I_{c0}-I_{dl}}\right) = 4.9284 \cdot \frac{\mu_0 fL}{\pi I_{c0}} \tag{4.50}$$

Therefore, I_{dl} is derived as

$$I_{dl} = 0.4347 I_{c0} \tag{4.51}$$

4.5.1.2 Corner field

We firstly introduced the corner field B_{cor} in Section 4.3 to characterize the non-linear variation of the $P_{dyn}(B_{ext})$ curve, which is defined as the field at which the changing rate of dynamic loss has increased by 10% compared with the linearly increasing part. In this section, as we have obtained the explicit formula for R_{dyn}, B_{cor} can thus be defined as the point where the changing rates of $R_{dyn,l}(B_{ext})$ and $R_{FF}(B_{ext})$ are the same, as shown in (4.52) when n is even. According to (4.52), we can quantify B_{cor} with an accurate value.

$$\sum_{p=0}^{n/2-1}\left\{\begin{aligned}&\frac{n!}{(2p)!\left[n-(2p+1)\right]!B_0}\left(\frac{B_{cor}}{B_0}\right)^{2p}\frac{2^{p+1}\cdot p!}{\pi\prod_{q=0}^{2p+1}(2q+1)}\\&+\frac{n!}{(2p+1)!\left[n-(2p+2)\right]!B_0}\left(\frac{B_{cor}}{B_0}\right)^{2p+1}\left(\frac{1}{2}\right)^{2p+2}\frac{(2p+2)!}{\left[(p+1)!\right]^2}\end{aligned}\right\}=\frac{4wf}{E_0 i^n} \tag{4.52}$$

When n is odd, the determination of B_{cor} follows

$$\begin{aligned}&\sum_{p=0}^{(n-1)/2}\frac{n!}{(2p)!\left[n-(2p+1)\right]!B_0}\left(\frac{B_{cor}}{B_0}\right)^{2p}\cdot\frac{2^{p+1}\cdot p!}{\pi\prod_{q=0}^{2p+1}(2q+1)}\\&+\sum_{p=0}^{(n-1)/2-1}\frac{n!}{(2p+1)!\left[n-(2p+2)\right]!B_0}\left(\frac{B_{cor}}{B_0}\right)^{2p+1}\left(\frac{1}{2}\right)^{2p+2}\cdot\frac{(2p+2)!}{\left[(p+1)!\right]^2}=\frac{4wf}{E_0 i^n}\end{aligned} \tag{4.53}$$

4.5.2 Validation of the defined demarcation currents and corner field

In order to validate the proposed equations, the ***T***-formulation based numerical modelling method and the experimental system to measure P_{dyn} and R_{dyn} mentioned in Section 4.3 have been adopted here. The specifications of the studied CC samples are shown in Table 7.

4.5.2.1 Demarcation currents

Under different external magnetic fields varying from 20 mT to 100 mT, with increasing load ratio ranging from 0.1 to 0.9, the simulated, measured, and calculated $R_{dyn}(I_t)$ curves for sample 1 are depicted together in Figure 4.5.1. It can be seen that, in general, the proposed equation (4.46) agrees well with the simulation and experiment, and all of them describe well the non-linearity of the $R_{dyn}(I_t)$ curves. It should be noted that the discrepancies between the experimental data and the analytical results calculated by (4.46) are attributed to the linear hysteretic resistance $R_{dyn,l}$, as shown in (4.42). Therefore, the effectiveness of the proposed equation (4.44) for calculating R_{FF} has not been affected. Generally, the mathematical expression of $R_{dyn,l}$ has been widely adopted to estimate the dynamic resistance of HTS CCs, and a bias of 10% is acceptable in industrial applications.

The calculated I_{dl} by (4.51) and I_{du} by (4.49) distinguish clearly the linear and non-linear sections. The linear region of the $R_{dyn}(I_t)$ curve is determined by the interval [I_{dl}, I_{du}], which shrinks with the increase of B_{ext}, since I_{du} increases inversely with B_{ext}, as shown in (4.49).

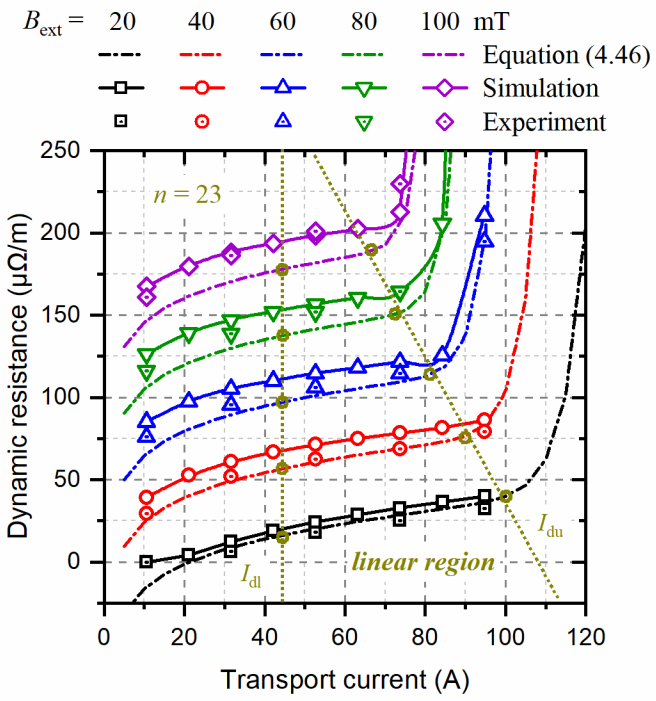

Figure 4.5.1 Comparison of the calculated, simulated and measured I_{dl}, I_{du} and R_{dyn}. The load rate i ranges from 0.1 to 0.9. The dash lines represent the analytical results calculated by (4.46), the solid lines with symbols denote the simulated results by the T-formulation based numerical method, and the symbols without lines are the experimental data.

I_{dl} is uniquely determined by the self-critical current, as shown in (4.51). However, I_{du} is a function with respect to the external field B_{ext}, self-field critical current I_{c0} and n-value. The correlations between I_{du} and B_{ext} under different n-value and I_{c0} have been illustrated in Figure 4.5.2 and Figure 4.5.3, respectively. From Figure 4.5.2, it can be seen that I_{du} increases inversely with B_{ext}, and the decreasing rate of I_{du} decreases with the increase of B_{ext}. In addition, for the same B_{ext}, the HTS CC with a higher I_{c0} has a higher I_{du}, which is in good accordance with the $J_c(\boldsymbol{B})$ dependence. In fact, a higher I_{c0} means a stronger capacity to withstand the inducted current by the externally applied magnetic field, i.e., it is harder for the DC transport current to exceed the real critical current $I_c(B)$, thus a higher demarcation current will be needed to cause the non-linearly fast rising of dynamic resistance. It should be noted that the differences regarding I_{du} for distinct I_{c0} shrink with the increasing B_{ext}, which also agrees well with the $J_c(\boldsymbol{B})$ dependence. Figure 4.5.3 shows the $I_{du}(B_{ext})$ curve under different n-values. It can be concluded that, in general, I_{du} decreases with the increase of n-value. However, the influence of n-value on I_{du} will be mitigated with the increasing n-value. For example, for B_{ext} = 100 mT, when n-value increases from 10 to 20, I_{du} is reduced from 77.5 A to 65 A with a difference of 12.5 A; however, when n-value increases from 20 to 30, I_{du} only decreases by 3

A. This phenomenon can be explained by (4.49), in that with the augment of *n*-value, *n*/(*n*-1) will approach 1, thus I_{du} will not be largely influenced by *n*-value.

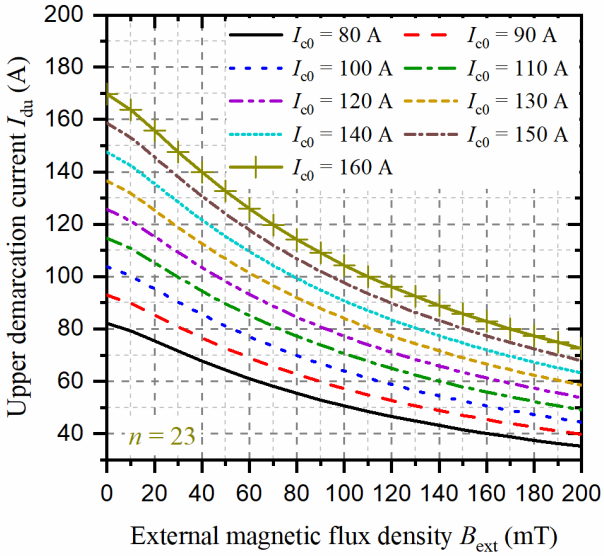

Figure 4.5.2 The correlation between I_{du} and B_{ext} for different I_{c0}. *n* = 23. B_{ext} varies from 0 to 200 mT. I_{c0} ranges from 80 A to 160 A.

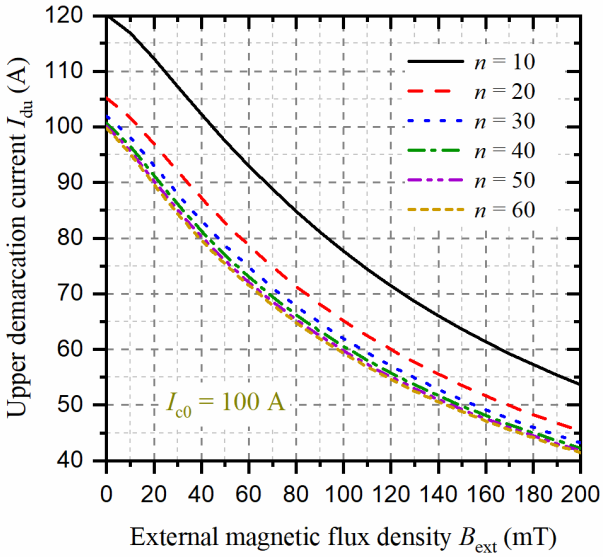

Figure 4.5.3 The correlation between I_{du} and B_{ext} for different *n*-value. I_{c0} = 100 A. B_{ext} varies from 0 to 200 mT. *n* ranges from 10 to 60.

4.5.2.2 Corner field

Figure 4.5.4 shows the $R_{dyn}(B_{ext})$ curves of the two tested CC samples, obtained by simulation, analytical equations (4.42) as well as (4.46), and experimental measurements, respectively. It can be concluded that the proposed (4.46), rather than (4.42), is in good accordance with the

simulated and measured results. The calculated B_{cor} by (4.52) and (4.53) identify well the transition of R_{dyn} from linear to non-linear sections.

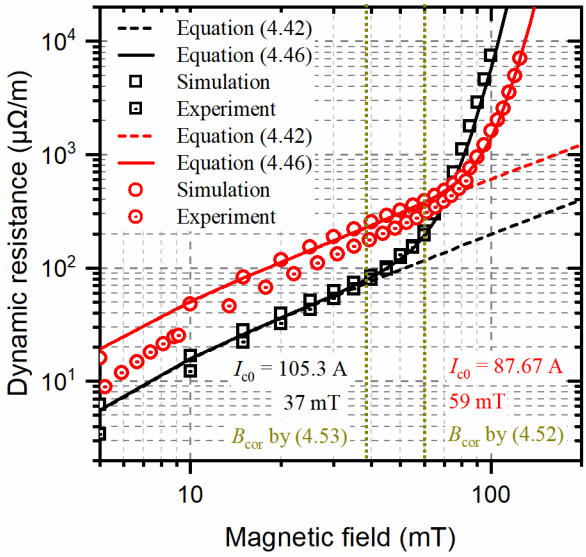

Figure 4.5.4 Comparison of the calculated, simulated and measured B_{cor} and R_{dyn}. The dash lines represent the analytical results calculated by (4.42), the solid lines denote the calculated results by (4.46), the hollow symbols are the simulated results by the *T*-formulation based numerical method, and the symbols with dots inside are the experimental data. i = 0.9. B_{ext} varies from 5 mT to 100 mT. For the CC sample with I_{c0} = 87.67 A, its effective width $2w$ = 3.51 mm [320].

According to (4.52) and (4.53), it can be found that corner field B_{cor} mainly depends upon two parameters, namely the initial load ratio i and n-value. To intuitively display the $B_{cor}(i, n)$ dependence, taking the sample 1 as an example, the variation of B_{cor} with respect to i under different n-values is shown in Figure 4.5.5. In general, according to Figure 4.5.5, B_{cor} increases inversely with i and n. In fact, for an HTS CC with a higher i, under the influence of the external magnetic field, it is easier for the real load ratio $I_t/I_c(\boldsymbol{B})$ to become greater than 1 because of the $J_c(\boldsymbol{B})$ dependence. In this case, the CC does not need a high B_{ext} to reach the critical-state, so its dynamic resistance can attain the corner point with a lower B_{cor} and then increase rapidly in a non-linear way. As shown in (4.43)-(4.46), the non-linear variation of dynamic resistance is in the form of a summation of power functions, of which the power indexes are decided by n-value. A higher n-value means a higher changing rate of dynamic resistance, which leads to a lower transition point from the linear region to the non-linear section. Therefore, with the increase of n-value, B_{cor} will be reduced. Furthermore, it should be pointed out that B_{cor} decreases more and more slowly with the increase of both i and n, so there exist no evident differences regarding B_{cor} in the cases where $i > 0.6$ and $n > 40$.

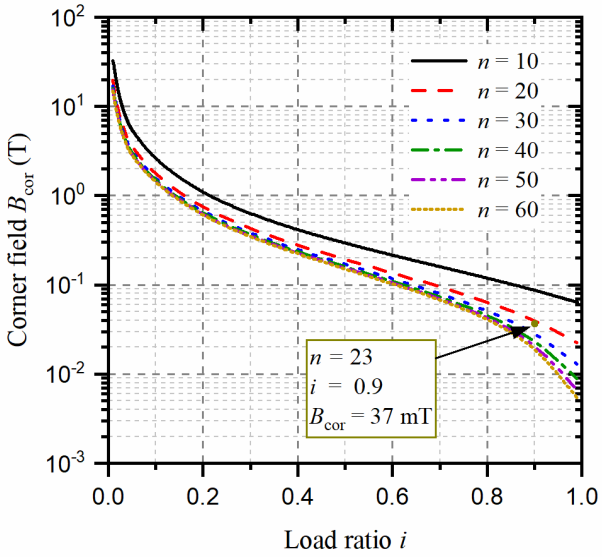

Figure 4.5.5 The correlation between B_{cor} and i for different n-value. I_{c0} = 105.3 A. i varies from 0 to 1. n ranges from 10 to 60.

4.5.3 Summary

Section 4.5 has defined three new parameters to characterize the variation properties of dynamic resistance for HTS CCs, namely the lower demarcation current, I_{dl}, the upper demarcation current I_{du}, as well as the corner field, B_{cor}. Analytical expressions for I_{dl}, I_{du}, B_{cor} have been prosed, which have been well validated by the ***T***-formulation based numerical modelling method and experimental measurements.

(1) I_{dl} is the turning current characterizing the transition of the $R_{dyn}(I_t)$ curve from the non-linear region to the linear section. I_{dl} is in a positive linear correlation with the self-field critical current I_{c0}, with $I_{dl} = 0.4347 I_{c0}$.

(2) I_{du} is the turning current characterizing the transition of the $R_{dyn}(I_t)$ curve from the linear region to the non-linearly fast rising section. I_{du} increases positively with I_{c0}, but inversely with B_{ext} and n-value. The influence of n-value on I_{du} will be mitigated with the increasing n-value, especially when n-value is greater than 30.

(3) B_{cor} is the turning magnetic flux density characterizing the transition of the $R_{dyn}(B_{ext})$ curve from the linear section to the fast rising region in the form of a summation of power functions. B_{cor} is in a genitive correlation with both the initial load ratio i and n-value, and it decreases more and more slowly with the increase of both i and n-value, especially when $i > 0.6$ and $n > 40$.

Both the proposed demarcation currents and corner field characterize well the non-linearity of dynamic resistance, which provides a significant reference for accurate loss controlling in HTS magnets, electric rotating machines, and flux pumps, etc.

4.6 Conclusion

Given that dynamic loss is crucial for evaluating the performance of HTS field windings in superconducting machines, this chapter has investigated the influence of the intrinsic properties of 2G HTSC (self-field critical current and *n*-value) on the dynamic loss of HTS CCs, proposed a novel full-range equation to calculate the dynamic loss and dynamic resistance, and defined three new parameters, namely lower demarcation current, upper demarcation current, as well as corner field, to describe the non-linearity of dynamic resistance. By comprehensively demonstrating the variation of dynamic loss and dynamic resistance through rigorous theoretical derivation, this chapter further adds upon the existing knowledge regarding the interaction of dynamic loss and dynamic resistance with transport current and magnetic field, which is particularly significant for accurate loss controlling in HTS magnets, rotating machines, and flux pumps.

Chapter 5. Frequency dependence of AC loss in HTS CCs, stacks, coils, and curved TFSs

5.1 Introduction

With the extension of superconducting applications, HTS CCs can be put into some complex electromagnetic environments, which could be composed of abundant frequency elements. For example, in superconducting machines, there exist some inevitable high-frequency harmonics. Aerospace generators and motors operate at very high speeds (7-50 krpm), then the superconductors in HTS machines ought to be capable of functioning in high-frequency magnetic fields (~0.2-2 kHz) [15]. HTS wireless power transfer is an emerging technology, and the commonly used resonance frequencies for electric vehicle chargers are within 20-100 kHz [321-322]. In these cases, HTS CCs may show unexpected performance distinguished from low frequency occasions. However, the detailed electromagnetic properties of HTS CCs under high-frequency or complex magnetic environments are still unclear. To quantitatively analyse the electromagnetic performance of HTS CCs, numerical methods have become popular tools, not only because of their conveniences over experiments but also the fact that only numerical models allow linking the losses of the HTS parts to their geometrical arrangement inside the equipment [127, 137]. This chapter is to investigate the frequency dependence of electromagnetic properties of HTS CCs, stacks, coils, and curved TFSs (which can serve as the field sources in superconducting machines) through numerical modelling, and therefore, to provide comprehensive analyses with the multilayer models reflecting their actual structures.

5.2 Frequency Dependence of AC Loss in a Single HTS CC

As mentioned by [127], the developed numerical models for HTS CCs can be applied in all situations characterized by a time-varying electromagnetic environment. In order to anticipate the variation of electromagnetic properties with frequency, AC signals are the most ideal electromagnetic environment because of their single-frequency characteristic with the sinusoidal waveform. In this section, the variation of AC magnetization loss and transport current loss within the frequency range from 50 Hz to 1 MHz has been simulated by the 4 different numerical models developped in Chapter 3, namely the ***T***-formulation based thin film

model, the ***T***-formulation based multilayer model, the ***H***-formulation based multilayer model, and the ***H***-formulation based homogenization model. The simulated results ontained by the four models have been compared. In addition, the effectiveness of the thin film approximation has been discussed with the variation of frequency. Besides, the frequency dependence of AC loss in each layer has been clarified. The current and magnetic flux density distribution in different layers have also been analysed in detail. Finally, a comparison between the ***T***- and ***H***-formulation based numerical models in terms of computional time and applicable frequency bands has been presented.

The specifications of the studied HTS CC sample are shown in Table 8, which is manufactured by SuperPower, Inc. It is 4 mm wide comprising a 1-μm thin film of YBCO, based on which the numerical models have been established.

Table 8. Specification for the studied HTS CC [163, 323-324]

Symbols	Quantity	Value
w	YBCO tape width	4 mm
h_{HTS}	YBCO film thickness	1 μm
h_{Cu}	Copper thickness	40 μm
h_{Ag}	Silver thickness	2 μm
h_{sub}	Substrate thickness	50 μm
σ_{Cu}	Copper conductivity at 77 K	5.076×10^8 S/m
σ_{Ag}	Silver conductivity at 77 K	3.704×10^8 S/m
σ_{sub}	Substrate conductivity at 77 K	8×10^5 S/m
t	YBCO tape thickness	0.1 mm
μ_0	Free space permeability	$4\pi \times 10^{-7}$ H/m
n	Power-law exponent	38
I_{c0}	Critical current in self field	99.23 A
E_0	Characteristic E-field	10^{-4} V/m
B_0	Magnetic field constant	42.65 mT

5.2.1 AC magnetization loss

Firstly, the frequency dependence of AC magnetization power loss per unit length (W/m) for the HTS CC has been studied. In this case, the transport current $I_{\mathrm{t}} = 0$ A. The external magnetic flux density perpendicular to the wide surface of the CC, B_{ext}, is chosen as 0.1 T, and the frequency varies from 50 Hz to 1 MHz.

Figure 5.2.1 shows the correlation between the magnetization loss and the frequency of the

externally applied magnetic field, in which a base-10 log scale is used for both axes. Here, the Brandt equation, shown as (2.9), is used for calculating the magnetization loss. It can be seen that, in general, the results calculated by the two single-layer models, namely the ***T***-formulation based thin film model and the ***H***-formulation based homogenization model, have good agreement with the Brandt equation. Similarly, the results obtained by the two multilayer models also comply with each other. However, there exists an obvious difference between the single-layer models and the multilayer models. For the single-layer models, the magnetization loss and the frequency of the magnetic field are in a linear correlation within the base-10 log scale. In other words, the magnetization loss increases more rapidly with the increase of frequency. In contrast, before 200 kHz, the calculated losses by the multilayer models are higher than those by the single layer models; however, after 200 kHz, the former are lower than the latter. This distinction between the two types of models is closely related to the loss distribution in different layers of the HTS CC, as shown in Figure 5.2.2 and Figure 5.2.3.

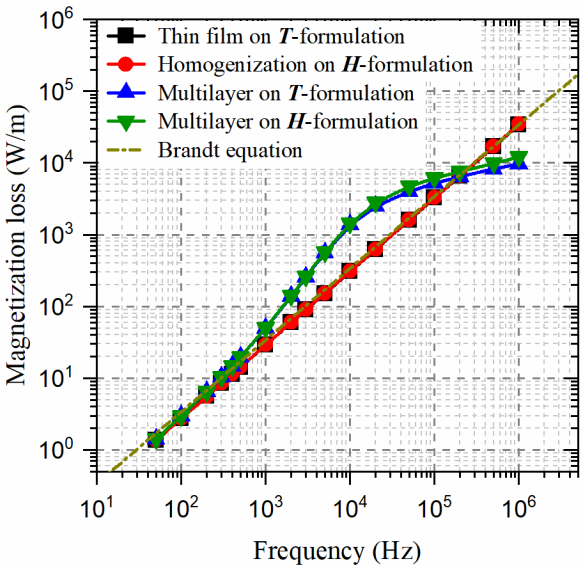

Figure 5.2.1 The correlation between the AC magnetization loss and the frequency of the external magnetic field, calculated by the 4 different numerical models. The amplitude of the external magnetic flux density is set as 0.1 T, and the frequency varies from 50 Hz to 1 MHz.

Figure 5.2.2 shows the frequency dependence of the magnetization loss in each layer. It can be found that, in general, the loss in each layer is in a positive correlation with frequency, but the loss in the copper stabilizers increases much faster than that of the HTS layer. Figure 5.2.3 shows the ratio of loss per layer to the total loss, calculated by the two multilayer models. Below 100 Hz, the loss generated in the HTS layer accounts for the majority of the total loss, with a loss ratio greater than 90%. However, with increasing frequency, the loss ratio of the HTS layer will decrease rapidly down to 50% at approximately 1.2 kHz. On the contrary, the

loss ratio for the copper stabilizer increases fast with frequency. After 1.2 kHz, the loss in the copper stabilizers begins to dominate. When the frequency is higher than 100 kHz, more than 85% of the total losses are generated in the copper stabilizers. In general, losses in the silver overlayer and the substrate only accounts for a very small fraction of the total loss.

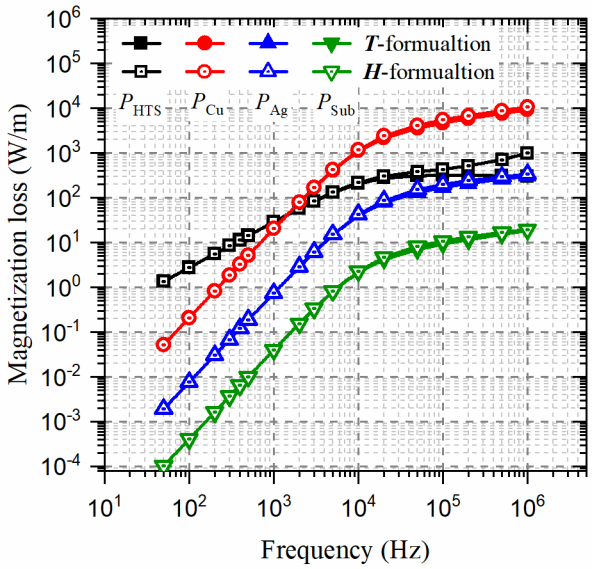

Figure 5.2.2 The correlation between the magnetization loss of each layer and the frequency of the external magnetic field, calculated by the 2 multilayer models. The amplitude of the external magnetic flux density is set as 0.1 T, and the frequency of the Magnetic field varies from 50 Hz to 1 MHz.

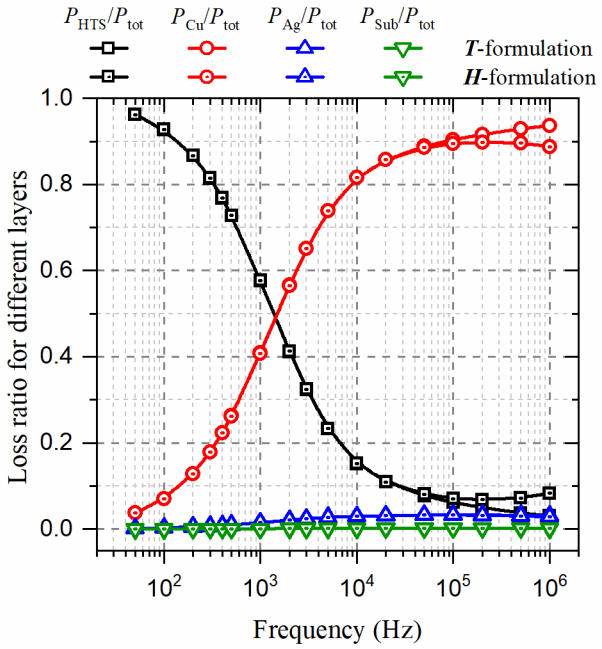

Figure 5.2.3 Ratio of magnetization loss per layer to the total loss, calculated by the 2 multilayer models. The amplitude of the external magnetic flux density is set as 0.1 T, and the frequency varies from 50 Hz to 1 MHz.

To further clarify the reasons for the loss change in each layer, the current density distribution and magnetic flux density profile of the copper and HTS layers are presented in Figure 5.2.4 and Figure 5.2.5, respectively.

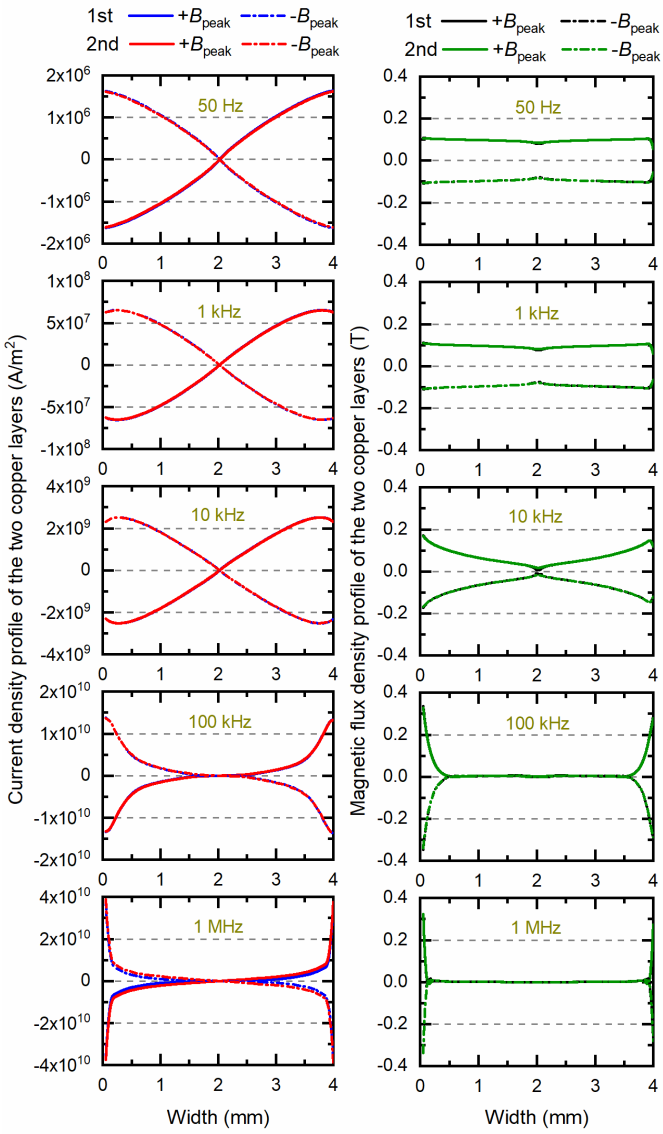

Figure 5.2.4 Current density and magnetic flux density distribution of the copper layer along the width of the HTS CC, calculated by the *T*-formulation based multilayer model. The frequency varies from 50 Hz to 1 MHz.

Figure 5.2.4 shows the current density and magnetic flux density profiles of the two copper layers (the 1st layer denotes the upper one, and the 2nd layer means the bottom one) with increasing frequency when the external flux density attains peak values. It is clearly seen that the highest current density increases from 1.6×10^6 A/m^2 at 50 Hz to approximately 4×10^{10} A/m^2 at 1 MHz with a change of almost 2.5×10^4 times, and the highest magnetic flux

density triples from 0.1 T at 50 Hz to 0.3 T at 1 MHz. Furthermore, the skin effect is well demonstrated with the rise of frequency, as the current and the magnetic field are driven towards the sides of the copper stabilizers. For example, at 50 Hz, the magnetic flux density is almost evenly distributed along the width of the layer; however, when the frequency reaches 1 MHz, no magnetic field penetrates into the middle section and both the current and the magnetic field are driven to both ends.

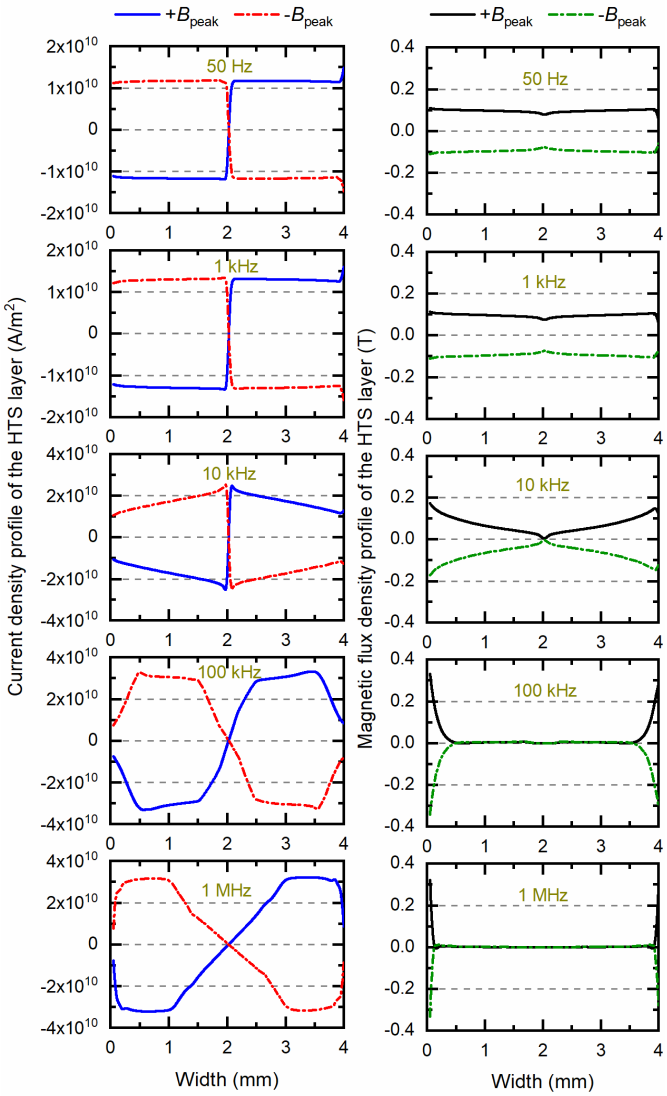

Figure 5.2.5 Current density and magnetic flux density distribution of the HTS layer along the width of the HTS CC, calculated by the *T*-formulation based multilayer model. The frequency varies from 50 Hz to 1 MHz.

Figure 5.2.5 shows the current density and magnetic flux density profiles of the HTS layer at rising frequencies. As shown, the highest current density increases from 1.2×10^{10} A/m^2 at 50 Hz to 3×10^{10} A/m^2 at 1 MHz with a change of around 2.5 times, and the highest magnetic flux

density triples from 0.1 T at 50 Hz to 0.3 T at 1 MHz. The current density profiles show a similar trend compared with the copper stabilizers in Figure 5.2.4, however, not as pronounced. Additionally, from 50 Hz to 100 kHz, the general current density in the HTS layer is much higher than that in the copper layers, in that σ_{HTS} is far superior to σ_{Cu}. However, at 1 MHz, the peak current density in the copper stabilizer becomes larger than that in the HTS layer, as the skin effect pushes the current to the outer layers of the CC. It should be noted that the current density in the copper stabilizers at high frequencies, e.g., 1 MHz, is far beyond the normal current carrying capacity of the copper material. In this case, damage to the HTS CC structure may occur due to excessive heat production.

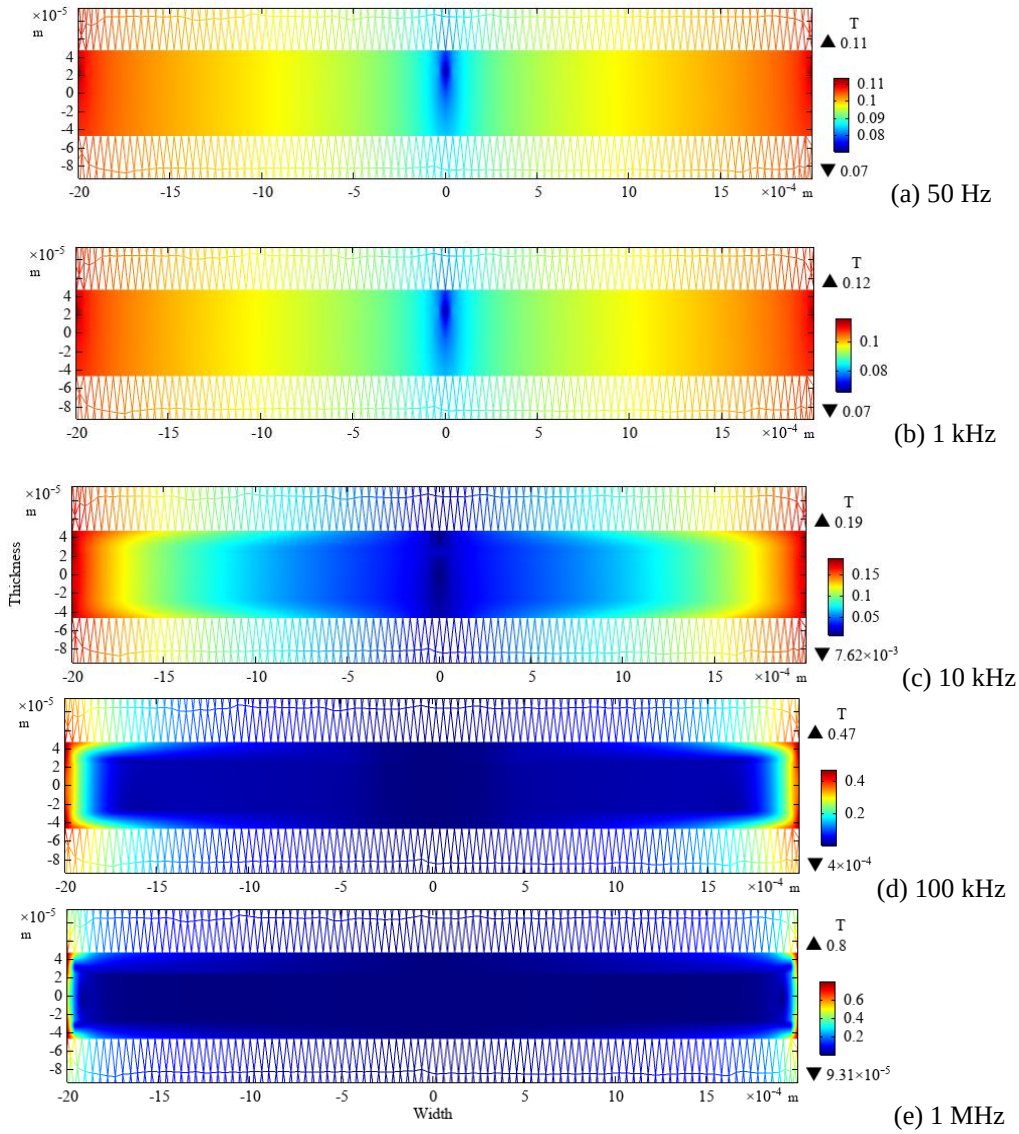

Figure 5.2.6 Magnetic flux density distribution of the HTS CC at the phase of 3π/2 when exposed to an AC magnetic field, with the frequency varying from 50 Hz to 1 MHz. These results are simulated by the *H*-formulation based multilayer model in COMSOL Multiphysics, and the amplitude of the applied magnetic flux density is set as 0.1 T.

In summary, at low frequency bands, e.g., 50 Hz, most magnetization loss is generated in the HTS layer because most of the current is concentrated there. However, with the increase in frequency, the distinction in current density of different layers gets smaller, In addition, the resistivity of the copper stabilizers is much larger than that of the HTS layer, and thus more loss will be generated in the copper stabilizers. When the frequency continues to grow, e.g., near 1 MHz, the skin effect plays a dominant role, i.e., the current will move towards the outer layers of the CC and the magnetic flux density will be driven to both ends, thus most loss will be concentrated in the copper stabilizers.

To show the variation of the magnetic flux density in the HTS CC more intuitively, the simulated results by the ***H***-formulation based multilayer model in COMSOL Multiphysics are presented in Figure 5.2.6. It can be seen that the magnetic flux moves towards both ends of the CC with the increase in frequency. Figure 5.2.6 complies well with the conclusions drawn before.

5.2.2 AC transport current loss

In the same way, the frequency dependence of AC transport current power loss per unit length (W/m) of the chosen HTS CC has been investigated. In this case, the external magnetic flux density is set to 0 T. The amplitude of the AC transport current I_t = 50 A, and the frequency varies from 50 Hz to 1 MHz.

Figure 5.2.7 shows the correlation between the transport current loss and the current frequency, in which a base-10 log scale is used for both two axes. The Norris equation for calculating transport current loss is formulated as (2.10). According to Figure 5.2.7, in general, the total loss is in a positive correlation with frequency. Before 10 kHz, there exists a difference of less than 5% among the calculated results by the four numerical models. However, between 10 kHz and 500 kHz, the losses simulated by the multilayer models are higher than those obtained from the single-layer models. After 500 kHz, the losses calculated by multilayer models become smaller than those by the single-layer models and Norris equation. Comparing Figure 5.2.7 and Figure 5.2.1, it can be seen that the distinction in simulation results caused by different models is less for transport current loss versus magnetization loss, especially at low frequency bands. In fact, the conductivity of the HTS layer is much higher than that of the other layers, thus the transport current will mainly flow through the HTS layer and most of the loss will be generated there. As a result, as far as the transport current loss is concerned, at frequency bands below 10 kHz, the thin film approximation for the HTS CC is still applicable.

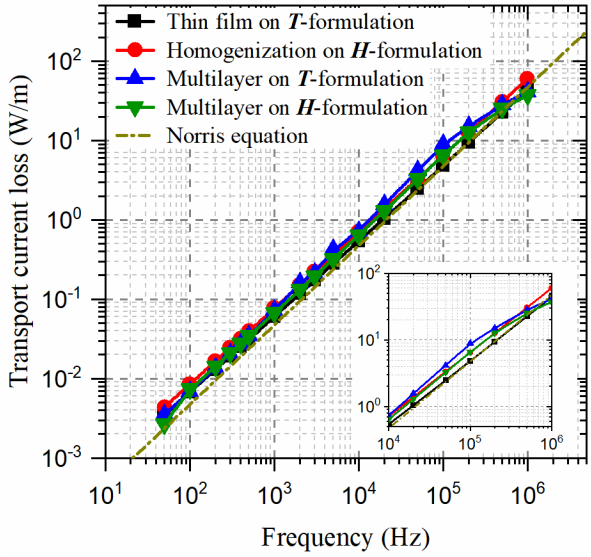

Figure 5.2.7 The correlation between the transport current loss of the YBCO CC and the current frequency, calculated by 4 different numerical models. The amplitude of the current is set as 50 A, and the frequency of the current varies from 50 Hz to 1 MHz.

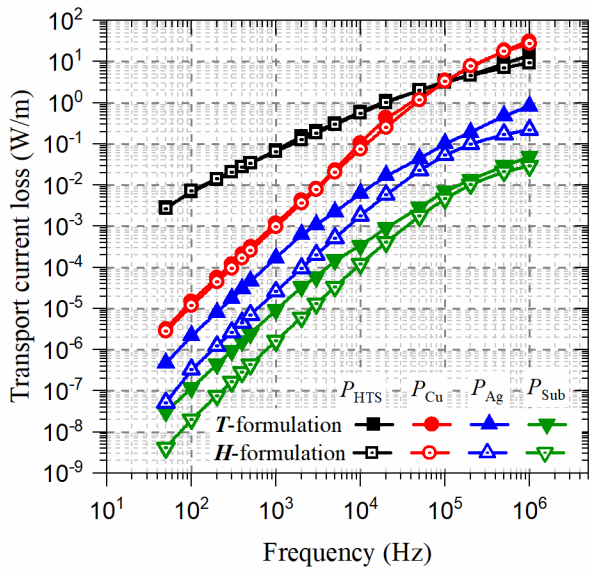

Figure 5.2.8 The correlation between the transport current loss in each layer and the current frequency, calculated by the 2 multilayer models. The amplitude of the applied transport current is set as 50 A, and the frequency of the current varies from 50 Hz to 1 MHz.

Figure 5.2.8 shows the frequency dependence of the AC transport current loss in each layer. Figure 5.2.9 presents the loss ratio curve for each layer with the variation of frequency. It can be found that, below 100 kHz, most of the loss is generated in the HTS layer. Furthermore, below 1 kHz, the HTS layer account for almost 100% of the total loss. However, above 100

kHz, the majority of losses are concentrated in the two copper layers. The losses in the silver overlayer and the non-magnetic substrate are always negligible compared to others. To further clarify the loss distribution in different layers, the current density and magnetic flux density profiles are presented in Figure 5.2.10 and Figure 5.2.11.

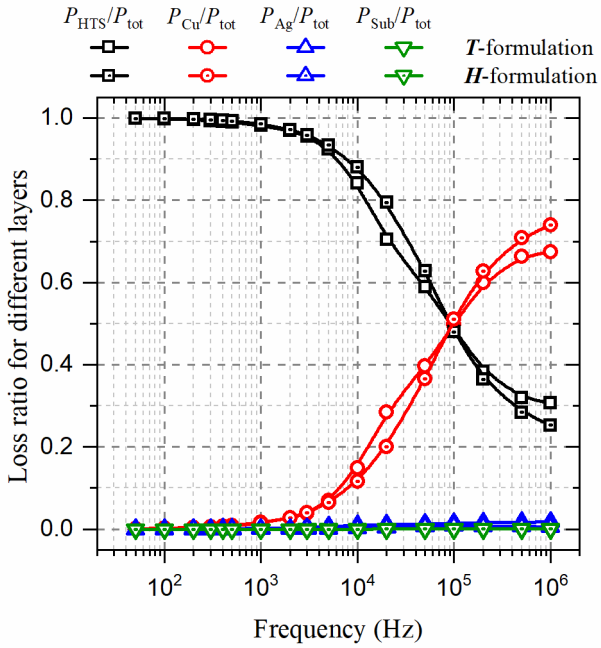

Figure 5.2.9 Ratio of transport current loss per layer to the total loss, calculated by the 2 numerical modeling methods. The amplitude of the current is set as 50 A, and the frequency varies from 50 Hz to 1 MHz.

Figure 5.2.10 shows the distribution of current density and magnetic flux density of the two copper stabilizers along the width of the HTS CC. For the first copper stabilizer, its highest current density increases from 3.5×10^5 A/m^2 at 50 Hz to 3.7×10^9 A/m^2 at 1 MHz with a change of approximately 1.06×10^4 times, and its largest magnetic flux density firstly increases from 18 mT at 50 Hz to almost 35 mT at 100 kHz, then reduces to 30 mT at 1 MHz. For the second copper stabilizer, its highest current density increases from 3.4×10^5 A/m^2 at 50 Hz to 3.8×10^9 A/m^2 at 1 MHz with a variation of approximately 1.12×10^4 times, and its largest flux density keeps increasing from 13 to 35 mT. Comparing the two stabilizers, it can be found that, at low frequency bands, i.e., below 100 kHz, the current density and the flux density of the first copper stabilizer are higher than those of the second one, but in high-frequency bands, e.g., 1 MHz, it is the opposite. This phenomenon is tightly related to the multilayer structure of the HTS CC. In fact, between the HTS layer and the first copper stabilizer, there is only a thin-film silver overlayer with a thickness of 2 μm; however, between the HTS layer and the second

copper stabilizer, there is a relatively thicker substrate of 50 μm. Therefore, the induced current and magnetic field are less in the second copper layer at low frequency bands. However, with the increase in frequency, e.g., at 1 MHz, the highest current density and flux density in the second copper stabilizer turn higher than those of the first one, which is a superimposed effect tightly linked to the electromagnetic properties of other layers under the influence of the skin effect.

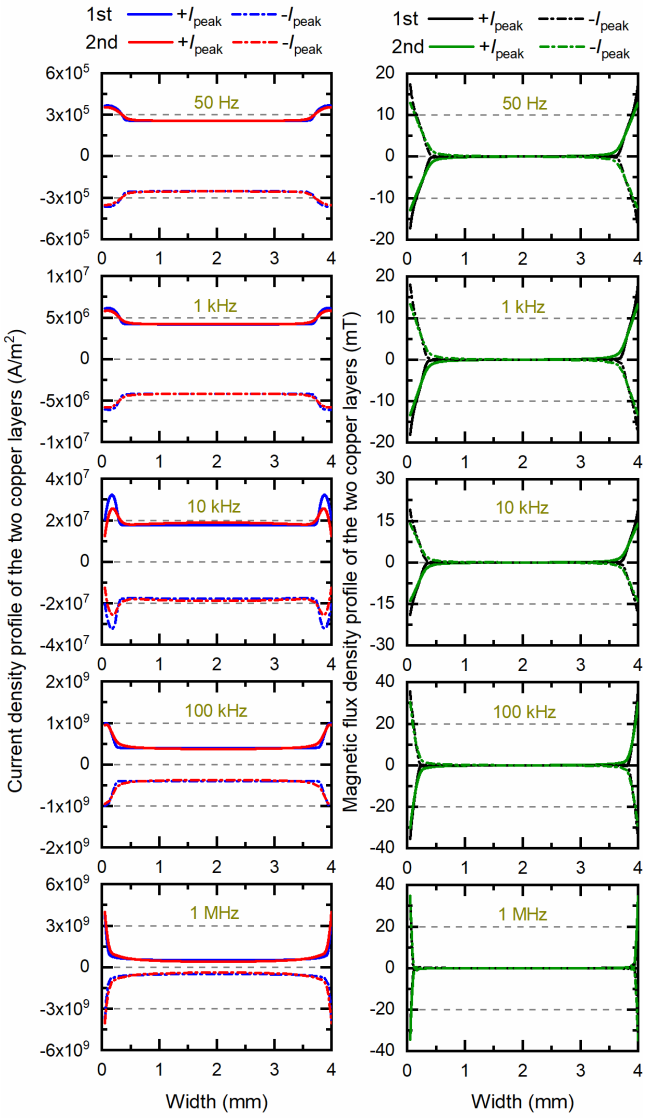

Figure 5.2.10 Current density and magnetic flux density distribution of the two copper layers along the width of the CC when carrying an AC transport current, calculated by the *T*-formulation based multilayer model. The amplitude of the current is set as 50 A, and *f* varies from 50 Hz to 1 MHz.

Figure 5.2.11 presents the current density and magnetic flux density profiles of the HTS layer. Overall, the amplitude of the highest current density does not vary much with frequency, but

the current tends to move towards the two sides of the layer. The amplitude of the flux density firstly increases from 18 to 37 mT then decreases to 34 mT, because the rise of the current density in other layers will, in turn, restrain the flux increase in the HTS layer. At high frequencies, under the skin effect, most of the current will be concentrated in the two sides of the CC, so is the magnetic field. Therefore, there are no obvious differences for the copper stabilizers and the HTS layer as far as the flux density distribution is concerned, except that the flux density in the HTS layer is marginally higher.

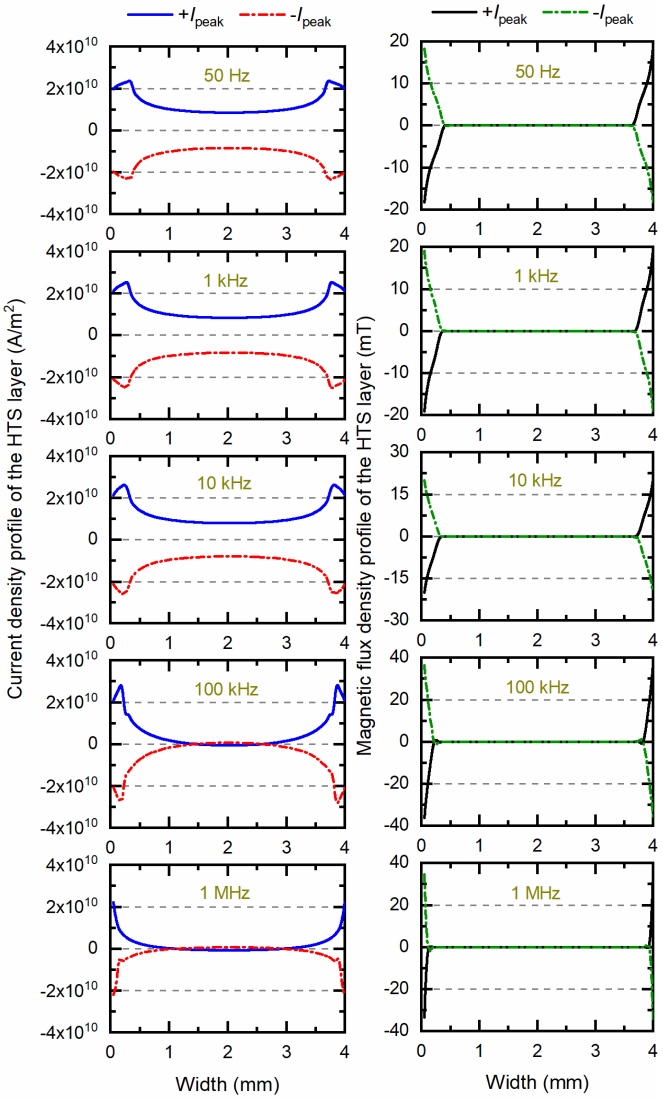

Figure 5.2.11 Current density and magnetic flux density distribution of the HTS layer along the width of the CC when carrying an AC transport current, calculated by the *T*-formulation based multilayer model. The amplitude of the current is set as 50 A, and the frequency varies from 50 Hz to 1 MHz.

It should be noted that for low frequency bands, e.g., below 100 kHz, there is an obvious distinction between the HTS layer and other layers as far as current density is concerned.

Therefore, the current in the HTS layer is the dominant factor to affect the electromagnetic property of each layer. However, with the increase in frequency, under the influence of the skin effect, the total current in the copper stabilizers achieves a high value comparable with the current in the HTS layer, taking into account the thickness ratios. For instance, at 1 MHz, the highest current density for the copper layer reaches approximately 3.8×10^9 A/m^2, which is 1/5 of the highest current density in the HTS layer. However, the total thickness ratio of the copper stabilizers to the HTS layer is 40. Additionally, the interaction amongst different layers determine together the electromagnetic properties for all layers. It is also the reason for which under the superimposed effect of different layers, the current density of the second copper layer is higher than the first one at 1 MHz, as mentioned before.

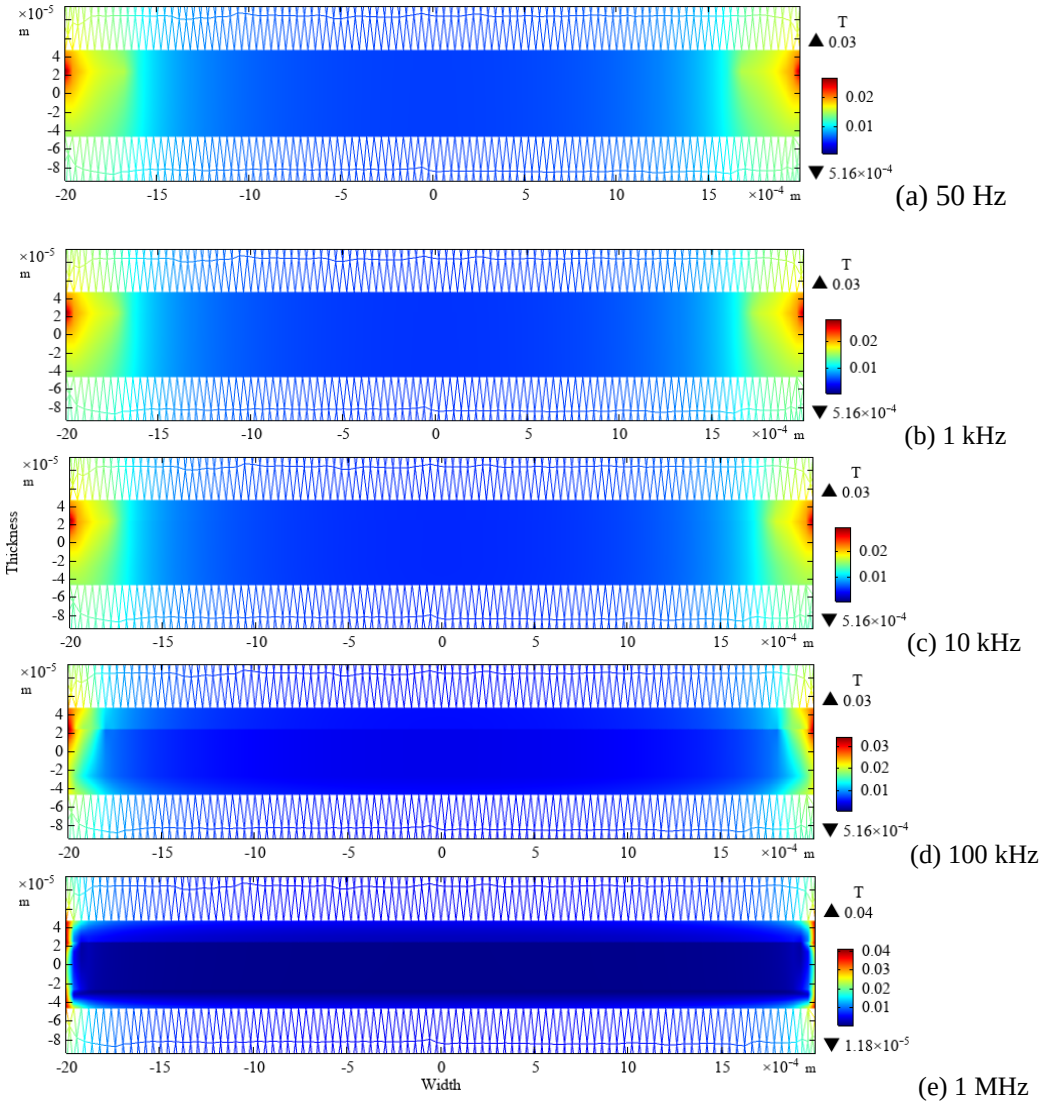

Figure 5.2.12 Magnetic flux density distribution of the HTS CC at the phase of 3π/2 when carrying an AC transport current, with the frequency varying from 50 Hz to 1MHz. These results are simulated by

the *H*-formulation based multilayer model in COMSOL Multiphysics, and the amplitude of the carried current is 50 A.

To exhibit the magnetic field distribution in the HTS CC more intuitively, the results obtained by the ***H***-formulation based multilayer model in COMSOL Multiphysics have been shown in Figure 5.2.12. It can be seen that the magnetic flux moves towards both ends of the CC with the increase in frequency. Figure 5.2.12 agrees well with the conclusions drawn before.

5.2.3 Average resistance

On the basis of the above analyses, it can be concluded that, the skin effect plays an increasingly important role with increasing frequency for the current and magnetic field distribution in HTS CCs. The rearrangement of current density inside the CC is directly linked to the variation of resistance in different layers.

The general formula for the skin depth is [325]

$$\delta = \sqrt{\frac{2}{\sigma\omega\mu}} \tag{5.1}$$

where σ is the conductivity of the conductor, ω denotes the angular frequency, and μ represents permeability of the conductor.

At low temperatures and simultaneous high frequencies, when the electronic mean free path becomes comparable with the generally calculated skin depth determined by (5.2.1), the anomalous skin effect should be considered [326]. The minimum skin depth (when the frequency attains the maximum 1 MHz) can be calculated as

$$\delta_{\min}\big|_{\mathrm{Cu}} = \sqrt{\frac{1}{\sigma_{\mathrm{Cu}}\pi f \mu_0}}\Big|_{f=1\ \mathrm{MHz}} = 22.34\ \mu\mathrm{m} \tag{5.2}$$

The adopted copper in HTS CCs is electrolytic copper, which is impure. The higher-purity copper has a higher conductivity at cryogenic temperatures compared with impure ones. As stated in [327], the resistivity for high-purity copper is inversely proportional to its mean free path. Therefore, it can be concluded that, for electrolytic copper its mean free path is smaller than that of high-purity copper. At 4.2 K, the resistivity of the 4-N high-purity copper is approximately 1.3×10^{-10} Ω·m and its mean free path is about 5 μm [327]. According to the temperature dependence of electron mean free path mentioned in [328], in our studies, at T = 77 K, the mean free path for impure electrolytic copper is far smaller than the minimum skin depth of the stabilizers. Therefore, the anomalous skin effect can be neglected. In addition, as shown in [327], the resistivity for copper is no longer frequency dependent for T > 70 K. Hence,

it is reasonable to assume the conductivity of the cooper stabilizers to be constant at 77 K, as shown in Table 8.

Given that the current density in each layer is both time and position dependent, we define the equivalent resistance per unit length, R_{eq} (Ω/m) as the ratio between the power dissipation per unit length (W/m) and the square of the average current in the time domain across the cross section of each layer (A^2). Therefore, R_{eq} can be written as

$$R_{eq} = \frac{\frac{2}{T}\int_{T/2}^{T}\iint_{S}\frac{J^2}{\sigma}dSdt}{\left(\frac{2}{T}\int_{T/2}^{T}\iint_{S}JdSdt\right)^2} \tag{5.3}$$

where S is the cross-sectional area of the studied layer. The correlation between the equivalent resistance ratio, R_{HTS}/R_{Cu}, and frequency has been presented in Figure 5.2.13.

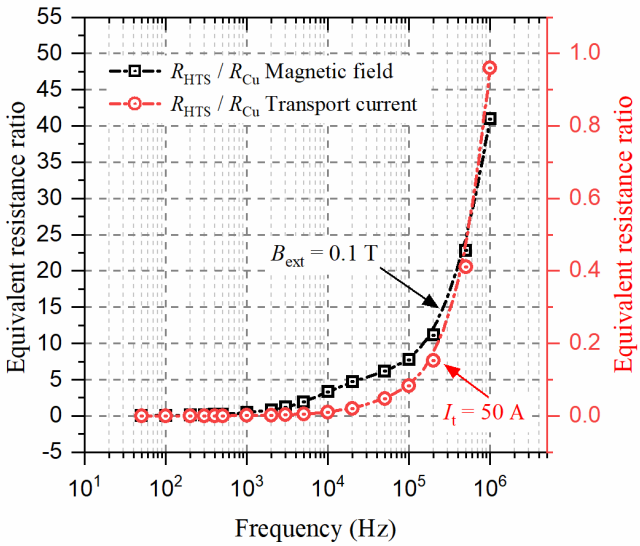

Figure 5.2.13 The variation of equivalent resistance ratio R_{HTS}/R_{Cu} with frequency, calculated by the T-formulation based numerical method. In the case of magnetization, B_{ext} = 0.1 T. For the case of transport current, I_t = 50 A.

It can be seen that, in general, the ratio between the equivalent resistance of the HTS layer and that of the copper stabilizers increases fast with frequency. For the case of magnetization, at low frequencies, e.g., f = 50 Hz, the resistance of the HTS layer is much less than that of the copper stabilizers, thus most of the induced current is concentrated in the HTS layer. However, when f goes beyond 30 kHz, due to the skin effect, the resistance of the HTS layer turns larger than the copper stabilizers, which accounts for the fact that the induced current begins to stay in the outer copper stabilizers and most losses will be generated there. In case of AC transport current, even though the resistance of the HTS layer stays below that of the copper stabilizers,

their difference shrinks rapidly with frequency. Therefore, when their resistances become comparable, a higher share of current will flow into the outer copper layers and most losses will be produced there. In general, the variation of resistance with frequency reflects well the current and loss distribution among different layers of HTS CCs.

5.2.4 Comparison of numerical models

According to Section 5.2.1 and 5.2.2, it can be found that, for different frequencies and loss studies, the four numerical models have distinct features. To better show their differences, some key characteristics have been summarized in Table 9.

Table 9. Comparison of the four numerical models

Numerical models	Formulation	Computational time*	Applicable frequency band	
			Magnetization	Transport current
Single-layer	$\boldsymbol{T}$	18 s	$f < 100$ Hz	$f < 10$ kHz
	$\boldsymbol{H}$ (*homoge.*)	72 s		
Multilayer	$\boldsymbol{T}$	357 s	0 Hz $\leq f \leq$ 1 MHz	
	$\boldsymbol{H}$	482 s		

*The computation time here represents the duration of each cycle for calculating the magnetization loss, with f = 50 Hz. The processor of the computer is Intel Xeon CPU E3-1230 v6 @ 3.5 GHz, with 16 GB RAM.

To compare the computational speed of the four models, the case of magnetization for one single tape has been taken as an example. The element number along the width of the tape is set as 60, and the frequency of the external magnetic field has been chosen as 50 Hz. It can be seen that, in general, the ***T***-formulation based numerical methods with FORTRAN 90 are faster than the ***H***-formulation based COMSOL modelling methods, especially for the two single-layer models. In addition, the single-layer models are much faster than the multilayer ones. However, it should be pointed out that the homogenization method has a significant advantage when studying stacks of tapes or superconducting coils, which can achieve 100 times faster than multilayer models as long as the number of tapes is high enough [163]. In the light of Table 9, when analysing the case of magnetization, the two single-layer models are only recommended when the frequency of the external magnetic field is less than 100 Hz, which have an error of less than 10 % compared with multilayer models. However, when it comes to the case of transport current, the single-layer models can be used in a relatively wide frequency band up to 10 kHz with an error of less than 10 %. After all, with the single-layer

numerical models, much computational time can be saved.

5.2.5 Summary

By use of four different numerical models, namely the ***T***-formulation based thin film model, the ***T***-formulation based multilayer model, the ***H***-formulation based multilayer model, as well as the ***H***-formulation based homogenization model, the variation of magnetization loss and transport current loss has been presented over a wide frequency range, from 50 Hz to 1 MHz. The single layer models based on the thin film approximation have proven to be inapplicable for magnetization loss at frequency bands above 100 Hz and for transport current loss at frequency bands over 10 kHz. In fact, at high-frequency bands the skin effect plays a dominant role, thus most current tends to move towards the copper layers and the magnetic fields will be driven to both ends of HTS CCs.

(1) With respect to magnetization loss, at low frequency bands below 1.2 kHz, most loss is generated in the HTS layer. However, above 1.2 kHz the loss of the copper layers accounts for the majority.

(2) Regarding transport current loss, the loss generated in the HTS layer dominates until 100 kHz, which is the reason for which at low frequency bands the single layer models and the multilayer models have a good agreement with each other. After 100 kHz, the loss in the copper layers becomes dominant.

With respect to numerical methods, the ***T***-formulation and ***H***-formulation based multilayer models are recommended for high-frequency applications, i.e., the magnetization loss calculation for $f > 100$ Hz, and the transport current loss calculation for $f > 10$ kHz.

5.3 Dynamic Loss and Magnetization Loss of HTS CCs, Stacks, and Coils

As illustrated in [32], the total AC loss of an HTS CC carring a DC which is exposed to an external AC magnetic field is contributed by both the dynamic loss and magnetization loss. In Chapter 4, the dynamic loss of a single HTS CC at low frequencies (below 100 Hz) has been systematically studied. However, it is unclear whether the definition and analytical formulae for dynamic loss are still applicable towards high frequencies at kHz level. Magnetization loss is the power dissipation of a superconductor carrying no transport current due to an externally applied time-varying magnetic field, which is mainly composed of hysteresis loss and eddy current loss at high frequencies. In Section 5.2, the AC transport current and magnetization losses of one single HTS CC over a wide frequency band up to 1 MHz have been analyzed. It

has been concluded that, when the frequency of the externally applied AC magnetic field is higher than 100 Hz, the loss contributions of the copper stabilizers, silver overlayer and substrate have to be taken into account. Furthermore, the skin effect plays a progressively important role with the increase in frequency. Therefore, under the skin effect, compared with magnetization loss, it should be investigated whether dynamic loss remains an essential concern for the design of high-speed propulsion machines. More importantly, machine windings are usually manufactured in the form of coils. The shielding effect among different turns can affect loss distributions, which should be explored in detail as well. In response to the above issues, the frequency dependence of dynamic loss and magnetization of HTS CCs, stacks, circular coils, as well as racetrack coils over a wide range, from 100 Hz to 20 kHz, will be investigated with the ***H***-formulation based multilayer numerical modelling method.

5.3.1 Dynamic region with frequency

5.3.1.1 Dynamic region at low frequencies

When an HTS CC carrying a DC is exposed to an AC magnetic field, its central part with a width of $2iw$ will be occupied by the DC transport current, which is named as the dynamic region. Here, i is the load ratio between the transport current, I_t, and the self-field critical current, I_{c0}, with $i = I_t/I_{c0}$. $2w$ is the width of the HTS CC.

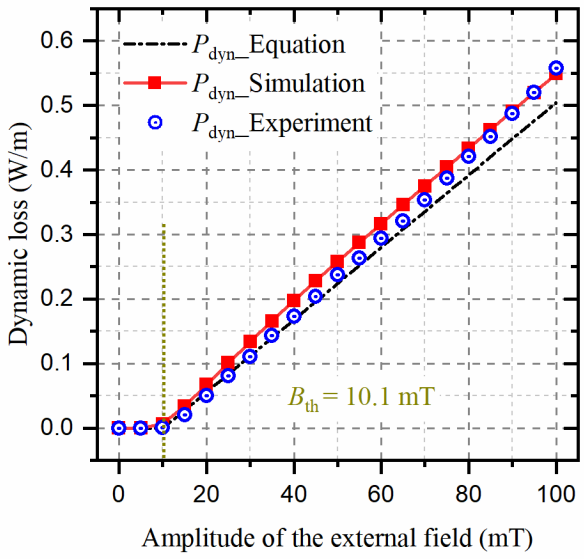

Figure 5.3.1 Analytical, simulated and measured dynamic loss of the HTS CC sample under varying B_{ext} from 0-100 mT. I_{c0} = 105.3 A at 77 K. n = 22.5. The frequency of the AC field f = 26.62 Hz. The threshold field, B_{th}, is determined by (2.19).

Taking the tested HTS CC sample in Section 4.1 as an example, I_{c0} = 105.3 A at 77 K, and n = 22.5. When the load ratio is 0.5 and the AC frequency of the magnetic field is 26.62 Hz,

the simulated dynamic power loss per unit length [P_{dyn} (W/m)] calculated by (4.15) with the ***H***-formulation based numerical model, the analytical results obtained by (4.13), and the experimental data have been depicted together in Figure 5.3.1. It can be seen that the simulated P_{dyn} is in good agreement with the analytical and experimental results. On the basis of the simulation, the magnetic flux density and current density along the width of the HTS layer have been presented in Figure 5.3.2. It can be found that, with the growth of B_{ext}, the amount of traversing magnetic flux during one AC cycle (shaded area) and the electric field increase accordingly, leading to the rise of P_{dyn}, which agrees well with Section 4.1. At low frequencies, e.g., 26.62 Hz, it can be found that the dynamic region to effectively carry DC transport current is determined by 2*iw*.

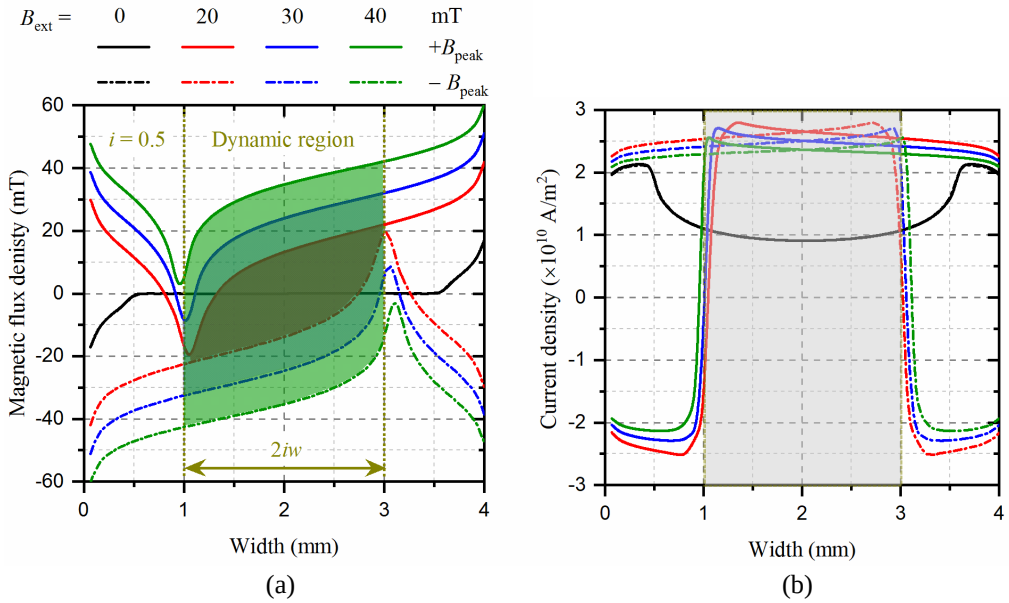

Figure 5.3.2 The magnetic flux density and current density profiles along the width of the HTS CC at the moment of ±peak field, under different external magnetic fields. Load ratio i = 0.5, and B_{ext} varies between 0 – 40 mT. (a) Magnetic flux density profiles. (b) Current density profiles.

5.3.1.2 Dynamic Region at High Frequencies

Taking the tested CC sample with a magnetic substrate in [202] as an example, the simulated transport current losses in different layers and measured results under distinct frequencies up to 15 kHz, have been shown in Figure 5.3.3. It can be seen that the simulated total transport current loss, $P_{tot_}$Simu., agrees well with the experimental data, $P_{tot_}$Expe. Also, as mentioned in Section 3.4 and Section 5.2, most loss occurs in the copper stabilizers when f exceeds 300 Hz because of the skin effect and the influence of the magnetic substrate. With the ***H***-formulation based numerical model, the studied HTS CC with a non-magnetic substrate in Section 5.2 has been considered here, with I_{c0} = 99.23 A at 77 K and n = 38. The magnetic

flux density and current density profiles in its HTS layer have been presented in Figure 5.3.4. It can be seen that the amount of traversing magnetic flux during one AC cycle shrinks rapidly with increasing frequency, as well as the width of the dynamic region. In other words, the width of the dynamic region cannot be determined by 2*iw* at high frequencies above 1 kHz, which in reality increases inversely with frequency. Additionally, the dynamic loss of the HTS layer during one cycle decreases with frequency, which however disagrees with (4.13). According to (4.13), dynamic power loss should be in a linear correlation with frequency, which means that the dynamic loss generated during one AC cycle should be independent of the frequency of external magnetic fields. Therefore, (4.13) is inapplicable for high frequencies at kHz level and above.

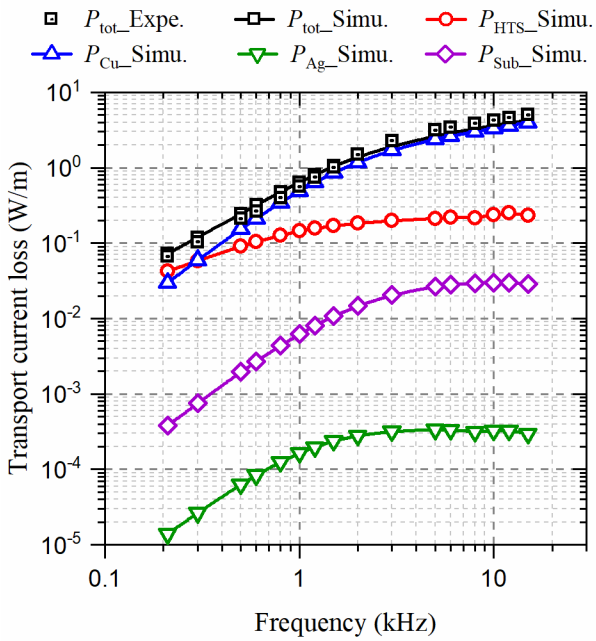

Figure 5.3.3 The simulated and measured AC transport current losses of the tested HTS CC mentioned in [202]. I_{c0} = 108 A at 77 K, I_t = 45 A, n = 30, and f varies from 210 Hz to 15 kHz.

To quantify the dynamic loss in high-speed machines, numerical models are thus recommended. According to [32], dynamic power loss (W) for a single CC or a stack can be calculated by

$$P_{dyn} = 2LN_t I_t f \cdot \int_{1/2f}^{1/f} \frac{1}{S} \int_S E(t) dS dt \tag{5.4}$$

where S is the total cross-sectional area of the HTS layers, and N_t is the total number of CCs.

However, for a coil composed of a number of CCs, the electric field distribution is tightly related to the direction of the externally applied magnetic field. Thus, for calculating P_{dyn} (W), the average electric field in the whole volume of the coil needs to be considered, as

$$P_{dyn} = 2L_{avg}N_t I_t f \cdot \int_{1/2f}^{1/f} \frac{1}{V}\int_V E(t)dVdt \tag{5.5}$$

where V is the total volume of the HTS layers, and L_{avg} represents the average length of the studied coil.

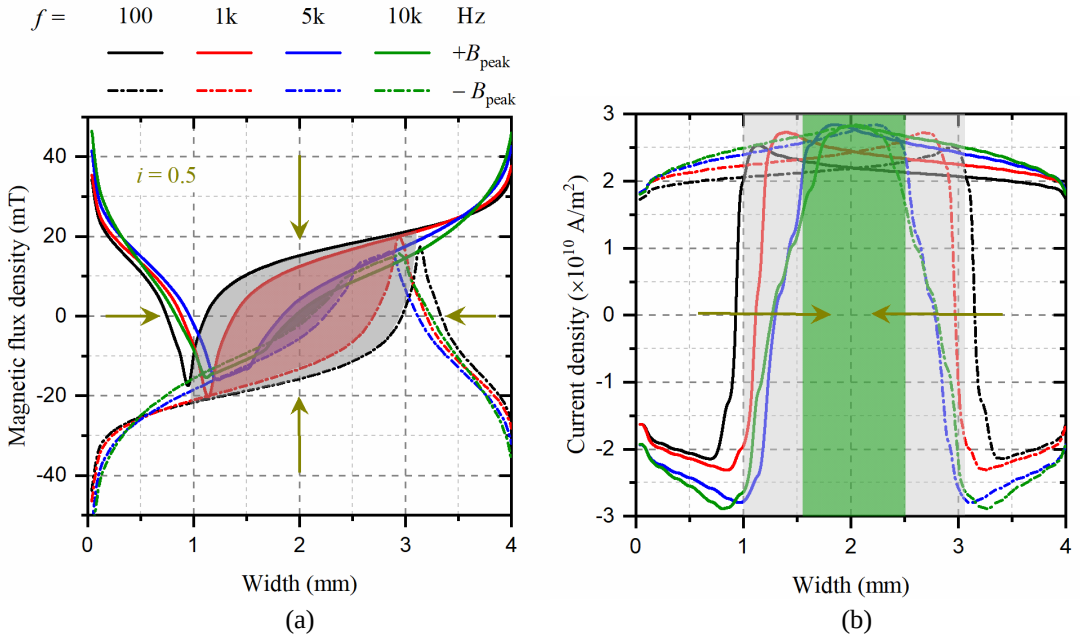

Figure 5.3.4 The magnetic flux density and current density profiles along the width of the HTS CC at the moment of ± peak field, under varying magnetic fields, of which f ranges from 100 Hz – 10 kHz. Load ratio i = 0.5. B_{ext} = 20 mT. (a) Magnetic flux density profiles. (b) Current density profiles.

5.3.2 Variation of dynamic loss and magnetization loss with frequency

5.3.2.1 Single HTS CC

For the same HTS CC discussed in Section 5.3.1.2, the simulated AC power dissipation P_{AC} (W/m) in different layers, dynamic power loss P_{dyn} (W/m) in the HTS layer, as well as magnetization power loss P_{mag} (W/m), per unit length, with varying frequency from 100 Hz to 20 kHz have been depicted together in Figure 5.3.5. Besides, the analytical P_{dyn} obtained by (4.13) has also been presented. It can be found that, at low frequencies below 1 kHz, the majority (more than 90%) of loss is concentrated in the HTS layer; however, with the growth of frequency, the loss in the copper stabilizers increase rapidly and goes over that of the HTS layer at 20 kHz. This phenomenon of loss redistribution is because of the skin effect, as shown in Figure 5.3.6. The magnetic flux density will be driven to both ends of the HTS CC, as well

as its outer copper stabilizers. Therefore, at high frequencies, magnetization loss plays a dominant role, e.g., at 10 kHz, P_{mag} accounts for 90% of the total AC loss, P_{AC_tot}. Compared with the HTS layer and copper stabilizers, the losses in the silver overlayer and substrate are always negligible, because they are inner layers and do not possess a high electrical conductivity that can be compared to that of the HTS layer.

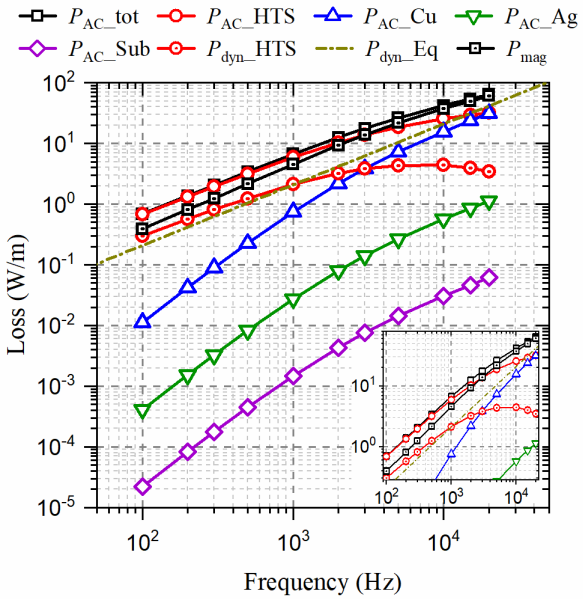

Figure 5.3.5 Variation of AC power losses per unit length (W/m) in different layers, dynamic loss and magnetization loss with frequency for the HTS CC with I_{c0} = 99.23 A at 77 K. f ranges from 100 Hz - 30 kHz. i = 0.5. B_{ext} = 20 mT.

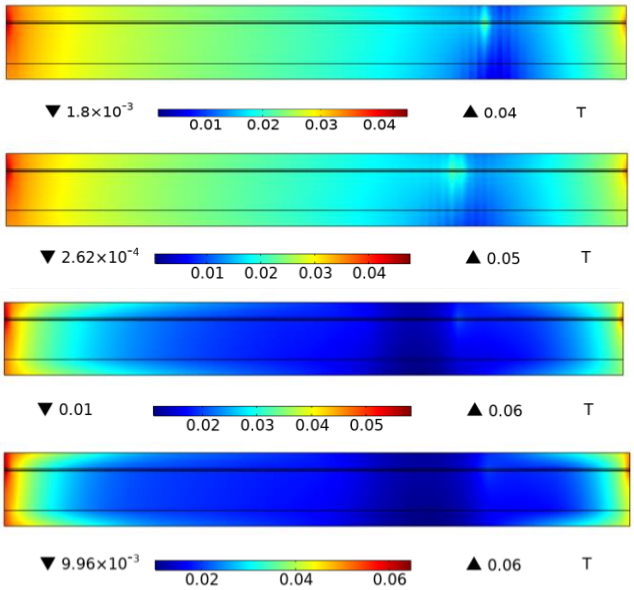

Figure 5.3.6 The magnetic flux density distribution in the cross-section of the HTS CC at the phase of 3/2π, under different frequencies. From top to bottom, f is 100 Hz, 1 kHz, 10 kHz, and 20 kHz, respectively. Load ratio i = 0.5. B_{ext} = 20 mT.

It should be underlined that dynamic power loss begins to decrease from 10 kHz, i.e., dynamic loss during one AC cycle increases inversely with frequency, which is in good accordance with Figure 5.3.4. In addition, the simulated P_{dyn_HTS} clearly differs from the analytical results calculated by (4.13) at high frequencies, especially for f greater than 1 kHz. Therefore, as mentioned in Section 5.3.1.2, (4.13) is inapplicable for HTS CCs at high frequencies above 1 kHz.

According to Figure 5.3.5, it seems that dynamic loss only accounts for one small fraction (less than 50 %) of the total AC loss, which is actually related to load ratio i and the amplitude of the externally applied magnetic field, B_{ext}. Figure 5.3.7 shows the correlation between the loss ratio, P_{dyn}/P_{AC_tot}, and load ratio i under distinct f. It can be found that, in general, for the same i and B_{ext}, P_{dyn}/P_{AC_tot} decreases rapidly with frequency. Taking i = 0.8 and B_{ext} = 100 mT as an example, when f increases from 100 Hz to 20 kHz, P_{dyn}/P_{AC_tot} drops dramatically from 95% to around 3.3%. In fact, as analysed before, when f goes beyond 1 kHz, the transport current and magnetic flux will be pushed to both ends and outer copper stabilizers of the HTS CC due to the skin effect, leading to a fast rise of magnetization loss. P_{dyn}/P_{AC_tot} is in a positive correlation with i, as it determines directly the width of the dynamic region. Besides, the existence of DC transport current is the key difference between dynamic loss and magnetization loss as far as their generation mechanism is concerned. Therefore, a higher DC load ratio results in a higher P_{dyn}/P_{AC_tot}.

As shown in Figure 5.3.7, at low frequencies, e.g., f = 100 Hz, P_{dyn}/P_{AC_tot} increases positively with B_{ext}. However, when f turns higher, e.g., f > 1 kHz, P_{dyn}/P_{AC_tot} begins to decrease with increasing B_{ext}. Actually, at low frequencies, as shown in Figure 5.3.2, a higher B_{ext} means more magnetic flux traversing the HTS CC, thus a higher dynamic loss is generated. At high frequencies, under the influence of the skin effect, magnetization loss plays a dominant role. In this case, as shown in Figure 5.3.6, most magnetic flux will be concentrated in both ends of the HTS CC, thus a higher B_{ext} means more magnetization loss generated on the two sides of the CC. To conclude, the amplitude of the external magnetic field has different influence on P_{dyn}/P_{AC_tot} with different frequencies. At low frequencies below 1 kHz, a higher B_{ext} contributes to a higher P_{dyn}; however, at higher frequencies above 1 kHz, a higher B_{ext} brings about a higher P_{mag}.

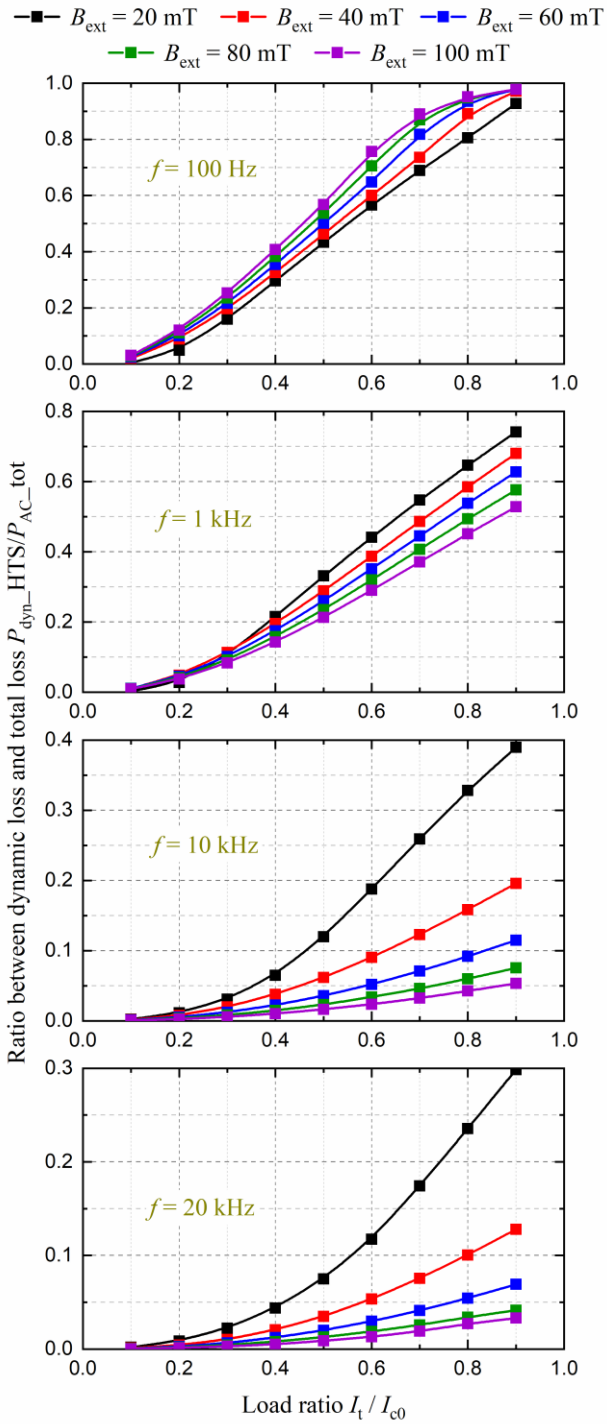

Figure 5.3.7 The correlation between loss ratio P_{dyn}_HTS/P_{AC}_tot and load ratio *i* under distinct external magnetic fields for different frequencies. *i* varies from 0.1 to 0.9, and magnetic flux density ranges from 20 mT to 100 mT. From top to bottom, *f* is 100 Hz, 1 kHz, 10 kHz, and 20 kHz, respectively.

Through the above analyses, it can be confirmed that, at low frequencies, dynamic loss is an essential parameter to consider for the design of HTS magnets, low-speed machines (e.g., ultra-low-speed wind-farm generators at ~10 rpm, and low-speed motors for ship propulsion at 100-250 rpm), as well as flux pump devices, etc. For instance, as shown in Figure 5.3.7, at 100 Hz, when B_{ext} is greater than 40 mT and i is above 0.6, P_{dyn} accounts for more than 60 % of the total loss. When i attains 0.8, P_{dyn} can become more than 80 % of the total loss even under a small B_{ext} like 20 mT. However, when it comes to HTS high-speed synchronous machines with a rotational speed higher than 7 krpm, the skin effect should also be accounted for, because high-frequency magnetic fields appear in such cases. For example, at f = 1 kHz, when i reaches 0.8 and B_{ext} gets 80 mT, P_{dyn} is equal to P_{mag}, both of which account for half of the total loss. In this case, dynamic loss and magnetization loss are both significant to be considered. If harmonics with higher frequency components above 1 kHz are to be included, magnetization loss deserves more attention.

5.3.2.2 HTS stack

In most HTS applications, to acquire a high current-carrying capacity, stacks or coils composed of many turns of HTS CCs are preferred and more practical. Therefore, in this section, the variation of dynamic loss and magnetization loss with frequency in a stack of HTS coils have been investigated. The 2D numerical model for a stack is an expansion of the multilayer model of one single HTS CC.

At first, to validate the 2D stack numerical models, the parameters of the tested stack of 15 HTS tapes in [148] have been adopted here. For every single tape, I_{c0} = 150 A (at 77 K), n = 36, and B_0 = 0.21 T. The thickness of the insulation between tapes is around 60 μm. The transport current loss calculated by the $\boldsymbol{H}$-formulation based 2D multilayer stack models and experimental data have been depicted together in Figure 5.3.8. It can be seen that the simulation agrees well with the experimental measurements. Additionally, at low frequencies below 100 Hz, the loss in the HTS layer per unit length, P_{HTS} (W/m), accounts for more than 95% of the total loss, P_{tot} (W/m), which is in good accordance with Figure 5.3.5 and the conclusions drawn in Section 5.2.

Then, in order to better show the differences between one single CC and a stack of CCs with respect to P_{dyn} and P_{mag}, the parameters of the studied HTS CC in Section 5.3.2.1 have been adopted. With this stack numerical model, the variation of P_{dyn} and P_{mag} with frequency has been investigated. Load ratio i is set as 0.5, B_{ext} has been chosen as 20 mT, and f ranges from 100 Hz to 20 kHz.

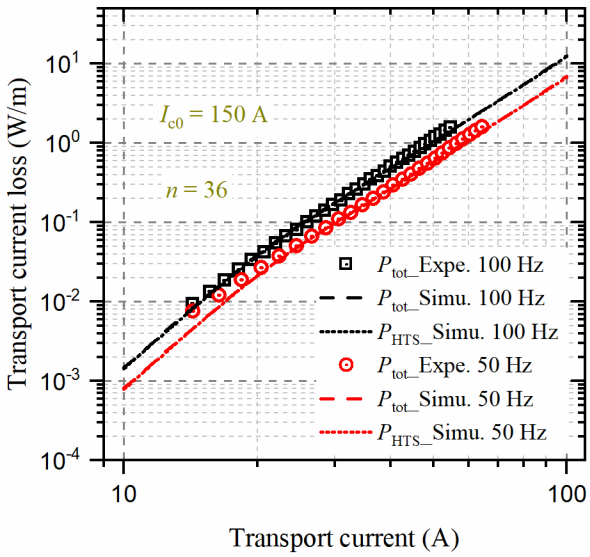

Figure 5.3.8 The simulated and measured transport current loss of the stack of 15 HTS CCs carrying varying AC transport current. The amplitude of the AC current varies from 10 to 100 A, and f has been chosen as 50 Hz and 100 Hz.

Figure 5.3.9 shows the magnetic flux density and current density distribution in the HTS stack under different frequencies when B_{ext} = 20 mT and i = 0.5. It can be seen that, with the increase of frequency, both the magnetic flux and transport current will be driven to both ends of the stack, which is due to the skin effect, as mentioned in Section 5.3.2.1. In addition, it appears that the skin effect is more influential to the HTS CCs in the middle part. In fact, because of the shielding effects of the external CCs on the internal ones, less magnetic flux can penetrate in the middle part of the stack, as shown in (a), (b) and (c). Therefore, in general, the $J_c(\boldsymbol{B})$ of the internal CCs is relatively higher than that of the external ones, leading to a lower $J/J_c(\boldsymbol{B})$ in the middle part of the stack, as shown in (d), (e) and (f). To conclude, under both the skin effect and shielding effect, at highest frequencies, the highest flux density and current density appear at both ends of the outermost CCs in an HTS stack, and they are in a positive correlation with frequency.

Figure 5.3.10 shows the total loss, dynamic loss and magnetization loss in 5 distinct CCs of the stack when f = 1 kHz. The 5 CCs are the first, fourth, eighth, twelfth, and fifteenth tape, respectively. It can be seen that, more losses are generated in the outermost CCs, namely the first and fifteen tapes, which is in good accordance with the conclusions drawn from Figure 5.3.9. Besides, the loss ratio P_{dyn}/P_{AC_tot} is the highest for the most middle CC because, as it is shielded by the outer turns, reducing the magnetisation loss. Therefore, at high frequencies, e.g., f = 1 kHz, dynamic loss can still play a dominant role in the middle parts of the HTS stack.

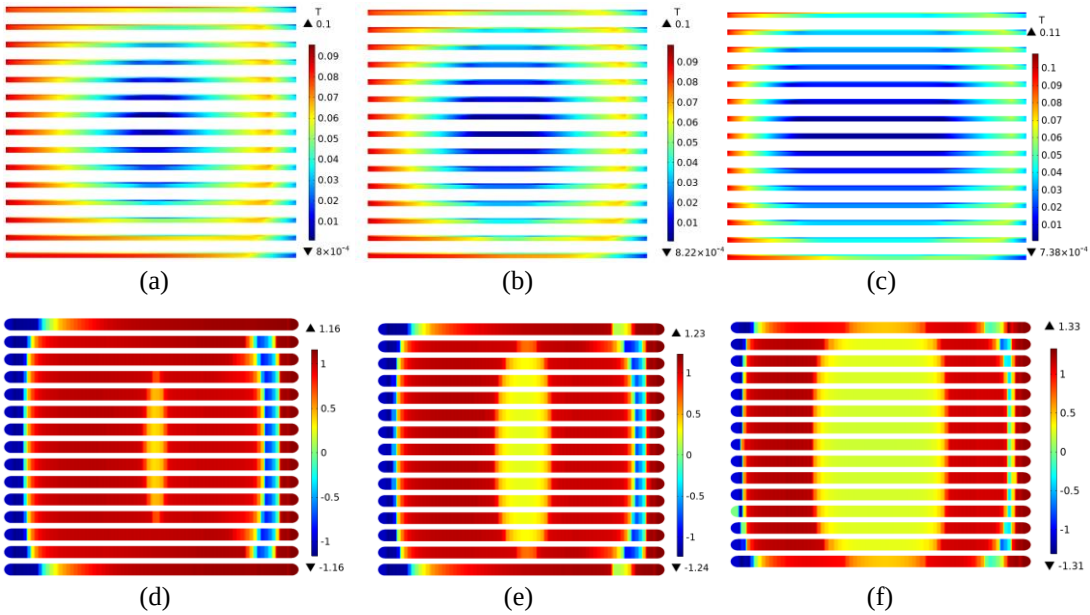

Figure 5.3.9 Magnetic flux density and current density distribution in the studied stack of 15 HTS CCs. B_{ext} = 20 mT, I_t = 49.5 A, and f varies from 100 Hz to 10 kHz. (a), (b) and (c) represent the magnetic flux density distribution at the phase of 3π/2 for f = 100 Hz, 1 kHz, and 10 kHz, respectively. (d), (e) and (f) show J/J_c in the HTS layer at the phase of 2π for f = 100 Hz, 1 kHz, and 10 kHz, respectively. For a better image effect, the thickness of each HTS CC has been adjusted accordingly.

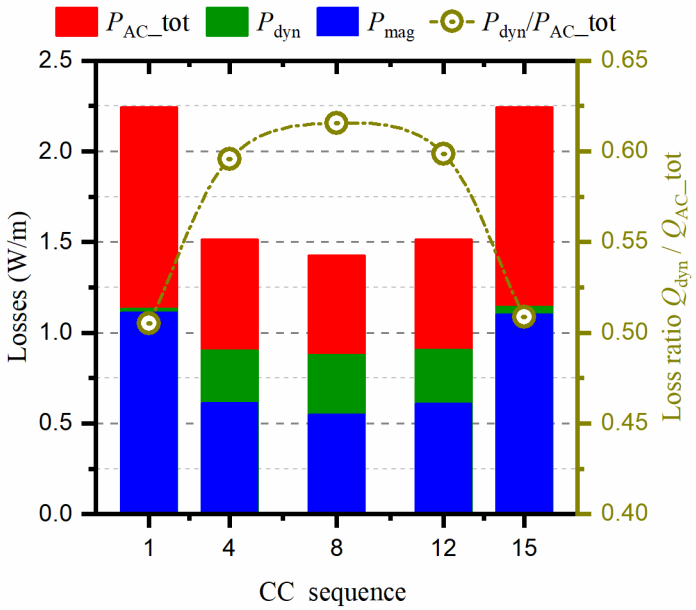

Figure 5.3.10 Total loss, dynamic loss and magnetization loss of the 1st, 4th, 8th, 12th and 15th CC in the HTS stack, when f = 1 kHz, B_{ext} = 20 mT, and I_t = 49.5 A.

Figure 5.3.11 shows the frequency dependence of dynamic loss and magnetization loss for the HTS stack. It can be found that, when f is less than 10 kHz, the loss generated in the HTS

layer accounts for the majority of the total loss. However, when *f* becomes greater than 10 kHz, most of the loss is concentrated in the copper stabilizers, which is due to the skin effect, as mentioned in Section 5.3.2.1. For frequencies lower than 3 kHz, dynamic loss dominates the total loss, but when *f* rises above 3 kHz, magnetization loss contributes more to the total loss and dynamic loss begins to decrease from 10 kHz. Therefore, with increasing frequency, the AC loss generated in the copper stabilizers, P_{AC_Cu}, will be approaching P_{mag} as well as P_{AC_tot}. In this case, the magnetic flux and transport current will be driven to both ends of each CC and its outer copper parts, as shown in Figure 5.3.9. In addition, it should be pointed out that since the total loss in the HTS layer starts to drop and most of the loss is generated in the copper stabilizers when *f* turns greater than 10 kHz, it can be inferred that when the frequency of the external field exceeds a certain threshold, the copper stabilizers can act as a protector for the HTS layer. This phenomenon deserves further research efforts in the future.

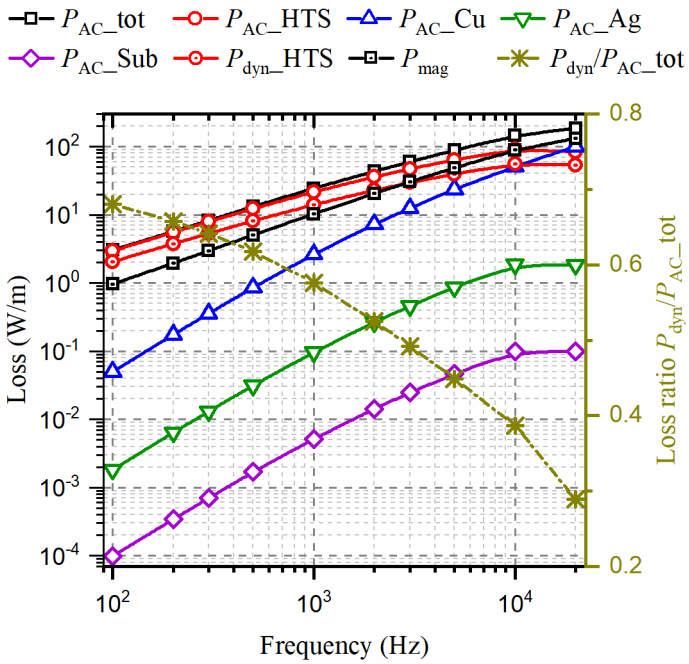

Figure 5.3.11 Variation of AC losses in different layers, dynamic loss magnetization loss, and loss ratio P_{dyn}/P_{AC_tot} with frequency for the HTS stack composed of 15 CCs. *f* ranges from 100 Hz to 20 kHz. i = 0.5. B_{ext} = 20 mT.

It should be noted that the HTS stack is composed of the same CC as discussed in Section 5.3.2.1. Comparing Figure 5.3.11 and Figure 5.3.5, it is interesting to note that, in Figure 5.3.5, the dynamic loss of one single CC is always less than the magnetization loss under different frequencies, from 100 Hz to 20 kHz. However, at the same B_{ext}, i, and frequency range, the magnetization loss of the HTS stack does not exceed the dynamic loss until 3 kHz in Figure 5.3.11. In fact, as mentioned before, this difference is due to the shielding effect of the outer

CCs on the middle ones, thus dynamic loss can still play a dominant role when f is below 3 kHz. However, when f continues to increase, because of the skin effect, magnetization loss will increase rapidly. Therefore, the loss ratio P_{dyn}/P_{AC_tot} decreases with frequency, from 68% at 100 Hz to 29% at 20 kHz. To conclude, at high frequencies, we need to consider both the skin effect and shielding effect for the loss quantification of an HTS stack. Compared with a single CC, the influence of dynamic loss in a stack is more significant.

5.3.2.3 HTS circular coil

HTS circular coils are important elements for superconducting magnets. The tested 2×18 circular double pancake coil in [329] has been referenced here, which was fabricated from 6 mm wide SuperPower SCS6050 CCs. The inner diameter of the coil is 50 mm, and its KAPTON insulation thickness is 100 μm. The self-field critical current of the single CC is 115 A at 77 K.

Given that the circular coil is both centrosymmetric and axisymmetric, its numerical model has been built with a 2D method based on the ***H***-formulation [146, 329]. However, unlike [329] which only models the HTS layer of the CC, the coil modelling in this paper has been conducted considering the multilayer structure of each single CC, as shown in Figure 5.3.12 (a). Similar to our previous modelling method for a single tape, the Dirichlet boundary condition has been chosen for applying external magnetic fields. Considering that $J_c(\boldsymbol{B})$ is primarily determined by the perpendicular component $B_\perp$, as shown in (2.4), the direction of the external magnetic field has been chosen to be perpendicular to the wide surface of the CCs and parallel to the cross-section of the coil, with the field intensity $H_r = B_{ext}/\mu_0 \cdot \sin(2\pi ft)$.

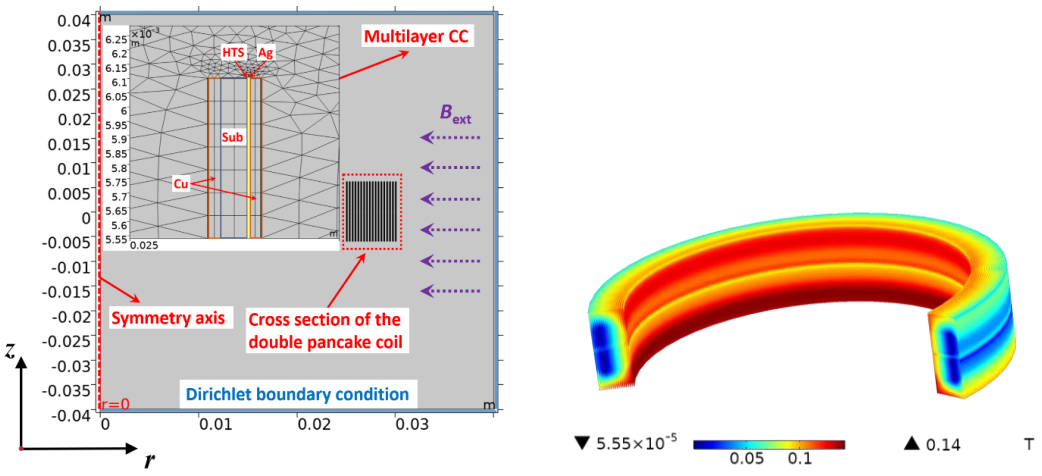

(a) (b)

Figure 5.3.12 2D coil model layout and 3D magnetic flux density distribution of the double pancake coil. f = 1 kHz. (a) Cross-section of the 2D model. B_{ext} is along the r-axis in the cylindrical coordinate system and perpendicular to the wide surfaces of the CCs. (b) Flux density distribution of the coil.

With this 2D numerical multilayer model, the simulated transport current power loss per unit length (W/m) and the experimental data of this double pancake coil are depicted together in Figure 5.3.13, both of which agree well with each other. Then, through this numerical model for the same double pancake circular coil, the variation of dynamic loss and magnetization loss with frequency from 100 Hz to 20 kHz has been investigated. Load ratio i has been chosen as 0.5, and B_{ext} is set to 50 mT. Figure 5.3.12 (b) presents the 3D magnetic flux density distribution of the double pancake coil at the phase of $3\pi/2$ with f = 1 kHz.

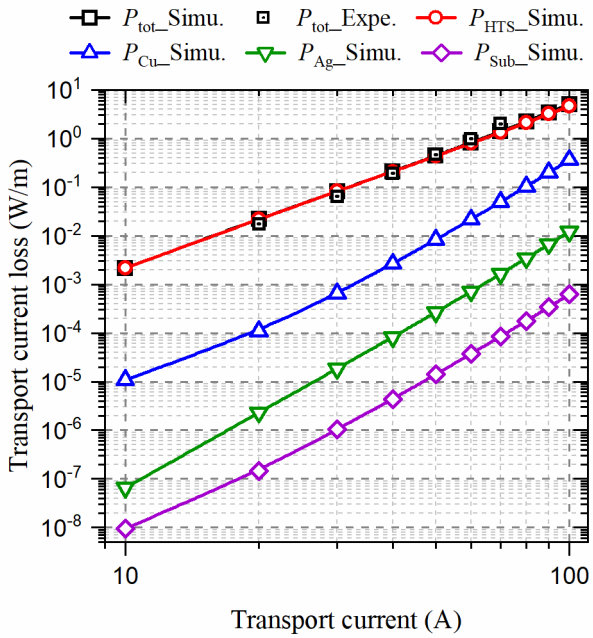

Figure 5.3.13 The simulated and measured transport current loss of the 2×18 double pancake circular coils. The amplitude of the AC current varies from 10 to 100 A, and f = 100 Hz.

Figure 5.3.14 shows the magnetic flux density and current density distribution in the cross-section of the double pancake coil when f varies from 100 Hz to 20 kHz. It can be seen that, in general, the magnetic flux and current have a symmetrical distribution in the two coils, and both the highest flux density and current density increase with frequency. Similar to the case of stacks, due to the skin effect, the magnetic flux and current have been pushed to the upper and lower borders of the pancake coil with increasing frequency. Like the shielding effect of the external CCs on the internal ones for a stack, here the coil shows the same trend. However, according to (a), (b), (c) and (d), it appears that the innermost turns have a shielding effect over the external parts. It has to be clarified that, the phenomenon that a large amount of magnetic flux has been concentrated in the internal turns is because of the high self fields generated by the coil, parallel to the wide surface of the CCs, rather than the shielding effect among different CCs. The critical current density $J_c(\boldsymbol{B})$ is determined by both the parallel and

perpendicular field components, thus in (e) and (f) $J/J_c(\boldsymbol{B})$ of the internal turns is generally higher than that of the external ones. However, $J_c(\boldsymbol{B})$ is mainly decided by the perpendicular field that is largely determined by the externally applied magnetic field, so the difference regarding $J/J_c(\boldsymbol{B})$ between internal and external parts is not significant. Especially, at high frequencies, this difference has been weakened by the skin effect, as shown in (g) and (h).

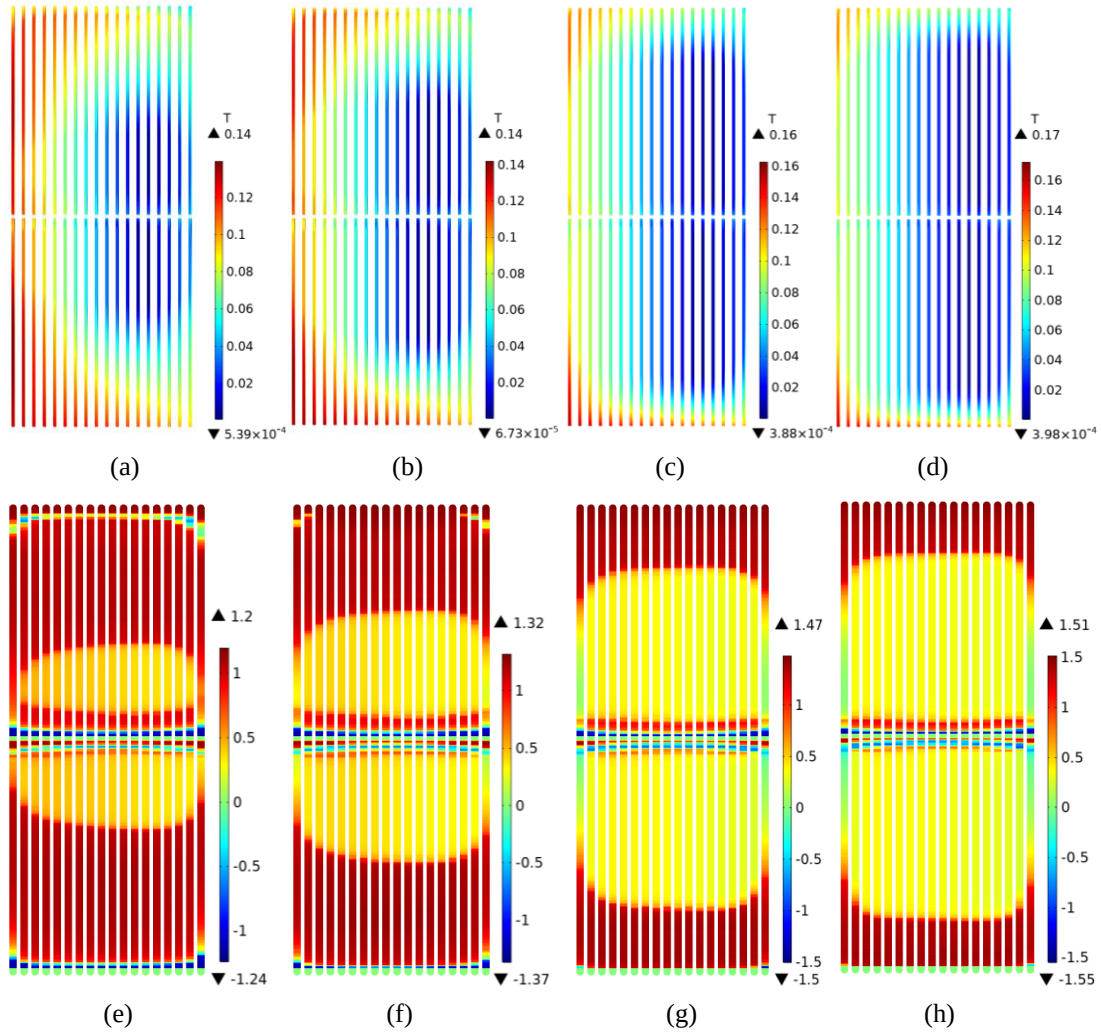

Figure 5.3.14 Magnetic flux density and current density distribution in the cross-section of the studied 2×18 double pancake coil. B_{ext} = 50 mT, for each tape I_t = 60 A, and f varies from 100 Hz to 20 kHz. (a), (b), (c) and (d) represent the magnetic flux density distribution at the phase of 3π/2 for f = 100 Hz, 1 kHz, 10 kHz, and 20 kHz respectively. (e), (f), (g) and (h) show J/J_c in the HTS layer at the phase of 2π for f = 100 Hz, 1 kHz, 10 kHz, and 20 kHz respectively. For a better image effect, the thickness of each HTS CC has been adjusted accordingly.

To better describe the shielding effect of the innermost and outermost turns over the middle parts, the total loss, dynamic loss and magnetization loss in 6 distinct double turns of the coil have been presented in Figure 5.3.15, with f = 1 kHz. The 6 turns are the first, fourth, eighth,

eleventh, fifteenth and eighteenth double turns, respectively. It can be seen that, the total loss for each double turn increases from inside to outside. More magnetization loss has been produced in the outermost turns, because they have a shielding effect on the middle parts, as mentioned before, leading to a higher dynamic loss in the middle turns. Therefore, the loss ratio P_{dyn}/P_{AC_tot} attains the highest at the 8th turn and becomes the smallest at the 18th. However, it needs to be pointed out that, even at high frequencies, e.g., f = 1 kHz, dynamic loss can still dominate the total power dissipation, which is different from the case of a single CC, as shown in Figure 5.3.7. Therefore, combined with Figure 5.3.10, we can conclude that, because of the shielding effect of the outermost CCs on the middle parts, the influence of dynamic loss has been enhanced in a stack or a coil.

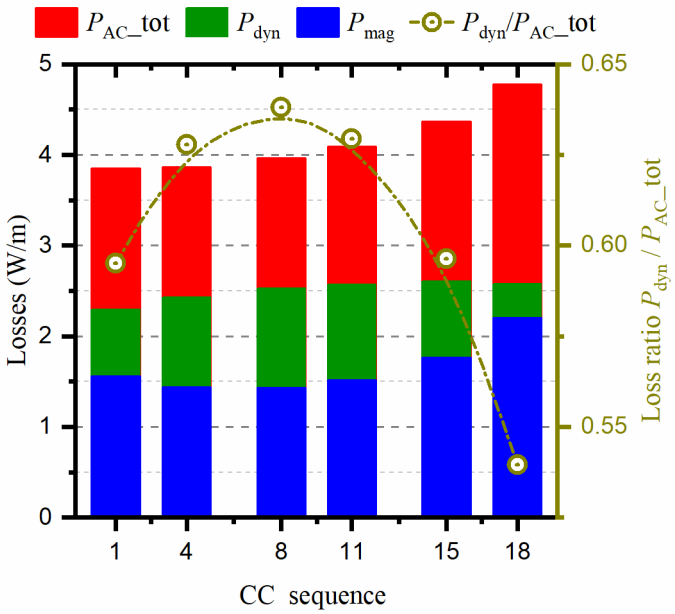

Figure 5.3.15 Total loss, dynamic loss and magnetization loss of the 1st, 4th, 8th, 11th, 15th, and 18th CC (from inside to outside) in the HTS coil, when f = 1 kHz, B_{ext} = 50 mT, and i = 0.5.

Figure 5.3.16 describes the frequency dependence of the AC losses in different layers, dynamic loss as well as magnetization loss over the cross-section of the double pancake coil. In general, Figure 5.3.16 shows the same trend as Figure 5.3.11, that both the total loss and magnetization loss increase rapidly with frequency due to the skin effect, and the loss generated in the copper stabilizers exceeds that of the HTS layer when f turns greater than 15 kHz. Although the proportion of dynamic loss over the total loss is decreasing rapidly, from 74% at 100 Hz to 32 % at 20 kHz, it is still above 50% within the frequency range below 3 kHz. Therefore, as concluded in Section 5.3.2.2, both dynamic loss and magnetization loss need to be taken into account for characterizing the electromagnetic performance of HTS coils operated at the kHz level.

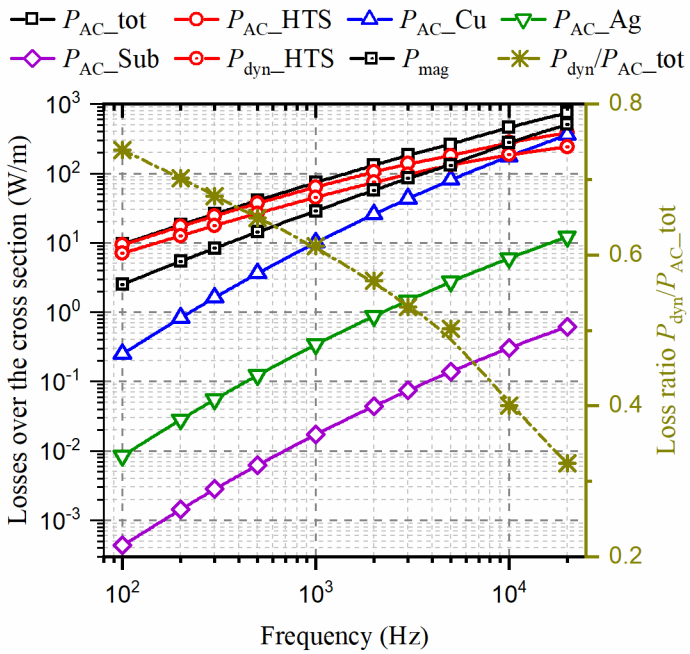

Figure 5.3.16 Variation of AC losses in different layers, dynamic loss magnetization loss, and loss ratio P_{dyn}/P_{AC_tot} with frequency for the double pancake HTS coil. f ranges from 100 Hz to 20 kHz. i = 0.5. B_{ext} = 50 mT.

5.3.2.4 HTS racetrack coil

HTS racetrack coils are widely adopted as superconducting machine windings. To accurately quantify the loss characteristics of a racetrack coil, a 3D numerical model is necessary, especially when the ratio between its thickness and diameter cannot be neglected. 3D modelling of HTS racetrack coils has been discussed in [163-164] with a homogenization method. Although the homogenization method can greatly save computational time, it cannot be used for studying the frequency dependence of losses in different layers of the HTS CC.

On the basis of the homogenized model in [163-164], a 3D numerical model for the racetrack coil taking into account the multilayer structure of each CC has been built in this section, as shown in Figure 5.3.17. It should be underlined here that, to reduce the computation complexity, it is reasonable to model only one part of the coil considering its central and axial symmetry. However, to study dynamic loss, AC external magnetic field needs to be applied so that the continuity of current flow or magnetic flux in certain boundaries has to be guaranteed. In this section, the direction of the externally applied magnetic field has been chosen to be perpendicular to the wide surface of CCs in the straight part, along the x-axis, with $H_x = B_{ext}/\mu_0 \cdot \sin(2\pi ft)$. Therefore, we have modelled only half of the circular part and one-quarter of the straight part as far as one coil is concerned. Different boundary conditions have to be applied separately: to keep the continuity of current flow, zero flux has been chosen for

current input and output boundaries; to keep the continuity of magnetic flux in the other boundaries, the Dirichlet boundary condition has been adopted.

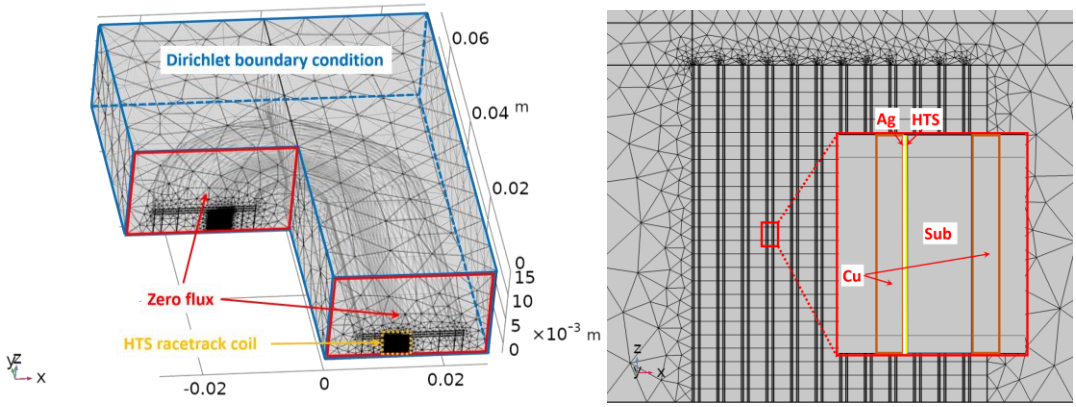

(a) (b)

Figure 5.3.17 3D numerical multilayer model of the HTS racetrack double pancake coil taking into account the physical structure of each CC, in which only one-eighth of the straight part and one-quarter of the circular section have been shown. (a) Whole mesh view and boundary condition. (b) Meshing of the cross-section of one coil.

It has to be noted that the $J_c(\boldsymbol{B})$ dependence for HTS CCs in a racetrack coil is closely linked to the angle between the magnetic field vector and the wide surface normal of the coil. We choose one racetrack coil in the *x*-*y* plane as an example, as shown in Figure 5.3.18. 2*l* and *R* are the length of the straight part and the radius of the circular part, respectively. $\boldsymbol{\tau}$ and $\boldsymbol{n}$ represent the unit tangent vector and unit normal vector at any studied point on the coil, $P(x_0, y_0, z_0)$. $\boldsymbol{B}_x$ and $\boldsymbol{B}_y$ denote separately the magnetic flux density components along the *x*-axis and *y*-axis. Then, the parallel and perpendicular field components can be expressed as

$$\begin{cases} \boldsymbol{B}_{\parallel} = \left(\boldsymbol{B}_x + \boldsymbol{B}_y\right) \cdot \boldsymbol{\tau} + \boldsymbol{B}_z \\ \boldsymbol{B}_{\perp} = \left(\boldsymbol{B}_x + \boldsymbol{B}_y\right) \cdot \boldsymbol{n} \end{cases} \tag{5.6}$$

In (5.6), $\boldsymbol{\tau}$ and $\boldsymbol{n}$ are actually piecewise function vectors depending on the position of the studied point $P(x_0, y_0, z_0)$. $\boldsymbol{\tau}$ and $\boldsymbol{n}$ can be expressed as (5.7) and (5.8), respectively.

The parameters of the tested racetrack double pancake coil studied in [148] have been adopted here. The inner radius is 10 mm, the length of the straight part is 70 mm, and the number of turns for each pancake is 12. This racetrack coil is composed of SuperOx HTS CCs, of which the self-field critical current for each CC I_{c0} = 150 A at 77.4 K, and n = 30. Based on the 3D racetrack coil model, the simulated transport current power loss (W) and measured results of the whole racetrack coil at low frequencies have been depicted together in Figure 5.3.19. The amplitude of transport current varies from 10 to 90 A, and the external magnetic

flux density B_{ext} = 0. It can be seen that the simulated results are in good agreement with the experimental data. The loss generated in the HTS layer P_{HTS} (W) is slightly lower than the total loss P_{tot} (W), thus at low frequencies, the most loss is concentrated in the HTS layer.

$$\boldsymbol{n}=\left(n_x,n_y\right)=\begin{cases}\left(\dfrac{x_0}{\sqrt{x_0^{\,2}+(y_0-l)^2}},\dfrac{y_0-l}{\sqrt{x_0^{\,2}+(y_0-l)^2}}\right), l<y_0\le l+R\\ \left(\mathrm{sign}(x_0),0\right), -l\le y_0\le l\\ \left(\dfrac{x_0}{\sqrt{x_0^{\,2}+(y_0+l)^2}},\dfrac{y_0+l}{\sqrt{x_0^{\,2}+(y_0+l)^2}}\right), -l-R\le y_0<-l\end{cases} \tag{5.7}$$

$$\boldsymbol{\tau}=\left(\tau_x,\tau_y\right)=\begin{cases}\left(\dfrac{y_0-l}{\sqrt{x_0^{\,2}+(y_0-l)^2}},\dfrac{-x_0}{\sqrt{x_0^{\,2}+(y_0-l)^2}}\right), l<y_0\le l+R\\ \left(0,-\mathrm{sign}(x_0)\right), -l\le y_0\le l\\ \left(\dfrac{y_0+l}{\sqrt{x_0^{\,2}+(y_0+l)^2}},\dfrac{-x_0}{\sqrt{x_0^{\,2}+(y_0+l)^2}}\right), -l-R\le y_0<-l\end{cases} \tag{5.8}$$

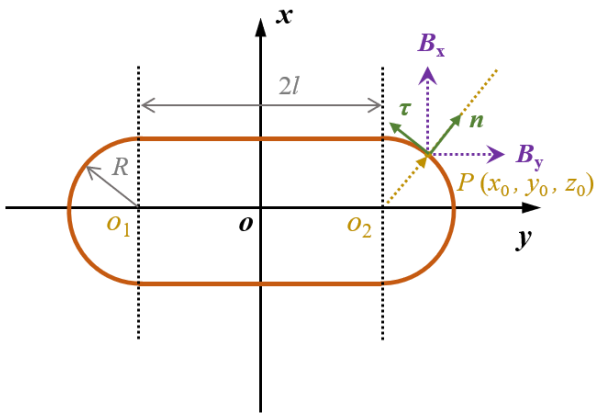

Figure 5.3.18 Diagram of the racetrack coil in the *x*-*y* plane. o_1 and o_2 are the centers of the two semicircle parts. The positive direction of the *z*-axis points to the inside of the paper.

Taking the 2×12 racetrack double pancake coil as the study object, the frequency dependence of dynamic loss and magnetization loss within 100 Hz - 20 kHz has been investigated. The DC transport current has been chosen as 50 A, and B_{ext} is set as 50 mT.

Figure 5.3.20 shows the current density and magnetic flux density distribution in the modelled part of the racetrack double pancake coil. (a), (b), and (c) present the $J/J_c(\boldsymbol{B})$ distribution in the HTS layers at the phase of 2π for f = 100 Hz, 1 kHz, and 10 kHz respectively. It can be found that, with increasing frequency, the transport current is driven towards the

edges of each CC, where the maximum $J/J_c(\boldsymbol{B})$ appears and increases positively with frequency. It should be noted that in the middle section of the circular coil part, the current density in the upper bound is much higher than that of the lower bound, which is due to the occurrence of eddy current induced by the external AC magnetic field, following Lenz's law. The skin effect at high frequencies can be seen earlier in (d), (e), and (f), inside which the magnetic flux is dragged to the edges of HTS CCs with the growth of frequency. From the cross-section of the coil, it can be found that, more magnetic flux as well as current are concentrated in the upper half compared to the lower half. This phenomenon is easy to understand because the studied part belongs to the upper pancake coil, which agrees well with the case of the double pancake circular coil in Figure 5.3.14.

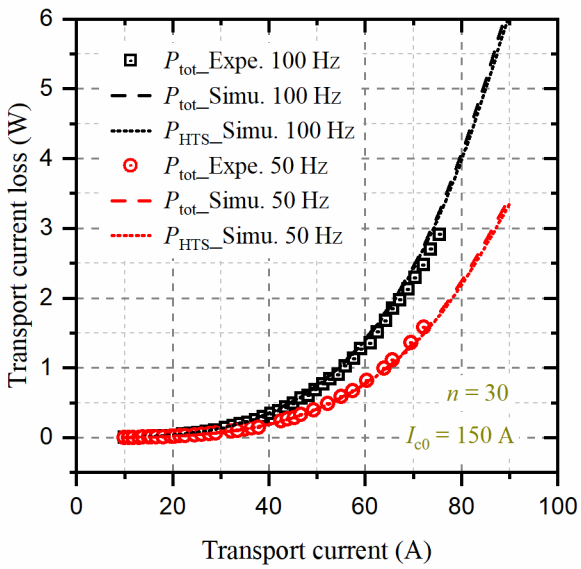

Figure 5.3.19 The simulated and measured transport current loss of the 2×12 racetrack double pancake coil carrying varying AC transport current. The amplitude of the AC current varies from 10 to 90 A, and f has been chosen as 50 Hz and 100 Hz.

Taking f = 1 kHz as an example, Figure 5.3.21 shows the magnetic field vector distribution in the 3D space surrounding the studied coil section as well as the current vector propagation on the surface of the outermost HTS layer. Among them, (a) and (b) describe the magnetic field vector at the phase of 3π/2 and 2π, respectively. We can see that at the phase of 2π, the generated magnetic field (self field) is distributed symmetrically as it is only determined by the DC transport current. However, at the phase of 3π/2, the externally applied AC magnetic field attains the peak value. In this case, the magnetic flux in the central portion of the coil is decided by both the self field and the external field, thus the direction of the field vector is towards the upper left. Figure 5.3.21 (c) and (d) present the current vector distribution on the

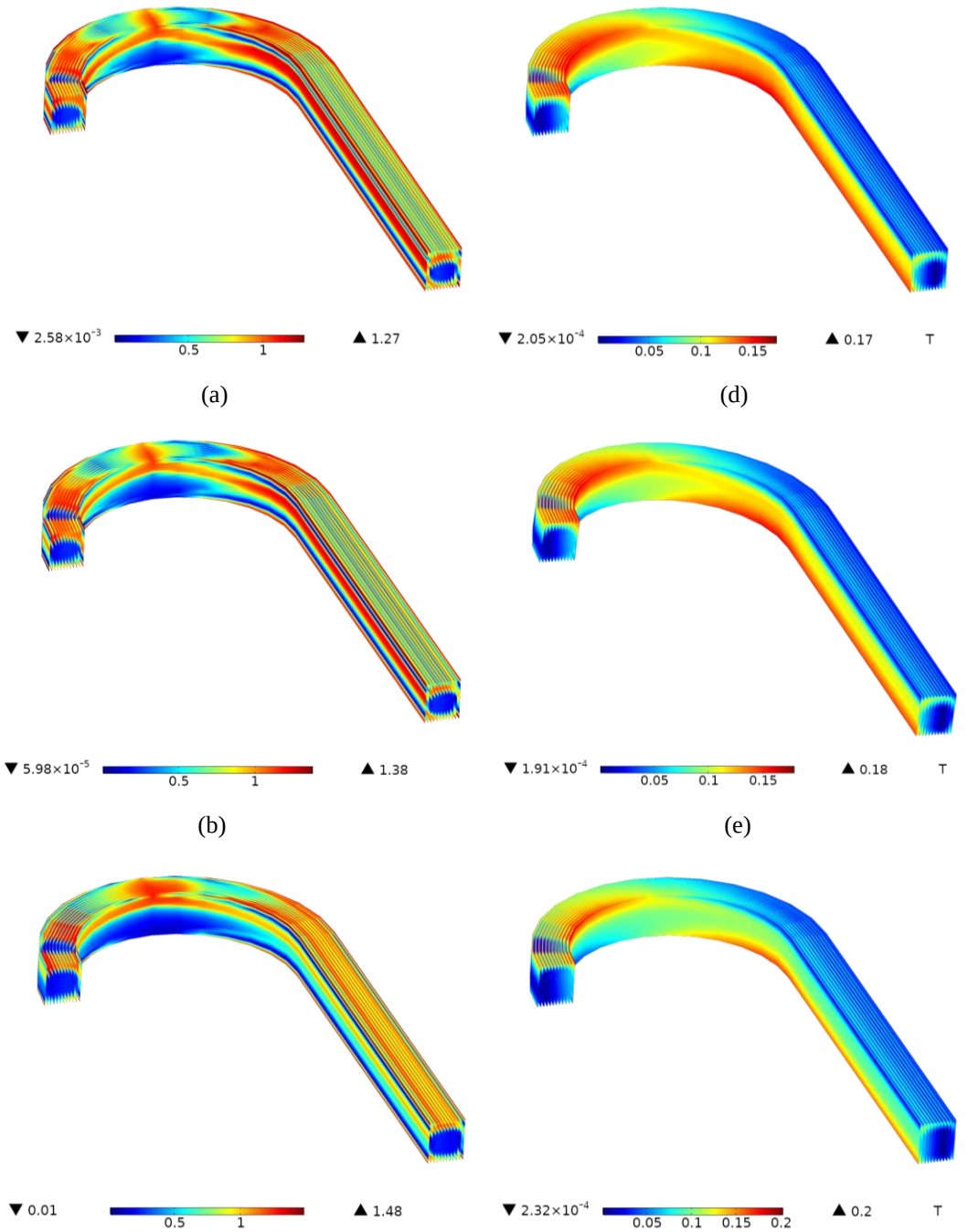

Figure 5.3.20 Current density and magnetic flux density distribution in the studied part of the 2×12 racetrack double pancake coil. B_{ext} = 50 mT, for each tape I_t = 50 A, and f varies from 100 Hz to 10 kHz. (a), (b), and (c) present the J/J_c distribution in the HTS layer at the phase of 2π for f = 100 Hz, 1 kHz, and 10 kHz, respectively. (d), (e), and (f) show the magnetic flux density distribution at the phase of 3π/2 for f = 100 Hz, 1 kHz, and 10 kHz respectively.

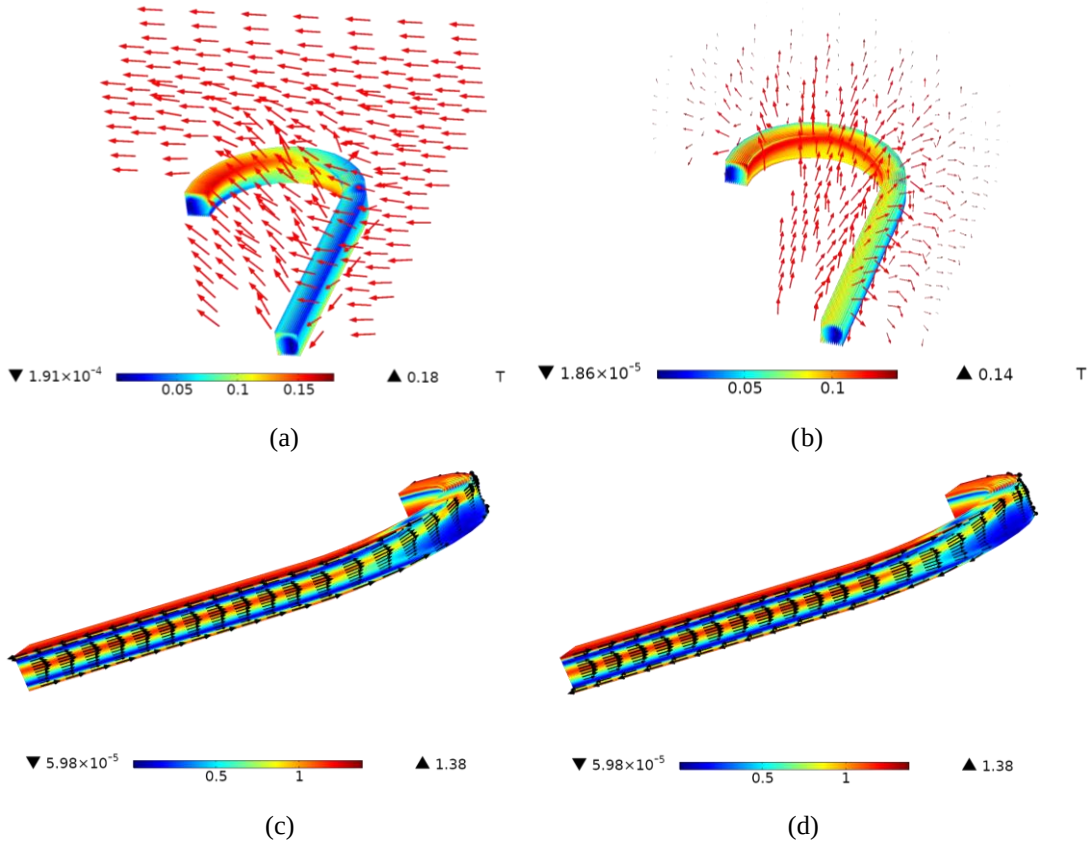

Figure 5.3.21 Magnetic field vector distribution in the space surrounding the studied coil part, and current vector distribution on the surface of the outermost HTS layer. B_{ext} = 50 mT, for each tape I_t = 50 A, and f = 1 kHz. (a) and (b) present the magnetic flux distribution at the phase of 3π/2 and 2π, respectively, inside which the red arrows represent the field vector. (c) and (d) show the current vector distribution on the surface of the outermost HTS layer at the phase of π and 2π, respectively, inside which the black arrows denote the current vector.

surface of the outermost HTS layer at the phase of π and 2π, respectively, inside which the black arrows denote the current vector. It can be observed that at these two moments, the middle section of the HTS layer shares the same current vector. In fact, this middle section corresponds to the dynamic region mentioned before, in which the current density is determined by the DC transport current thus the current vector remains the same direction. As a comparison, the vector directions in both edges at the two moments are opposite, which can be explained by Lenz's law and the current gathered in the edges of the HTS layer is the eddy current leading to magnetization loss. It should be underlined here that Figure 5.3.21 also confirms the continuity of the current and magnetic field in the corresponding boundaries, which further illustrates the effectiveness of the 3D model for the pancake racetrack coil.

Figure 5.3.20 and Figure 5.3.21 also show the shielding effect of the outermost and innermost HTS turns over the middle parts. To quantify this interaction among different layers, the total

loss, dynamic loss and magnetization loss in 6 distinct double turns of the racetrack coil have been presented in Figure 5.3.22, with f = 1 kHz. The 6 turns are the first, fourth, sixth, seventh, ninth and twelfth double turns, respectively. It can be found clearly that in general, there exists a higher total loss in the outermost turns and the least loss is generated in the middle turns. Besides, in the outermost CCs, the magnetization loss is much higher than the dynamic loss, however, in the middle parts, the dynamic loss accounts for the majority of the total loss. Therefore, the loss ratios P_{dyn}/P_{AC_tot} attain the highest at the 6th and 7th turns, which are all beyond 50%, and becomes the smallest at the 12th one. To conclude, the outer turns have an evident shielding effect over the inner parts of the racetrack coil, and the shielding effect enhances the significance of dynamic loss, which agrees well with the conclusions drawn from the case of the circular coil. Thence, we need to realize that, even at high frequencies of kHz level, dynamic loss can still dominate the total power dissipation in the middle turns of racetrack coils.

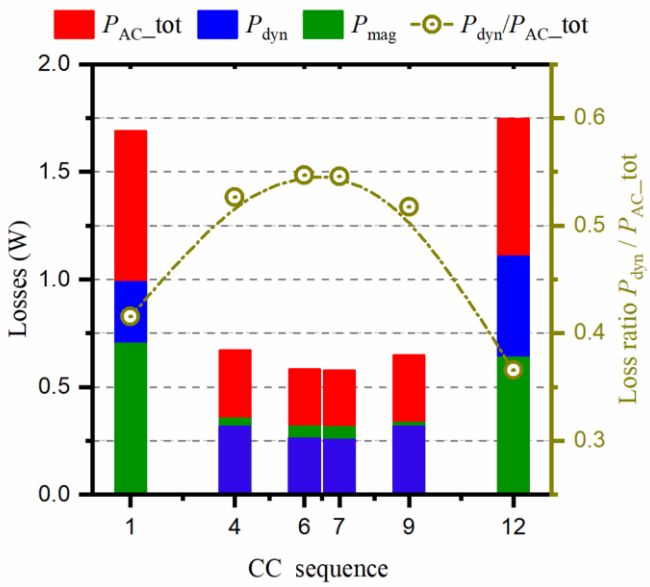

Figure 5.3.22 Total loss, dynamic loss and magnetization loss of the 1st, 4th, 6th, 7th, 9th and 12th double turn (from inside to outside) in the racetrack coil, when f = 1 kHz, B_{ext} = 50 mT, and I_t = 50 A.

It should be pointed out that in Figure 5.3.15 the total loss of each turn of the circular coil increases from the inside out, which is different from Figure 5.3.22. In fact, the modelling of the circular coil is based on a 2D method, in which the externally applied magnetic field is centrosymmetric as described in [330], thus the shielding effect on the inner parts is from the outermost turn. However, the modelling of the racetrack coil here is a 3D method, and the externally applied magnetic field is not centrosymmetric, thus both the innermost and outermost turns share the shielding effect on the middle ones. From this point of view, it can

only be achieved by 3D modelling methods to set a complex spatial magnetic field based on different boundary conditions, which is a distinguished advantage over 2D numerical models.

Figure 5.3.23 describes the variation of the AC losses in different layers, dynamic loss as well as magnetization loss in the racetrack double pancake coil. Generally, Figure 5.3.23 shows the same trend as Figure 5.3.16 and Figure 5.3.11, that the total loss, the magnetization loss and the loss generated in the copper stabilizers increase rapidly with frequency due to the skin effect. The magnetization loss becomes greater than the dynamic loss for frequencies higher than 200 Hz, and the loss ratio P_{dyn}/P_{AC_tot} drops from 51% at 100 Hz to approximately 40% at 20 kHz. Therefore, in the studied frequency range, the magnetization loss generally plays a dominant role ; however, the portion of dynamic loss over the total loss remains above 45% within the frequency band below 3 kHz. Hence, as concluded in Section 5.3.2.3, both dynamic loss and magnetization loss are significant for the HTS coils operated in a high-speed synchronous machine.

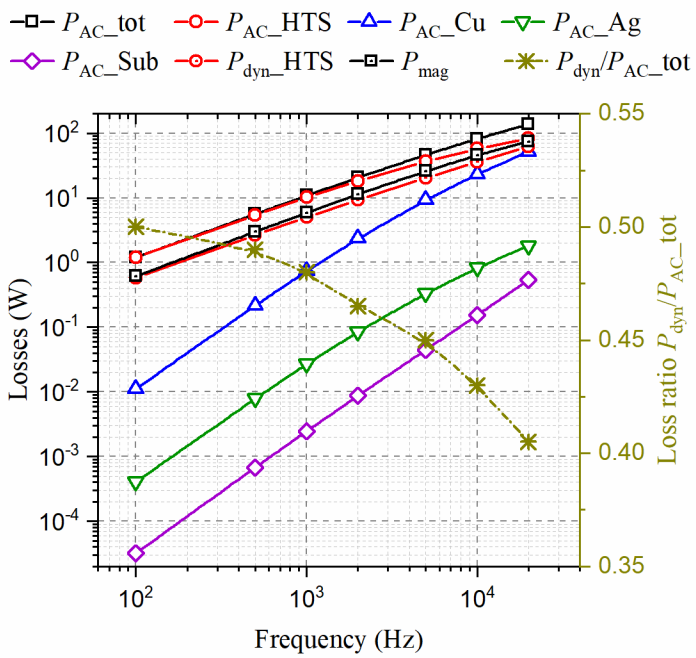

Figure 5.3.23 Variation of AC losses in different layers, dynamic loss magnetization loss, and loss ratio P_{dyn} /P_{AC_tot} with frequency for the HTS racetrack double pancake coil. *f* ranges from 100 Hz to 20 kHz. I_t = 50 A. B_{ext} = 50 mT.

5.3.3 Summary

In Section 5.3, through an ***H***-formulation based numerical modelling method, the frequency dependence of dynamic loss and magnetization loss for an HTS CC, a stack, a circular double pancake coil as well as a racetrack double pancake coil over a wide range, from 100 Hz to 20

kHz has been systematically investigated. The adopted numerical multilayer models have taken into account the physical structure of a CC, namely the copper stabilizers, HTS layer, silver overlayer as well as substrate, which have been validated by multiple experimental measurements from other published work.

The existing definition of the dynamic region and analytical equations for calculating dynamic loss have been found to be not applicable at the kHz level, in that the dynamic region of a single CC shrinks rapidly with increasing frequency and the skin effect results in a redistribution of magnetic flux and current among different layers. Therefore, the ***H***-formulation based numerical multilayer model has been proposed to quantify the dynamic loss and magnetization loss. Afterward, the correlation between dynamic loss, magnetization loss, and the total loss has been discussed in detail.

(1) In general, magnetization power loss is in a positive correlation with frequency. Under the skin effect, both current and magnetic flux inside the CC will be driven to both ends and outer copper stabilizers with increasing frequency, thus the losses in the copper stabilizers will be approaching magnetization loss as well as the total loss.

(2) There exists a positive correlation between dynamic loss and frequency followed by a negative one because at higher frequencies the amount of traversing magnetic flux during one AC cycle shrinks rapidly. For example, the peak value of dynamic loss appears at f = 10 kHz for the studied stack with i = 0.5 and B_{ext} = 20 mT.

(3) At low frequencies, dynamic loss occupies the majority of the total AC loss for HTS CCs, stacks and coils. For example, when f = 100 Hz, I_t = 50 A and B_{ext} = 50 mT, the loss ratio between dynamic loss and total loss of the double pancake racetrack coil is above 50%. However, as the frequency increases, the magnetization loss becomes more important due to the skin effect, indicated by a reduction in the loss ratio to 40% at 20 kHz.

(4) At low frequencies, e.g., f = 100 Hz, a higher B_{ext} leads to a higher dynamic loss because of more magnetic flux traversing the HTS CC. However, at higher frequencies above 1 kHz, a higher B_{ext} results in a higher magnetization loss due to the skin effect and the loss contribution from copper stabilizers.

(5) Compared with a single CC, the influence of dynamic loss in HTS stacks or coils is more significant because the shielding effect among different turns can enhance the significance of dynamic loss, bringing about a higher magnetization loss ratio in the outermost turns and a higher dynamic loss proportion in the middle parts.

To conclude, under the skin effect and shielding effect, both dynamic loss and magnetization loss should be attached to high importance for the design of HTS magnets and machine windings operated in a high-frequency environment, e.g., at the kHz level or even higher. For quantifying the loss characteristics over a wide frequency range, the numerical multilayer model considering the physical CC structure has to be used. With respect to modelling of HTS racetrack coils carrying transport current under varying magnetic fields, the 3D numerical model is recommended with different boundary conditions, so that a complex external magnetic field can be applied. This research work can be used for accurate loss controlling in HTS machine windings and magnets operated in a high-frequency environment, providing some reference for the design of future aerospace electric propulsion systems.

It should be underlined that this work concentrates on the electromagnetic characteristics of HTS windings applied in high-speed machines. Therefore, the field dependence of critical current of HTS CCs has been considered and we assume that the cooling power of the cryocooler is sufficient to remove the heat dissipation in the coils instantaneously. In this case, the temperature dependence of critical current and the overall design of cryogenic systems have not been considered here. However, the predicted loss distribution and quantified loss level provide a reference to the overall design of highly efficient cryogenic systems. In the future, more research should be carried out to explore the thermal properties of HTS windings and the design of highly efficient cryocoolers for aerospace superconducting machines.

5.4 Electromagnetic Properties of Curved HTS TFSs Under High-frequency Cross Fields

The high field source in superconducting machines can be superconducting coils and super permanent magnets. For aerospace machines operating at very high speeds (7-50 krpm), no active windings on the rotor seem to be an ideal choice to reduce the influence of the significant centrifugal stress [15, 331]. Besides, using superconducting coils as field sources generally requires a high current power supply, and they are likely to encounter a sudden failure through quench [96]. Super permanent magnets are composed of bulk superconductors and TFSs. HTS bulks have shown great flux trapping capacity, achieving a world record of 17.6 T at 26 K [90]. However, a crucial problem with HTS bulks is their thermal instability at low temperatures, which makes it difficult to take advantage of the high critical current below 30 K [95]. Besides, external mechanical reinforcement is needed in the application of bulks due to their imperfect mechanical strength. As a comparison, HTS TFSs made of CCs have better thermal stability, because the silver overlayer and copper stabilizers in HTS CCs have a

thermal conductivity over an order of magnitude higher than REBCO. Additionally, as far as mechanical strength is concerned, the Hastelloy substrate in HTS CCs has a stronger tensile strength compared to REBCO, thus they can support higher magnetic stresses [95].

Electromagnetic simulation of HTS TFSs is necessary to estimate their field-trapped capacity before the production. Most of the existing numerical models regarding magnetization of HTS stacks are 2D, and the flat stack is modelled as an anisotropic bulk (square or round) in many cases to save computational time [29, 332-334]. For example, in [334] a 2D-axisymmetric model has been employed given that the field trapped in square and round stacks differs by less than 4%. However, we have to note that the magnetic flux density and current density distributions in the round and rectangular tapes are different [335], and 3D modelling is inevitable for a curved spatial geometry [336]. Besides, a comprehensive analysis of curved HTS TFSs is still lacking, which possess geometrical applicability for cylindrical rotating shafts. In many applications, it is sufficient to know the maximum possible trapped field, thus the critical state model assumption can be applied to the simulation of stacks [337]. To achieve the highest trapped field, pulsed filed magnetization (PFM) has been proposed [147, 338-339]. Nevertheless, the magnetization methods and trapped field amplitude are not the focus of this section. In this study, I aim to investigate the electromagnetic distribution properties of curved HTS TFSs, and it is necessary to consider the field dependence of critical current and model the complete dynamic magnetization process.

Exposed to AC cross fields, HTS stacks experience a decrease of the trapped field [97, 340-342], and thus a possible demagnetization can happen in a certain situation. The demagnetization of trapped field magnets would be disastrous for aircraft propulsion and generation systems. In high-speed (7-50 krpm) rotating machines for future aviation, high-frequency AC ripple fields always exist within the range of ~0.2-2 kHz, and the fields transverse to the surface of CC are abundant. For now, the electromagnetic behaviour of HTS TFSs under high-frequency fields remains unclear. In addition, according to Section 5.2 and 5.3, at frequencies higher than 100 Hz, it is necessary to consider the multilayer physical structure of HTS CCs to quantify magnetization loss due to the skin effect. The existence of the copper stabilizers, silver overlayer, and substrate can influence the loss distribution inside CCs. [343] has studied the effect of stabilizers on trapped fields of TFSs magnetized by PFM, and demonstrated that the trapped field is insensitive to the stabilizer thickness. However, the influence of high-frequency cross fields on HTS TFSs considering the multilayer structure of each CC is still unknown, i.e., a corresponding 3D numerical modelling work is still lacking.

In response to the above-mentioned issues, here I adapt the 3D numerical model in Section 5.3 to a curved HTS TFS. Firstly, I have studied the electromagnetic characteristics of a single curved square CC under perpendicular field magnetization. Then, its electromagnetic performance in the time domain during PFM has been presented. Next, under the influence of high-frequency cross fields varying from 50 Hz to 20 kHz, the current and magnetic flux density distributions as well as loss properties of the curved CC after PFM have been investigated. In the end, a case study has been conducted on an HTS TFS composed of 5 CCs within the same frequency range. This research work is believed to add upon the existing knowledge of HTS TFSs, providing a useful reference for their design and application in high-speed rotating machines for future aviation.

5.4.1 Numerical model

The ***H***-formulation based 3D numerical modelling method has been adopted here. The studied HTS CC sample was originally a square tape with a side length of 12 mm, which has been bent into a curved surface with a central angle of 1.2 rad, as shown in Figure 5.4.1. The sample is a cold-rolled Hastelloy C276 tape, with the functional layers deposited by the IBAD-MgO/PLD-GdBCO route [343]. It is composed of 5 layers, namely two copper stabilizers with the thickness of 20 μm for each one, a 2 μm-thick silver overlayer, a 1 μm-thick GdBCO layer as well as a 60 μm-thick substrate.

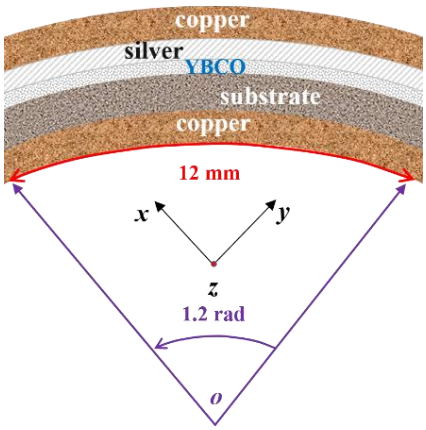

Figure 5.4.1 Cross section of the multilayer structure of the studied curved HTS CC, manufactured by SuperOX. (The thickness of each layer does not reflect the real scale). *x*, *y*, and *z* stand for the axes of the 3D Cartesian coordinate system.

The ***H***-formulation can be implemented into COMSOL Multiphysics and solved by FEM. The 3D multilayer FEM numerical model of the whole curved square CC is shown in Figure 5.4.2. The curved CC is surrounded by air, and the Dirichlet boundary condition has been exploited on its outer surface to apply the perpendicular and cross fields.

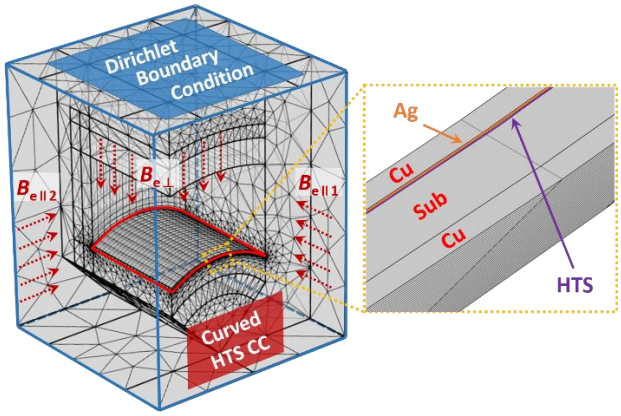

Figure 5.4.2 Meshing view of the curved multilayer HTS CC and surrounded air in COMSOL Multiphysics. $B_{e\perp}$ is the externally applied perpendicular magnetic field, $B_{e\parallel 1}$ and $B_{e\parallel 2}$ represent the externally applied cross fields.

The specifications and parameter values for simulation of the studied CC sample are summarized in Table 10.

Table 10. Specification of the modelled square HTS CC [343]

Symbols	Quantity	Value
w	CC side length	12 mm
h_{HTS}	HTS film thickness	1 μm
h_{Cu}	Single stabilizer thickness	20 μm
h_{Ag}	Silver thickness	2 μm
h_{sub}	Substrate thickness	60 μm
T	Single CC thickness	103 μm
σ_{Cu}	Copper conductivity at 77 K	5.076×10^8 S/m
σ_{Ag}	Silver conductivity at 77 K	3.704×10^8 S/m
σ_{sub}	Substrate conductivity at 77 K	8×10^5 S/m
μ_0	Free space permeability	$4\pi \times 10^{-7}$ H/m
n	Power-law exponent	21
I_{c0}	Self-field critical current at 77 K	100 A
E_0	Characteristic E-field	10^{-4} V/m
B_0	Magnetic field constant	1.3 T

It should be noted that for the magnetization due to perpendicular magnetic fields, we can model one-quarter of the whole geometry to reduce the numbers of the degree of freedom (DOF) and save computational time, as presented in [336]. However, once considering the

application of cross fields with arbitrary orientation, the boundary condition on the symmetry plane of the quarter model can not be simply determined by the zero flux or Dirichlet boundary condition. Therefore, to apply simultaneously perpendicular and parallel magnetic fields with arbitrary orientations, we have chosen to model the whole geometry at the sacrifice of computational time. It needs to be clarified that here the perpendicular and parallel fields are defined in terms of the 3D Cartesian coordinate system rather than the curved surface, so that a field with arbitrary orientation can always be decomposed into different components along three axes. As shown in Figure 5.4.1 and Figure 5.4.2, $\boldsymbol{B}_{e\perp}$ refers to the externally applied perpendicular magnetic field, which is along the symmetry line between the *x*-axis and *y*-axis. $\boldsymbol{B}_{e\parallel 1}$ and $\boldsymbol{B}_{e\parallel 2}$ represent the parallel external magnetic fields, which are parallel and perpendicular to the *z*-axis, respectively.

In order to validate the proposed 3D numerical modelling method, we have built firstly a 3D model based on the ***H***-formulation for the flat cubic bulk superconductor employed in Benchmark #5 in HTS Modelling Workgroup [344], and then compared the modelling results with the benchmark solutions. The established numerical model in COMSOL Multiphysics and the bulk dimensions can be found in Figure 5.4.3. Considering the symmetry of the cubic bulk, to save computational time, we have chosen to model a quarter of it. It should be noted that the zero flux boundary condition needs to be applied to the symmetrical cross sections because the external magnetic field is along the *z*-axis. The applied magnetic field is sinusoidal with the amplitude of 200 mT and the frequency of 50 Hz. The critical current density of the bulk superconductor is set as $J_{c0} = 10^8$ A/m^2.

Taking J/J_{c0} at the phase of 2π at the plane z = 0.12 mm as an example, the benchmark solution and the modelled result are both shown in Figure 5.4.4. Besides, the current density ratio J_z/J_{c0} along the *x*-axis at y = 2.07 mm and z = 1.1 mm is presented in Figure 5.4.5. The benchmark solutions in Figure 5.4.4 and Figure 5.4.5 are obtained by using the Minimum electro-magnetic entropy production (MEMEP) method [344]. It can be seen that the simulation results are in good accordance with the benchmark solutions, thus it is believed that the adopted 3D modelling method in this paper is validated. In the ***H***-formulation based model, we have then replaced the cubic bulk superconductor with the curved HTS CC and stack. Afterwards, this section has centred around the modelling work of the curved HTS CC and stack.

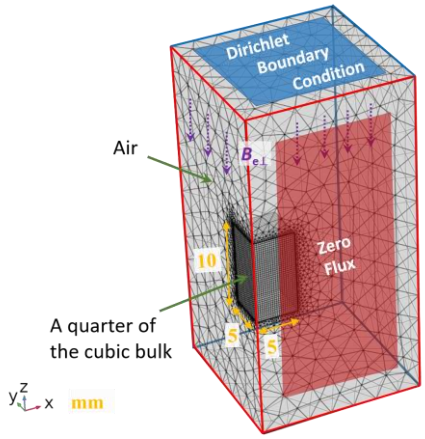

Figure 5.4.3 One quarter meshing view of the falt cubic bulk superconductor and surrounded air in COMSOL Multiphysics. $B_{e\perp}$ is the externally applied perpendicular sinusoidal magnetic field.

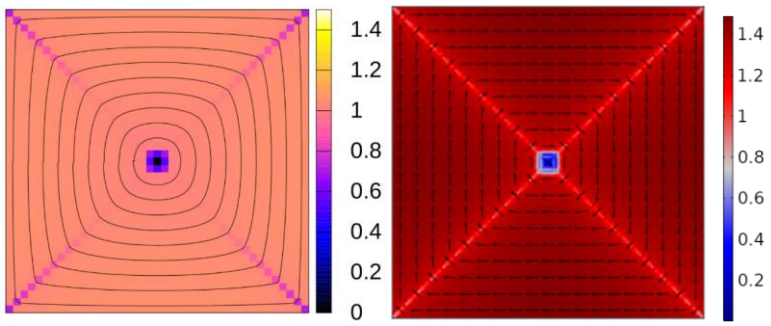

(a) (b)

Figure 5.4.4 J/J_{c0} at the phase of 2π at the plane z = 0.12 mm for the benchmark cubic bulk superconductor model and the model built in this paper. (a) represents the benchmark solution [344]. (b) shows the modelled result, in which the black arrows illustrate the current direction along with the current streamlines.

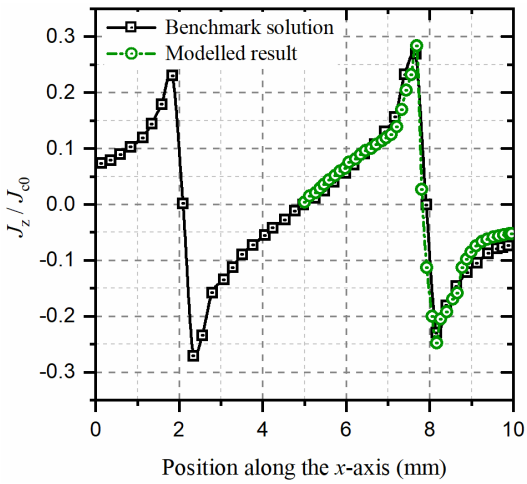

Figure 5.4.5 J_z/J_{c0} along the x-axis at y = 2.07 mm and z = 1.1 mm for the benchmark cubic bulk superconductor model and the model built in this paper. The benchmark solution is obtained using MEMEP, and the relevant data are extracted from Figure 7 in [344].

5.4.2 Electromagnetic properties of a single curved CC

In this section, we have simulated the magnetization process of a single curved square HTS CC under AC perpendicular magnetic fields and a pulsed field, respectively. Cross fields of distinct frequencies have been applied to the trapped field CC, and the multilayer electromagnetic distributions have been explored.

5.4.2.1 Magnetization by AC perpendicular fields

In this section, the applied perpendicular magnetic field is determined by $\boldsymbol{B}_{e\perp} = B_{ext}\cdot\sin(2\pi ft)\,\vec{x} + B_{ext}\cdot\sin(2\pi ft)\,\vec{y}$. B_{ext} is set as 100 mT, and the frequency of the applied field, f, varies from 50 Hz to 20 kHz.

Figure 5.4.6 demonstrates the magnetic flux density [(a)-(d)] and current density [(e)-(h)] distributions in the curved square HTS layer at the phase of $3\pi/2$. Although a benchmark model for 3D simulation of a curved square multilayer HTS CC is lacking, the J/J_c distributions in the HTS layer at low frequencies, e.g., at 50 Hz presented in (e), are still comparable to those of the benchmarked flat superconductor in [344]. In (e)-(h), the black arrows describe the current flow direction along the current streamlines, which complies well with Lenz's law. The current streamlines exhibit a rectangular shape and they bend sharply in the 'discontinuity lines' with a lower current density, which coincides with the zero vortex velocity passing through the four corners. More related explanations can be found in [335, 345-346]. Here, we define the 'discontinuity lines' as 'electromagnetic criss-cross', which divides the curved square surface into 4 roughly equivalent subdomains.

According to Figure 5.4.6 (a)-(d), it can be found that the penetrated magnetic flux will be driven towards the four sides with increasing frequencies, and their amplitudes augment accordingly in a positive way. The same trend also occurs to the current density distribution, i.e., the maximum current density increases positively with frequency and the induced current is pushed to the four sides of the CC. Nevertheless, it is interesting to note that at higher frequencies in (g) and (h), different from (e) and (f), the current flow direction in the central section is opposite to that in the regions near the edges of the CC. In fact, as shown in (a)-(d), the magnetic flux penetrates into the CC starting from the middle edges, thus the change of current flow directions happens from outside to inside. At low frequencies, after one complete AC cycle, the overturn of current flow directions can be finished. However, at high frequencies, it becomes harder for the magnetic flux to penetrate into the central region due to the skin effect, as shown in (c) and (d). As a result, the induced current in the central part demonstrates a kind of 'lag effect' and seems less sensitive to the variation of external magnetic fields.

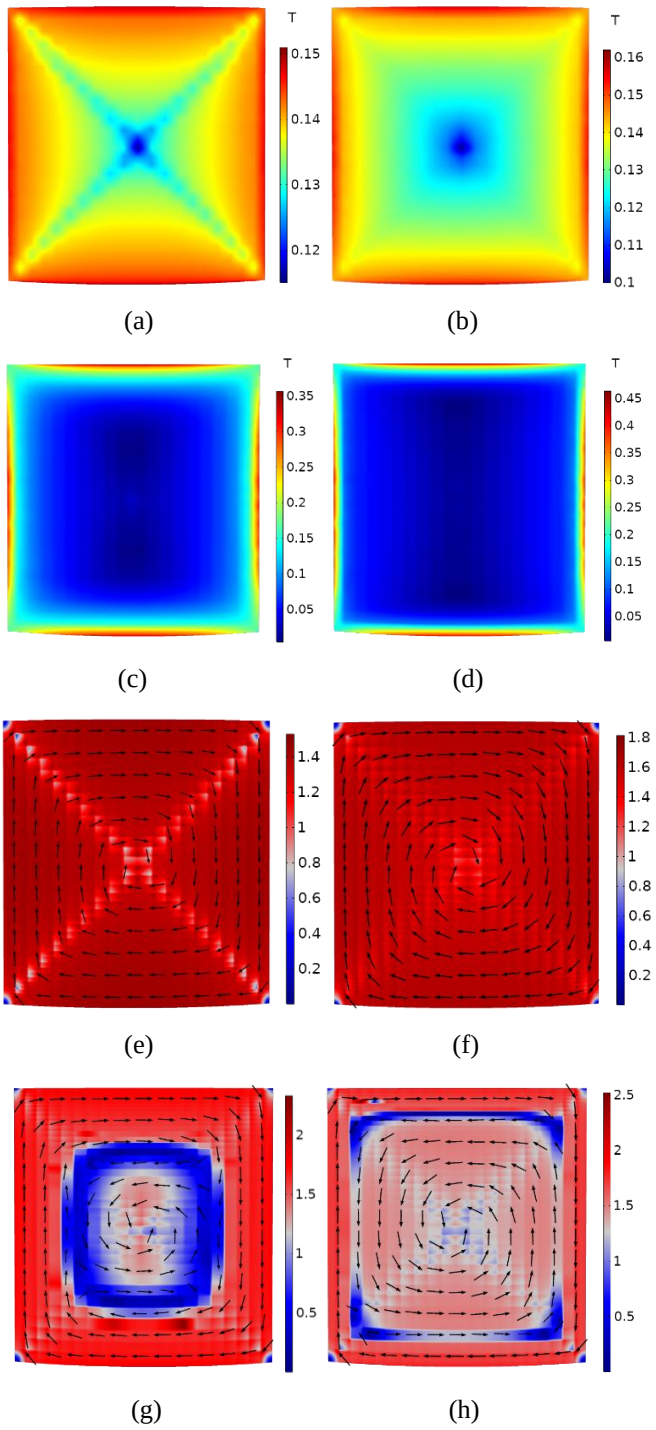

Figure 5.4.6 Magnetic flux density and current density distribution in the curved HTS layer. B_{ext} = 100 mT, and f varies from 50 Hz to 20 kHz. (a)-(d) represent the magnetic flux density distribution at the phase of 3π/2 for f = 50 Hz, 1 kHz, 10 kHz, and 20 kHz, respectively. (e)-(h) show separately J/J_c at the phase of 2π for f = 50 Hz, 1 kHz, 10 kHz, and 20 kHz. The black arrows illustrate the current flow direction along with the current streamlines.

The loss per unit volume distributions at the phase of 2π in different layers, defined by $\boldsymbol{E}\cdot\boldsymbol{J}$ (W/m^3), have been presented in Figure 5.4.7. Figure 5.4.7 (a)-(d) show the loss density

distributions in the HTS layer at 50 Hz, 1 kHz, 10 kHz, and 20 kHz, respectively. In the same way, (e)-(h), (i)-(l), (m)-(p) correspond separately to the loss properties in the silver overlayer, substrate, as well as upper copper layer. It is easily understood that, the highest loss density within the frequency range 50 Hz-20 kHz is always generated in the HTS layer because it has the highest electrical conductivity compared to other layers, thus most induced current is concentrated in the HTS layer. Similarly, the loss density in the copper stabilizer is comparable to that of the silver overlayer, both of which are much higher than the loss density in the substrate. For each layer, the power dissipation tends to gather at the CC edges with increasing frequencies, under the skin effect. Consequently, the maximum loss density in every layer grows positively with increasing frequencies.

It can also be found that, for every layer, most of the loss is concentrated on the middle edges of the CC, which cannot be predicted by 2D modelling methods, especially the 2D-axisymmetric model. Evidently, the loss density distribution is determined by both the electric field and current density distributions. Brandt has systematically studied the electric field in superconductors with rectangular cross sections and concluded that, in the critical state flux penetrates mainly from the middle of the edges of the rectangular rather than from the corners [335]. As a result, the varying $\boldsymbol{E}\cdot\boldsymbol{J}$ due to the penetrated magnetic field will be generated starting from the middle edges. At low frequencies, e.g., 50 Hz, Figure 5.4.6 (a) and (e), as well as Figure 5.4.7 (a), comply well with the magnetic field, current, and electric field profiles in [335].

It is interesting to note that the $\boldsymbol{E}\cdot\boldsymbol{J}$ distribution pattern in the substrate at 50 Hz is peculiar, as shown in Figure 5.4.7 (i), not only different from other layers at the same frequency but also different from the same layer at higher frequencies. It appears that in the vertical and horizontal regions of (i), the power dissipation per unit volume is much lower. In fact, this phenomenon is tightly related to the curvature of the CC. Given that the studied CC is curved and the applied magnetic field, $\boldsymbol{B}_{e\perp}$, is perpendicular to the *z*-axis, $\boldsymbol{B}_{e\perp}$ is thus not strictly perpendicular to the wide surface of the CC everywhere. In other words, there exist some local parallel field components in the curved CC surface. Under the time-varying local parallel magnetic fields, an eddy current will be induced across the 5 layers of the CC. Considering that the conductivity of the substrate is much lower than the other layers, and the substrate belongs to the middle layers of the multilayer structure, the eddy current passes through the substrate but does not gather here. A a result, the eddy current will strengthen the current density in the regions located on the current loop, scilicet in these regions, $\boldsymbol{E}\cdot\boldsymbol{J}$ gets higher compared with the vertical and horizontal regions in (i). Figure 5.4.8 (a) shows the current

streamlines on the cross section of the CC in the *x-y* plane at 50 Hz. In order to better reflect the current density distribution in different layers, the current density has been interpreted by the log transformation with a logarithm base of 10. It can be seen that in the higher $\boldsymbol{E}\cdot\boldsymbol{J}$ regions there exist eddy currents passing through the substrate, rather than in the middle part (lower $\boldsymbol{E}\cdot\boldsymbol{J}$ region), which agrees well with the above analyses. In the two higher $\boldsymbol{E}\cdot\boldsymbol{J}$ regions, the current loop directions are distinct because the local parallel field vectors are different. However, as the frequency increases, the eddy current loops will be driven towards both ends of the CC cross section, i.e., the area in the substrate through which the induced current passes will be reduced. Figure 5.4.8 (b) demonstrates the current streamlines on the cross section of the CC in the *x-y* plane at 20 kHz. It can be found that the eddy current generated by the local parallel fields is confined to both ends of the cross section. Besides, the bending angle of the CC is only 1.2 rad, thus the local perpendicular field components are dominant compared to the parallel ones, and this dominance of the local perpendicular fields plays a more significant role at higher frequencies in that the power dissipation increases fast with frequency due to the skin effect. Therefore, at high frequencies, the influence of the local parallel fields on the $\boldsymbol{E}\cdot\boldsymbol{J}$ distribution pattern gets weaken and the penetration effect of the local perpendicular field from the middle edges becomes enhanced.

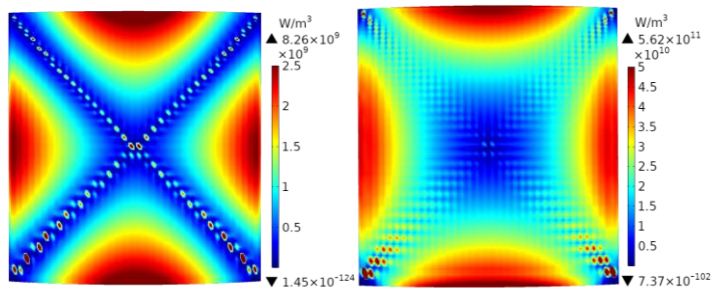

(a) (b)

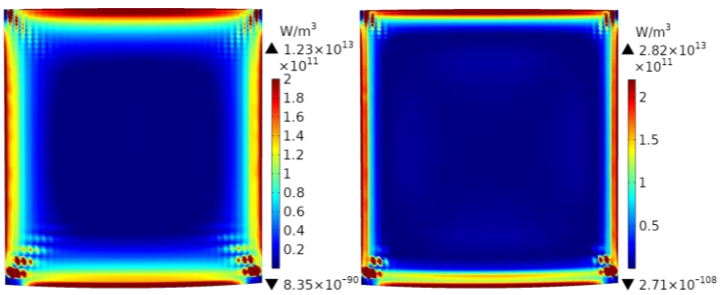

(c) (d)

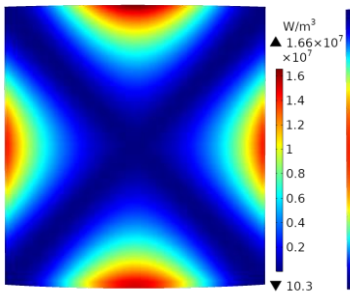
W/m³
▲ 1.66×10⁷
×10⁷
1.6
1.4
1.2
1
0.8
0.6
0.4
0.2
▼ 10.3

(e)

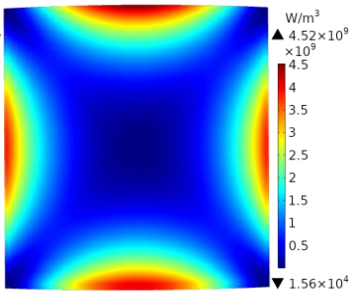
W/m³
▲ 4.52×10⁹
×10⁹
4.5
4
3.5
3
2.5
2
1.5
1
0.5
▼ 1.56×10⁴

(f)

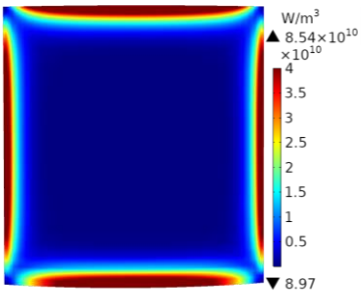
W/m³
▲ 8.54×10¹⁰
×10¹⁰
4
3.5
3
2.5
2
1.5
1
0.5
▼ 8.97

(g)

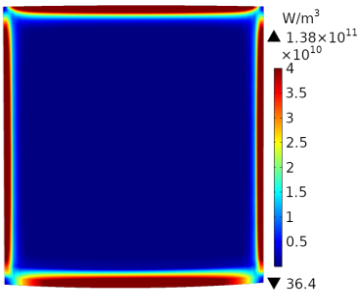
W/m³
▲ 1.38×10¹¹
×10¹⁰
4
3.5
3
2.5
2
1.5
1
0.5
▼ 36.4

(h)

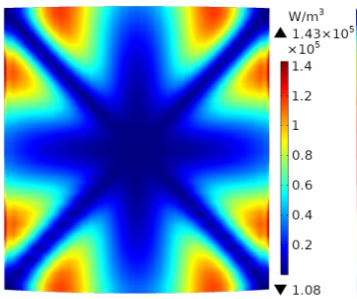
W/m³
▲ 1.43×10⁵
×10⁵
1.4
1.2
1
0.8
0.6
0.4
0.2
▼ 1.08

(i)

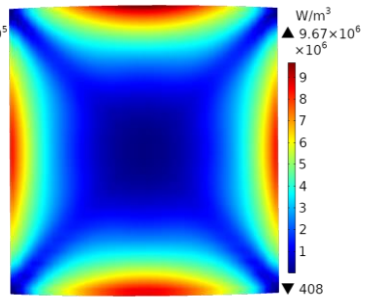
W/m³
▲ 9.67×10⁶
×10⁶
9
8
7
6
5
4
3
2
1
▼ 408

(j)

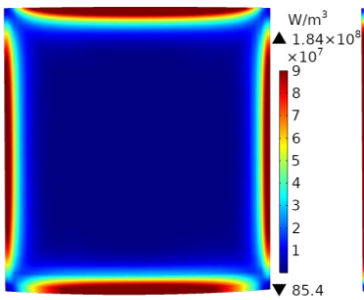
W/m³
▲ 1.84×10⁸
×10⁷
9
8
7
6
5
4
3
2
1
▼ 85.4

(k)

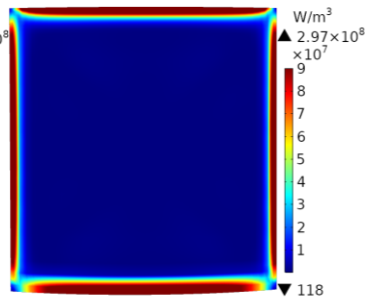
W/m³
▲ 2.97×10⁸
×10⁷
9
8
7
6
5
4
3
2
1
▼ 118

(l)

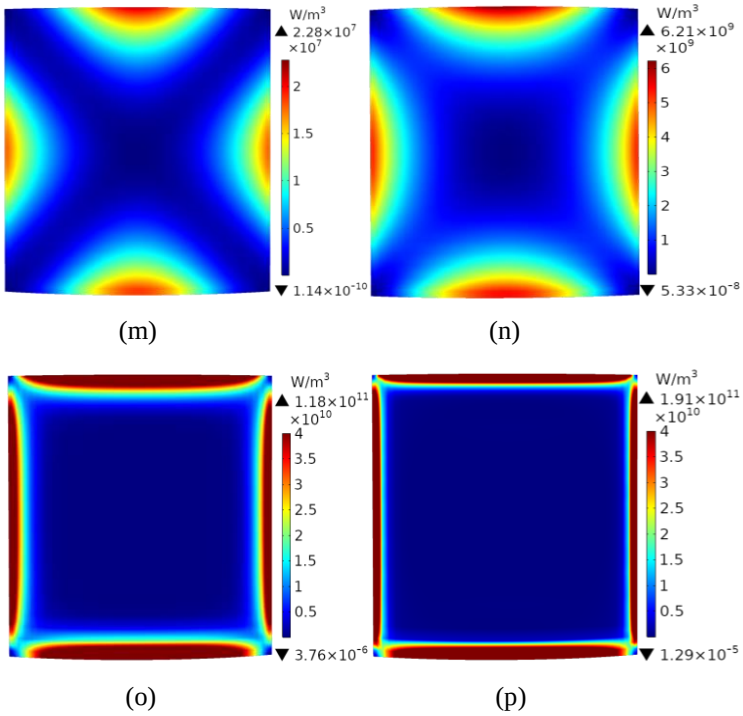

Figure 5.4.7 Distribution of loss per unit volume in different layers. B_{ext} = 100 mT, and f varies from 50 Hz to 20 kHz. (a)-(d) represent the loss distribution of the HTS layer at the phase of 2π for f = 50 Hz, 1 kHz, 10 kHz, and 20 kHz, respectively. In the same way, (e)-(h) show separately the loss distribution for the silver overlayer, (i)-(l) stand for the loss distribution of the substrate, and (m), (n), (o) and (p) refer to the loss distribution in the upper copper layer.

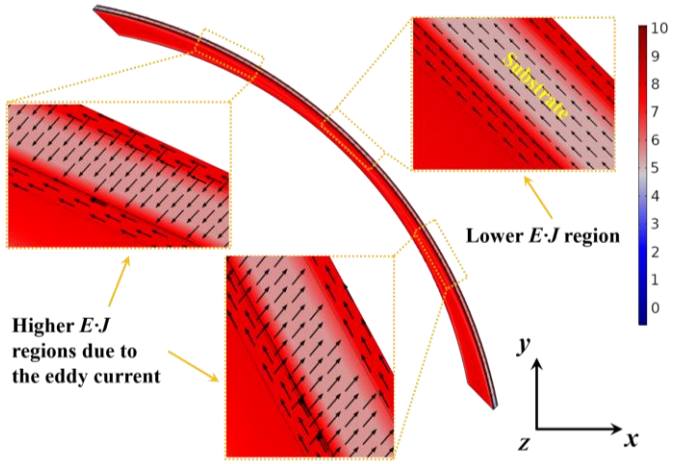

(a)

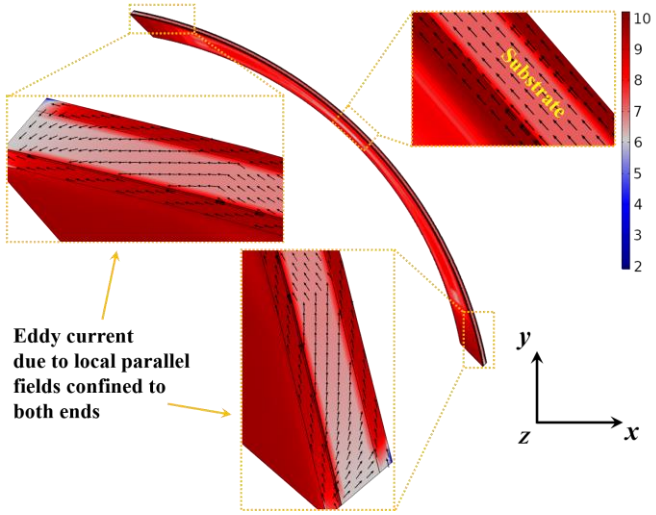

(b)

Figure 5.4.8 Logarithmized current density distribution in different layers and current flow arrows on the cross section of the curved HTS CC in the *x*-*y* plane at the phase of 2π, under the perpendicular field, $B_{e\perp}$. The color discrepancy represents the current density after the log transformation, and the logarithm base is 10. (a) f = 50 Hz. (b) f = 20 kHz.

Figure 5.4.7 shows that the maximum loss density always appears in the HTS layer. However, at high frequencies, when considering the volume of different layers, the majority of loss does not necessarily occur in the HTS layer. The losses produced in distinct layers with varying frequencies have been presented together in Figure 5.4.9. The total power dissipation (W) in each layer is calculated by

$$\boldsymbol{P} = 2f\int_{1/(2f)}^{1/f}\int_{V}\boldsymbol{E}\cdot\boldsymbol{J}dVdt \tag{5.9}$$

where V is the total volume of the studied layer.

It can be seen that, from Figure 5.4.9, generally most of the magnetization loss is concentrated in the HTS layer and copper stabilizers in that they have higher electrical conductivity at 77 K compared to the Hastelloy substrate and silver overlayer. Below 400 Hz, the majority of loss is generated in the HTS layer. However, when the frequency exceeds 400 Hz, the most loss is produced in the copper stabilizers, which is due to the skin effect. The loss ratio between the loss in the HTS layer and the total loss of all the layers, P_{HTS}/P_{tot}, decreases rapidly from 85% at 50 Hz to approximately 5% at 20 kHz. Therefore, in terms of the quantification of magnetization loss in stacked HTS CCs, it is not accurate to just model the HTS layer, even at power frequencies. On this basis, in the next section, we will investigate the electromagnetic characteristics of the curved square HTS CC magnetized by a typical pulsed field.

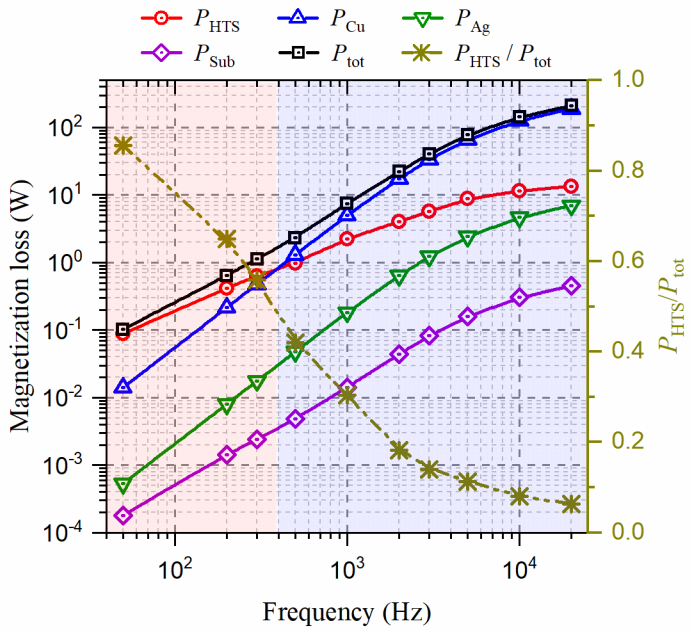

Figure 5.4.9 Variation of magnetization losses in different layers, and loss ratio P_{dyn}/P_{AC_tot} with frequency for the curved square HTS stack. f ranges from 50 Hz to 20 kHz. B_{ext} = 100 mT.

5.4.2.2 Trapped field CC under cross fields

As mentioned in [147] and [339], PFM serves as a practical method to magnetize HTS stacks in virtue of its low cost, compactness, and mobility. The frequency band of a pulse is usually abundant, of which the upper cutoff frequency depends closely on its rise time, τ (here rise time refers to the duration in which the pulse amplitude increase from zero to its maxima). We use the single pulse adopted in [147] as the applied perpendicular magnetic field, which is defined by

$$B_{\perp} = \begin{cases} B_{ext} \sin^2\left(\dfrac{\pi}{2\tau}t\right), & t < \tau \\ B_{ext} \cos^2\left[\dfrac{\pi}{10\tau}(t-\tau)\right], & \tau \le t \le 6\tau \end{cases} \tag{5.10}$$

where B_{ext} denotes the maximum amplitude of the pulsed field. Here B_{ext} is set as 2 T, and τ = 10 ms. The time-frequency characteristics of the magnetic field pulse are shown in Figure 5.4.10, obtained by short-time Fourier transform (STFT). It can be seen that most of the frequency components are concentrated in the band 0-150 Hz, and most of the signal energy is within the time window 0-40 ms.

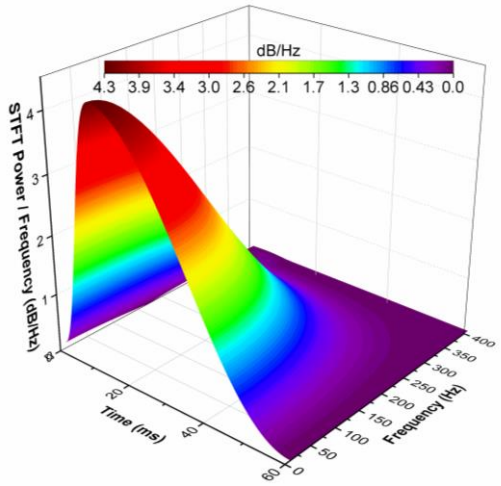

Figure 5.4.10 Time-frequency spectrum of the pulsed filed. B_{ext} = 2 T, and τ = 10 ms. STFT: short-time Fourier transform.

5.4.2.2.1 Perpendicular PFM

Before applying AC cross fields, we need to investigate the electromagnetic properties of the curved square CC under perpendicular PFM. Given that the primary frequency components of the applied field pulse are within the band of 150 Hz, we just focus on the HTS layer in this section. The magnetic flux density and current density distribution of the curved HTS layer at different time nodes, namely 10 ms, 12 ms, 15 ms, 60 ms, have been presented in Figure 5.4.11, respectively. (a)-(d) demonstrate the flux density distribution at the four different time nodes, and (e)-(f) show the J/J_c distribution, accordingly. (a)-(d) clearly illustrate that the applied field pulse penetrates into the HTS layer from the middle edges of the curved CC, which agrees well with [335] and the previous analysis. The magnetic flux moves towards the centre and finally, the highest flux density is kept in the central area. The distribution of the trapped flux density also exhibits an electromagnetic criss-cross on the surface of the HTS layer, which cannot be obtained by the conventional 2D modelling methods. (e)-(f) demonstrate the same trend as (a)-(d), that the induced current gradually occupies all the HTS layer surface from the edges towards the CC centre. It should be underlined that (f) is actually the intermediate state between (e), the beginning of the current direction change, and (g), the end of the direction change, with the variation of the external pulsed field. Despite the discrepancy of frequencies, Figure 5.4.11 (f) has the same variation characteristics as Figure 5.4.6 (g) and (h), both of which reflect the field trapping routes.

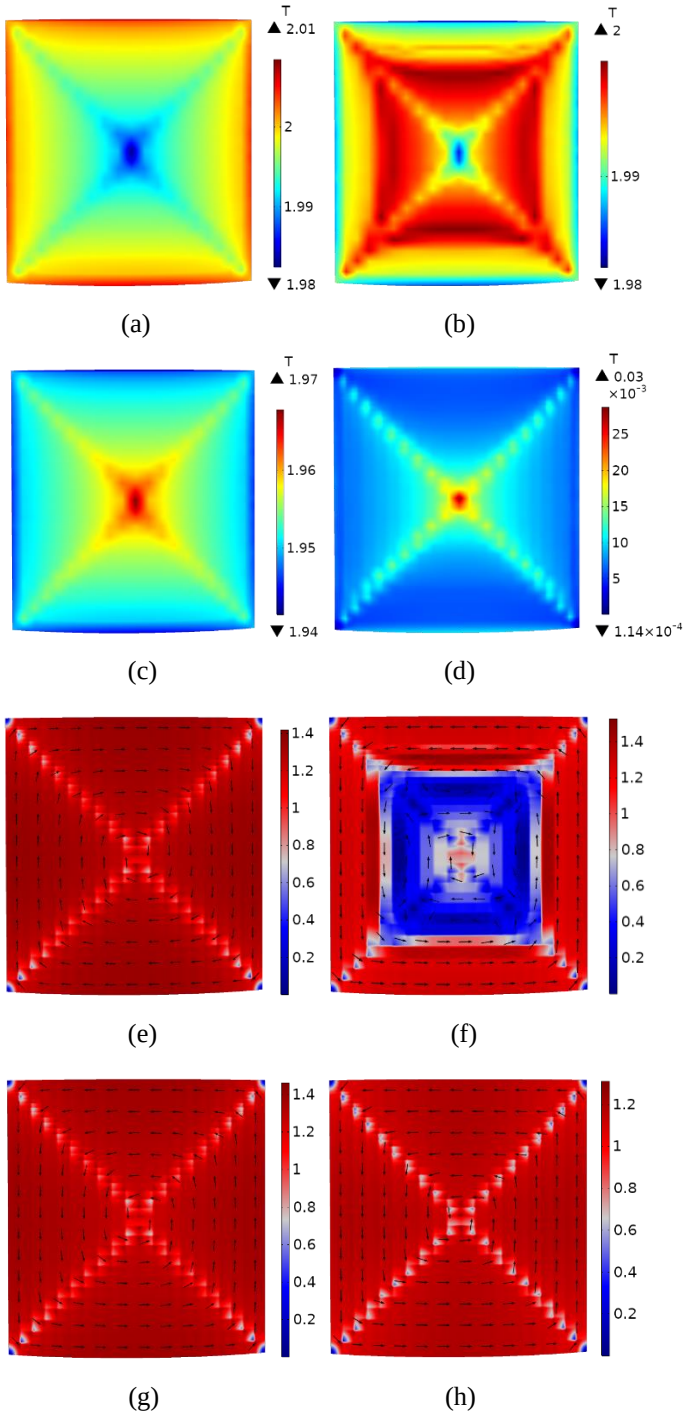

Figure 5.4.11 Magnetic flux density and current density distribution in the curved HTS layer under PFM. B_{ext} = 2 T, and τ = 10 ms. (a)-(d) represent the magnetic flux density distribution at the time nodes of 10 ms, 12 ms, 15 ms, and 60 ms, respectively. (e)-(h) show separately J/J_c at the time nodes of 10 ms, 12 ms, 15 ms, and 60 ms. The black arrows illustrate the current flow direction along with the current streamlines.

On the basis of Section 5.4.2.2.1, the influence of cross fields at different frequencies on the trapped field CC will be explored hereinafter. As shown in Figure 5.4.2, two types of

transverse fields, $\boldsymbol{B}_{e\parallel 1}$ and $\boldsymbol{B}_{e\parallel 2}$ will be separately applied to the CC after PFM, and their amplitude is set as 100 mT.

5.4.2.2.2 Cross field parallel to the z-axis

$\boldsymbol{B}_{e\parallel 1}$ is the externally applied cross field parallel to the *z*-axis. With frequency varying from 50 Hz to 20 kHz, the flux density and current density distribution in the HTS layer at the phase of 2π are presented in Figure 5.4.12. In general, at frequencies lower than 1 kHz, $\boldsymbol{B}_{e\parallel 1}$ does not have a significant influence on the field flux density and current density properties, especially for the trapped magnetic field, compared to Figure 5.4.11 (d) and (h). However, it is interesting that a discrepancy regarding electromagnetic distribution in the direction of the external transverse field appears, which can be found more clearly at high frequencies, as shown in Figure 5.4.12 (c)-(d) and (g)-(h). In fact, at the phase of 2π, the externally applied transverse field is along the negative direction of the *z*-axis, i.e., from bottom to top as far as the geometrical arrangement of the studied CC in Figure 5.4.12 is concerned. The electromagnetic criss-cross divides the HTS layer into four parts. Due to the variation of $\boldsymbol{B}_{e\parallel 1}$, a current will be induced in the HTS layer, which flows from left to right across the layer surface, named transverse current here. As a result, the current density in the bottom quarter is strengthened, and that in the top quarter part is weakened, as shown in (g) and (h). Accordingly, the current flow direction represented by black arrows in the left and right quarter parts becomes more inclined (not parallel to the edges) under the influence of the transverse current.

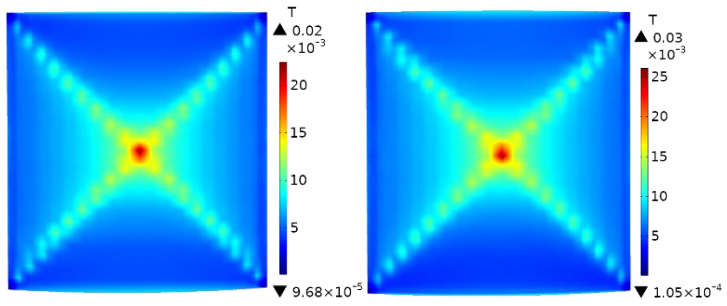

(a) (b)

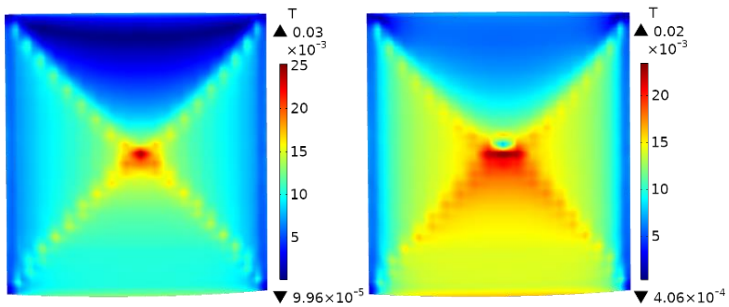

(c) (d)

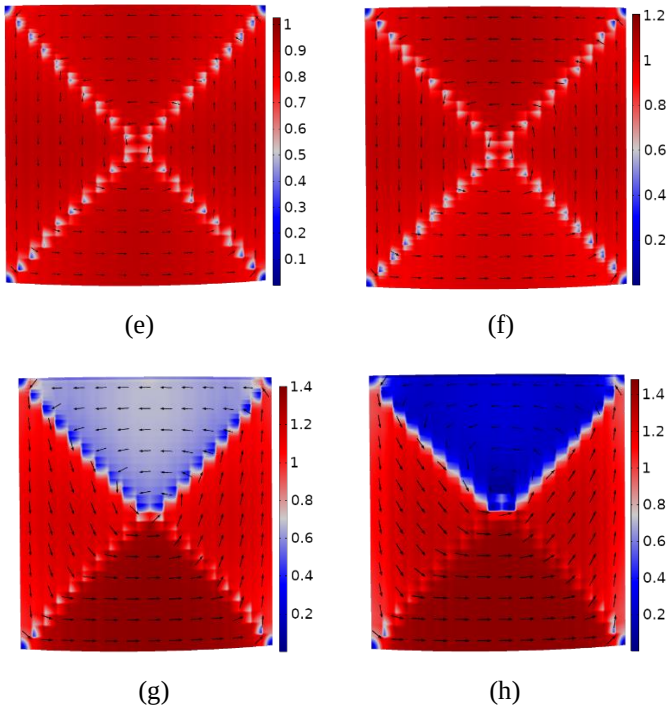

Figure 5.4.12 Magnetic flux density and current density distribution in the curved HTS layer. $B_{e\|1}$= 100 mT, and f varies from 50 Hz to 20 kHz. (a)-(d) represent the magnetic flux density distribution at the phase of 2π for f = 50 Hz, 1 kHz, 10 kHz, and 20 kHz, respectively. (e)-(h) show separately J/J_c at the phase of 2π for f = 50 Hz, 1 kHz, 10 kHz, and 20 kHz. The black arrows illustrate the current flow direction along with the current streamlines.

To further illustrate the flowing path of the transverse current, taking f = 20 kHz as an example, the current arrows along the streamlines on the cross sections of the curved CC have been presented in Figure 5.4.13. Figure 5.4.13 (a) shows the current density distribution on the cross section in the *y*-*x* plane located in the bottom quarter part of Figure 5.4.12 (h), and accordingly (b) demonstrates the current density distribution on the cross section in the *x*-*y* plane located in the top quarter region. At the phase of 2π, the applied cross field vector is along the negative direction of the *z*-axis and the field amplitude is decreasing, thus a counterclockwise current loop has been generated across all the 5 layers in the *y*-*x* plane as shown in (a), which complies well with the Lenz's law. In the same way, a clockwise current loop has been generated in the *x*-*y* plane as shown in (b).

Taking Figure 5.4.13 (a) as an example for detailed analysis, we have enlarged a region of the HTS layer and characterised the amplitude of current density by logarithmic arrow length, as shown in the lower right window (only in the smallest windows of Figure 5.4.13, the arrow length is logarithmized). It can be seen that the induced current direction due to the cross field coincides with the original current circulating on the wide curved surface, thus the total current

has been enhanced, which agrees well with the current variation in the bottom quarter part of Figure 5.4.12 (h). As a comparison, in (b) the induced current direction is opposite to the original circulating current thus the total current has been mitigated in the top quarter section. In addition, according to the color discrepancies, it can be clearly seen that the current density in the HTS layer of (a) is higher than that of (b). To conclude, the defined transverse current is generated by the externally applied AC cross field, which complies well with Lenz's law.

As for the reason for which this discrepancy appears more obvious at high frequencies, it can be well explained by Faraday's law, in that a higher rate of change of magnetic field leads to a higher induced current, as shown in Equation (3.2).

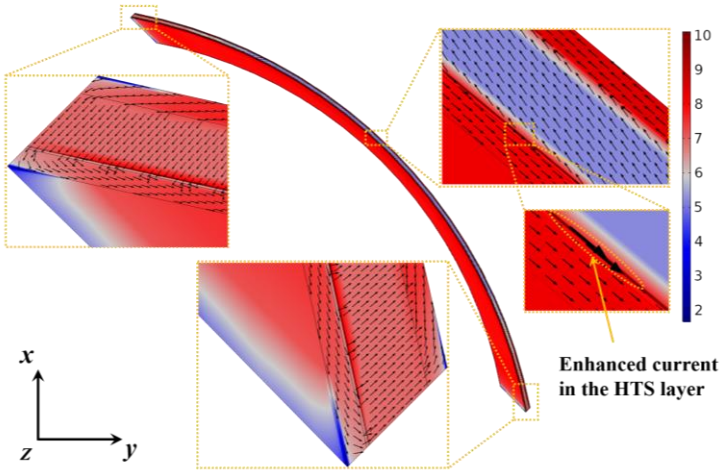

(a)

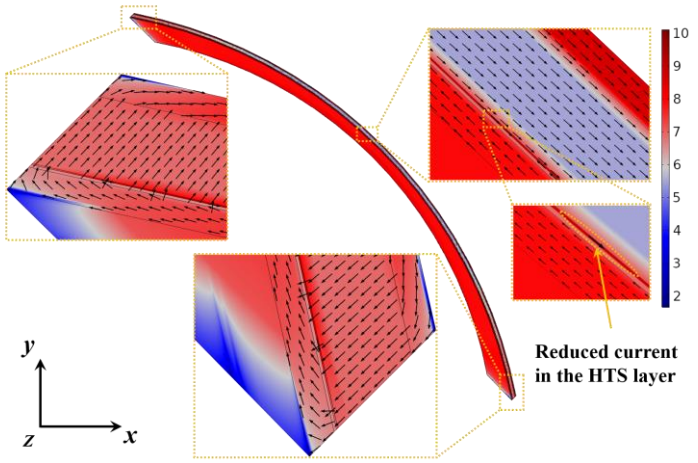

(b)

Figure 5.4.13 Logarithmized current density distribution in distinct layers and current flow arrows on the cross sections of the curved CC at the phase of 2π for f = 20 kHz, under the cross field $B_{e\|1}$= 100 mT. The color discrepancy represents the current density after the log transformation, and the logarithm base is 10. (a) Cross section in the *y*-*x* plane, located in the bottom quarter part of Figure 5.4.12 (h). (b) Cross section in the *x*-*y* plane, located in the top quarter part of Figure 5.4.12 (h).

5.4.2.2.3 Cross field perpendicular to the z-axis

As the studied square HTS CC has been curved around the *z*-axis, thus the transverse field perpendicular to the *z*-axis, $\boldsymbol{B}_{e\parallel 2}$, is not parallel to the whole curved surface. Similarly, when the frequency of $\boldsymbol{B}_{e\parallel 2}$ varies from 50 Hz to 20 kHz, the flux density and current density distributions in the HTS layer at the phase of 2π are presented in Figure 5.4.14. Different from the case of $\boldsymbol{B}_{e\parallel 1}$, though with the same amplitude, the existence of $\boldsymbol{B}_{e\parallel 2}$ has completely changed the electromagnetic distribution of the original trapped field CC, whether at low or high frequencies. In other words, the transverse field $\boldsymbol{B}_{e\parallel 2}$ has caused the demagnetization of the original trapped field CC.

At frequencies lower than 1 kHz, as shown in Figure 5.4.14 (a), (b), (e), and (f), the whole HTS layer can be decomposed into two symmetric curved rectangular CCs, each of which possesses independent magnetization centres and current paths. This phenomenon can be easily explained by Lenz's law, given that $\boldsymbol{B}_{e\parallel 2}$ is propagating from right to left when the phase approaches 2π, and its amplitude is simultaneously decreasing. Comparing (a)-(d), it can be found that, with increasing frequency, the penetrated flux is driven towards the left and right edges of the CC under the skin effect. The current streamlines presented in (e)-(h) also show the same trend. However, it is interesting to note that, at frequencies higher than 1 kHz, the streamlines in the central region are no longer parallel to the left or right edge. For example, in (h) the whole HTS layer can be decomposed into three different parts: one current loop in the central section, and two independent current paths near the edges. The current paths on both sides in (h) are similar to those in (e) and (f), though they have been pushed to the left and right edges of the CC under the skin effect. To understand the current loop in the central area, we need to refer to Figure 5.4.6 (g) and (h), because they have the same mechanism. As illustrated before, at high frequencies, the penetrated flux and induced current are constrained near the edges due to the skin effect, thus the current streamlines in the centre tend to remain the same as those of the previous phase. As a result, it becomes harder to change the current path in the central area with increasing frequencies, leading to a 'lag effect'. However, at high frequencies, the current density and magnetic flux density in the central area are much lower than those near the edges, thus this 'lag effect' of electromagnetic distribution does not play a significant role if we only consider where most of the flux and current are concentrated.

Nevertheless, it should be underlined that high-frequency cross fields can easily lead to the demagnetization of the trapped field CC. Therefore, for the design of high-speed superconducting machines equipped with TFSs, the influence of transverse fields, especially $\boldsymbol{B}_{e\parallel 2}$, has a significant effect, which must be considered.

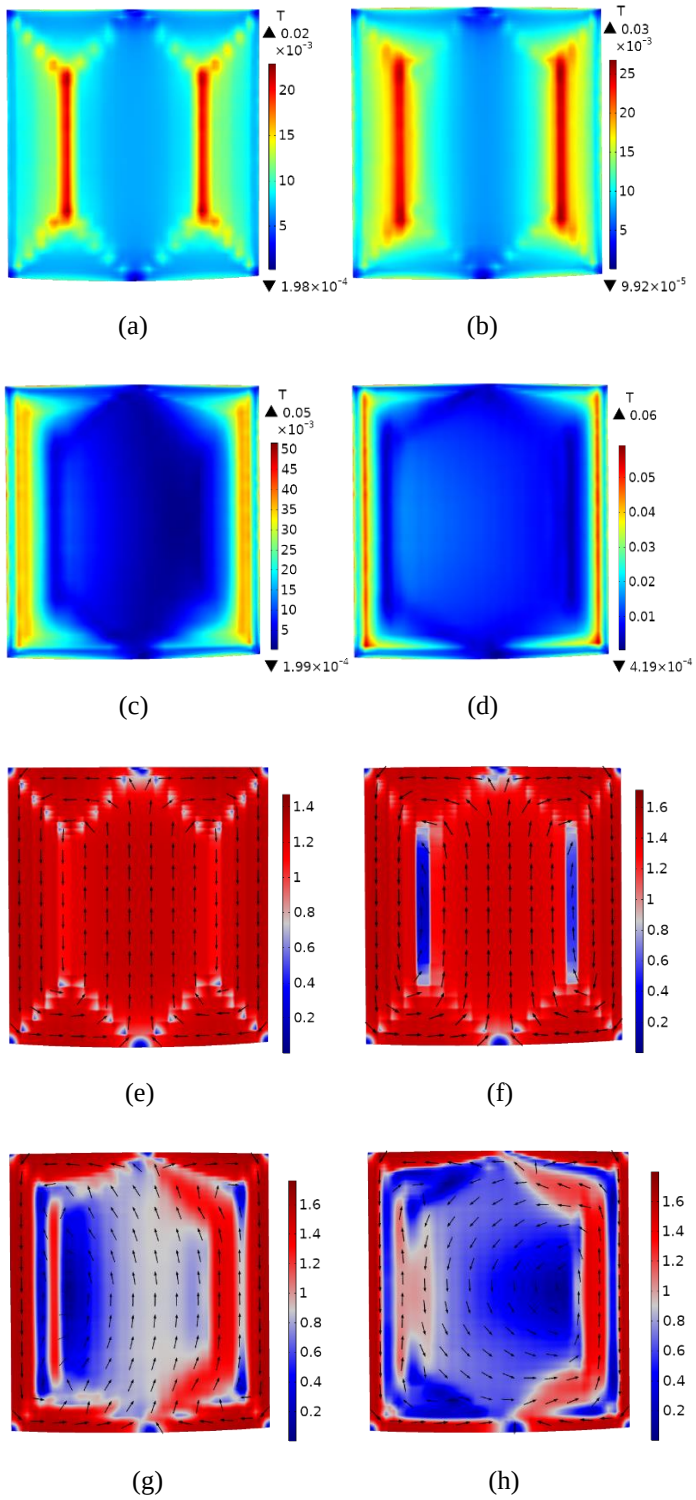

Figure 5.4.14 Magnetic flux density and current density distribution in the curved HTS layer. $B_{e\|2}$ = 100 mT, and f varies from 50 Hz to 20 kHz. (a), (b), (c), and (d) represent the magnetic flux density distribution at the phase of 2π for f = 50 Hz, 1 kHz, 10 kHz, and 20 kHz, respectively. (e), (f), (g), and (h) show separately J/J_c at the phase of 2π for f = 50 Hz, 1 kHz, 10 kHz, and 20 kHz. The black arrows illustrate the current flow direction along with the current streamlines.

5.4.3 Case study of an HTS stack

In this section, we will model a TFS composed of 5 CCs and study the electromagnetic performance of different layers under cross fields with an arbitrary propagation direction. The applied cross field is the combination of $\boldsymbol{B}_{e\|1}$ and $\boldsymbol{B}_{e\|2}$, with $B_{e\|1}$ = 100 mT and $B_{e\|2}$ = 100 mT.

Before the application of cross fields, the HTS stack is firstly magnetized by the pulsed field adopted in Section 5.4.2.2. Figure 5.4.15 shows the magnetic flux density distribution in the whole curved stack and the current density distribution in the HTS layers. In Figure 5.4.11 (d), it can be found that the trapped flux in a single curved square CC is concentrated in a small central region. As a comparison, in Figure 5.4.15 (a), the trapped magnetic field in the HTS stack occupies a larger area with a higher flux density, i.e., more flux gets trapped in the stack. Similar to Figure 5.4.11 (h), an electromagnetic criss-cross occurs in Figure 5.4.15 (b) to characterize the current density distribution.

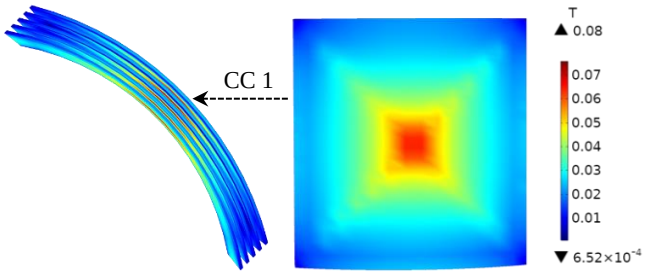

(a)

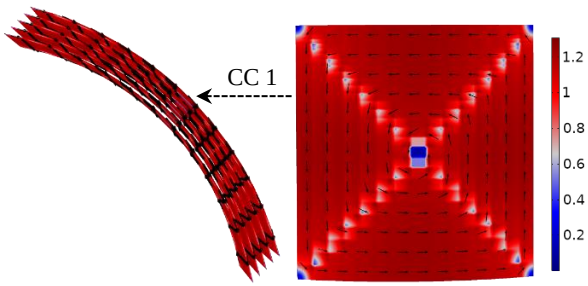

(b)

Figure 5.4.15 Magnetic flux density and current density distribution in the curved HTS stack after PFM, at 60 ms. B_{ext} = 2 T, and τ = 10 ms. (a) presents the flux density distribution in the whole stack. (b) shows the current density distribution in the HTS layers. The black arrows illustrate the current direction along with the current streamlines.

To further describe the trapped field in the stack, the flux density distributions along the *z*-axis on the upper surface of each CC, namely the top copper surfaces, have been presented in Figure 5.4.16.

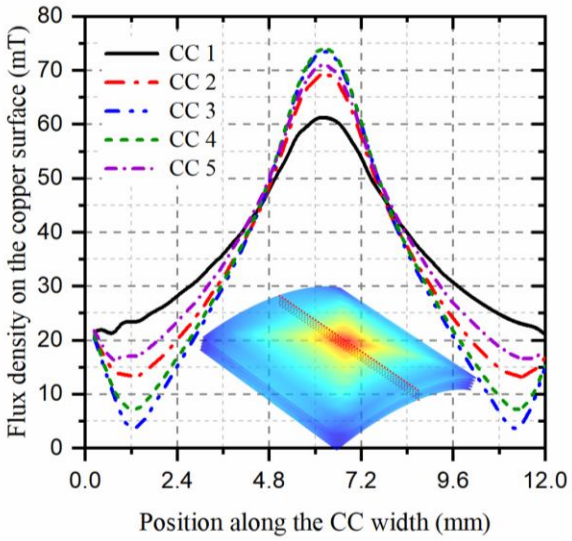

Figure 5.4.16 Magnetic flux density distribution along the *z*-axis on the upper surface of each curved square CC of the HTS stack after PFM, at 60 ms. The CC number is decided from top to bottom.

It can be seen that the highest trapped flux density appears in the center of the middle CC (CC 3), which is positioned at the central region of the flux flow traversing the stack. We need to note that, the performance of the TFS is determined by the flux density values in the most top CC, namely CC 1. Although the highest flux density trapped in CC 1 is lower than that of the other CCs, its flux density distribution is more uniform with a smaller variance.

On the basis of the modelling results after one single PFM, the cross fields with different frequencies have been applied. In this section, the cross field is a combination of $\boldsymbol{B}_{e\|1}$ and $\boldsymbol{B}_{e\|2}$, with $B_{e\|1} = B_{e\|2} = 100$ mT. Figure 5.4.17 shows the magnetic flux density in the curved stack at the phase of $3\pi/2$ for $f = 50$Hz, 1 kHz, 10 kHz, and 20 kHz, respectively. (a)-(d) refer to the flux density distribution in the upper surface of CC 1. Compared to Figure 5.4.15 (a), it can be seen that, the field distribution under PFM has been changed by the applied transverse fields, i.e., the demagnetization of the TFS has happened. In Figure 5.4.15 (a), most of the trapped flux is concentrated in the central region of the stack. However, in Figure 5.4.17 (a)-(d), the majority of the penetrated magnetic flux appears at the bottom right of the studied surface, along the diagonal (represented by gray dotted lines). In fact, the propagation direction of the synthetic transverse field is approximately along the dotted diagonal, thus it is easy to understand that the highest penetrated flux density appears along the diagonal according to Lenz's law, as shown in (a) and (b). However, at higher frequencies above 1 kHz, the highest flux density emerges on the bottom edges due to the skin effect, as shown in (c) and (d). In other words, the demagnetization of the TFS due to cross fields has become more severe with increasing frequency. To further illustrate the skin effect, the magnetic flux density properties

on the diagonal cross section perpendicular to the field propagation direction have been presented in (e)-(h). It can be clearly found that the trapped flux tends to be driven towards the outermost CCs with increasing frequency.

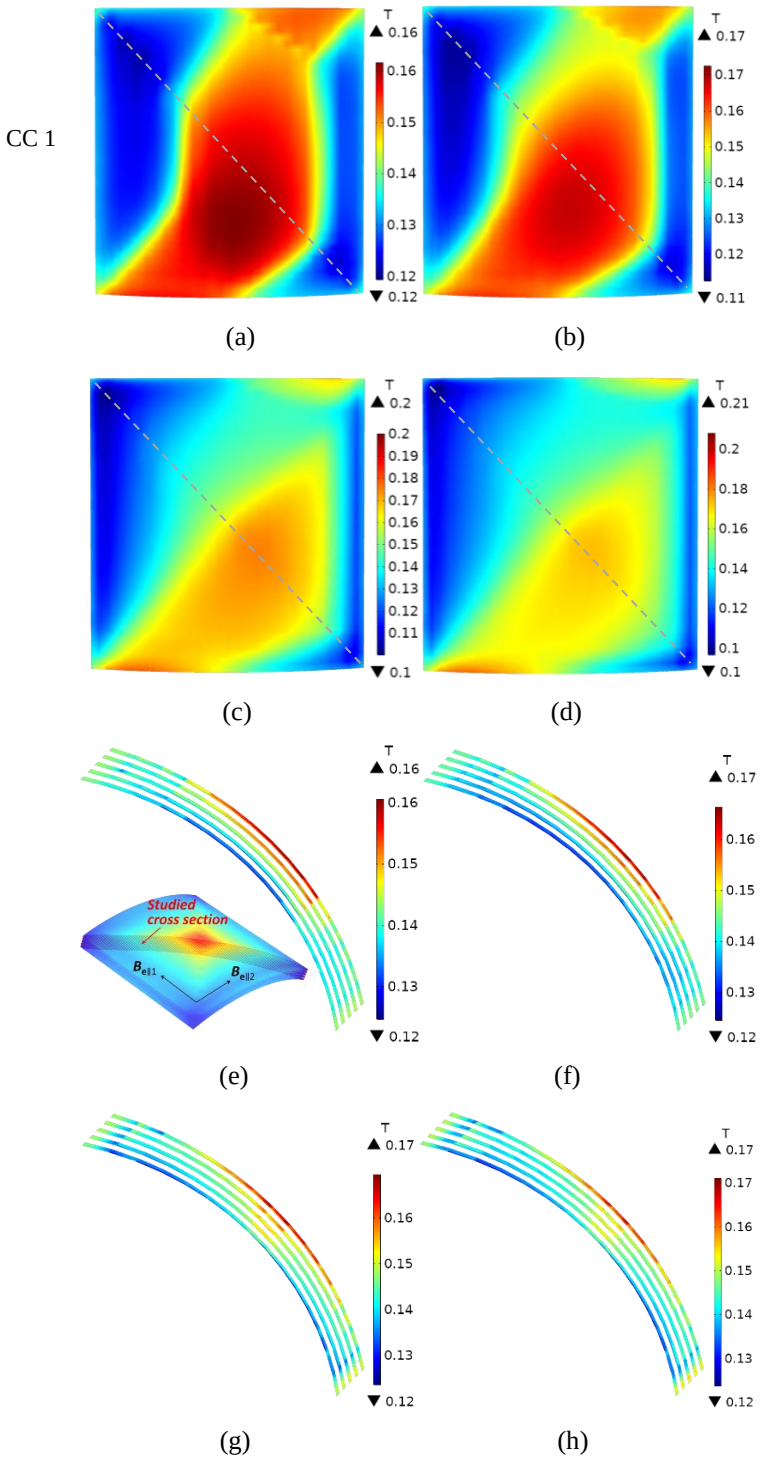

Figure 5.4.17 Magnetic flux density distribution in the upper surface of the outermost CC and on the cross section of the curved HTS stack at the phase of $3\pi/2$ under traverse external fields with different frequencies. $B_{e\parallel 1} = B_{e\parallel 2} = 100$ mT. (a)-(d) represent the flux density distribution in the upper surface of

the stack at f = 50 Hz, 1 kHz, 10 kHz, and 20 kHz, respectively. (e)-(f) stand for separately the flux density distribution on the diagonal cross section of the stack at f = 50 Hz, 1 kHz, 10 kHz, and 20 kHz.

Figure 5.4.18 shows the magnetization loss in different layers of the curved HTS stack under cross fields with varying frequencies from 50 Hz to 20 kHz. It can be seen that, in general, the losses in different layers are in a positive correlation with the frequency of the external cross fields. When f < 200 Hz, the loss in the HTS layer accounts for more than 90% of the total loss. However, with increasing frequencies, the loss ratio P_{HTS}/P_{tot} decreases rapidly and attains less than 50% when f exceeds 5 kHz. Therefore, it can be concluded that high-frequency cross fields can lead to high losses in the non-superconducting parts of the HTS stack due to the skin effect. In this case, the multilayer structure of each CC has to be considered in modelling work to accurately predict the electromagnetic performance of the HTS stack under cross fields.

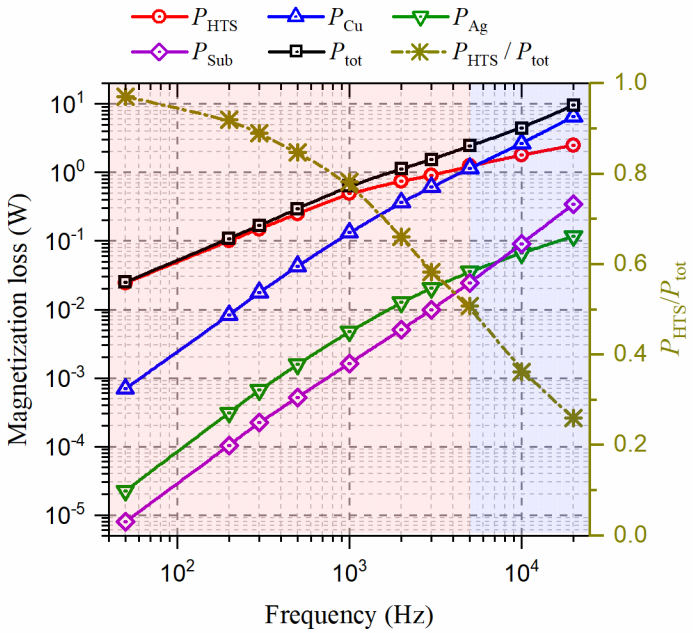

Figure 5.4.18 Variation of magnetization losses in different layers, and loss ratio P_{dyn}/P_{AC_tot} with frequency for the curved square HTS stack under transverse AC fields. f ranges from 50 Hz to 20 kHz. $B_{e\|1} = B_{e\|2}$ = 100 mT.

It should be noted that the field dependence of the critical current of the HTS layer is more sensitive to the perpendicular magnetic fields compared to parallel fields, as shown in Equation (2.4). As a result, under the same frequency and field amplitude, the loss in the HTS layer under cross fields is much lower than that under perpendicular fields. Therefore, in terms of value, the loss of the HTS layer in Figure 5.4.18 is much lower than that in Figure 5.4.9 though for the latter there is only one single CC. Besides, magnetization loss increases positively with

the surface area exposed to external magnetic fields, which also explains well the fact that the loss values of all the layers in Figure 5.4.18 are lower than those in Figure 5.4.9. Due to the same reason, when f > 7 kHz the loss in the substrate exceeds that in the silver overlayer in Figure 5.4.18, given that the cross-sectional area of the substrate is 30 times larger than that of the silver overlayer, different from the case in Figure 5.4.9.

5.4.4 Discussion

5.4.4.1 Temperature dependence

In order to get high trapped flux density, many researchers choose to apply muti-pulse field magnetization techniques to a great number of CCs at very low temperatures, as reported in [147, 338-339]. Nevertheless, targeted at the design of high-speed HTS machines, this work aims to illustrate the electromagnetic characteristics inside the curved HTS stack under the effect of high-frequency cross fields, rather than study the best magnetization method or to obtain the highest trapped field. Therefore, the magnitude of the trapped field is not a crucial parameter in this study. From this point, here, the temperature has been chosen as 77 K, and a stack composed of only 5 CCs after one single PFM process has been studied

To model the magnetization of bulk superconductors, normally the temperature dependence of critical current density needs to be taken into account. However, as mentioned in [95], TFSs have better thermal stability compared to bulks in that the silver overlayer and copper stabilizers have a much higher thermal conductivity. Therefore, given that the studied stack is not composed of numerous CCs and only one cycle of fields has been applied, in this paper, we assume that the power dissipation can be removed instantaneously, and thus the temperature can be approximated as a constant, 77 K. To verify this assumption, considering the $J_c(\boldsymbol{B},T)$ dependence, we have modelled the magnetization of a single curved square CC under the AC perpendicular fields used in Section 5.4.2.1, based on the simulation method presented in [347-348]. The Heat Transfer in Solids physics module has been coupled to the $\boldsymbol{H}$-formulation, with a boundary heat transfer coefficient of 400 W/(m^2·K). All the parameters regarding thermal conductivity, heat capacity, and mass density of different materials have been taken from [348]. Taking f = 50 Hz as an example, the temperature distribution in the HTS layer after one AC cycle is shown in Figure 5.4.19.

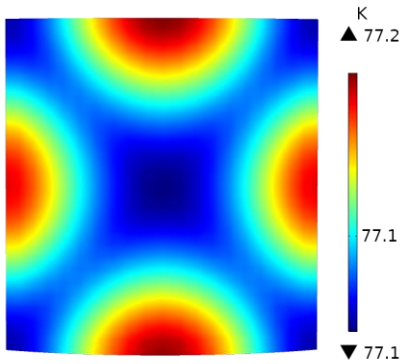

Figure 5.4.19 Temperature distribution in the HTS layer of the curved HTS CC under AC perpendicular field magnetization. B_{ext} = 100 mT, and f = 50 Hz.

It can be seen that the generated heat accumulates starting from the middle edges of the CC, which complies well with Figure 5.4.7 (a) and the conclusions drawn before. Most importantly, the temperature is approximately unchanged with a variation of only 0.2 K. Therefore, it is reasonable to approximate the temperature as a constant in this research. However, we have to clarify that, the heat accumulation is dependent on the number of cycles of the applied AC fields. To study the demagnetization of TFSs due to cross fields of a great number of cycles, more information can be found in a recent publication by E. Pardo [349].

5.4.4.2 Magneto-angular anisotropy

The adopted $J_c(\boldsymbol{B})$ dependence in Section 5.4, described by Equation (2.4), is a semi-empirical Kim model with an orthonormal field dependence, which has been validated experimentally and extensively used in the modelling of HTS stacks and coils. As mentioned in Section 2.2.4.2, Coombs and Ruiz et al have also studied the magneto-angular dependence of J_c, and put forward a more general $J_c(\boldsymbol{B}, \theta)$ dependence as shown in (2.5).

Four different material law models have been systematically compared in [112], including (2.4) and (2.5). It is concluded that when at a low transport current (below 0.4 I_{c0}), the magnetization losses obtained by (2.4) and (2.5) are almost the same. In fact, (2.4) is in essence a simplified version of (2.5) with specific parameters. In Section 5.4, the transport current in HTS stacks is zero, thus it is reasonably considered that (2.4) can reflect well the magneto-angular anisotropy of CCs in terms of loss quantification.

In addition, to avoid ambiguity, it should be clarified here that though the studied HTS stack is curved, the orthonormal field dependence has been well considered. As illustrated in Figure 5.3.18 in Section 5.3.2.4, the $J_c(\boldsymbol{B})$ dependence is closely linked to the angle between the field vector and the wide surface normal of the CC. Then, the local parallel and perpendicular flux densities at the studied point can be expressed as (5.6).

5.4.5 Summary

Section 5.4 is a follow-up work of Section 5.2 and 5.3. TFSs are a potential field source applied to high-speed HTS machines. With the ***H***-formulation based 3D numerical modelling method, the electromagnetic characteristics of curved TFSs under the influence of frequency-varying perpendicular and cross fields have been investigated, within the range of 50 Hz-20 kHz. The adopted 3D multilayer numerical model has been validated through comparison with Benchmark #5 in terms of a flat cubic bulk superconductor in HTS Modelling Workgroup [344]. The whole modelling work has considered the multilayer physical structure of each HTS CC, namely the HTS and non-superconducting layers.

The electromagnetic characteristics of magnetized HTS stacks, including current density and magnetic flux density distributions, cannot be correctly predicted by the widely adopted 2D-axisymmetric models because of the emergence of the electromagnetic criss-cross. The defined electromagnetic criss-cross in this paper divides the CC wide surface into four roughly equivalent subdomains. Therefore, 3D numerical modelling methods need to be adopted. As for loss properties, the multilayer physical structure of HTS CCs has to be considered, especially for perpendicular field magnetization even at low-frequency band, e.g., at 50 Hz. For cross field magnetization, the multilayer structure has to be taken into account at frequencies higher than 200 Hz.

For perpendicular field magnetization of curved HTS stacks, the applied field starts to penetrate into the stack from the middle edges. As a result, at high frequencies, the skin effect can focus the penetrated flux and induced current due to Lenz's law near the edges. In other words, the induced current in the central part of the curved square CC demonstrates a kind of 'lag effect' in the time domain and seems less sensitive to the variation of external magnetic fields.

Two types of cross fields have been studied. Under the cross field completely parallel to the curved surface, $\boldsymbol{B}_{e\parallel 1}$, a transverse current can be generated. The transverse current can enhance the current in one quarter subdomain of the HTS layer and mitigate the current in another quarter section, which agrees well with Lenz's law on the macro level. Under the cross field traversing the curved surface, $\boldsymbol{B}_{e\parallel 2}$, the curved surface can be decomposed into two symmetric curved rectangular CCs, each of which possesses independent magnetization centres and current paths. Due to the influence of cross fields on the electromagnetic distributions and loss characteristics, demagnetization can happen to the TFS. With increasing frequencies of cross fields, the originally trapped flux after PFM in the stack can be deteriorated more severely due to the skin effect.

To sum, different from other researchers' work, Section 5.4 has not looked into the best magnetization method or highest trapped field in terms of TFSs, but has focused on their dynamic electromagnetic characteristics under high-frequency perpendicular and cross fields. This work further adds upon the existing knowledge regarding TFSs, and is believed to provide a useful reference for their application in high-speed superconducting propulsion machines for future aviation. The proposed 3D numerical model for TFSs can be extended to the study of HTS stacks (flat and curved) without copper stabilizers, or with magnetic substrates.

5.5 Conclusion

Chapter 5 has illustrated the electromagnetic characteristics of HTS CCs, stacks, circular coils, racetrack coils, and curved TFSs over a wide frequency band, from the power frequency to the kHz level, with the ***T***-formulation and ***H***-formulation based 1D, 2D, and 3D multilayer numerical models. The widely adopted thin film approximation for HTS CCs has proven inapplicable for modelling the magnetization loss at high frequencies above 100 Hz and for calculating the transport current loss at frequencies higher than 10 kHz under the influence of the skin effect and the electromagnetic interactions between the superconducting and non-superconducting layers. Therefore, the normal conductor parts of HTS CCs have to be taken into account, too, when they are employed in a high-frequency environment, e.g., inside high-speed synchronous superconducting machines. The conventional definition of the dynamic region for HTS CCs has proven not applicable at the kHz level due to the skin effect, which thus cannot be used to calculate dynamic loss in this case; therefore, the numerical modelling method has been recommended for the quantification of dynamic loss. The shielding effect among different turns in an HTS coil has also been clarified, which can lead to a higher dynamic loss proportion in the middle parts and a higher magnetization loss ratio in the outermost turns. In general, both dynamic loss and magnetization loss should be attached to great importance for the design of high-speed superconducting machines. Given that curved TFSs, as a promising field source, possess geometrical applicability for cylindrical rotating shafts in superconducting rotating machines, their high-frequency electromagnetic performance under perpendicular and cross fields has been illuminated, respectively. The widely adopted 2D-axisymmetric models have proven inapplicable to study the electromagnetic distributions of TFSs because of the emergence of the electromagnetic criss-cross. Therefore, in this case 3D numerical modelling is necessary. High-frequency ripple fields can drive induced current towards the periphery of the HTS TFS due to the skin effect, leading to a fast rise of AC loss and even an irreversible demagnetization of the stack. This chapter has qualitatively and quantitatively analyzed the high-frequency electromagnetic

behaviors of HTS CCs, stacks, coils, and TFSs, which can provide a useful reference for their loss controlling, and anti-quench or anti-demagnetization design in high-speed propulsion machines.

It should be underlined that though the AC power loss of HTS CCs increases fast with frequency, they can still be applied in a high-frequency electromagnetic environment. Taking high-speed superconducting machines as an example, the AC loss generated in the superconducting windings can be well minimized by decreasing the current load ratio, lowering the operating temperature, and utilizing the loss reduction techniques (as reviewed in Section 2.6). Additionally, the attachment of the HTS layer to a material with a high thermal conductivity in a CC can help with the propagation of a possible hot spot, plus a highly efficient cryogenic system, the heat generated from the HTS CC can be transferred to the cryogen immediately so that a quench can be avoided.

As is known, the happening of a quench is directly determined by the accumulated energy inside the superconductor over a period of time, i.e., a high power loss does not necessarily lead to a quench as long as the operating time is sufficiently short. Let us consider an HTS CC (as studied in Section 5.2) carrying a micro-second-class current pulse covering a wide frequency band up to the MHz level, the power loss is estimated to attain the kW/m level according to Figure 5.2.7. However, such a high power loss will not easily lead to a quench even though the amplitude of the current pulse exceeds the critical current of the HTS layer given the very short period of time at the micro-second level. Therefore, it is believed that superconductors possess the potential to be used in large-scale pulse generators so that the current pulse with high amplitude can be conducted without much heat generated.

The conventional wireless power transfer (WPT) using copper coils can achieve a charging power of several hundred kW with an efficiency higher than 90%. However, the limited power density of conventional WPT has largely restricted the efficiency and transfer distance. Therefore, superconducting WPT working at the kHz level provides a possibility to increase the efficiency of WPT and expand the relevant application scenarios (e.g., autonomous robots, electric vehicles, etc.) [321].

In addition, a typical very high-frequency (at the GHz level) application of superconductors is the superconducting radio frequency (SRF) technology. The ultra-low electrical resistivity of superconductors allows an RF resonator (also called a superconducting cavity) to obtain a very high quality factor, which enables the construction of high-performance particle accelerators. (https://en.wikipedia.org/wiki/Superconducting_radio_frequency).

Chapter 6. Design of Air-cored HTS machines

6.1 Introduction

In the previous chapters, the electromagnetic characteristics of superconducting field sources applicable to superconducting machines, including HTS coils and TFSs, have been investigated systematically. In this chapter, the HTS materials will be applied to the design of superconducting machines. Air-cored electrical machines have attracted increasing attention in power industry and transport because they can eliminate core losses and decrease the total mass. However, the limited magnetic flux in air-cored machines has restricted their power level. In order to improve the power density and efficiency while further reducing the weight of air-cored electrical machines, a novel field winding topology composed of HTS Halbach Array magnets (HAMs) has been proposed in this chapter. The HTS Halbach array topology has been applied to a 1 MW C-GEN wind turbine generator prototype and an electrodynamic wheel (EDW) for maglev. The AC loss of the HTS HAMs employed in the EDW has also been estimated through numerical modelling.

6.2 HTS Halbach Array Topology for Air-cored C-GEN Generators

Air-cored electrical machines have prompted widespread interests in multiple domains such as aircraft [350], flywheel energy storage systems [351], as well as wind turbines [352-353], in that they constitute magnetic circuits without heavy ferromagnetic material and, thus, can not only reduce the total weight but also get rid of core losses [354]. C-GEN is a multi-stage air-cored PM generator technology developed at the University of Edinburgh, which can be used for wind, tidal and wave energy converters [355-356]. A C-GEN generator is composed of a number of stator and rotor modules. Each stator module includes several copper coils, which are mounted onto the stator blade. A single rotor module comprises C-cores with magnets mounted in the inside surface, which produces an axial magnetic flux. As clean and renewable energy, wind power has aroused increasing attention and the wind turbine market has been growing rapidly. C-GEN wind turbines have been designed for improving wind power utilization efficiency, which have many advantages, such as no cogging torque, high degree of modularity, low capital expenditures, etc. [353-356]. However, they still have some drawbacks to be overcome, such as low capacity, large size, and heavy weight.

A conventional Halbach Array is composed of PMs that can concentrate the magnetic flux on one side of the array and cancel it on the other side [357]. It is usually applied in linear machines to improve their power efficiency by condensing the magnetic flux density exposed to coils [358-360]. However, it is hard for the conventional Halbach Array to achieve an intensity higher than 1 T. Therefore, the concept of a superconducting Halbach Array magnet (HAM) has been proposed for MRI scanners [361-362].

On the basis of the above research, to further improve the performance air-cored electrical machines, taking a C-GEN wind turbine prototype as the studied example machine, a novel field winding topology composed of HTSHAM has been put forward in this paper. Firstly, founded on a 4-stage 1 MW PM C-GEN prototype, a 2D model of the generator module has been built in COMSOL Multiphysics and its magnetic field distribution has been simulated. Then, the PMs used in the studied module has been replaced with HTS HAMs, of which the modelling has been conducted based on the ***H***-formulation with the homogenization method.

6.2.1 Shear Stress

C-GEN wind turbines work by producing shear stress in the air-gap. The schematic diagram of an example C-GEN module (only copper coils are presented here for ease of understanding and more details regarding the C-GEN structure can be found in Section 6.2.2) is shown in Figure 6.2.1. We can define the average air-gap shear stress of the entire generator, noted as τ, as [363-364]

$$\tau = \frac{T}{Sl} = \frac{T}{\pi \cdot \left(r_o^{\,2} - r_i^{\,2}\right) \cdot l} \tag{6.1}$$

where T is the total developed torque, S is the effective action area of the shear stress, determined by the outer radius r_o and inner radius r_i of the copper coils, and l represents the length of the air-gap.

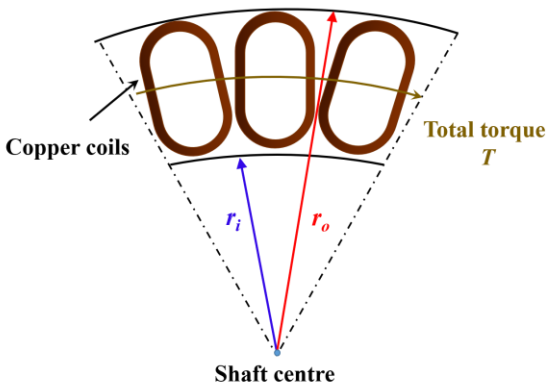

Figure 6.2.1 Schematic diagram of an example axial gap-type C-GEN module.

As both the flux density $B(\theta)$ and the stator surface current density $J(\theta)$ for the copper coils are sinusoidal flux waves, then we have

$$\tau = \frac{1}{2\pi}\int_0^{2\pi} K \cdot B d\theta = \frac{J_{max} B_{max}}{2} \tag{6.2}$$

where J_{max} and B_{max} are respectively the amplitude of the current density and magnetic flux density. Then, the power density transferred by the rotor movement can be obtained as

$$\frac{P}{Sl} = \frac{T \cdot \omega}{Sl} = \tau \cdot \omega = \frac{J_{max} B_{max}}{2} \cdot \omega \tag{6.3}$$

where ω is the angular velocity.

From (6.1)-(6.3), it can be seen that the average shear stress represents the torque density in the stator region of the C-GEN wind turbine. The augment of magnetic flux density can directly increase the torque density then improve the power density. Therefore, magnetic flux density is the key parameter to be studied in this section.

6.2.2 Modelling of PM C-GEN generator module

The diagram of a PM C-GEN generator is shown in Figure 6.2.2. It can be seen that the whole generator is composed of multiple detachable C-core modules, and each module contains several couples of PMs (rotor) and copper coils (stator). The magnetic flux is established by PMs, which passes through the copper coils. All the parameters of the 1MW PM C-GEN generator can be found in Table 11.

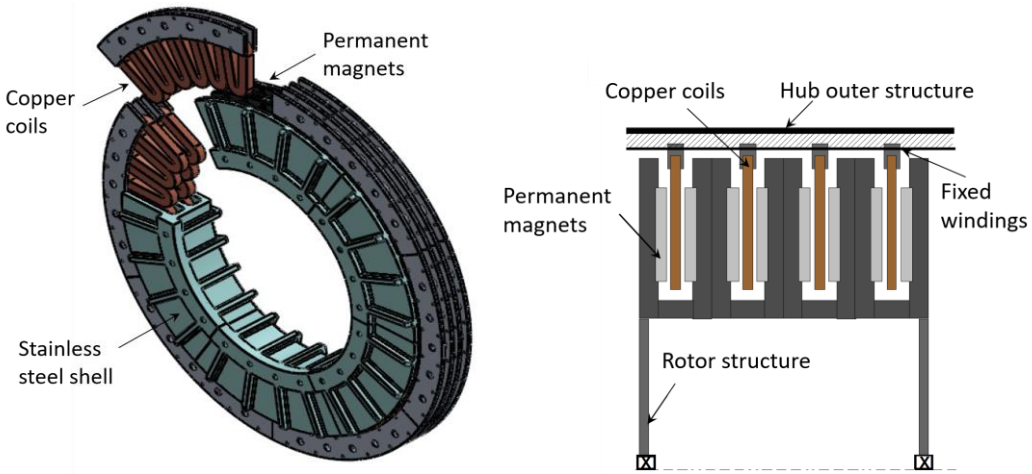

(a) (b)

Figure 6.2.2 Diagram of the PM C-GEN design. (a) Whole body. (b) C-core module cross-section.

Table 11 Parameter specification for the C-GEN prototype

Parameter	Quantity	Value
R_i	inner radius	2655 mm
R_o	outer radius	3190 mm
L	magnet length	312 mm
w_a	magnet average width	78 mm
t_m	magnet thickness	15 mm
ρ_{mm}	magnet mass density	7.7 g/cm^3
B_r	residual magnetism	1.28 T
l	air-gap between magnets	34 mm
d_a	adjacent magnet distance	21 mm
t_c	copper coil width	22 mm

According to the parameters presented in Table 11, a 2D model of the PM C-GEN generator module has been established in COMSOL Multiphysics, as shown in Figure 6.2.3. This modelling is based on the middle cross-section of the generator module. The dark green parts represent the generator shell made of stainless steel, the orange parts represent the copper coils, and the grey parts are PMs. The used PM is of type-NdFeB Grade N42, and its residual magnetism is 1.28 T. The simulated magnetic field distribution is shown in Figure 6.2.4 (the copper coils have been hidden for a better view). It can be found that the highest flux density appears in the part of the stainless steel shell, which is due to its high permeability. To figure out the properties of the magnetic flux that passes through copper coils, a rectangular region between permanent magnets has been especially studied, as marked in white in Figure 6.2.4. The magnetic flux density distribution of this area has been presented in Figure 6.2.5, which exhibits an approximate saddle face. It can be found that the highest flux density attains around 0.6 T, but it is concentrated in the region adjacent to the magnets of the module middle position, where two magnets are put together closely in parallel. The lowest flux density, around 0.5 T, appears at both ends of the stator region along the x-axis. In general, the average flux density, B_{avg}, in the stator region is approximately 0.56 T.

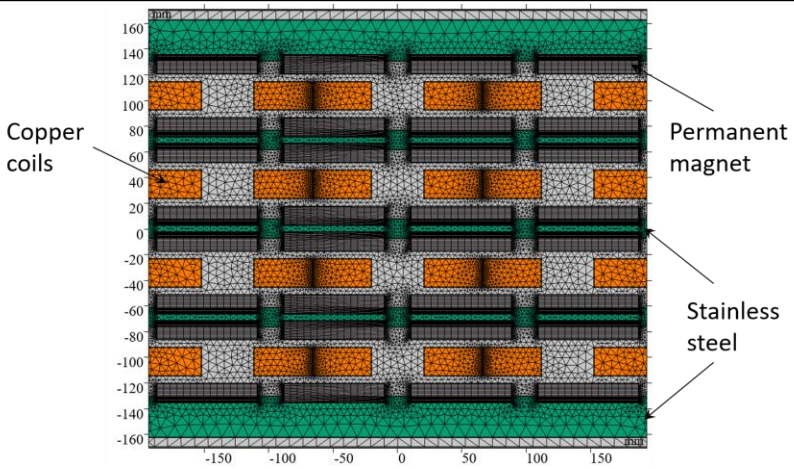

Figure 6.2.3 Modelling of the C-GEN generator module in COMSOL Multiphysics.

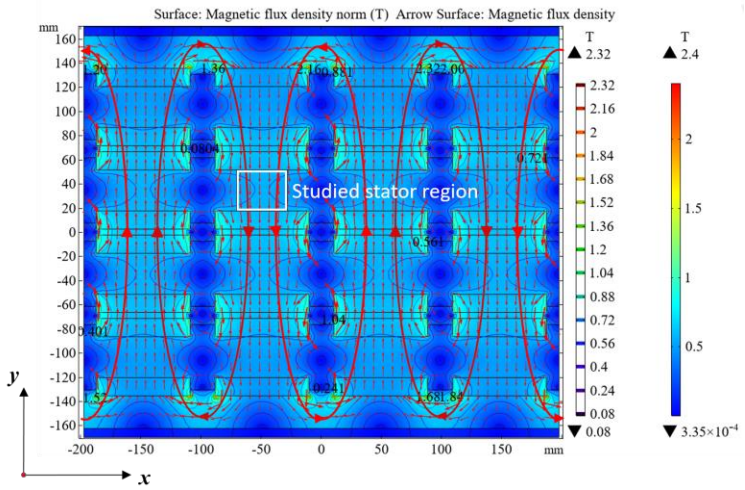

Figure 6.2.4 Magnetic field distribution inside the 1 MW C-GEN generator module.

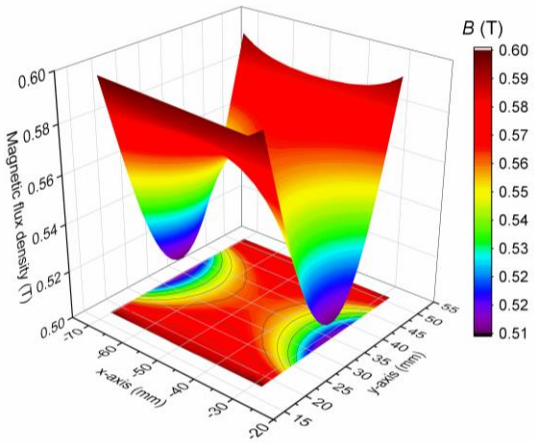

Figure 6.2.5 Flux density distribution in the stator area between PMs. The average flux density B_{avg} = 0.56 T.

As far as the weight of each permanent magnet is concerned, it should be equal to $\rho_{mm} \times t_m \times w_a \times L \approx 2.81$ kg. For the 4-stage 1 MW C-GEN wind turbine, there are totally 22 modules and 32 pieces of magnets in each module, thus the total weight of the magnets is around 1980 kg.

6.2.3 Modelling of HTS HAM

In the new design for the HTS C-GEN generator, HTS HAMs have been used to replace PMs to obtain higher magnetic field flux density, as shown in Figure 6.2.6. The two groups of golden coils represent the HTS HAMs, and the borrow coils represent the copper coils. The basic idea of the HTS HAM is to create a continuous magnetic channel with a group of HTS coils carrying DC.

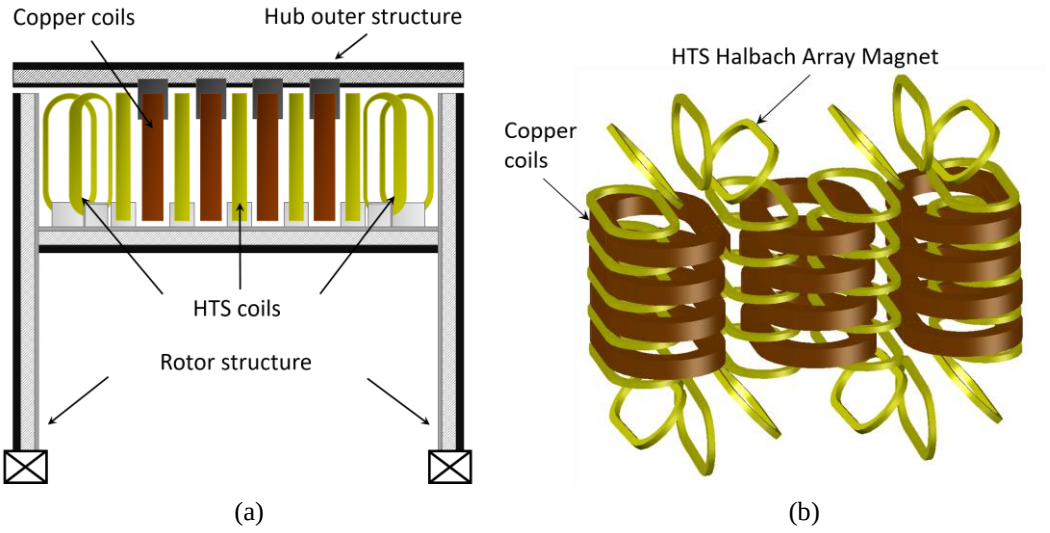

Figure 6.2.6 Diagram of the HTS Halbach array implemented into the C-GEN module. (a) Cross-section of the C-core module equipped with the HTS Halbach array. (b) 3D view of the coil parts.

As mentioned in [365], with the NI winding technique, the absence of both turn-to-turn insulation and the extra stabilizer can make the NI HTS magnet highly compact and enhance its overall current density. Therefore, in this section, the HTS HAM model has been constructed with NI technique on the basis of stabilizer-free HTS coated conductors (CCs) manufactured by SuperPower, Inc., SF12050. It is composed of a 1-μm thin film of YBCO material, and all its parameters used for modelling are shown in Table 12.

Considering that each HTS HAM coil is composed of many HTS CCs, and each HTS CC contains several typical layers (namely silver layers, one substrate layer, and one HTS layer), it can be quite computationally intensive and time-consuming to build a multilayer model for the HTS HAM. Therefore, to simplify the modelling and save computational time, the ***H***-formulation based homogeneous model has been adopted here in that the C-GEN wind turbine generator normally operates at low speed with a typical value of 5-20 rpm and thus the HTS HAM functions in a low-frequency

environment.

Table 12. Parameter specification for HTSHAM [361-362]

Symbol	Quantity	Value
w	HTS CC width	12 mm
h_{HTS}	YBCO film thickness	1 μm
t	HTS CC thickness	0.055 mm
T	operation temperature	77 K
I_{c0}	critical current in self field	300 A
n	n-value	21
I_t	applied current	225 A
B_0	magnetic field constant	0.426 T
ρ_m	mass density	8.96 g/cm^3
E_0	characteristic E-field	10^{-4} V/m
μ_0	Free space permeability	$4\pi \times 10^{-7}$ H/m

6.2.4 Results and analysis

A 2D model for the HTS HAM has been built in COMSOL Multiphysics, as shown in Figure 6.2.7. Compared with Figure 6.2.3, all the PMs have been replaced by HTS coils, which form two groups of HTS HAMs. The basic principle is not to change the whole dimension of the generator module along the x-axis and the air-gap between the rotor and the stator.

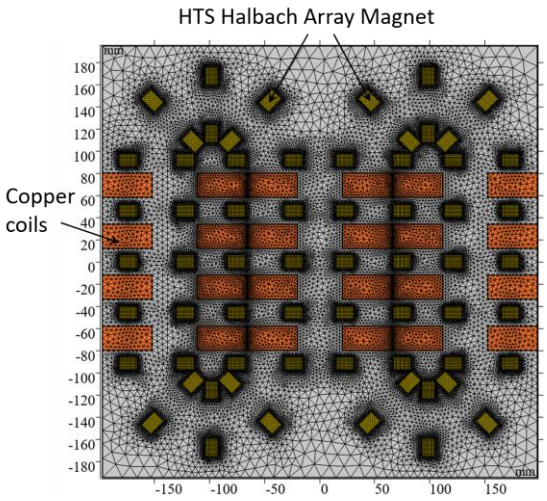

Figure 6.2.7 Diagram of the HTSHAM modelling in COMSOL Multiphysics.

6.2.4.1 Preliminary design

The air-gap between HTS coils along the *x*-axis is set as 30 mm, and each coil is composed of 300 turns of HTS tapes. The simulated results are shown in Figure 6.2.8. It can be found that a closed magnetic field loop has been established in each HTS HAM, and almost all the magnetic fields are confined inside the HTS HAM. The highest flux density attains 3.85 T, which appears onto the inner parts of the coils in the Halbach area, so the cryogenic condition here ought to be well guaranteed especially. It should be noted that the magnetic flux is parallel to the surface of the HTS tapes, but the critical current of the coils is mostly influenced by the perpendicular components of the field, of which the peak amplitude (~0.3 T) is less than B_0. Therefore, a current-carrying rate of no more than 75% is acceptable for this HSTHAM design.

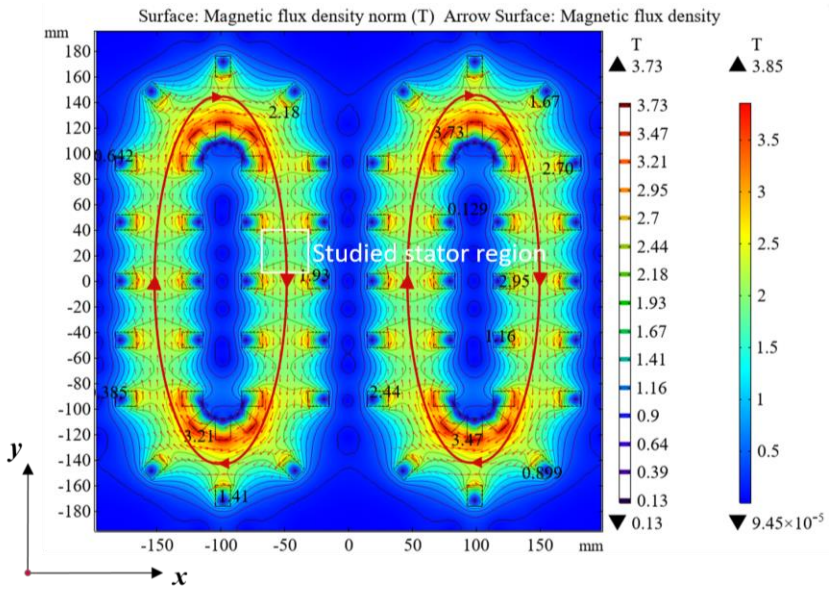

Figure 6.2.8 Magnetic field distribution inside the HTSHAM C-GEN generator module.

To study the magnetic flux density in the stator region, their distribution in the white rectangular region (same size as before) of Figure 6.2.8 has been shown in Figure 6.2.9. It can be seen that the flux density in this area also exhibits an approximate saddle face, with the highest value attaining 2.59 T in the area next to the HTS coils. Through calculation, the average flux density of this studied region is 1.91 T, which is about 3.4 times that of the PM design.

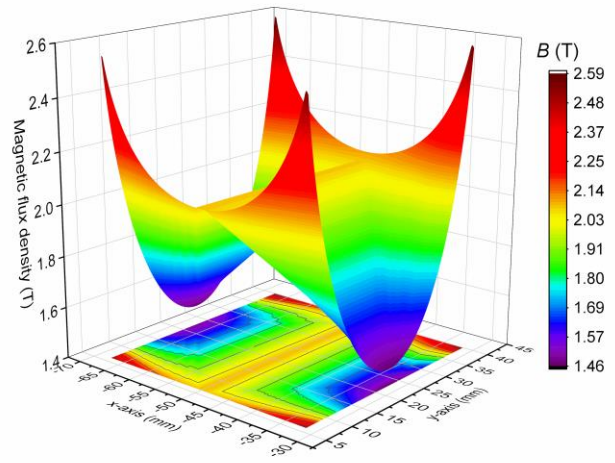

Figure 6.2.9 Flux density distribution in the stator area between HTS coils. B_{avg} = 1.91 T.

The cross-sectional area of each HTS coil is 16.5 mm×12 mm = 198 mm^2, and the average length of the coil is π×46.5 mm+312 mm×2 ≈ 770 mm. Considering that the 4-stage HTSHAM C-GEN contains 32×22 superconducting coils, thus the total weight of the magnets should be ρ_m×198 mm^2×770 mm×32×22 ≈ 961.4 kg < 1980 kg. Therefore, the design with HTSHAMs can decrease the total magnet weight to less than half of the PM C-GEN.

6.2.4.2 Design Optimization

In order to further increase the flux density in the stator area, the air-gap between two groups of HTS HAMs has been reduced and the number of HTS tapes in each coil has been increased accordingly. When the air-gap decreases from 30 mm to 20 mm and the number of tapes increases from 300 to 330, the average flux density in the same studied region attains 2.11 T; while the air-gap drops to 10 mm, and the turn number augments to 360, the average flux density reaches 2.31 T.

Figure 6.2.10 and Figure 6.2.11 show respectively the magnetic field and flux density distribution for the 10 mm-air-gap case. In this case, the cross-sectional area of the HTS coil is 19.8 mm×12 mm, and its average length is π×58.85 mm+312 mm×2. Therefore, the total HAM weight amounts to 1212.2 kg, which accounts for about 60% of the magnet weight in the PM design.

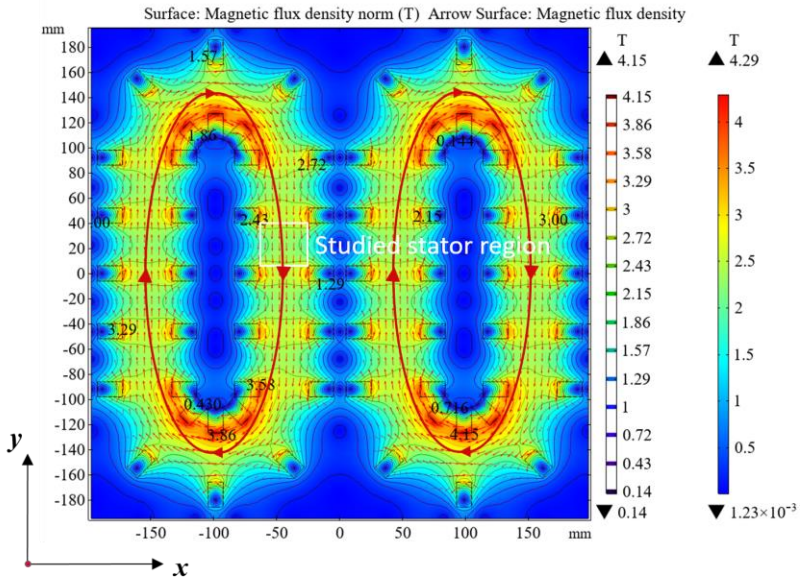

Figure 6.2.10 Magnetic field distribution inside the optimised HTSHAM C-GEN generator module.

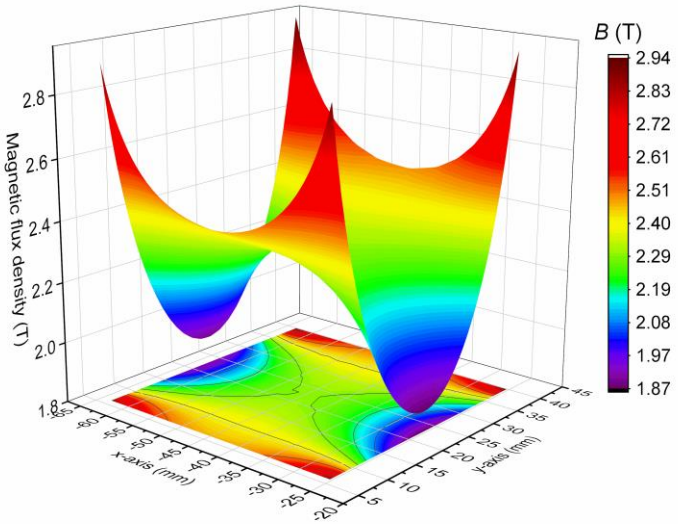

Figure 6.2.11 Flux density distribution in the stator area between HTS coils. B_{avg} = 2.31 T.

To compare the HTSHAM designs with the conventional PM C-GEN more comprehensively, their power levels and magnet weight have been summarized in table 13.

Table 13. Comparison between the HTSHAM designs and the PM C-GEN

C-GEN design	PM	HTSHAM 1	HTSHAM 2	HTSHAM 3
Air-gap along *x*-axis (mm)	30	30	20	10
Number of CCs in a coil	/	300	330	360
Power level (MW)	1	3.41	3.77	4.13
Magnet weight (kg)	1980	961.4	1096.8	1212.2

6.2.5 Summary

A novel HTS Halbach Array topology for air-cored electric machines has been proposed in this Section. The average shear stress represents the torque density of synchronous machines, which is in a positive correlation to the magnetic field distribution in the stator region. Therefore, the magnetic flux density has been specially studied in this paper. Both the 1 MW PM C-GEN generator prototype and the new HTS HAM design have been modelled and analysed in COMSOL Multiphysics. The application of HTS HAMs can increase the average magnetic flux density from 0.56 T to 2.31 T in the stator region without changing key dimensions. In other words, the power level of the proposed C-GEN generator with HTS HAMs can attain approximately 4.13 MW. Besides, the total magnet weight of the C-GEN generator with HTS HAMs can be reduced to approximately 60% compared with the conventional PM design. The proposed HTS HAM can not only generate a higher power density and decrease the magnet weight for the example C-GEN machine, but also represents a generic topology/approach for the design of fully air-cored superconducting machines, eliminating heavy iron cores.

6.3 Conceptual Design of EDWs Based on HTS HAMs

Maglev technologies have been widely studied all around the world because it provides a possibility for high-speed ground transportation [366-367]. Maglev technologies are mainly composed of three typical levitation methods, namely electromagnetic suspension (EMS), electrodynamic suspension (EDS), and hybrid electromagnetic suspension (HEMS) [368-369]. Most of the existing maglev projects are based on classical EMS, such as German and Chinese Transrapid, Korean UTM, as well as Japanese HSST, etc. [369]. Compared to EMS, the system of EDS is more stable because of the equilibrium of the lift force and the weight of the vehicle [366, 369]. However, the commonly used field sources, such as PMs and coils

made of conventional conductors, can only provide limited power density, which has restricted the development of maglev. HTS magnet technologies have provided a solution to the limited thrust and lift forces of the conventional maglev [370-372]. Nevertheless, the existing maglev technologies have mainly been applied to transportation systems with fixed tracks. In the future, if conventional on-road vehicles can be combined with superconducting maglev, an innovative transport system can be achieved while greatly improve the traffic conditions even the ecosystem as well as the environment.

EDWs have been proposed for use in EDS since 2003, by Bird and Lipo [373-375]. The rotation of a magnetic source can induce eddy currents in the passive conductive guideway, then the interaction of magnetic fields between the magnetic source and the guideway can produce both lift and thrust forces simultaneously. EDWs provide a possible solution to on-road maglev vehicles. The conventional EDW is composed of PMs, which form a Halbach array and serve as a magnetic source. Although it appears to have promise as a low-cost method for maglev transportation, EDWs still have some drawbacks to overcome, such as the limit of remanence in PMs (no more than 1.5 T at present), difficulty to manufacture large magnetic circuits, and low power density.

In order to enhance the feasibility of EDWs in maglev vehicles, a conceptual design of EDW based on HTS HAMs has been proposed in this section. It is composed of 2G HTS coils, which are arranged in a Halbach array. The proposed HTS HAM EDW has been modeled in COMSOL Multiphysics. The magnetic flux density in the airgap, both thrust and lift forces, the magnet weight, as well as the coil loss properties, have been quantified and analyzed in detail.

6.3.1 Modelling method

The proposed HTS HAM EDW has been modelled in COMSOL Multiphysics within the Rotating Machinery, Magnetic interface.

6.3.1.1 Modeling strategies

The preliminary design of the proposed HTS HAM EDW is shown in Figure 6.3.1 (a), which has 4 pole pairs. The golden parts are HTS coils, which are arranged in a Halbach array. The remaining parts are the non-magnetic support structure made of lightweight composite materials. More design specifications can be found in Table 14. Considering the symmetrical structure of the EDW, a 2D numerical model has been adopted as shown in Figure 6.3.1 (b). The rotating EDW is composed of HTS double pancake coils, inside the boundary named

identity pair. The aluminium track is positioned below the EDW, and between them there is an air gap, *g*.

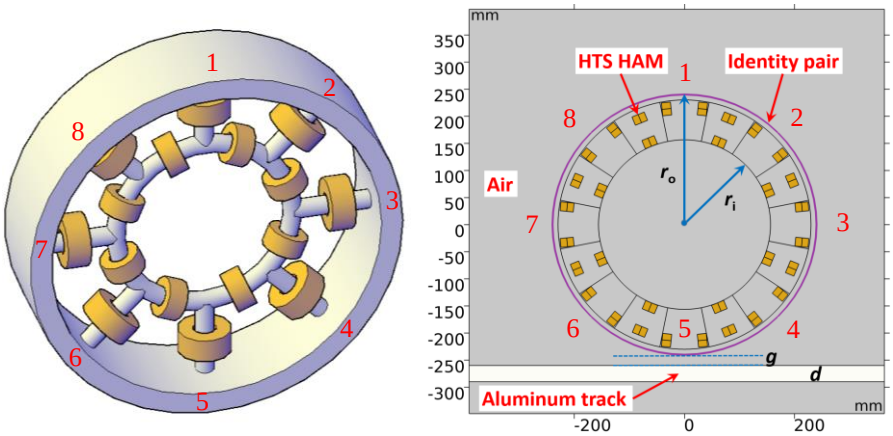

(a) (b)

Figure 6.3.1 Design and modelling of the HTS HAM EDW. (a) Structure of the HTS HAM EDW. (b) 2D modelling in COMSOL Multiphysics.

For a racetrack HTS coil, it is practical to apply 2D modelling methods to predict its cross-sectional electromagnetic properties, when the carried current is not too large, and the effect of the round sections becomes negligible [164]. However, in our case, the HAM is composed of circular HTS coils, thus the conventional 2D modelling technique using two stacks carrying opposite currents becomes inapplicable. It is complicated to set a symmetry axis for each coil, and it is very time-consuming to study the dynamic process of the EDW equipped with several thousand HTS tapes. Therefore, we have conducted the modelling work as follows: (1) replace the HTS coils with conventional coils carrying the same direct current (DC) to obtain the magnetic fields generated in the airgap; (2) apply the spatial magnetic fields due to the interaction between the rotating EDW and the track to specific HTS coils to explore their loss characteristics. For the first step, we have applied the Multi-Turn Coil feature to model the circular HTS coils.

Table 14. Specifications for HTS HAM EDW [361-362]

Symbol	Quantity	Value
w	HTS tape width	12 mm
h_{HTS}	YBCO film thickness	1 μm
t	HTS tape thickness	0.055 mm
T	operation temperature	74 K
I_{c0}	critical current in self-field	396 A
n	n-value	21
I_{t}	applied current	200 A
ρ_{ms}	mass density of HTS CC	8.96 g/cm^3
ρ_{mp}	mass density of PM	7.7 g/cm^3
E_0	characteristic E-field	10^{-4} V/m
r_{o}	outer radius	230 mm
r_{i}	inner radius	156 mm
g	height of the air-gap	30 mm
d	thickness of the guideway	30 mm

To illustrate the rationality of the proposed modelling strategy, a comparison among three 2D modelling cases in term of the spatial filed distribution has been presented in Figure 6.3.2: Case 1 - two parallel conventional conductors carrying opposite currents modelled with the ***A***-formulation; Case 2 - a conventional conductor coil modelled with the ***A***-formulation; Case 3 - a homogenized HTS coil modelled with the ***T***-formulation [151]. In Case 3, the transport DC is 200 A in each HTS turn, and there are in total 300 turns of tapes with no insulation between them. Equivalently, the total transport DC is 60 kA in Cases 1 and 2, no matter the material. It can be seen that, from Figure 6.3.2, the spatial field distributions in Cases 2 and 3 are similar, most of the magnetic flux being concentrated near the inner part of the coil. However, the flux density in Case 1 is much lower compared to Cases 2 and 3, with a different flux distribution, thus the conventional 2D modelling technique using parallel conductors is inapplicable for circular coils. To further compare the three cases, the flux density distributions along with the studied two lines represented by short dash lines in Figure 6.3.2, have been presented in Figure 6.3.3. It can be seen that the flux density distributions in Cases 2 and 3 are quite similar with an average difference of less than 5%, though the maximum flux density in Case 3 is slightly higher than that in Case 2. Consequently, it is reasonable to replace HTS circular coils with conventional coils to obtain the spatial flux density used for the generation of lift and thrust forces of the EDW.

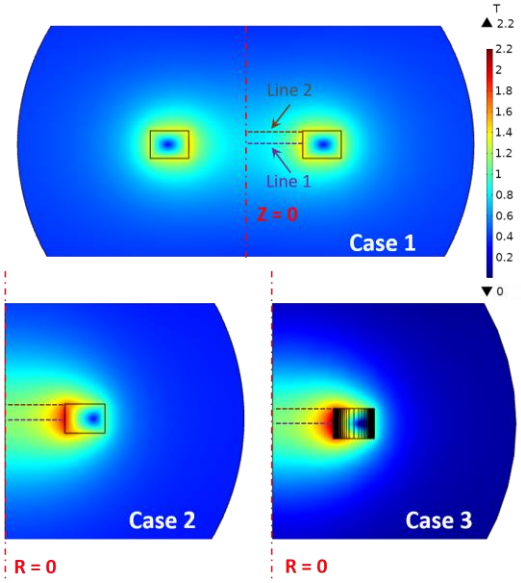

Figure 6.3.2 Spatial magnetic field distributions of the studied three cases: Case 1 - two parallel conventional conductors carrying opposite currents modelled with the *A*-formulation; Case 2 - a conventional conductor coil modelled with the *A*-formulation; Case 3 - a homogenized HTS coil modelled with the *T*-formulation.

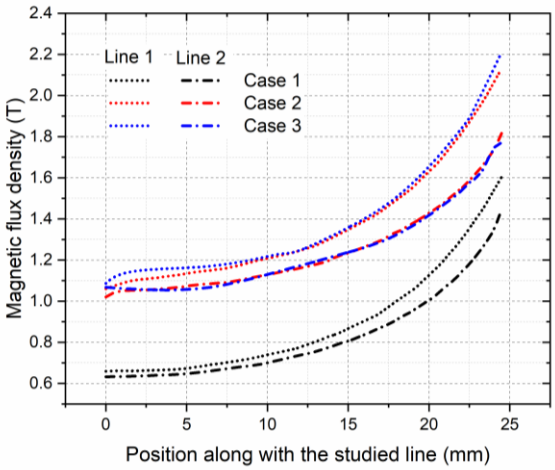

Figure 6.3.3 Magnetic flux density distributions along with the studied lines, in the three different cases.

6.3.1.2 Modeling principles

For the first step, to obtain the spatial magnetic fields, the ***A***-formulation has been implemented into the Rotating Machinery, Magnetic interface in COMSOL Multiphysics. According to Maxwell's equations, Constitutive law, Ohm's law, we have

$$\nabla\times\left[\frac{1}{\sigma}\nabla\times\left(\frac{1}{\mu_0\mu_r}\nabla\times\boldsymbol{A}\right)\right]=-\frac{\partial\left(\nabla\times\boldsymbol{A}\right)}{\partial t} \tag{6.4}$$

where the magnetic vector potential $\boldsymbol{A}$ is defined as

$$\nabla \times \boldsymbol{A} = \boldsymbol{B} \tag{6.5}$$

For the second step, the time-varying magnetic fields are mainly introduced by the electromagnetic interaction between the rotating EDW and the aluminium guideway. Once we acquire the time-varying magnetic fields around one specific coil, they can be applied to the 2D HTS coil model based on the $\boldsymbol{T}$-formulation [151], as external fields. Here, we can consider the studied HTS coil stationary because though the flux density in the air gap is position-dependent, the position variation of the coil is decided by the rotating time [the initial position of the coils is shown in Figure 6.3.1 (b)]. Therefore, in general, this is a time-dependent problem, and the time-varying magnetic fields can reflect this property.

The governing equation of the $\boldsymbol{T}$-formulation can be written as

$$\nabla \times \left(\frac{1}{\sigma} \nabla \times \boldsymbol{T} \right) + \frac{\partial \boldsymbol{B}}{\partial t} = 0 \tag{6.6}$$

The conductivity of the HTS parts is written as Equation (3.36). The homogenization method has been applied to the HTS coil, thus the equivalent critical current density for each tape can be described by (2.25). In (2.25), the parameters have been determined as follows: $B_0 = 0.426$ T, $k = 0.186$, and $\alpha = 0.7$ [362]. The three coefficients have been obtained by performing a regression on experimental data.

6.3.2 Results and analysis

Following the two steps mentioned in section 6.3.1.2, this section will analyse the general electro-mechanical performance of the EDW and the electromagnetic characteristics of the HTS HAMs, respectively.

6.3.2.1 Electro-mechanical performance of the HTS HAM EDW

The modelling parameters are taken from Table 14. The rotational velocity is chosen as 250 rpm, namely $\omega_m = 26.18$ rad/s, and the translational speed $v_x = 0$. Figure 6.3.4 shows the spatial magnetic flux density distribution and the current density induced in the aluminium track for the example PM EDW and the proposed HTS HAM EDW, respectively. The two EDWs possess the same inner and outer radius. The remanent flux density for the PM is 1.42 T, and the transport current for each HTS tape is 200 A. It can be clearly seen that the EDW is composed of 8 identical poles, and the application of HTS HAMs has largely increased the flux density as well as the induced current in the track. To further illustrate the improvement in terms of flux density brought by the HTS HAM, the average airgap flux density (in the

white frame region represented by solid lines) has been presented and compared in Figure 6.3.5. It can be seen that the average flux density, B_{avg}, has been increased by 45%.

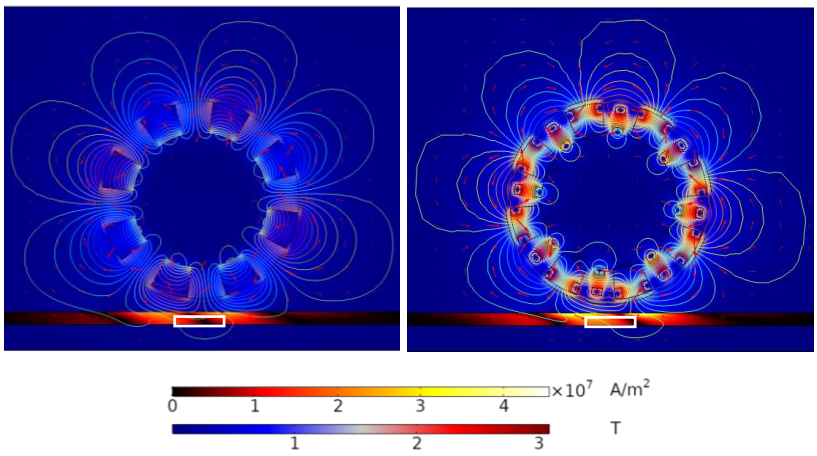

Figure 6.3.4 Spatial magnetic flux density and current density induced in the aluminium track, at t = 0.2 s. (a) PM EDW, with a remanent flux density of 1.42 T. (b) HTS HAM EDW, with a transport current of 200 A per turn.

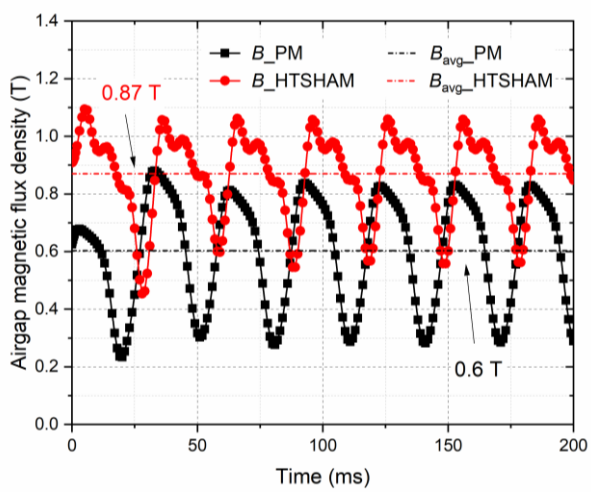

Figure 6.3.5 Comparison of the magnetic flux density in the air gap between the HTS HAM EDW and the conventional PM design.

To study the uniformity of the magnetic flux density in the time domain, the deviation s has been introduced, as

$$s = \sqrt{\sum_{i=1}^{N} (B_i - B_{avg})^2 \Big/ (N-1)} \tag{6.7}$$

where B_i is the flux density at a certain time, and N is the number of sampling points. Compared to the PM design, the flux density in the airgap of the HTS HAM EDW has a better uniformity as s decreases from 0.2 to 0.15.

Figure 6.3.6 shows the calculated thrust force, F_T, and lift force, F_L, for the HTS HAM EDW and PM EDW, based on Maxwell stress tensor (MST) and Lorentz force (LF), respectively. It can be found that MST agrees well with LF, and both the lift and thrust forces have been increased by approximately 2.5 times with the application of HTS HAMs, compared with the PM design. In fact, the thrust and lift forces depend on the relative slip speed, defined as the difference between the circumferential speed and the translational speed of the EDW. The slip speed is written as [376]

$$S = \omega_m r_o - v_x \tag{6.8}$$

where ω_m denotes the angular velocity of the EDW.

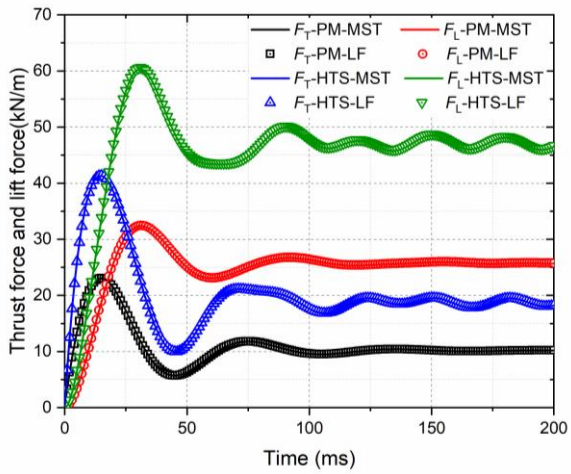

Figure 6.3.6 Comparison of the thrust/lift forces between the HTS HAM EDW and the conventional PM design. F_T: thrust force. F_L: lift force. MST: Maxwell stress tensor. LF: Lorentz force.

To explore the dependence of thrust and lift forces on the slip speed, S has been changed from – 40 to 80 m/s, with ω_m = 26.18 rad/s. The variation of the two forces with S for the PM EDW and HTS HAM EDW has been presented in Figure 6.3.7. It can be seen that, in general, the application of HTS HAMs can largely increase the amplitude of both forces, especially for the lift force. When $S > 0$, a thrust force can be generated; otherwise, a braking force can be produced. As far as the lift force is concerned, when $S = 0$, it attains the minima, i.e., no lift force is generated in this case.

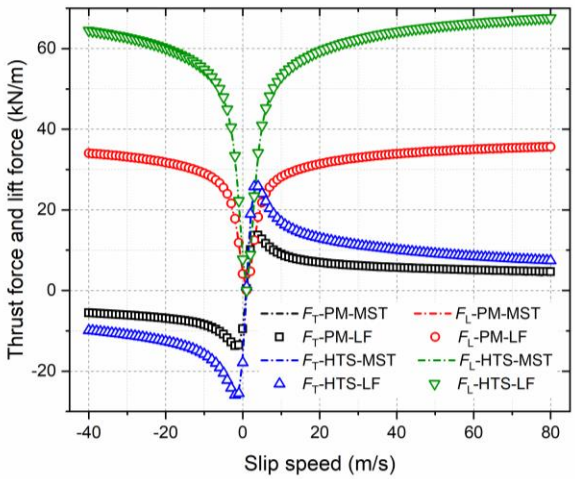

Figure 6.3.7 Variation of the thrust/lift forces with the slip speed for the PM EDW and HTS HAM EDW. F_T: thrust force. F_L: lift force. MST: Maxwell stress tensor. LF: Lorentz force.

In addition, with the same dimension and number of pole pairs, the magnet weight of the PM design is approximately 38.5 kg. However, as a comparison, the application of HTS HAMs can decrease the magnet weight by 2/3, reaching around 12.8 kg.

6.3.2.2 Loss properties of the HTS HAM

As the second step of this research, we need to study the loss properties of the HTS HAM. When a single HTS coil only carries a DC, the DC flux density distribution has been shown as Case 3 in Figure 6.3.2. However, when the DC fields generated by the HTS HAM interact with the aluminium track, the flux density around the HTS coils becomes time-varying, as illustrated in Figure 6.3.5. As a result, the HTS coil carrying a DC will be exposed to time-varying magnetic fields, thus dynamic loss will be generated.

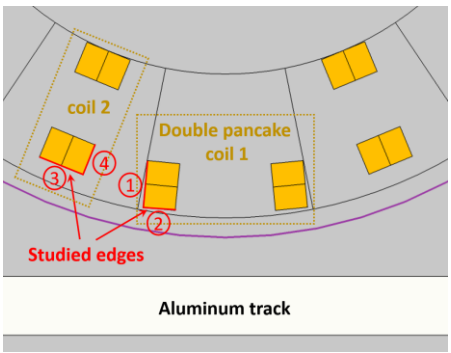

Figure 6.3.8 Studied coils and edges of the HTS HAM EDW.

As shown in Figure 6.3.8, I have chosen two coils and four edges as the study object to extract the spatially average flux density applied to the HTS coil in COMSOL Multiphysics. The variations of flux density on the four edges are shown in Figure 6.3.9.

In Figure 6.3.9, the flux density generated due to the interaction between the rotating EDW and the aluminium track has been extracted, as presented on the right four subfigures, which is the difference (Diff.) between the synthetic field (Syn.) in the case where the EDW rotates above the track and the self-field (Self.) in the case where the EDW rotates in the air. For the modelling of HTS coils, this Diff. flux density needs to be applied in addition to the DC transport current, in that the DC transport current serves as the field source of the EDW, and the discrepancy field is the time-varying field introduced by the rotating EDW system. The axisymmetric homogenization model for the studied double pancake coil has been established, as shown in Figure 6.3.10. For Coil 1, we have taken the average value of Diff. flux density on Edge 1 and Edge 2 as the applied fields, with the Dirichlet boundary condition. For Coil 2, Edge 3 and Edge 4 have been considered in the same way. The applied fields are presented in Figure 6.3.11, including the components perpendicular and parallel to the wide surface of the coil so that the $J_c(\boldsymbol{B})$ dependence described by Equation (2.4) can be taken into account. One cycle of the applied field signals is shaded in Figure 6.3.11, and three cycles of fields have been applied.

From inside to outside, the 1st, 75th, 150th, 225th, and 300th double pancake turns of the studied two coils have been chosen to study the AC power dissipation, P_{AC} (mW), and dynamic power loss, P_{dyn} (mW), as shown in Figure 6.3.12. It can be found that the generated AC loss and dynamic loss in each double pancake turn are in the order of milliwatt, and most of the AC loss and dynamic loss are focused on the middle parts of the coils. In Section 5.3, we have drawn the conclusion that most of the AC loss is concentrated in the inner and outer parts of one coil under the influence of the perpendicular AC magnetic fields, which is different from the phenomenon in Figure 6.3.12. In fact, here although the time-varying magnetic fields have been applied to the coils as the external fields, their amplitudes are much lower than the fields generated by the DC transport current, namely the self-field. As a result, the flux density and loss distributions are mainly determined by the DC transport current.

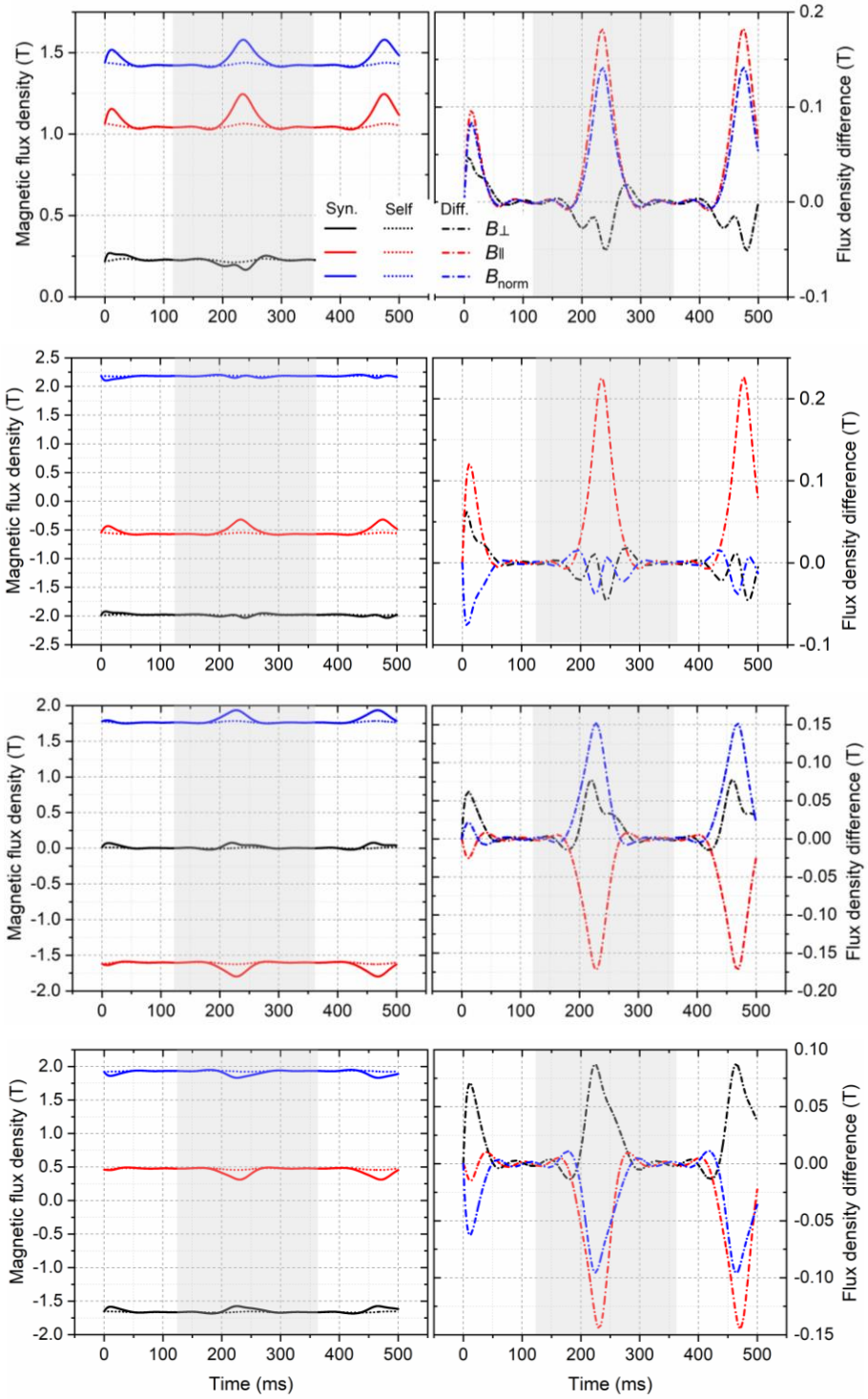

Figure 6.3. 9 Variation of the flux density on the studied edges in the time domain. From top to bottom, the four subfigures represent the flux density on edges 1-4, respectively. $B_\perp$ and $B_\parallel$ separately stand for the flux density perpendicular and parallel to the wide surface of the coil, B_{norm} being the flux density norm. The solid lines refer to the synthetic (Syn.) field when the EDW interacts with the aluminium track, the dot lines represent the self (Self) flux density when the EDW purely rotates in

the air without tracks, and the dash-dot lines on the right are the flux density difference (Diff.) between the two former cases.

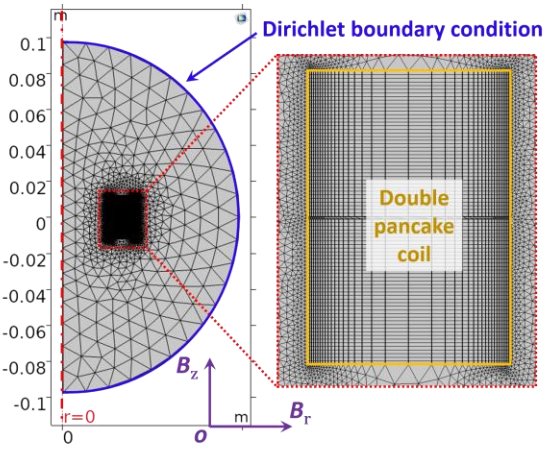

Figure 6.3.10 The axisymmetric numerical model of the double pancake HTS coil.

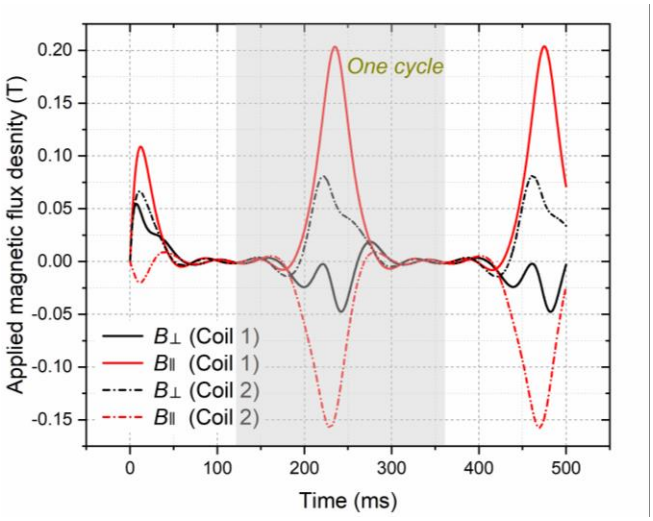

Figure 6.3.11 Externally applied magnetic fields perpendicular and parallel to the wide surface of the HTS coil.

As shown in Figure 6.3.13, the highest perpendicular flux density, B_r, and the loss per unit volume, $\boldsymbol{E}\cdot\boldsymbol{J}$, appear in the middle parts of Coil 1, where most of the power dissipation is thus produced. As for the loss ratio, P_{dyn}/P_{AC} of each double pancake turn, it decreases from inside to outside, in that the external time-varying magnetic fields induces higher magnetization losses in the outer turns of the coil under the shielding effect of the outer turns on the inner ones, which agrees well with the conclusions drawn in Section 5.3. Therefore, P_{dyn} occupies the majority of the AC loss (over 50%) for the inner and middle turns. Besides, it can be seen that the losses in Coil 1 are higher than those in Coil 2, which is reasonable because Coil 1 is closer to the aluminium guideway. In general, the total AC power dissipation for each double

pancake coil of the EDW is estimated to be no higher than 12 W. By decreasing the transport current or the cryogenic temperature, the load ratio in each HTS coil can be reduced, and therefore, the total AC loss. In the future, a specific loss controlling strategy needs to be developed to achieve the best operating efficiency for the HTS EDW.

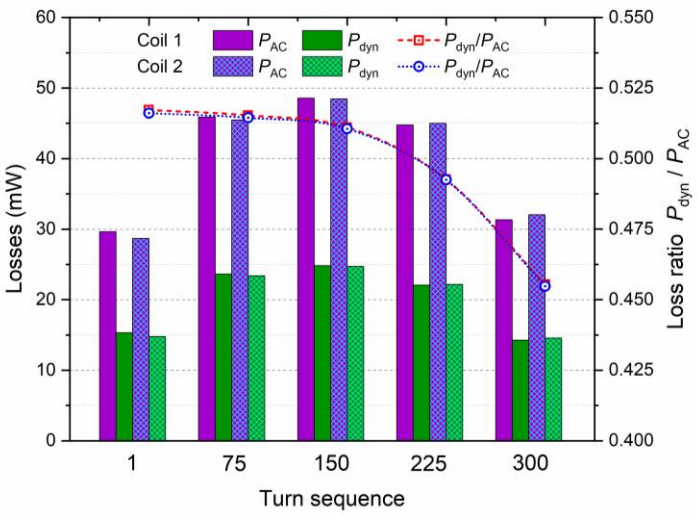

Figure 6.3.12 AC loss, P_{AC}, dynamic loss, P_{dyn}, and the loss ratio, P_{dyn}/P_{AC}, of the studied double pancake turns, from inside to outside.

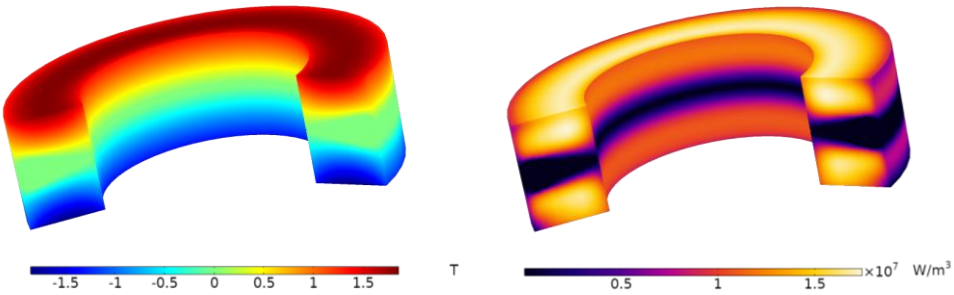

(a) (b)

Figure 6.3.13 Distributions of the magnetic flux density, B_r, and the AC loss per unit volume, $\boldsymbol{E \cdot J}$, of Coil 1, after one complete cycle. (a) B_r. (b) $\boldsymbol{E \cdot J}$.

6.3.3 Summary

Section 6.3 has put forward a novel design for electrodynamic wheels based on the HTS Halbach array magnets. The proposed HTS HAM can largely increase the magnetic flux density in the air gap between the EDW and the passive conductive guideway, and thus higher thrust and lift forces can be generated for the EDW. Additionally, the weight of the applied magnets can be reduced. In this research, under the same EDW dimension, both the thrust and lift forces have been increased by 2.5 times and the magnet weight has been reduced by 2/3 with the application of HTS HAMs, compared to the example PM EDW. The AC loss and

dynamic loss of the HTS HAMs have been studied with the 2D axisymmetric modelling method, and the dynamic loss accounts for approximately half of the total AC loss.

As far as the modelling method is concerned, the modelling process has been divided into two procedures. At first, the HTS coils have been equivalized to be conventional coils carrying the same DC transport current, and the dynamic electro-mechanical performance of the EDW has been simulated with the ***A***-formulation. Then, the time-varying magnetic fields introduced by the interaction between the EDW and the aluminium track have been extracted as the external fields and applied to the HTS double pancake coils, in addition to the DC transport current. The loss characteristics of the HTS coil has been modelled with the ***T***-formulation. It has been illustrated that, for studying the electro-mechanical performance of large-scale HTS devices, e.g., synchronous electric machines, the HTS field coils can be reasonably equivalized as conventional ones carrying the same DC so that the computation complexity can be largely decreased.

It should be pointed out that the thrust and lift forces in the centre plane of the two EDWs have been compared, thus 2D modelling has been chosen and the unit "kN/m" has been used. As is known, the magnetic field at the centre of the circular current loop is the highest in the axial direction. However, the magnetic field at the coil centre can be the lowest in the current loop plane. In other words, the field in the current loop plane can increase positively with the distance from the centre when the distance is less than the radius of the coil, as demonstrated in Figure 6.3.3. Therefore, in Section 6.3, the least thrust and lift forces per meter (kN/m) in the axial direction of the EDW have been presented. Consequently, it is believed that just comparing the forces in the centre plane through 2D modelling is sufficient to demonstrate the effectiveness of the proposed HTS Halbach array that it can greatly increase the thrust and lift forces of the EDW compared to the conventional PM one. The proposed EDW remains at the preliminary stage of design, thus the cryogenic system and its weight have not been discussed. Once the energization method and the cooling method for the HTS coils is determined, the overall electro-mechanical performance and operation efficiency of the proposed HTS EDW deserves further investigation. Section 6.3 is believed to open the way to future maglev on-road vehicles.

6.4 Conclusion

Chapter 6 has proposed an HTS Halbach array topology for air-cored superconducting machines, in which the HTS coils carrying DC are arranged in a certain form so that the magnetic flux can be focused in the same way as a permanent magnet Halbach array. With the

application of the HTS HAMs, the superconducting machines can benefit not only from high electric loading, but also high magnetic loading. In addition, with the removal of the iron core and iron support as well as the replacement of the conventional PMs, the weight of the machine can be largely decreased. As a result, the HTS Halbach array topology can bring about higher power density for electrical machines compared to conventional machines with normal conductors and superconducting machines with conventional topologies. By applying the HTS HAMs to the designs of a MW-level C-GEN wind turbine generator and an electrodynamic wheel used for maglev, it has been demonstrated that the HTS HAMs can greatly increase the magnetic flux density in the airgap. The developed C-GEN generator built with HTS HAMs is capable of producing more than 4 times the power as the PM machine within the same volume, and the proposed EDW equipped with HTS HAMs opens the way to future on-road maglev vehicles.

Chapter. 7 Conclusions and Future Works

7.1 Conclusions

AC loss remains a significant issue for the realization of superconducting machines, which can lead to the quench of HTS coils and the demagnetization of HTS trapped field magnets. This thesis has investigated the electromagnetic characteristics and loss properties of HTS CCs applied to electric machines through numerical modelling and experimental measurements and proposed an HTS Halbach array topology which has then been applied to the designs of an air-cored wind turbine generator and an electrodynamic wheel used for maglev. Dynamic loss typically occurs in the field windings of synchronous superconducting machines. Transport current loss and magnetization loss are mainly generated in the armature windings of superconducting motors and generators, respectively. Therefore, the three types of AC losses have been focused on in the entire research. The current density, magnetic flux density, and power dissipation distributions in HTS CCs, stacks, coils, as well as TFSs over a wide frequency range, from the power frequency to the kHz level, have been systematically explored. To address the issue identified in the thesis statement, the work completed in this thesis can be concluded as below:

"This work has illuminated the electromagnetic characteristics and loss properties of different HTS topologies applied to superconducting machines over a wide frequency band, from 50 Hz to 20 kHz, with the development of a ***T***-formulation based multilayer numerical model, the derivation of a novel full-range formulation for dynamic loss, the definition of demarcation current and corner field for dynamic resistance, the investigation into the skin effect and shielding effect of HTS coils at high frequencies, and the exploration of the possible demagnetization of TFSs under high-frequency cross fields. Besides, the proposed HTS Halbach array topology represents a generic approach for the design of fully air-cored superconducting machines, eliminating heavy iron cores."

Key Contributions of this Thesis

The primary targets of this project have been achieved and the key scientific contributions can be summarised as follows:

(1) The state of the art of AC loss related research has been reviewed, including the adopted superconducting materials in electric machines, loss calculation formulae, modelling methods, measurement approaches, as well as loss reduction techniques. This overview is believed to help researchers better understand the research status of AC loss in superconductors and to provide a useful reference for superconducting machine designs, especially for those functioning at high speeds for future aviation.

(2) The widely adopted thin film approximation for the modelling of HTS CCs has proven inapplicable when they are exposed to a high-frequency electromagnetic environment, e.g., for the calculation of magnetization loss at frequencies higher than 100 Hz. At high frequencies, the physical multilayer structure of the HTS CC has to be taken into account, i.e., both the HTS layer and non-superconducting parts (typically including the copper stabilizer, the silver overlayer, and the magnetic or non-magnetic substrate) need to be modelled.

(3) In order to model the high-frequency performance of HTS CCs, a ***T***-formulation based multilayer numerical model has been developed with open source code under FORTRAN 90, which has been validated by comparison against the ***H***-formulation based multilayer numerical model and the experimental data. As far as the modelling of a single HTS CC is concerned, the proposed ***T***-formulation based open-source-code models have higher computational speed compared to the ***H***-formulation based numerical models. As the most extensively adopted modelling method, the ***H***-formulation based numerical model is intuitive and can be easily implemented into commercial software, e.g., COMSOL Multiphysics. Besides, the ***H***-formulation based models have a wider scope of application as they can be used to study HTS systems made of various geometries, especially in 3D space.

(4) The dependence of dynamic loss and dynamic resistance on the intrinsic material properties of HTSCs, including the self-field critical current, I_{c0}, and the n-value, has been studied in detail. It has been found that though dynamic loss and dynamic resistance decrease along with increasing I_{c0}, their changing rates decrease in a non-linear way with the increase of I_{c0}; thus, it is not always cost-efficient to reduce dynamic loss by simply increasing the critical current during the manufacture of HTS CCs.

(5) In general, both the dynamic loss and the dynamic resistance increase linearly with the external magnetic field, B_{ext}, until it reaches the corner field B_{cor}. When B_{ext} goes beyond B_{cor}, dynamic loss increases non-linearly with the B_{ext}, leading to a fast rise of power dissipation. The higher the n-value is, the faster the dynamic loss and dynamic resistance increases along with B_{ext}, and the smaller B_{cor} becomes. The previously existing analytical equations cannot accurately predict the non-linearity of dynamic loss. In order to explain and quantitatively

describe the non-linear variation of dynamic loss, a novel formulation has been derived taking into account the $J_c(\boldsymbol{B})$ dependence of HTSCs through a rigorous process, which can be used for full ranges of both magnetic fields and current load ratios for HTS CCs. The non-linearity of dynamic loss is found to be in the form of a summation of a series of power functions.

(6) In order to avoid quench, the turning points of rapid changes in dynamic resistance (dynamic loss) need to be determined. Therefore, lower demarcation current and upper demarcation current have been defined to characetize the transition of the dynamic resistance curve with respect to transport current from the non-linear region to the linear section and from the linear region to the non-linearly fast-rising section, respectively. The corner field B_{cor} is the turning magnetic flux density characterizing the transition of the dynamic resistance curve with respect to external field from the linear section to the non-linearly fast-rising region. The three parameters have been expressed with explicit formulae, which provide a significant reference for accurate loss controlling in HTS magnets, electric machines, and flux pumps, etc.

(7) In high-speed superconducting machines, e.g., propulsion motors for future aviation, the employed HTS CCs have to operate in a high-frequency electromagnetic environment, and thus the physical multilayer structure of HTS CCs has to be taken into account. With the ***T***-formulation and ***H***-formulation based multilayer numerical modelling methods, the wide-frequency electromagnetic characteristics of HTS CCs, stacks, circular coils, racetrack coils, as well as TFSs have been systematically studied, from the power frequency to the kHz level.

The existing definition of the dynamic region and analytical equations for calculating dynamic loss have proven not applicable at the kHz level, in that the dynamic region of a single CC shrinks rapidly with increasing frequency and the skin effect results in a redistribution of magnetic flux and current among different layers. Therefore, multilayer numerical models are recommended to quantify the dynamic loss and magnetization loss. In general, magnetization power loss is in a positive correlation with frequency. Under the skin effect, both current and magnetic flux inside the CC will be driven to both ends and outer copper stabilizers with increasing frequency, thus the loss in the copper stabilizers will be approaching magnetization loss as well as the total AC loss. There exists a positive correlation between dynamic loss and frequency followed by a negative one because at higher frequencies the amount of traversing magnetic flux during one AC cycle shrinks rapidly. At low frequencies, dynamic loss can occupy the majority of the total AC loss for HTS CCs, stacks, and coils; however, the magnetization loss becomes more important due to the skin effect with increasing frequency. At low frequencies, e.g., f = 100 Hz, a higher B_{ext} leads to a higher dynamic loss in an HTS CC because of more magnetic flux traversing the CC. However, at higher frequencies above

1 kHz, a higher B_{ext} results in a higher magnetization loss due to the skin effect and the loss contribution from copper stabilizers. Compared with a single CC, the influence of dynamic loss in HTS stacks or coils is more significant because the shielding effect among different turns can enhance the significance of dynamic loss, bringing about a higher magnetization loss ratio in the outermost turns and a higher dynamic loss proportion in the middle parts. Therefore, in summary, both dynamic loss and magnetization loss should be attached to high importance for the design of HTS magnets and machine windings operating in a high-frequency environment.

The current density and magnetic flux density distributions of a TFS cannot be correctly predicted by the widely adopted 2D-axisymmetric models because of the emergence of the defined electromagnetic criss-cross, which divides the CC wide surface into four roughly equivalent subdomains. Therefore, 3D numerical modelling methods need to be adopted. As for loss properties, the multilayer physical structure of HTS CCs has to be considered, especially for perpendicular field magnetization even at low-frequency band, e.g., at 50 Hz. For cross field magnetization, the multilayer structure has to be taken into account at frequencies higher than 200 Hz. For perpendicular field magnetization of curved HTS stacks, the applied field starts to penetrate into the stack from the middle edges. As a result, at high frequencies, the skin effect can focus the penetrated flux and induced current due to Lenz's law near the edges. In other words, the induced current in the central part of the curved square CC demonstrates a kind of 'lag effect' in the time domain and seems less sensitive to the variation of external magnetic fields. Due to the influence of cross fields on the electromagnetic distributions and loss characteristics, demagnetization can happen to the TFS. With increasing frequencies of cross fields, the originally trapped flux after PFM in the stack can be deteriorated more severely due to the skin effect.

(8) In order to increase the power density of electric machines, an HTS Halbach array topology has been proposed for air-cored superconducting machines. The HTS Halbach array is composed of a series of HTS coils arranged in a certain form so that the magnetic flux can be focused inside the coils. The superconducting machines can benefit from both high electric loading and magnetic loading with the application of the HTS HAMs.

By applying the HTS HAMs to the designs of a MW-level C-GEN wind turbine generator and an electrodynamic wheel used for maglev, it has been demonstrated that the HTS HAMs can greatly increase the magnetic flux density in the airgap. The developed C-GEN generator built with HTS HAMs is capable of producing more than 4 times the power as the PM machine within the same volume. Under the same EDW dimension, both the thrust and lift forces have

been increased by 2.5 times with the application of HTS HAMs, compared to the example PM EDW. The proposed EDW equipped with HTS HAMs opens the way to future on-road maglev vehicles. Additionally, with the removal of the iron core and iron support as well as the replacement of the conventional PMs, the weight of the machine can be largely decreased. In summary, the HTS Halbach array topology can bring about higher power density for electrical machines compared to conventional machines with normal conductors and superconducting machines with conventional topologies.

Last but not the least, for studying the electro-mechanical performance of large-scale HTS devices, e.g., synchronous electric machines, the HTS field coils can be reasonably equivalized as conventional ones carrying the same DC so that the computational complexity can be largely decreased. Afterwards, to study the loss characteristics of employed HTS CCs, the periodic spatial magnetic fields around the HTS CCs can be extracted and then applied to them in a FEM based numerical model.

To conclude, this thesis is believed to help researchers better comprehend the electromagnetic behaviours and loss properties of HTS CCs applied to electric machines, deepen people's understanding of the AC loss mechanism, and provide a useful reference for the design of air-cored superconducting machines.

7.2 Future Works

A calculation-efficient ***T***-formulation based 2D numerical model taking into account the multilayer structure of HTS CCs has been developed with open source code under FORTRAN during this PhD project. This model will be extended to 3D in the future so that it can be utilized to simulate the high-frequency behaviors of complex HTS structures and devices.

The derived novel formulation of dynamic loss explains well the non-linear variation of dynamic loss and dynamic resistance of HTS CCs, which can be applied to a full range of external magnetic fields and load ratios. However, this formulation is now only applicable for a single thin HTS layer at low frequencies. Therefore, I aim to adapt the formulation to 2D stacks and 3D coils shortly to conveniently predict the dynamic loss in HTS field windings.

Inside a practical electrical machine, the electromagnetic environment is quite complex, composed of high-frequency harmonics and the electromagnetic signals are not purely sinusoidal. Therefore, in the future, I would like to build an HTS machine demonstrator and study experimentally the non-sinusoidal performance of HTS coils and trapped field magnets besides numerical modelling. 3D models are indispensable for accurately study the electromagnetic properties of HTS coils and trapped field magnets, but they are normally

computationally complicated and time-consuming, demanding a lot of memory for storage. In addition, the magnetic field distribution inside HTS machines is determined by both the superconducting and non-superconducting parts, thus just modelling the superconductors is not sufficient to reflect the overall power dissipation of the machine that decides the design of cryogenic systems. The non-superconducting parts can contain conventional conductors of HTS CCs, iron cores, and permanent magnets, thus their electromagnetic interaction with the superconductors have to be considered. Therefore, in order to accurately predict the electromagnetic behaviors of HTS coils and trapped field magnets applied to a practical electric machine, we need to build a highly efficient 3D model composed of all the superconductors and normal conductors in a fixed machine topology. To this end, I will adopt the combined formulations to increase the computational efficiency, e.g., the ***T*-*A*** formulation, the ***H*-*A*** formulation, and the ***H*-ϕ** formulation. Additionally, to further decrease the DOF and computational complexity, I will exploit the simplification approaches, e.g., the multi-scaling and densification methods. Besides the electromagnetic properties, the thermal characteristics of superconductors should also be considered because they directly affect the design of cryocoolers and quench protection. In addition, the high centrifugal force in high-speed electrical machines brings a big challenge to the design of rotating field coils. Therefore, an efficient electro-thermal-mechanical numerical model for high-speed HTS machines remains to be developed.

The existing AC loss reduction techniques are composed of the filamentation of HTS CCs, the 3S wire, the Roebel structure, the Rutherford concept, the CORC® wire, the application of flux diverters, as well as the winding techniques. I will study their applicability and effectiveness in a practical machine environment, based on which I will explore an efficient and reliable loss reduction approach for HTS coils applied to high-speed electric machines while maintaining acceptable mechanical strength of the HTS materials.

The proposed HTS Halbach array topology can largely increase the power density of electric machines, eliminating heavy iron cores, which has been preliminarily demonstrated in the designs of the HTS C-GEN wind turbine generator and the HTS EDW equipped with HAMs. It should be pointed out that the proposed HTS C-GEN generator and HTS EDW remain at the preliminary stage of design, thus the corresponding cryogenic systems and their weight have not been much discussed in this thesis. Once the energization method (HTS flux pump is a promising alternative) and the cooling method for the HTS HAM are determined, the overall electro-thermal-mechanical performance and operating efficiency of the proposed air-cored

machines can be further investigated. In the future, I will focus on the design of the whole machine system and validate the design by experimental measurements.

References

1. G. Lei, J. G. Zhu, Y. G. Guo, C. C. Liu and B. Ma, "A review of design optimization methods for electrical machines", *Energies*, vol. 10, no. 12, 2017.
2. T. Wildi, Electrical Machines Drives and Power Systems, USA, NJ, Englewood Cliffs: Prentice-Hall, 2005.
3. R. Saidur, "A review on electrical motors energy use and energy savings", *Renew Syst. Energy Rev*., vol. 14, no. 3, pp. 877-898, 2010.
4. M. S. Hossain, "Panel estimation for CO2 emissions, energy consumption, economic growth, trade openness and urbanization of newly industrialized countries", *Energy Policy*, vol. 39, no.11, pp. 6991-6999, 2011.
5. M. Cheng, L. Sun, G. Buja and L. Song, "Advanced electrical machines and machine-based systems for electric and hybrid vehicles", *Energies*, vol. 8, no. 9, pp. 9541-9564, 2015.
6. M. Cheng and Y. Zhu, "The state of the art of wind energy conversion systems and technologies: A review", *Energy Convers. Manage*., vol. 88, pp. 332-347, 2014.
7. R. Wrobel and B. Mecrow, "A Comprehensive Review of Additive Manufacturing in Construction of Electrical Machines," *IEEE Trans. Energy Convers.*, vol. 35, no. 2, pp. 1054-1064, 2020.
8. S. Li et al, "Modeling, Design Optimization, and Applications of Switched Reluctance Machines—A Review," *IEEE Trans. Ind. Appl.*, vol. 55, no. 3, pp. 2660-2681, 2019.
9. D. Lee, G. Park, B. Son and H. Jung, "Efficiency improvement of IPMSG in the electric power generating system of a range-extended electric vehicle," *IET Electric Power Applications*, vol. 13, no. 7, pp. 943-950, 2019.
10. X. Sun et al, "Analysis and Design Optimization of a Permanent Magnet Synchronous Motor for a Campus Patrol Electric Vehicle," *IEEE Trans. Veh. Technol.*, vol. 68, no. 11, pp. 10535-10544, 2019.
11. S. Sahoo, X. Zhao, K. Kyprianidis, "A Review of Concepts, Benefits, and Challenges for Future Electrical Propulsion-Based Aircraft," *Aerospace*, vol. 7, no. 4, 2020.
12. I. Jlassi and A. J. M. Cardoso, "Fault-Tolerant Back-to-Back Converter for Direct-Drive PMSG Wind Turbines Using Direct Torque and Power Control Techniques," *IEEE Trans. Power Electron.*, vol. 34, no. 11, pp. 11215-11227, 2019.
13. E. Taherian-Fard, R. Sahebi, T. Niknam, A. Izadian and M. Shasadeghi, "Wind Turbine Drivetrain Technologies," *IEEE Trans. Ind. Appl.*, vol. 56, no. 2, pp. 1729-1741, 2020.
14. F. Grilli et al, "Superconducting motors for aircraft propulsion: the Advanced Superconducting Motor Experimental Demonstrator project," *J. Phys.: Conf. Ser.*, vol. 1590, 012051, 2020
15. Kiruba S. Haran et al., "High power density superconducting machines—Development status and technology roadmap", *Supercond. Sci. Technol*., vol. 30, no. 12, 123002, 2017.
16. H. Yamasaki and M. Furuse, "Feasibility study project to realize the merits of 10 MW class superconducting wind turbine generators", Cryogenic Eng. Conf. Int. Cryogenic Mater. Conf., Jul. 2015.
17. R. Fair et al., "Development of an HTS hydroelectric power generator for the Hirschaid power station", Proc. 9th Eur. Conf. Appl. Supercond, 2009.
18. C. Lewis, "Direct drive superconducting wind generators" in Wind Power Generation and Wind Turbine Design, Southampton: WIT Press, pp. 303-328, 2010.

19. AMSC (June 2012), "SeaTitan 10 MW wind turbine," [Online] Available at: https://www.amsc.com/wp-content/uploads/wt10000_DS_A4_0212.pdf.
20. J. Sun, S. Sanz and H. Neumann, "Conceptual design and thermal analysis of a modular cryostat for one single coil of a 10 MW offshore superconducting wind turbine", Proc. CEC/ICMC 2015, pp. 1-8, 2015.
21. J. Sun et al., "Preliminary test of the prototype modular cryostat for a 10 MW offshore superconducting wind turbine," IOP Conference Series: Materials Science and Engineering, vol. 171, pp. 012121, 2017.
22. The Troubled Quest for the Superconducting Wind Turbine. [Online] Available at: https://spectrum.ieee.org/green-tech/wind/the-troubled-quest-for-the-superconducting-wind-turbine.
23. A. B. Abrahamsen et al., "Comparison of levelized cost of energy of superconducting direct drive generators for a 10-MW offshore wind turbine", IEEE Trans. Appl. Supercond., vol. 28, no. 4, 2018.
24. A. Bergen et al., "Design and in-field testing of world's first ReBCO rotor for a 3.6 MW wind generator", Supercond. Sci. Technol., vol. 32, no. 12, 2019.
25. US DoE backs push for wind turbines up to 15MW. [Online] Available at: https://supernode.energy/us-doe-backs-push-for-wind-turbines-up-to-15mw/.
26. J. L. Felder, G. V. Brown, H. D. Kim and J. Chu, "Turboelectric distributed propulsion in a hybrid wing body aircraft", Proc. Int. Symp. Air Breath. Engines Conf., pp. 1-20, 2011.
27. Low ac-loss magnesium diboride superconductors for turboelectric aircraft propulsion systems NASA 2009 Phase 1, SBIR, NNX09CC75P Hyper Tech Research, Inc.
28. ASuMED. [Online] Available at: http://asumed.oswald.de/index.php
29. A. Patel et al., "A trapped field of 17.7 T in a stack of high temperature superconducting tape", Supercond. Sci. Technol., vol. 31, no. 9, 2018.
30. M. Boll et al., "A holistic system approach for short range passenger aircraft with cryogenic propulsion system", Supercond. Sci. Technol., vol. 33, no. 4, 044014, 2020.
31. M. Filipenko et al., "Concept design of a high power superconducting generator for future hybrid-electric aircraft", Supercond. Sci. Technol., vol. 03, no. 5, 054002, 2020.
32. M. D. Ainslie, et al., "Numerical modelling of dynamic resistance in high-temperature superconducting coated-conductor wires", *Supercond. Sci. Technol.*, vol. 31, no. 7, 074003, 2018.
33. M. Feddersen, K. S. Haran and F. Berg, "AC loss analysis of MgB_2-based fully superconducting machines", *IOP Conf. Mater. Sci. Eng*., vol. 279, no. 1, 012026, 2017.
34. R. Fair et al., "Development of an HTS hydroelectric power generator for the Hirschaid power station", *J. Phys.: Conf. Ser*., vol. 234, 032008, 2010.
35. M. Corduan et al, "Topology Comparison of Superconducting AC Machines for Hybrid Electric Aircraft," *IEEE Trans. Appl. Supercond*, vol. 30, no. 2, pp. 1-10, 2020.
36. E. Demenčík et al., "AC Loss and Coupling Currents in YBCO Coated Conductors With Varying Number of Filaments," *IEEE Trans. Appl. Supercond*, vol. 24, no. 6, pp. 1-8, 2014.
37. F. Grilli et al, "Computation of Losses in HTS Under the Action of Varying Magnetic Fields and Currents," *IEEE Trans. Appl. Supercond*., vol. 24, no. 1, pp. 78-110, 2014.
38. H. K. Onnes, "The Superconductivity of Mercury," Comm. Phys. Lab. Univ., Leiden, pp. 122-124, 1911.
39. W. Meissner and R. Ochsenfeld, "A new effect when superconductivity occurs," Naturewiss, vol. 21, no. 44, pp. 787-788, 1933.

40. F. and H. London, "The electromagnetic equations of the supraconductor," Proc. Roy. Soc., vol. 149, no. 866, pp. 71–88, 1935.
41. E. T. S. Appleyard, J. R. Bristow, H. London, "Variation of field penetration with temperature in a superconductor, " Nature, vol. 143, pp. 433–434, 1939.
42. G. Aschermann, E. Friedrich, E. Justi, and J. Kramer, "Supraleitfähige Verbindungen mit extrem hohen Sprungtemperaturen (NbH und NbN)," Phys. Z., vol. 42, pp. 349–360, 1941.
43. L. D. Landau and V. L. Ginzburg, "On the theory of superconductivity," Zh. Eksp. Teor. Fiz., vol. 20, pp.1064, 1950.
44. A. A. Abrikosov, "The magnetic properties of superconducting alloys," Journal of Physics and Chemistry of Solids, vol. 2, no. 3, pp. 199-208, 1957.
45. G. F. Hardy and J. D. Hulm, "Superconducting silicides and germanides," *Phys. Rev*., vol. 89, pp. 884, 1953.
46. B. T. Matthias, T. H. Geballe, S. Geller, and E. Corenzwit, "Superconductivity of Nb3Sn," Phys. Rev., vol. 95, no. 6, pp. 1435, 1954.
47. J. Bardeen, L. N. Cooper, and J. R. Schrieffer, "Microscopic theory of superconductivity," Phys. Rev., vol. 106, pp. 162–164, 1957.
48. J. Bardeen, L. N. Cooper and J. R. Schrieffer, "Theory of superconductivity," Phys. Rev., vol. 108, pp. 1175–1204, 1957.
49. B. D. Josephson, "Possible new effects in superconductive tunnelling," Phys. Lett., vol. 1, pp. 251–253, 1962.
50. T. G. Berlincourt and R. R. Hake, "Pulsed-Magnetic-Field Studies of Superconducting Transition Metal Alloys at High and Low Current Densities," Bull. Am. Phys. Soc., vol. 2, no.7, pp. 408, 1962.
51. R. D. Blaugher et al, "Superconductivity at Westinghouse," IEEE/CSC & ESAS European Superconductivity News Forum, no. 20, 2012. https://snf.ieeecsc.org/sites/ieeecsc.org/files/RN26e.pdf.
52. D. Jérome, A. Mazaud, M. Ribault, and K. Bechgaard, "Superconductivity in a synthetic organic conductor (TMTSF)2PF6," J. Phys. Lett., vol. 41, pp. 201–204, 1980.
53. J. G. Bednorz and K. A. Müller, "Possible high T_c superconductivity in the Ba-La-Cu-O system," Zeitschrift für Physik B, vol. 64, no. 2, pp. 189–193, 1986.
54. M. K. Wu, J. R. Ashburn, C. J. Torng, P. H. Hor, R. L. Meng, L. Gao, Z. J. Huang, Y. Q. Wang, and C. W. Chu, "Superconductivity at 93 K in a new mixed-phase Y-Ba-Cu-O compound system at ambient pressure," Phys. Rev. Lett., vol. 58, no. 9, pp. 908-910, 1987.
55. Z. Z. Sheng and A. M. Hermann, "Bulk superconductivity at 120 K in the Tl–Ca/Ba–Cu–O system". Nature, vol. 332, no. 6160, pp. 138–139, 1988.
56. A. Schilling, M. Cantoni, J. D. Guo, and H. R. Ott, "Superconductivity above 130 K in the Hg–Ba–Ca–Cu–O system," Nature, vol. 363, pp. 56–58, 1993.
57. J. Nagamatsu, N. Nakagawa, T. Muranaka, Y. Zenitani, and J. Akimitsu, "Superconductivity at 39 K in magnesium diboride," Nature, vol. 410, pp. 63–64, 2001.
58. Y. Kamihara, T. Watanabe, M. Hirano, and H. Hosono, "Iron-based layered superconductor La[$O_{1-x}F_x$]FeAs (x=0.05-0.12) with T_c = 26 K," J. Am. Chem. Soc., vol. 130, pp. 3296–3297, 2008.
59. K. Deguchi , Y. Mizuguchi, Y. Kawasaki, T. Ozaki, S. Tsuda, T. Yamaguchi and Y. Takano, "Alcoholic beverages induce superconductivity in $FeTe_{1-x}S_x$," Supercond. Sci. Technol., vol. 24, 055008, 2011.

60. P. J. Ray (2016), Master's thesis: Structural investigation of La(2-x)Sr(x)CuO(4+y)-Following staging as a function of temperature. https://doi.org/10.6084/m9.figshare.2075680.v2.
61. A. Drozdov, M. Eremets, I. Troyan, et al. "Conventional superconductivity at 203 kelvin at high pressures in the sulfur hydride system," Nature, vol. 525, pp. 73–76, 2015.
62. A. P. Drozdov, P. P. Kong, V. S. Minkov, et al, "Superconductivity at 250 K in lanthanum hydride under high pressures," Nature, vol. 569, pp. 528–531, 2019.
63. E. Snider, N. Dasenbrock-Gammon, R. McBride, et al. "Room-temperature superconductivity in a carbonaceous sulfur hydride," Nature, vol. 586, pp. 373–377, 2020.
64. P. W. Anderson, "The Resonating Valence Bond State in La2CuO4 and Superconductivity," Science, vol. 235, no. 4793, pp. 1196-1198, 1987.
65. B. Dalla Piazza, M. Mourigal, N. Christensen et al, "Fractional excitations in the square-lattice quantum antiferromagnet," Nature Phys, vol. 11, pp. 62–68, 2015.
66. P. Monthoux, A. V. Balatsky, and D. Pines, "Toward a theory of high-temperature superconductivity in the antiferromagnetically correlated cuprate oxides," Phys. Rev. Lett., vol. 67, no. 24, pp. 3448-3451, 1991.
67. Y. Cao, V. Fatemi, S. Fang, et al, "Unconventional superconductivity in magic-angle graphene superlattices," Nature, vol. 556, pp. 43–50, 2018.
68. Y. Cao, V. Fatemi, A. Demir, et al, "Correlated insulator behaviour at half-filling in magic-angle graphene superlattices," Nature, vol. 556, pp. 80–84, 2018.
69. S. Miura, et al., "Lightweight Design of Tens-MW Fully-Superconducting Wind Turbine Generators with High-Performance REBa2Cu3Oy Wires," IEEE Trans. Appl. Supercond., vol. 30, no. 4, pp. 1-6, 2020.
70. W. Stautner, "Cryocoolers for Superconducting Generators," Cryocoolers, pp. 121-154: Springer, 2020.
71. J. Sun, et al., “Design and construction of the cryogenic cooling system for the rotating magnetic validator of the 10 MW SUPRAPOWER offshore superconducting wind turbine,” IEEE Trans. Appl. Supercond, vol. 28, no. 3, pp. 1-5, 2017.
72. M. Tomsic, M. Rindfleisch, J. Yue, K. McFadden and J. Phillips, "Overview of MgB2 superconductor applications", Int. J. Appl. Ceram. Technol., vol. 4, no. 3, pp. 250-259, 2007.
73. G. Nam, H. Sung, B. Go, M. Park and I. Yu, "Design and Comparative Analysis of MgB2 and YBCO Wire-Based-Superconducting Wind Power Generators," IEEE Trans. Appl. Supercond., vol. 28, no. 3, pp. 1-5, 2018.
74. F. Lin, R. Qu, D. Li, Y. Cheng and J. Sun, "Electromagnetic Design of 13.2 MW Fully Superconducting Machine," IEEE Trans. Appl. Supercond., vol. 28, no. 3, pp. 1-5, 2018.
75. X. Song, N. Mijatovic, B. B. Jensen and J. Holbøll, "Design Study of Fully Superconducting Wind Turbine Generators," IEEE Trans. Appl. Supercond., vol. 25, no. 3, pp. 1-5, 2015.
76. M. Saruwatari et al., "Design Study of 15-MW Fully Superconducting Generators for Offshore Wind Turbine," IEEE Trans. Appl. Supercond., vol. 26, no. 4, pp. 1-5, 2016.
77. A. Patel et al., "A trapped field of 17.7 T in a stack of high temperature superconducting tape", Supercond. Sci. Technol., vol. 31, no. 9, 09LT01, 2018.
78. F. Gömöry, J. Šouc, E. Pardo et al., “AC loss in pancake coil made from 12 mm wide REBCO tape,” IEEE Trans. Appl. Supercond, vol. 23, no. 3, pp. 5900406-5900406, 2013.
79. K. Hayashi, “Commercialization of Bi-2223 Superconducting Wires and Their Applications,” SEI TECHNICAL REVIEW, no. 91, pp. 68-74, 2020. https://global-sei.com/technology/tr/bn91/pdf/E91-12.pdf.

80. M.-H. Ku, M.-H. Kang, H.-J. Lee et al., “The Critical Current Characteristics and n-value Measurement of HTS Tapes,” Progress in Superconductivity and Cryogenics, vol. 12, no. 1, pp. 12-16, 2010.
81. S. A. Ishmael, S. Rogers, F. Hunte et al., “Current Density and Quench Behavior of MgB2/Ga Composite Wires,” IEEE Trans. Appl. Supercond, vol. 25, no. 6, pp. 1-8, 2015.
82. M. Park, “Realization of a large-scale superconducting generator for a wind power generation system,” ESAS Summer School on HTS Technology for Sustainable Energy and Transport System, Bologna, Italy, 2016. http://www.die.ing.unibo.it/pers/morandi/didattica/Temporary-ESAS-summer-school-Bologna-2016/Park.pdf.
83. D. Haught, "Recent HTS activities in the US." pp. 1-47, IEA HTS Executive Committee Meeting, Milan, Italy, June 19, 2014. http://www.superpower-nc.com/system/files/2014_0619_Haught+IEA+HTS+ExCo.pdf.
84. T. Yagai et al., “Development of design for large scale conductors and coils using MgB2 for superconducting magnetic energy storage device,” Cryogenics, vol. 96, pp. 75-82, 2018.
85. M. Elsherif, P. Taylor and S. Blake, "Investigating the potential impact of superconducting distribution networks," 22nd International Conference and Exhibition on Electricity Distribution (CIRED 2013), Stockholm, 2013, pp. 1-4.
86. Y. Rammah, A. Salama, and M. Elkhatib, “Magnetic Moment and its Correlation with the Critical Temperature in YBCO,” Interceram-International Ceramic Review, vol. 68, no. 5, pp. 34-41, 2019.
87. K. Tsuchiya, A. Kikuchi, A. Terashima et al., “Critical current measurement of commercial REBCO conductors at 4.2 K,” Cryogenics, vol. 85, pp. 1-7, 2017.
88. B. B. Jensen, N. Mijatovic, and A. B. Abrahamsen, “Development of superconducting wind turbine generators,” J. Renew. Sustain. Energy, vol. 5, no. 2, 023137, 2013.
89. N. Bykovskiy, S. Kaal, A. Dudarev et al., “Demonstration of engineering current density exceeding 1 kA mm− 2 in ultra-thin no-insulation, soldered coil windings using NbTi/Cu wires with CuNi cladding,” Supercond. Sci. Technol, vol. 33, no. 11, 114001, 2020.
90. J. H. Durrell et al., "A trapped field of 17.6 T in melt-processed bulk Gd-Ba-Cu-O reinforced with shrink-fit steel", Supercond. Sci. Technol., vol. 27, no. 8, 082001, 2014.
91. T. Hirano et al., "A record-high trapped field of 1.61 T in MgB2 bulk comprised of copper plates and soft iron yoke cylinder using pulsed-field magnetization," Supercond. Sci. Technol., vol. 33, no. 8, 085002, 2020.
92. E. Kurbatova et al, "Electromagnetic Analysis of HTS Generator with Bulk Superconductor," 2018 20th International Symposium on Electrical Apparatus and Technologies (SIELA), Bourgas, 2018, pp. 1-4.
93. Y. Zhang, D. Zhou, T. Ida, M. Miki and M. Izumi, "Meltgrowth bulk superconductors and application to an axial gap-type rotating machine," Supercond. Sci. Technol., vol. 29, no. 4, 044005, 2016.
94. A. Colle et al, "Analytical Model for the Magnetic Field Distribution in a Flux Modulation Superconducting Machine," IEEE Trans. Magn., vol. 55, no. 12, pp. 1-9, 2019.
95. A. Patel, et al., "Trapped fields greater than 7 T in a 12 mm square stack of commercial high-temperature superconducting tape", Appl. Phys. Lett., 102, 102601, 2013.
96. A. Patel et al, "Design considerations for fully superconducting synchronous motors aimed at future electric aircraft," 2018 IEEE International Conference on Electrical Systems for Aircraft, Railway, Ship Propulsion and Road Vehicles & International Transportation Electrification Conference (ESARS-ITEC), Nottingham, 2018, pp. 1-6.

97. M. Kapolka et al., "Cross-field demagnetization of stacks of tapes: 3D modelling and measurements", Supercond. Sci. Technol., vol. 33, no. 4, 044019, 2020.
98. H. Maeda and Y. Yanagisawa, "Recent Developments in High-Temperature Superconducting Magnet Technology (Review)," IEEE Transactions on Applied Superconductivity, vol. 24, no. 3, pp. 1-12, 2014.
99. Part of the lattice structure of YBCO, by Rswarbrick-Own work, based on Wikipedia's Ybco002.jpg, CC BY-SA 3.0, https://commons.wikimedia.org/w/index.php?curid=5617262.
100. G. Fuchs and L. Schultz, Concise Encyclopedia of Magnetic and Superconducting Materials 2nd Edition, Elsevier Ltd., 2005.
101. Y. Yasukawa, et al, "Consequence of isovalent rare earth substitution to magnetic irreversibility in cation-stoichiometric CuBa2RECu2O693±001," Appl. Phys. Lett., vol. 78, pp. 2917-2919, 2001.
102. C. P. Bean, "Magnetization of hard superconductors," Phys. Rev. Lett., vol. 8, no. 6, pp. 250-253, 1962.
103. Y. B. Kim, C. F. Hempstead, and A. R. Strnad, “Critical persistent currents in hard superconductors,” Phys. Rev. Lett., vol. 9, no. 7, pp. 306–309, 1962.
104. P. W. Anderson, “Theory of flux creep in hard superconductors,” Phys. Rev. Lett., vol. 9, no. 7, pp. 309–311, 1962.
105. J. Rhyner, “Magnetic properties and AC-losses of superconductors with power law current-voltage characteristics,” Physica C, vol. 212, pp. 292–300, 1993.
106. C. P. Poole, Superconductivity, 2nd ed. Elsevier Ltd., 2007.
107. D. Dew-Hughes, "The critical current of superconductors: an historical review," *Fiz. Nizk. Temp.*, vol. 27, pp. 967-979, 2001.
108. H. Kamerlingh Onnes, "Further Experiments with liquid helium. H. On the electrical resistance of pure metals etc. VII The potential difference necessary for the electric current through mercury below 4.19 K (continuation)," *Comm. Physical Lab.*, Leiden, 133b, 29, 1913.
109. N. Nibbio, S. Stavrev and B. Dutoit, "Finite element method simulation of AC loss in HTS tapes with B-dependent *E-J* power law," IEEE Transactions on Applied Superconductivity, vol. 11, no. 1, pp. 2631-2634, 2001.
110. F. Gömöry, "Improvement of the self-field critical current of a high-T_c superconducting tape by the edge cover from soft ferromagnetic material," *Appl. Phys. Lett.*, vol. 89, 072506, 2006.
111. X. Zhang, Z. Zhong, H. S. Ruiz, J. Geng and T. A. Coombs, "General approach for the determination of the magneto-angular dependence of the critical current of YBCO coated conductors", *Supercond. Sci. Technol.*, vol. 30, 025010, 2017.
112. B. C. Robert, M. U. Fareed and H. S. Ruiz, "How to Choose the Superconducting Material Law for the Modelling of 2G-HTS Coils", Materials, vol. 12, 2679, 2019.
113. M. D. Ainslie (2012). Transport AC loss in high temperature superconducting coils (Doctoral thesis). https://doi.org/10.17863/CAM.14029.
114. E. H. Brandt and M. Indenbom, “Type-II superconductor strip with current in a perpendicular magnetic field,” Phys. Rev. B, vol. 48, no. 17, pp. 12893–12906, 1993.
115. M. R. Halse, "AC face field losses in a type II superconductor", J. Phys. D Appl. Phys., vol. 3, no. 5, pp. 717-720, 1970.
116. E. Zeldov, J. Clem, M. McElfresh and M. Darwin, "Magnetization and transport currents in thin superconducting films", Phys. Rev. B, vol. 49, no. 14, pp. 9802-9822, 1994.
117. W. T. Norris, “Calculation of hysteresis loss in hard superconductors carrying ac: isolated conductors and edges of thin sheets,” J. Phys. D: Appl. Phys., vol. 3, pp. 489–507, 1969.

118. S. Farinon et al, "Applicability of the Adaptive Resistivity Method to Describe the Critical State of Complex Superconducting Systems", J. Supercond. Nov. Magn., vol. 25, pp. 2343–2350, 2012.
119. G. P. Mikitik, Y. Mawatari, A. T. S. Wan and F. Sirois, "Analytical Methods and Formulae for Modeling High Temperature Superconductors," IEEE Trans. Appl. Supercond, vol. 23, no. 2, pp. 8001920-8001920, 2013.
120. Y. Mawatari, "Critical state of superconducting strip array systems in perpendicular magnetic fields," IEEE Trans. Appl. Supercond, vol. 7, no. 2, pp. 1216-1219, 1997.
121. Y. Mawatari, "Critical state of periodically arranged superconducting-strip lines in perpendicular fields", Phys. Rev. B Condens. Matter, vol. 54, no. 18, pp. 13215-13221, 1996.
122. H. Zhang, et al., "Dependence of Dynamic Loss on Critical Current and n-Value of HTS Coated Conductors," IEEE Trans. Appl. Supercond., vol. 29, no. 8, pp. 1-7, 2019.
123. H. Zhang, et al., "A full-range formulation for dynamic loss of HTS coated conductors," Supercond. Sci. Technol., vol. 33, no. 5, 05LT01, 2020.
124. J. J. Rabbers, B. ten Haken, O. A. Shevchenko and H. H. J. ten Kate, "An engineering formula to describe the AC loss of BSCCO/Ag tape," IEEE Trans. Appl. Supercond., vol. 11, no. 1, pp. 2623-2626, 2001.
125. A. Naoyuki, M. Shun-ichi, B. Nobuya and M. Kengo, "Numerical modelings of superconducting wires for AC loss calculations," *Physica C Supercond*, vol. 310, no. 1-4, pp. 16-29, 1998.
126. S. Sugita and H. Ohsaki, “Numerical analysis of AC losses in REBCO thin film for coated conductor and fault current limiter,” *Physica C Supercond*, vol. 392–396, pp. 1150–1155, 2003.
127. F. Sirois, F. Grilli, "Potential and limits of numerical modeling for supporting the development of HTS devices", *Supercond. Sci. Technol.*, vol. 28, no. 4, 043002, 2015.
128. E. H. Brandt, "Superconductors of finite thickness in a perpendicular magnetic field: Strips and slabs", *Phys. Rev. B*, vol. 54, no. 6, pp. 4246-4264, 1996.
129. S. Otten and F. Grilli, "Simple and Fast Method for Computing Induced Currents in Superconductors Using Freely Available Solvers for Ordinary Differential Equations," *IEEE Trans. Appl. Supercond*., vol. 29, no. 8, pp. 1-8, 2019.
130. Website of the HTS Modelling Workgroup, 2019. [online] Available: http://www.htsmodelling.com.
131. N. Nibbio, S. Stavrev, and B. Dutoit, "Finite element method simulation of AC loss in HTS tapes with B-dependent E-J power law, " *IEEE Trans. Appl. Supercond*., vol. 11, no. 1, pp. 2631–2634, 2001.
132. M. Costa et al., "3D modeling of coupling between superconducting filaments via resistive matrix in AC magnetic field," *IEEE Trans. Appl. Supercond*., vol. 13, no. 2, pp. 3634-3637, 2003.
133. A. Stenvall and T. Tarhasaari, "Programming finite element method based hysteresis loss computation software using non-linear superconductor resistivity and $\boldsymbol{T}$-$\boldsymbol{\phi}$ formulation", *Supercond. Sci. Technol.*, vol. 23, no. 7, 075010, 2010.
134. A. Stenvall and T. Tarhasaari, "An eddy current vector potential formulation for estimating hysteresis losses of superconductors with FEM", *Supercond. Sci. Technol*., vol. 23, no. 12, 125013, 2010.

135. V. Lahtinen et al, "Comparison of three eddy current formulations for superconductor hysteresis loss modelling", *Supercond. Sci. Technol*., vol. 25, no. 11, pp. 115001-1-115001-14, 2012.
136. E. Vinot, G. Meunier, and P. Tixador, "Different formulations to model superconductors," *IEEE Trans. Magn.*, vol. 36, no. 4, pp. 1226-1229, 2002.
137. F. Grilli, "Numerical Modeling of HTS Applications," *IEEE Trans. Appl. Supercond*, vol. 26, no. 3, pp. 1-8, 2016.
138. B. Shen, F. Grilli and T. A. Coombs, "Review of the AC loss computation for HTS using H formulation", *Supercond. Sci. Technol*., vol. 33, 033002, 2020.
139. B. Shen et al, "Overview of H-Formulation: A Versatile Tool for Modeling Electromagnetics in High-Temperature Superconductor Applications," *IEEE Access*, vol. 8, pp. 100403-100414, 2020.
140. V. Lahtinen, and A. Stenvall, "Scientific Research in the Field of Mesh Method Based Modeling of AC Losses in Superconductors: A Review." *J. Supercond. Nov. Magn*., vol. 27, no.3, pp. 641-650, 2014.
141. A. Arsenault, F. Sirois and F. Grilli, "Implementation of the H-ϕ Formulation in COMSOL Multiphysics for Simulating the Magnetization of Bulk Superconductors and Comparison With the H-Formulation," *IEEE Trans. Appl. Supercond*, vol. 31, no. 2, pp. 1-11, 2021.
142. D. N. Nguyen et al., "A new finite-element method simulation model for computing AC loss in roll assisted biaxially textured substrate YBCO tapes", *Supercond. Sci. Technol.*, vol. 23, 025001, 2009.
143. M. D. Ainslie et al, "An improved FEM model for computing transport AC loss in coils made of RABiTS YBCO coated conductors for electric machines", *Supercond. Sci. Technol.*, vol. 24, no. 4, pp. 045005, 2011.
144. Y. Z. Liu et al., "Comparison of 2D simulation models to estimate the critical current of a coated superconducting coil", *Supercond. Sci. Technol.*, vol. 32, no. 1, 014001, 2019.
145. F. Liang et al., "A finite element model for simulating second generation high temperature superconducting coils/stacks with large number of turns", *J. Appl. Phys*., vol. 122, no. 4, 043903, 2017.
146. P. Machura et al, "Loss characteristics of superconducting pancake, solenoid and spiral coils for wireless power transfer", *Supercond. Sci. Technol*., vol. 33, 074008, 2020.
147. S. Zou, V. M. R. Zermeño and F. Grilli, "Simulation of Stacks of High-Temperature Superconducting Coated Conductors Magnetized by Pulsed Field Magnetization Using Controlled Magnetic Density Distribution Coils," *IEEE Trans. Appl. Supercond*., vol. 26, no. 3, pp. 1-5, 2016.
148. V. V. Zubko et al., "AC losses analysis in stack of 2G HTS tapes in a coil", *J. Phys. Conf. Ser*., 1559, 012115, 2020.
149. T. Benkel et al., "T–A-Formulation to Model Electrical Machines With HTS Coated Conductor Coils," *IEEE Trans. Appl. Supercond.*, vol. 30, no. 6, pp. 1-7, 2020.
150. L. Wang, J. Zheng, Y. Song and Y. Wan, "Multiscale Model for Simulation of Large-Scale YBCO Solenoid Coils With J Infinite-Turn," *IEEE Trans. Appl. Supercond.*, vol. 29, no. 2, pp. 1-5, 2019.
151. E. Berrospe-Juarez et al, "Real-time simulation of large-scale HTS systems: Multi-scale and homogeneous models using the T–A formulation", *Supercond. Sci. Technol*., vol. 32, no. 6, 065003, 2019.

152. G. G. Sotelo, M. Carrera, J. Lopez-Lopez and X. Granados, "H-formulation FEM modeling of the current distribution in 2G HTS tapes and its experimental validation using hall probe mapping", *IEEE Trans. Appl. Supercond.*, vol. 26, no. 8, pp. 1-10, 2016.
153. J. Kapek et al, "2-D Numerical Modeling of a Bulk HTS Magnetization Based on H Formulation Coupled With Electrical Circuit," *IEEE Trans. Appl. Supercond.*, vol. 29, no. 5, pp. 1-5, 2019.
154. Y. Ru et al., "Numerical simulation of dynamic fracture behavior in bulk superconductors with an electromagnetic-thermal model," *Supercond. Sci. Technol.*, vol. 32, no. 7, 074001, 2019.
155. R. Brambilla et al, "A Finite-Element Method Framework for Modeling Rotating Machines With Superconducting Windings," *IEEE Trans. Appl. Supercond.*, vol. 28, no. 5, pp. 1-11, 2018.
156. Y. Yang, H. Yong, X. Zhang and Y. Zhou, "Numerical Simulation of Superconducting Generator Based on the T–A Formulation," *IEEE Trans. Appl. Supercond.*, vol. 30, no. 8, pp. 1-11, 2020.
157. X. Huang, Z. Huang, X. Xu, L. Wang, W. Li and Z. Jin, "A Fully Coupled Numerical Method for Coated Conductor HTS Coils in HTS Generators," *IEEE Trans. Appl. Supercond*, vol. 30, no. 4, pp. 1-6, 2020.
158. Y. Gao et al., "Design, Fabrication, and Testing of a YBCO Racetrack Coil for an HTS Synchronous Motor With HTS Flux Pump," *IEEE Trans. Appl. Supercond*, vol. 30, no. 4, pp. 1-5, 2020.
159. C. R. Vargas-Llanos, S. Lengsfeld and F. Grilli, "T-A Formulation for the Design and AC Loss Calculation of a Superconducting Generator for a 10 MW Wind Turbine," *IEEE Access*, vol. 8, pp. 208767-208778, 2020.
160. Numerical modelling of superconductors and components. [online] Available: http://www.itep.kit.edu/english/67.php.
161. P. Dular and C. Geuzaine.{GetDP} reference manual: The documentation for {GetDP}, a general environment for the treatment of discrete problems. University of Liège, 2019, http://getdp.info.
162. L. Burger, C. Geuzaine, F. Henrotte, and B. Vanderheyden. "Modelling the penetration of magnetic flux in thin superconducting films with shell transformations. *COMPEL*, vol. 38, no. 5, pp.1441–1452, 2019.
163. V. M. R. Zermeno, A. B. Abrahamsen, N. Mijatovic, B. B. Jensen and M. P. Soerensen, "Calculation of AC losses in stacks and coils made of second generation high temperature superconducting tapes for large scale applications", *J. Appl. Phys.*, vol. 114, no. 17, pp. 173901-1-173901-9, 2013.
164. V. M. R. Zermeño and F. Grilli, "3D modeling and simulation of 2G HTS stacks and coils", *Supercond. Sci. Technol.*, vol. 27, no. 4, 044025, 2014.
165. H. Zhang et al, "High Temperature Superconducting Halbach Array Topology for Air-cored Electrical Machines", *J. Phys.: Conf. Ser*, vol. 1559, 012140, 2020.
166. V. M. R. Zermeno et al., "Towards Faster FEM Simulation of Thin Film Superconductors: A Multiscale Approach," *IEEE Trans. Appl. Supercond.*, vol. 21, no. 3, pp. 3273-3276, 2011.
167. L. Quéval, V. M. R. Zermeño and F. Grilli, "Numerical models for ac loss calculation in large-scale applications of HTS coated conductors", *Supercond. Sci. Technol.*, vol. 29, no. 2, 024007, 2016.

168. E. Berrospe-Juarez, F. Trillaud, V. Zermeno, and F. Grilli, "Advanced electromagnetic modeling of large-scale high temperature superconductor systems based on H and T-A formulations", *Supercond. Sci. Technol.*, 2021, in press https://iopscience.iop.org/article/10.1088/1361-6668/abde87.
169. M. Solovyov et al., "A-V formulation for numerical modelling of superconductor magnetization in true 3D geometry", *Supercond. Sci. Technol*., vol. 32, no. 11, 115001, 2019.
170. H. Zhang et al., "Electromagnetic properties of curved HTS trapped field stacks under high-frequency cross fields for high-speed rotating machines", *Supercond. Sci. Technol*., 2021, in press https://doi.org/10.1088/1361-6668/abe4b6.
171. V. Zermeno, F. Grilli and F. Sirois, "A full 3D time-dependent electromagnetic model for Roebel cables", *Supercond. Sci. Technol*., vol. 26, no. 5, 052001, 2013.
172. H. Zhang, M. Zhang and W. Yuan, "An efficient 3D finite element method model based on the T–A formulation for superconducting coated conductors," *Supercond. Sci. Technol*., vol. 30, no. 2, 024005, 2016.
173. M. Zhang and T. A. Coombs, "3D modeling of high-Tc superconductors by finite element software", *Supercond. Sci. Technol*., vol. 25, no. 1, 015009, 2012.
174. M. Kapolka and E. Pardo, "3D modelling of macroscopic force-free effects in superconducting thin films and rectangular prisms", *Supercond. Sci. Technol.*, vol. 32, no. 5, 054001, 2019.
175. D. Hu et al., " DC characterization and 3D modelling of a triangular, epoxy-impregnated high temperature superconducting coil", *Supercond. Sci. Technol*., vol. 28, no. 6, 065011, 2015.
176. J. Sheng et al, "Numerical Study on Magnetization Characteristics of Superconducting Conductor on Round Core Cables," *IEEE Trans. Appl. Supercond.*, vol. 27, no. 4, pp. 1-5, 2017.
177. D. Hu et al., "3D modelling of all-superconducting synchronous electric machines by the finite element method", Proc. COMSOL Conf., 2014, [online] Available: https://www.comsol.com/paper/download/199173/hu_paper.pdf.
178. R. Brambilla, F. Grilli, L. Martini, and F. Sirois, "Integral equations for the current density in thin conductors and their solution by finite element method," *Supercond. Sci. Technol*., vol. 21, no. 10, 105008, 2008.
179. E. Pardo et al, "Current distribution and ac loss for a superconducting rectangular strip with in-phase alternating current and applied field," *Supercond. Sci. Technol*., vol. 20, no. 4, pp. 351–364, 2007.
180. E. Pardo, J. Souc, and L. Frolek, "Electromagnetic modelling of superconductors with a smooth current-voltage relation: Variational principle and coils from a few turns to large magnets," *Supercond. Sci. Technol*., vol. 28, no. 4, 044003, 2015.
181. S. Li, J. Kovac, and E. Pardo, "Coupling loss at the end connections of REBCO stacks: 2D modelling and measurement," *Supercond. Sci. Technol*., vol. 33, no. 7, 075014, 2020.
182. S. Farinon et al, "Critical state and magnetization loss in multifilamentary superconducting wire solved through the commercial finite element code ANSYS," *Supercond. Sci. Technol*., vol. 23, 115004, 2010.
183. K. Zhang et al, "Magnetization Simulation of Rebco Tape Stack With a Large Number of Layers Using the Ansys A-V-A Formulation," *IEEE Trans. Appl. Supercond*, vol. 30, no. 4, pp. 1-5, 2020.
184. AC Losses in a Superconducting Magnet in the Presence of a Time-Dependent Transport Current (ANSYS 15.0), [online] Available: http://www.htsmodelling.com/?page_id=748.

185. H. Zhang et al., "Modelling of electromagnetic loss in HTS coated conductors over a wide frequency band", *Supercond. Sci. Technol.*, vol. 33, no. 2, 025004, 2020.
186. H. Zhang, et al., "Dynamic loss and magnetization loss of HTS coated conductors, stacks, and coils for high-speed synchronous machines," *Supercond. Sci. Technol*., vol. 33, no. 8, 084008, 2020.
187. K. Kails, H. Zhang, P. Machura, M. Mueller and Q. Li, "Dynamic loss of HTS field windings in rotating electric machines", *Supercond. Sci. Technol*., vol. 33, no. 4, 045014, 2020.
188. A. Musso et al, "Analysis of AC Loss Contributions From Different Layers of HTS Tapes Using the A−V Formulation Model," *IEEE Trans. Appl. Supercond*., vol. 31, no. 2, pp. 1-11, 2021.
189. Z. Hong, W. Yuan, M. Ainslie, Y. Yan, R. Pei and T. A. Coombs, "AC Losses of Superconducting Racetrack Coil in Various Magnetic Conditions," *IEEE Trans. Appl. Supercond.*, vol. 21, no. 3, pp. 2466-2469, 2011.
190. V. Lahtinen et al, "Ripple field losses in direct current biased superconductors: Simulations and comparison with measurements", *J. Appl. Phys*., vol. 115, no. 11, 113907, 2014.
191. K. Kails, M. Yao, H. Zhang, P. Machura, M. Mueller and Q. Li, "T-formulation based numerical modelling of dynamic loss with a DC background field", *J. Phys.: Conf. Ser*, vol. 1559, 012145, 2020.
192. B. J. De Bruyn, J. W. Jansen and E. A. Lomonova, "AC losses in HTS coils for high-frequency and non-sinusoidal currents", *Supercond. Sci. Technol*., vol. 30, no. 9, 095006, 2017.
193. Y. S. Wang et al, "Review of AC loss measuring methods for HTS tape and unit," 2*013 IEEE International Conference on Applied Superconductivity and Electromagnetic Devices*, Beijing, 2013, pp. 560-566.
194. S. Kawabata et al, "Standardization of the pickup coil method for AC loss measurement of three-component superconducting wires," *Physica C Supercond*, vol. 392–396, Part 2, pp. 1129-1133, 2003.
195. Y. Yang, E. Martinez, and W. T. Norris, "Configuration and calibration of pickup coils for measurement of ac loss in long superconductors," *J. Appl. Phys*, vol. 96, no. 4, 2141, 2004.
196. J. Souc, E. Pardo, M. Vojenciak and F. Gomory, "Theoretical and experimental study of AC loss in high temperature superconductor single pancake coils," *Supercond. Sci. Technol*., vol. 22, 015006, 2009.
197. J. Ogawa et al, "AC losses in a HTS coil carrying DC current in AC external magnetic field," *Physica C Supercond*, vol. 392-396, pp. 1145-1149, 2003.
198. N. Amemiya et al, "Coupling time constants of striated and copper-plated coated conductors and the potential of striation to reduce shielding current-induced fields in pancake coils," *Supercond. Sci. Technol.*, vol. 31, no. 2, 025007, 2018.
199. K. Kajikawa et al, "Influences of geometrical configuration on AC loss measurement with pickup-coil method," *IEEE Trans. Appl. Supercond.*, vol. 9, no. 2, pp. 746-749, 1999.
200. J. Souc, F. Gmry and M. Vojeniak, "Calibration free method for measurement of the AC magnetization loss", *Supercond. Sci. Technol*., vol. 18, no. 5, pp. 592-595, 2005.
201. G. Messina et al, "AC Loss Measurements of a Trapezoidal Shaped HTS Coil Using an Electrical Method," International Journal of Superconductivity, vol. 2014, 391329, https://doi.org/10.1155/2014/391329.
202. P. Zhou et al., "Transition frequency of transport ac losses in high temperature superconducting coated conductors", *J. Appl. Phys*., vol. 126, no. 6, 063901, 2019.

203. M. Majoros et al, "Transport AC losses in YBCO coated conductors," *Supercond. Sci. Technol*., vol. 20, pp. S299-pp.S304, 2007.
204. J Šouc et al, "AC loss of the short coaxial superconducting cable model made from ReBCO coated tapes," *J. Phys.: Conf. Ser*., vol. 97, 012198, 2008.
205. D. Hu et al., "Transport AC Loss Measurements of a Triangular Epoxy-Impregnated High-Temperature Superconducting Coil," *IEEE Trans. Appl. Supercond.*, vol. 27, no. 4, pp. 1-6, 2017.
206. D. P. Pappas et al, "Enhanced superconducting transition temperature in electroplated rhenium," *Appl. Phys. Lett*., vol. 112, 182601, 2018.
207. R. Pei et al, "High-precision digital lock-in measurements of critical current and AC loss in HTS 2G-tapes," 2008 SICE Annual Conference, Tokyo, 2008, pp. 3147-3150.
208. Ján Šouc and Fedor Gömöry, "New approach to the ac loss measurement in the superconducting secondary circuit of an iron-core transformer," *Supercond. Sci. Technol*., vol. 15, pp. 927-pp. 932, 2002.
209. Y. Liao et al., "An Automatic Compensation Method for Measuring the AC loss of a Superconducting Coil," *IEEE Trans. Appl. Supercond.*, vol. 26, no. 7, pp. 1-5, 2016.
210. X. Pei, A. C. Smith and M. Barnes, "AC Losses Measurement and Analysis for a 2G YBCO Coil in Metallic Containment Vessels," *IEEE Trans. Appl. Supercond.*, vol. 27, no. 4, pp. 1-5, 2017.
211. L. Shen et al, "A distinct method to eliminate the induced voltage in AC loss determination without phase control," *AIP Advances*, vol. 10, 105111, 2020.
212. M. Breschi et al, "An electromagnetic method for measuring AC losses in HTS tapes without lock-in amplifier," *J. Phys.: Conf. Ser*., vol. 1559, 012066, 2020.
213. V. E. Sytnikov et al, "The AC Loss Analysis in the 5 m HTS Power Cables," *IEEE Trans. Appl. Supercond.*, vol. 19, no. 3, pp. 1706-1709, 2009.
214. S. Lee et al, "Performance Analysis of Real-Scale 23 kV/60 MVA Class Tri-Axial HTS Power Cable for Real-Grid Application in Korea," *Energies*, vol. 13, no. 8, 2020.
215. J. J. Rabbers, B. ten Haken, and H. H. J. ten Kate, "Advanced ac loss measurement methods for high-temperature superconducting tapes," *Rev. Sci. Instrum*., vol. 72, no. 5, 2001.
216. Z. Jiang and N. Amemiya, "An experimental method for total AC loss measurement of high Tc superconductors," *Supercond. Sci. Technol*., vol. 17, pp. 371-pp. 379, 2004.
217. S. Pamidi, D. Nguyen, G. Zhang, D. Knoll, U. Trociewitz and J. Schwartz, "Variable Temperature Total AC Loss and Stability Characterization Facility," *IEEE Trans. Appl. Supercond*, vol. 17, no. 2, pp. 3179-3182, 2007.
218. M. Vojenciak et al, "Influence of the voltage taps position on the self-field DC and AC transport characterization of HTS superconducting tapes," *Cryogenics*, vol. 57, pp. 189-194, 2013.
219. K. Zhu et al, "AC loss measurement of HTS coil under periodic current", *Physica C: Superconductivity*, vol. 569, 1353562, 2020.
220. Z. Jiang et al, "Dynamic resistance of a high-T_c coated conductor wire in a perpendicular magnetic field at 77 K", *Supercond. Sci. Technol*., vol. 30, no. 3, 03LT01, 2017.
221. Y. Liu et al, "Dynamic resistance measurement in a YBCO wire under perpendicular magnetic field at various operating temperatures," *J. Appl. Phys*., vol. 126, 243904, 2019.
222. Z. Jiang, R. Toyomoto, N. Amemiya, C. W. Bumby, R. A. Badcock and N. J. Long, "Dynamic Resistance Measurements in a GdBCO-Coated Conductor," *IEEE Trans. Appl. Supercond.*, vol. 27, no. 4, pp. 1-5, 2017.

223. H. Zhang, C. Hao, Y. Xin and M. Mueller, "Demarcation Currents and Corner Field for Dynamic Resistance of HTS-Coated Conductors," *IEEE Trans. Appl. Supercond.*, vol. 30, no. 8, pp. 1-5, 2020.
224. M. P. Oomen (2000), AC Loss in Superconducting Tapes and Cables (Doctoral thesis). https://www.elibrary.ru/item.asp?id=5312717.
225. University of Florida-Department of Physics, PHY4803L-Advanced Physics Laboratory, "AC Susceptibility Measurements in High-Tc Superconductors", [online] Available: https://www.phys.ufl.edu/courses/phy4803L/group_II/high_Tc/hightc.pdf.
226. E. Pardo et al, "AC Loss and Voltage Signal in a Pancake Coil Made of Coated Conductor With Ferromagnetic Substrate," *IEEE Trans. Appl. Supercond.*, vol. 19, no. 3, pp. 2223-2227, 2009.
227. F. Gömöry, "Characterization of high-temperature superconductors by AC susceptibility measurements," *Supercond. Sci. Technol.*, vol. 10, no. 8, 523, 1997.
228. K. Kajikawa et al, "A new experimental technique to evaluate perpendicular-field losses of superconducting tape wires with meter-class length," *Physica C Supercond*, vol. 357–360, Part 2, pp. 1201-1204, 2001.
229. M. Iwakuma et al., "AC loss properties of a 1 MVA single-phase HTS power transformer," *IEEE Trans. Appl. Supercond.*, vol. 11, no. 1, pp. 1482-1485, 2001.
230. M. Iwakuma et al, "Theoretical investigation on the detection ratio of the magnetization in superconducting wires by a saddle-shaped pick-up coil," *Supercond. Sci. Technol.*, vol. 16, no. 5, pp. 545-556, 2003.
231. K. Funaki et al., "Transport AC Loss Properties of a Bi-2223 Superconducting Coil From 0.1 Hz to 10 Hz," *IEEE Trans. Appl. Supercond.*, vol. 23, no. 3, pp. 4700804-4700804, 2013.
232. H. Sasa et al, "Estimation Method for AC Loss of Perpendicularly Stacked REBa2Cu3Oy Superconducting Tapes under Magnetic Field," *Physica C Supercond*, vol. 580, 1353801, 2021.
233. L. Muzzi1 and M. Spadoni, "Magnetic method for AC losses measurement of coil wound CICCs in pulsed regimes," *Supercond. Sci. Technol.*, vol. 16, pp. 19-23, 2003.
234. L. M. Fisher, A.V. Kalinov, and I. F. Voloshin, " Simple calibration free method to measure ac magnetic moment and losses," *J. Phys.: Conf. Ser.*, vol. 97, 012032, 2008.
235. M. Chiletti (2020). Coupling losses in large superconducting Cable in Conduit Conductors for fusion reactors: Analytical modelling and experimental investigations (Doctoral thesis). Electromagnetism. AMU - Aix Marseille Université.
236. V. A. Anvar, "AC loss and contact resistance of different CICC cable patterns: Experiments and numerical modeling," *Fusion Engineering and Design*, vol. 161, 111898, 2020.
237. D. N. Nguyen et al, "AC loss measurement with a phase difference between current and applied magnetic field," *IEEE Trans. Appl. Supercond.*, vol. 15, no. 2, pp. 2831-2834, 2005.
238. M Vojenciak et al, "Study of ac loss in Bi-2223/Ag tape under the simultaneous action of ac transport current and ac magnetic field shifted in phase," *Supercond. Sci. Technol.*, vol. 19, pp. 397-404, 2006.
239. R. D. McConnell and P. R. Critchlow, "Variable temperature apparatus using a thermal conductivity measurement technique for the determination of superconducting ac power loss", *Rev. Sci. Instrum.*, vol. 46, no. 511, 1975.
240. C. Schmidt and E. Specht, "ac loss measurements on superconductors in the microwatt range", *Rev. Sci. Instrum.*, vol. 61, no. 988, 1990.

241. P. Dolez et al, "Calorimetric ac loss measurements of silver sheathed Bi-2223 superconducting tapes", *Supercond. Sci. Technol*, vol. 9, pp. 374-378, 1996.
242. P. Dolez et al, "Improvements and validation of the null calorimetric method for a.c. loss measurements in superconductors", *Cryogenics*, vol. 38, pp. 429-434, 1998.
243. S. P. Ashworth and M. Suenaga, "The calorimetric measurement of losses in HTS tapes due to AC magnetic fields and transport currents", *Physica C Supercond*, vol. 315, pp. 79-84, 1999.
244. K. W. See, C. D. Cook and S. X. Dou, "Innovative Calorimetric AC Loss Measurement of HTSC for Power Applications," *IEEE Trans. Appl. Supercond.*, vol. 21, no. 3, pp. 3261-3264, 2011.
245. K. W. See et al, "Calorimetric AC loss measurement of MgB2 superconducting tape in an alternating transport current and direct magnetic field," *Supercond Sci. Technol.*, vol. 25, 115016, 2012.
246. P. Ghoshal, T. Coombs and A. Campbell, "Calorimetric method of ac loss measurement in a rotating magnetic field", *Rev. Sci. Instrum*., vol. 81, 074702, 2010.
247. J. Hartwig et al, "New Test Rig to Measure Alternating Current Losses of Both Low and High Critical Temperature Superconductors", NASA/TM—2019-220046, [online] Available : https://ntrs.nasa.gov/api/citations/20190025926/downloads/20190025926.pdf.
248. J. S. Dai et al, "A novel calorimetric method for measurement of AC losses of HTS tapes by optical fiber Bragg grating," 2013 IEEE International Conference on Applied Superconductivity and Electromagnetic Devices, Beijing, 2013, pp. 124-127.
249. C. H. Jones and H. L. Schenk, "A.C. losses in hard superconductors" *Advances in Cryogenic Engineering*, New York: Plenum, vol. 8, pp. 579-584, 1963.
250. K. Kuroda, "ac losses of superconducting solenoidal coils", *J. Appl. Phys*., vol. 53, 578, 1982.
251. K. Kuroda, "Modified boil-off method for measuring AC losses of superconducting composites", *Cryogenics*, vol. 26, pp. 566-568, 1986.
252. H. Okamoto, F. Sumiyoshi, K. Miyoshi and Y. Suzuki, "The Nitrogen Boil-Off Method for Measuring AC Losses in HTS Coils," *IEEE Trans. Appl. Supercond.*, vol. 16, no. 2, pp. 105-107, 2006.
253. W. Yuan, et al, "Measurements and calculations of transport AC loss in second generation high temperature superconducting pancake coils", *J. Appl. Phys*., vol. 110, 113906, 2011.
254. J. P. Murphy et al., "Experiment Setup for Calorimetric Measurements of Losses in HTS Coils Due to AC Current and External Magnetic Fields," *IEEE Trans. Appl. Supercond.*, vol. 23, no. 3, pp. 4701505-4701505, 2013.
255. M. Iwakuma et al., "AC loss properties of YBCO superconducting tapes fabricated by IBAD-PLD technique", *Physica C Supercond*, vol. 412–414, pp. 983-991, 2004.
256. Z. Jiang, "Total AC loss characteristics in a stacked YBCO conductor", *IEEE Trans. Appl. Supercond*., vol. 17, no. 2, pp. 2442-2445, 2007.
257. B. Shen et al., "Investigation of AC losses in horizontally parallel HTS tapes", *Supercond. Sci. Technol*., vol. 30, no. 7, 075006, 2017.
258. M. D. Ainslie et al, "Modeling and Electrical Measurement of Transport AC Loss in HTS-Based Superconducting Coils for Electric Machines," *IEEE Trans. Appl. Supercond*., vol. 21, no. 3, pp. 3265-3268, 2011.
259. M. Zhang et al., "AC Loss Measurements for 2G HTS Racetrack Coils With Heat-Shrink Tube Insulation," *IEEE Trans. Appl. Supercond*., vol. 24, no. 3, pp. 1-4, 2014.

260. J. Kim, C. H. Kim, G. Iyyani, J. Kvitkovic and S. Pamidi, "Transport AC loss measurements in superconducting coils", *IEEE Trans. Appl. Supercond*., vol. 21, no. 3, pp. 3269-3272, 2011.
261. M. Zhang, J. Kvitkovic, S. Pamidi and T. A. Coombs, "Experimental and numerical study of a YBCO pancake coil with a magnetic substrate", *Supercond. Sci. Technol*., vol. 25, no. 12, 125020, 2012.
262. B. Liu et al., "Research on AC losses of racetrack superconducting coils applied to high-temperature superconducting motors", *Supercond. Sci. Technol*., vol. 32, 115010, 2019.
263. M. Zhang et al., "Total AC loss study of 2G HTS coils for fully HTS machine applications", *Supercond. Sci. Technol*., vol. 28, 115011, 2015.
264. F. Weng, M. Zhang, T. Lan, Y. Wang and W. Yuan, "Fully superconducting machine for electric aircraft propulsion: Study of AC loss for HTS stator", *Supercond. Sci. Technol*., vol. 33, no. 10, 104002, 2020.
265. N. Amemiya et al., "AC loss reduction of YBCO coated conductors by multifilamentary structure", *Supercond. Sci. Technol*., vol. 17, no. 12, pp. 1464-1471, 2004.
266. M. D. Sumption, P. N. Barnes and E. W. Collings, "AC losses of coated conductors in perpendicular fields and concepts for twisting", *IEEE Trans. Appl. Supercond*., vol. 15, no. 2, pp. 2815-2818, 2005.
267. M. Marchevsky et al, "AC losses and magnetic coupling in multifilamentary 2G HTS conductors and tape arrays", *IEEE Trans. Appl. Supercond*., vol. 19, no. 3, pp. 3094-3097, 2009.
268. F. Grilli and A. Kario, "How filaments can reduce AC losses in HTS coated conductors: A review", *Supercond. Sci. Technol*., vol. 29, no. 8, 083002, 2016.
269. A. Godfrin et al., "Influence of the Striation Process and the Thickness of the Cu-Stabilization on the AC Magnetization Loss of Striated REBCO Tape," *IEEE Trans. Appl. Supercond*., vol. 27, no. 6, pp. 1-9, 2017.
270. J. Herrmann, K. H. Muller, N. Savvides, G. Gnanarajan, A. Thorley and A. Katsaros, "AC losses in YBCO strips on YSZ/Hastelloy substrates", *Physica C Supercond*, vol. 341, no. 4, pp. 2493-2494, 2000.
271. C. B. Cobb, P. N. Barnes, T .J. Haugan, J. Tolliver, E. Lee, M. Sumption, et al., "Hysteresis loss reduction in striated YBCO", *Physica C Supercond*, vol. 382, pp. 52-56, 2002.
272. M. Majoros et al, "Hysteresis losses in YBCO coated conductors on textured metallic substrates," *IEEE Trans. Appl. Supercond*., vol. 13, no. 2, pp. 3626-3629, 2003.
273. M. Majoros, B. A. Glowacki, A. M. Campbell, G. A. Levin, P. N. Barnes and M. Polak, "AC losses in striated YBCO coated conductors," *IEEE Trans. Appl. Supercond*., vol. 15, no. 2, pp. 2819-2822, 2005.
274. Y. Zhang et al., "AC Loss Reduction in Filamentized YBCO Coated Conductors With Virtual Transverse Cross-Cuts," *IEEE Trans. Appl. Supercond*., vol. 21, no. 3, pp. 3301-3306, 2011.
275. S. P. Ashworth and F. Grilli, "A strategy for the reduction of AC losses in YBCO coated conductors", *Supercond. Sci. Technol*., vol. 19, no. 2, pp. 227-232, 2006.
276. D. Abraimov et al., "Significant reduction of AC losses in YBCO patterned coated conductors with transposed filaments", *Supercond. Sci. Technol.*, vol. 21, no. 8, 082004, 2008.
277. J. C. Prestigiacomo et al., "Use of Laser Lithography for Striating 2G HTS Conductors for AC Loss Reduction," *IEEE Trans. Appl. Supercond*., vol. 27, no. 8, pp. 1-5, 2017.
278. M. Wang, M. Zhang, M. Song and Z. Li, "An effective way to reduce AC loss of second-generation high temperature superconductors", *Supercond. Sci. Technol.*, vol. 32, 01LT01, 2019.

279. V. Hussennether, M. Oomen, M. Leghissa and H. Neumuller, "DC and AC properties of Bi-2223 cabled conductors designed for high-current applications", *Phys. C Supercond*, vol. 401, pp. 135-139, 2004.
280. W. Goldacker et al., "Roebel cables from REBCO coated conductors: A one-century-old concept for the superconductivity of the future", *Supercond. Sci. Technol.*, vol. 27, no. 9, 093001, 2014.
281. N. J. Long, R. Badcock, P. Beck, M. Mulholl, N. Ross, M. Staines, H. Sun, J. Hamilton, and R. G. Buckley, "Narrow strand YBCO Roebel cable for lowered AC loss," *J. Phys., Conf. Ser*., vol. 97, 012280, 2008.
282. M. N. Wilson, Superconducting Magnets. London, UK: Oxford Press, 1970.
283. C. E. Oberly, B. Razidlo, and F. Rodriguez, "Conceptual approach to the ultimate low AC loss YBCO superconductor," *IEEE Trans. Appl. Supercond*., vol. 15, no. 2, pt. 2, pp. 1643–1646, 2005.
284. D. C. van der Laan, " $YBa_2Cu_3O_{7-\delta}$ coated conductor cabling for low ac-loss and high-field magnet applications", *Supercond. Sci. Technol*., vol. 22, no. 6, pp. 065013-065015, 2009.
285. J. Weiss et al, "Introduction of CORC wires: Highly flexible, round high-temperature superconducting wires for magnet and power transmission applications," *Supercond. Sci. Technol*., vol. 30, no. 1, 014002, 2016.
286. D. C. van der Laan, D. M. McRae and J. D. Weiss, "Status of CORC cables and wires for use in high-field magnets and power systems a decade after their introduction", *Supercond. Sci. Technol*., vol. 32, 033001, 2019.
287. N. Glasson et al, "Development of a 1 MVA 3-Phase Superconducting Transformer Using YBCO Roebel Cable," *IEEE Trans. Appl. Supercond*, vol. 21, no. 3, pp. 1393-1396, 2011.
288. LHC Machine Outreach: Super conducting cable. [online] Available: http://lhc-machine-outreach.web.cern.ch/components/cable.htm.
289. M. Takayasu, L. Chiesa, L. Bromberg and J. V. Minervini, "HTS twisted stacked-tape cable conductor", *Supercond. Sci. Technol*., vol. 25, no. 1, 014011, 2012.
290. D. Uglietti, N. Bykovsky, R. Wesche and P. Bruzzone, "Development of HTS Conductors for Fusion Magnets," *IEEE Trans. Appl. Supercond*, vol. 25, no. 3, pp. 1-6, 2015.
291. D. Uglietti et al., "Test of 60 kA coated conductor cable prototypes for fusion magnets", *Supercond. Sci. Technol.*, vol. 28, no. 12, 124005, 2015.
292. M. Vojenčiak et al., "Magnetization ac loss reduction in HTS CORC cables made of striated coated conductors", *Supercond. Sci. Technol*., vol. 28, no. 10, 104006, 2015.
293. R. Terzioglu, M. Vojenciak, J. Sheng, F. Gomory, T. F. Ccedil;avus and I. Belenli, "AC loss characteristics of CORC® cable with a Cu former", *Supercond. Sci. Technol.*, vol. 30, no. 8, 085012, 2017.
294. K Yagotintsev et al, "AC loss and contact resistance in REBCO CORC®, Roebel, and stacked tape cables", *Supercond. Sci. Technol*., vol. 33, 085009, 2020.
295. F. Gomory, M. Vojenciak, E. Pardo and J. Souc, "Magnetic flux penetration and AC loss in a composite superconducting wire with ferromagnetic parts", *Supercond. Sci. Technol*., vol. 22, 034017, 2009.
296. S. Safran, F. Gomory and A. Gencer, "AC loss in stacks of Bi-2223/Ag tapes modified with ferromagnetic covers at the edges", *Supercond. Sci. Technol.*, vol. 23, 105003, 2010.
297. P. Kruger et al, "Superconductor/ferromagnet heterostructures exhibit potential for significant reduction of hysteretic losses", *Appl. Phys. Lett*., vol. 102, 202601, 2013.

298. E. Pardo, J. Souc and M. Vojenciak, "AC loss measurement and simulation of a coated conductor pancake coil with ferromagnetic parts", *Supercond. Sci. Technol.*, vol. 22, 075007, 2009.
299. M. D. Ainslie et al, "Numerical Analysis of AC Loss Reduction in HTS Superconducting Coils Using Magnetic Materials to Divert Flux," *IEEE Trans. Appl. Supercond.*, vol. 23, no. 3, pp. 4700104-4700104, 2013.
300. G. Liu, G. Zhang, L. Jing and H. Yu, "Numerical study on AC loss reduction of stacked HTS tapes by optimal design of flux diverter", *Supercond. Sci. Technol.*, vol. 30, no. 12, 125014, 2017.
301. G. Liu et al., "Study on the AC Loss Reduction of REBCO Double Pancake Coil," *IEEE Trans. Appl. Supercond.*, vol. 28, no. 8, pp. 1-6, 2018.
302. G. Liu et al., "Experimental and numerical study of the frequency-dependent transport ac losses of the YBa2Cu3O7−δ coil with and without flux diverters", *Supercond. Sci. Technol.*, vol. 32, no. 5, 055002, 2019.
303. A. Kawagoe, F. Sumiyoshi, M. Nakanishi, T. Mito and T. Kawashima, "A new winding method to reduce AC losses in stable LTS pulse coils," *IEEE Trans. Appl. Supercond*, vol. 13, no. 2, pp. 2404-2407, 2003.
304. H. Heydari et al, "New approach for AC loss reduction in HTS transformer using auxiliary windings case study: 25 kA HTS current injection transformer", *Supercond. Sci. Technol.*, vol. 21, no. 1, 015009, 2008.
305. J. M. Kim et al, "Investigation about the effects of metal-clad winding on the electromagnetic characteristics of the GdBCO racetrack coils in a time-varying magnetic field," *Results in Physics*, vol. 11, pp. 400-405, 2018.
306. Y. Wang et al., "No-Insulation High-Temperature Superconductor Winding Technique for Electrical Aircraft Propulsion," *IEEE Trans. Transp. Electrification*, vol. 6, no. 4, pp. 1613-1624, 2020.
307. N. Simpson et al, "Additive Manufacturing of Shaped Profile Windings for Minimal AC Loss in Electrical Machines," *IEEE Trans. Ind. Appl.*, vol. 56, no. 3, pp. 2510-2519, 2020.
308. Z. Jiang et al, "15% reduction in AC loss of a 3-phase 1 MVA HTS transformer by exploiting asymmetric conductor critical current," *J. Phys. Commun.*, vol. 5, 025003, 2021.
309. T. Sorokina and S, Zhang, "An interpolated Galerkin finite element method for the Poisson equation," arXiv:2010.01460 [math.NA].
310. M. Yao (2019). Numerical modelling of superconducting power cables with second generation high temperature superconductors (Doctoral thesis). https://era.ed.ac.uk/handle/1842/36640.
311. B. Shen *et al.*, "Investigation and comparison of AC losses on stabilizer-free and copper stabilizer HTS tapes", *Phys. C: Supercond. Appl.*, vol. 541, pp. 40-44, 2017.
312. M. P. Oomen, et al., "Dynamic resistance in a slab-like superconductor with Jc(B) dependence", *Supercond. Sci. Technol.*, vol. 12, no. 6, pp. 382-387, 1999.
313. Q. Li, M. Yao, Z. Jiang, C. W. Bumby and N. Amemiya, "Numerical Modeling of Dynamic Loss in HTS-Coated Conductors Under Perpendicular Magnetic Fields," IEEE Transactions on Applied Superconductivity, vol. 28, no. 2, pp. 1-6, 2018.
314. T. Matsushita, *Flux Pinning and Electromagnetic Phenomenon*. Tokyo, Japan: Sangyo Tosho, Inc., pp.99, 1994.
315. Z. Jiang, *et al.*, "Dynamic resistance of a high-Tc superconducting flux pump." *Applied Physics Letters*, vol. 105, no. 11, 3600104, 2014

316. G. P. Mikitik and E. H. Brandt, "Generation of a dc voltage by an ac magnetic field in type-II superconductors," *Physical Review B*, vol. 64, no. 9, 092502, 2001.
317. Y. Liu, Z. Jiang, Q. Li, C. W. Bumby, R. A. Badcock and J. Fang, "Dynamic Resistance Measurement in a Four-Tape YBCO Stack With Various Applied Field Orientation," *IEEE Trans. Appl. Supercond.*, vol. 29, no. 5, pp. 1-7, 2019.
318. Y. Enomoto, et al, "Simulation study on the first penetration field in type-II superconductors", *Journal of Physics: Condensed Matter*, vol. 9, pp. 10203-10209, 1997.
319. Z. Jiang, et al., "Dynamic Resistance Measurement of a Four-Tape YBCO Stack in a Perpendicular Magnetic Field," *IEEE Trans. Appl. Supercond*., vol. 28, no. 4, pp. 1-5, 2018.
320. Z. Jiang, et al., "The dynamic resistance of YBCO coated conductor wire: Effect of DC current magnitude and applied field orientation," *Supercond. Sci. Technol*., vol. 31, no. 3, pp. 035002, 2018.
321. P. Machura and Q. Li, "A critical review on wireless charging for electric vehicles," *Renew. Sust. Energ. Rev.*, vol. 104, pp. 209-234, 2019.
322. D. M. Vilathgamuwa, J. P. K. Sampath, "Wireless Power Transfer (WPT) for Electric Vehicles (EVs)-Present and Future Trends", *Plug In Electric Vehicles in Smart Grids*, pp. 33-60, 2015.
323. D. R. Lide, CRC Handbook of Chemistry and Physics (CRC Press, 2005).
324. J. Lu, E. S. Choi, H. D. Zhou, "Physical properties of Hastelloy C-276 at cryogenic temperatures", *J. Appl. Phys.*, vol. 103, no. 6, 2008.
325. H. Zhang, Y. Xie, T. Yi, X. Kong, L. Cheng and H. Liu, "Fault Detection for High-Voltage Circuit Breakers Based on Time–Frequency Analysis of Switching Transient *E*-Fields," IEEE Transactions on Instrumentation and Measurement, vol. 69, no. 4, pp. 1620-1631, 2020.
326. R. G. Chambers, "The Anomalous Skin Effect", *Proc. Roy. Soc. (London)*, vol. A215, pp. 481-497, 1952.
327. H. Nakane, "Frequency dependence of Resistivity of High-purity Copper at Low Temperature", *JJAP*, vol. 32, pp. 3199-3203, 1993.
328. W. Royall Cox and J. D. Gavenda, "Temperature Dependence of Electron Mean Free Paths in Cadmium and Copper," *Phys. Rev. B*, vol. 3, no. 10, pp. 3577-3579, 1971.
329. B. Shen, C. Li, J. Geng, X. Zhang, J. Gawith, J. Ma, Y. Liu, F. Grilli and T. A. Coombs, "Power dissipation in HTS coated conductor coil under the simultaneous action of AC and DC currents and fields," *Supercond. Sci. Technol*., vol. 31, no. 7, 075005, 2018.
330. M. D. Ainslie, D. Hu, J. Zou and D. A. Cardwell, "Simulating the In-Field AC and DC Performance of High-Temperature Superconducting Coils," *IEEE Trans. Appl. Supercond.*, vol. 25, no. 3, pp. 1-5, 2015.
331. S. Kalsi, K. Hamilton, R. Buckley and R. Badcock, "Superconducting AC homopolar machines for high-speed applications", *Energies*, vol. 12, no. 1, 2019.
332. T. B. Mitchell-Williams et al., "Uniform trapped fields produced by stacks of HTS coated conductor tape", *Supercond. Sci. Technol.*, vol. 29, no. 8, 2016.
333. W. Yang, X. D. Li, M. Ye, L. Yao and D. P. Liao, "Simulation and Analysis of an (RE)BCO Tape Stack Magnet Under the Pulsed Field Magnetization," *IEEE Trans. Appl. Supercond.*, vol. 28, no. 4, pp. 1-5, June 2018.
334. A. Baskys, A. Patel, S. C. Hopkins and B. A. Glowacki, "Modeling of Trapped Fields by Stacked (RE)BCO Tape Using Angular Transversal Field Dependence," *IEEE Trans. Appl. Supercond.*, vol. 26, no. 3, pp. 1-4, 2016.

335. E. Brandt, "Electric field in superconductors with rectangular cross section", *Phys. Rev. B Condens. Matter*, vol. 52, no. 21, pp. 15442-15457, 1995.
336. S. Zou (2017). Magnetization of high temperature superconducting trapped-field magnets Doctoral thesis). https://www.ksp.kit.edu/9783731507154.
337. V. M. R. Zermeno et al., "Estimation of maximum possible trapped field in superconducting permanent magnets in 2D and 3D," arXiv:1606.01817, 2016.
338. A. Baskys, A. Patel, S. C. Hopkins, V. Kalitka, A. Molodyk and B. A. Glowacki, "Self-Supporting Stacks of Commercial Superconducting Tape Trapping Fields up to 1.6 T Using Pulsed Field Magnetization," *IEEE Trans. Appl. Supercond.*, vol. 25, no. 3, pp. 1-4, June 2015.
339. S. Zou et al., "Simulation and experiments of stacks of high temperature superconducting coated conductors magnetized by pulsed field magnetization with multi-pulse technique", *Supercond. Sci. Technol.*, vol. 30, no. 1, 2017.
340. M. Baghdadi, H. S. Ruiz and T. A. Coombs, "Crossed-magnetic-field experiments on stacked second generation superconducting tapes: Reduction of the demagnetization effects", *Appl. Phys. Lett.*, vol. 104, no. 23, Jun. 2014.
341. A. Dadhich et al., "Time constant of the transverse-field demagnetization of superconducting stacks of tapes", S*upercond. Sci. Technol.*, vol. 33. 065003, 2020.
342. M. D. Ainslie and H. Fujishiro, "Modelling of bulk superconductor magnetization", *Supercond. Sci. Technol.*, vol. 28, 053002, 2015.
343. A. G. Page et al., "The effect of stabilizer on the trapped field of stacks of superconducting tape magnetized by a pulsed field", *Supercond. Sci. Tech.*, vol. 28, no. 8, 085009, 2015.
344. M. Kapolka et al. Cubic bulk as benchmark for 3D modelling of superconductors under slowly varying magnetic fields. 2016.
available at: https://www.htsmodelling.com/?wpdmpro=b5_results-3
345. A. Badia-Majos and C. Lopez, "Electric field in hard superconductors with arbitrary cross section and general critical current law", *J. Appl. Phys.*, vol. 95, 8035, 2004.
346. A. Badia-Majos and C. Lopez, "Critical state model in superconducting parallelepipeds", *Appl. Phys. Lett.*, vol. 86, 202510, 2005.
347. J. Ma, J. Geng, W. K. Chan, J. Schwartz and T. Coombs, "A temperature-dependent multilayer model for direct current carrying HTS coated-conductors under perpendicular AC magnetic fields", *Supercond. Sci. Technol.*, vol. 33, no. 4, 2020.
348. C. Lacroix and F. Sirois, "Concept of a current flow diverter for accelerating the normal zone propagation velocity in 2G HTS coated conductors", *Supercond. Sci. Technol.*, vol. 27, no. 3, 2014.
349. E. Pardo and A. Dadhich, "Cross-field demagnetization behavior of superconducting stacks and bulks: modeling up to 100 tapes and 2 million cycles", arXiv:2008.12006 [physics.app-ph]. https://arxiv.org/abs/2008.12006.
350. S. De, et al, "Low inductance axial flux BLDC motor drive for more electric aircraft," *IET Power Electron.*, vol. 5, no. 1, pp. 124–133, 2012.
351. X. Luo et al, "Overview of current development in electrical energy storage technologies and the application potential in power system operation," *Appl. Energy*, vol.137, pp. 511–536, 2015.
352. A. S. McDonald et al, "A multi-stage axial flux permanent magnet machine for direct drive wind turbines," *IET Conference on Renewable Power Generation (RPG 2011)*, Edinburgh, 2011, pp. 1-6.

353. O. Keysan, M. Mueller et al, "Designing the c-gen lightweight direct drive generator for wave and tidal energy," *IET Renew. Power Gener.*, vol. 6, no. 3, pp. 161-170, 2012.
354. B. Xia et al, "Comparative Study of Air-Cored Axial-Flux Permanent-Magnet Machines With Different Stator Winding Configurations," *IEEE Trans. Ind. Electron.*, vol. 62, no. 2, pp. 846-856, 2015.
355. A. S. McDonald et al., "1MW multi-stage air-cored permanent magnet generator for wind turbines," *6th IET International Conference on Power Electronics, Machines and Drives (PEMD 2012)*, Bristol, 2012, pp. 1-6.
356. O. Keysan et al, "C-GEN, a lightweight direct drive generator for marine energy converters," *5th IET International Conference on Power Electronics, Machines and Drives (PEMD 2010)*, Brighton, UK, 2010, pp. 1-6.
357. K. Halbach, "Design of permanent multipole magnets with oriented rare earth cobalt material", *Nuclear Instruments and Methods*, vol. 169, no. 1, pp. 1-10, 1980.
358. A. K. M. Parvezlqbal et al, "A Review of Permanent Magnet Linear Motor with Halbach Array", *Journal of Engineering and Applied Sciences*, vol. 11, no. 38, pp. 1752-1761, 2016.
359. L. Xu et al, "High-Performance Fault Tolerant Halbach Permanent Magnet Vernier Machines for Safety-Critical Applications," *IEEE Trans. Magn.*, vol. 52, no. 7, pp. 1-4, 2016.
360. S. L. Ho et al, "A novel magnetic-geared tubular linear machine with halbach permanent-magnet arrays for tidal energy conversion," *2015 IEEE International Magnetics Conference (INTERMAG)*, Beijing, 2015, pp. 1-1.
361. B. Shen et al, "Optimization study on the magnetic field of superconducting Halbach array magnet," *Phys. C: Supercond. its Appl.*, vol. 538, pp. 46–51, 2017.
362. B. Shen et al, "Design of a superconducting magnet for Lorentz force electrical impedance tomography," *IEEE Trans. Appl. Supercond.*, vol. 26, no. 3, 2016.
363. M. Mueller and A. Zavvos, "Electrical generators for direct drive systems: A technology overview", *Electrical Drives for Direct Drive Renewable Energy Systems*, U.K., Oxford:Woodhead, pp. 1-29, 2013.
364. A. McDonald, M. Mueller, and A. Zavvos, "Electrical thermal and structural generator design and systems integration for direct drive renewable energy systems", *Electrical Drives for Direct Drive Renewable Energy Systems*, U.K., Oxford:Woodhead, pp. 51-79, 2013.
365. S. Hahn et al, "No-insulation multi-width winding technique for high temperature superconducting magnet", *Appl. Phys. Lett.*, vol. 103, no. 17, Oct. 2013.
366. R. Nasiri-Zarandi and A. Hekmati, "A Review of Suspension and Traction Technologies in Maglev Trains," *2019 International Power System Conference (PSC)*, Tehran, Iran, 2019, pp. 129-135.
367. J. Gou, "Development Status and Global Competition Trends Analysis of Maglev Transportation Technology Based on Patent Data," *Urban Rail Transit*, vol. 4, no. 3, pp. 117-129, 2018.
368. L. Yan, "Development and Application of the Maglev Transportation System," *IEEE Trans. Appl. Supercond.*, vol. 18, no. 2, pp. 92-99, 2008.
369. Q Hyung-Woo Lee, Ki-Chan Kim and Ju Lee, "Review of maglev train technologies," *IEEE Trans. Magn.*, vol. 42, no. 7, pp. 1917-1925, 2006.
370. J. S. Wang et al., "The first man-loading high temperature superconducting Maglev test vehicle in the world", *Physica C*, vol. 378–381, pp. 809-814, 2002.
371. H. Maeda and Y. Yanagisawa, "Recent Developments in High-Temperature Superconducting Magnet Technology (Review)," *IEEE Trans. Appl. Supercond.*, vol. 24, no. 3, pp. 1-12, 2014.

372. Y. Wen, Y. Xin, W. Hong, C. Zhao, and W. Li, "Comparative study between electromagnet and permanent magnet rails for HTS maglev," *Supercond. Sci. Technol*., vol. 33, 035011, 2020.
373. J. Bird and T. A. Lipo, "An electrodynamic wheel: An integrated propulsion and levitation machine", *Proc. IEEE Int. Electric Machines Drives Conf. 2003. IEMDC'03*, pp. 1410-1416, 2003.
374. J. Bird and T. A. Lipo, "Characteristics of an Electrodynamic Wheel Using a 2-D Steady-State Model," *IEEE Trans. Magn.*, vol. 43, no. 8, pp. 3395-3405, 2007.
375. J. Bird and T. A. Lipo, "Calculating the forces created by an electrodynamic wheel using a 2-D steady-state finite-element method", *IEEE Trans. Magnetics*, vol. 44, no. 3, pp. 365-372, 2008.
376. J. Bird, “An investigation into the use of electrodynamic wheels for highspeed ground transportation,” Ph.D. thesis, Dept. Elect. Eng., Univ. of Wisconsin-Madison, Madison, WI, USA, 2007. Online. [Available]: https: //search.library.wisc.edu/catalog/9910040357202121.